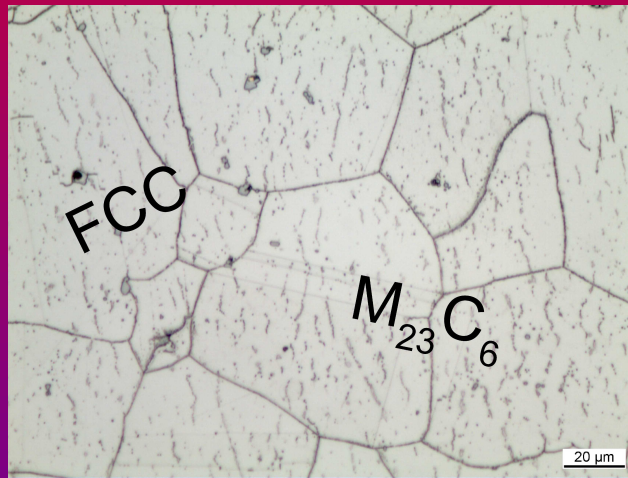


# Thermodynamic Modeling and Experimental Investigations of High Temperature Corrosion and Oxidation due to Increased Power Plant Cycling



Roger Abang

September 2016



# **Thermodynamic Modeling and Experimental Investigations of High Temperature Corrosion and Oxidation due to Increased Power Plant Cycling**

Von der Fakultät für Maschinenbau, Elektro- und Energiesysteme der Brandenburgischen Technischen Universität Cottbus–Senftenberg zur Erlangung des akademischen Grades eines Doktors der Ingenieurwissenschaften

genehmigte Dissertation

vorgelegt von:

Roger Atini Abang, MSc.

geboren am 09.08.1985 in Tiko (Kamerun)

Vorsitzender: Prof. Dr.-Ing. Gerhard Lappus

Gutachter: Prof. Dr.-Ing. Hans Joachim Krautz

Gutachter: Prof. Dr.-Ing. habil. Sabine Weiß

Tag der mündliche Prüfung: 19. September 2016



**Email:** [roger.abang@b-tu.de](mailto:roger.abang@b-tu.de)

**Telephone:** 0049 (0) 355 69 4028

**Version:** 1.1

Produced with ~~ET~~<sub>E</sub>X



*“The true life cycle cost of operating and maintaining a powerplant includes the penalties incurred during starts, stops, and cycling operation – the ‘wear and tear’ on equipment that degrades efficiencies, increases forced-outage rates, and swells maintenance budgets.”*

[S. A. Lefton, P. M. Besuner, G. P. Grimsrud]





# Summary

With the rapid growth of Renewable Energy Sources (RES) in the power generation mix in accordance with the German energy transition policy (*Energiewende*), fewer baseload coal power plants will be required. Future power generation will be supplied through decentralized power utilities such as off-shore wind parks and also through high operational flexibility of existing conventional coal power units. High operational flexibility means conventional power plants have to increase cyclic operations to cope with feed-ins from variable Renewable Energy Sources (v-RES) such as wind and solar.

Unlike medium and peak load power plants that can react quickly to load changes and power ramps, baseload power plants are not suited for such operations. Important technical requirements for flexible operation include among others; frequent start-ups and shut-downs, a minimum downtime, shorter startup time and short operational periods. Baseload coal power plants however do not meet these requirements.

This increased cyclic mode of operation can have severe impacts on vital power plant components such as superheater and reheater tubes resulting in high temperature cyclic oxidation/corrosion especially because these plants were not designed for frequent cyclic operations. To optimize plant operations, minimize material damage and reduce operational and maintenance cost, it is therefore important to understand the oxidation and corrosion risk to plants materials associated with this flexible mode of operation.

In this context, thermochemical modeling in FactSage 6.4<sup>TM</sup> as well as experimental investigations were carried out. For the experimental investigations, five commercial coal boiler superheater and reheater materials, namely T91, VM12-SHC, TP347-HFG, DMV304 HCu and DMV310 N were exposed for 1000 hours under discontinuous isothermal oxidation conditions and 1000 hours thermo-cyclic oxidation conditions at a metal surface temperature of 650 °C. The synthetic corrosive flue gas consisted of a mixture of CO<sub>2</sub>, O<sub>2</sub>, SO<sub>2</sub>, N<sub>2</sub> and H<sub>2</sub>O. The test material samples were partly covered in fly ash to investigate the effect ash deposits on the corrosion and oxidation behavior of the test materials. After exposure metallographic analysis (LOM and SEM-EDS) were carried out to study the oxide morphology and micro-structural properties of the materials.

The oxidation kinetics (weight change) results showed significant oxide growth rates (weight gain) under cyclic oxidation conditions especially in the martensitic alloys – T91,

VM12-SHC. Furthermore, metallographic analysis revealed severe oxide spallation in the ash covered sections of these alloys. The austenitic materials (TP374-HFG, DMV310 N) with the exception of DMV304 HCu showed good oxidation behavior with minimal oxide growth both under isothermal and thermal cyclic conditions. However, severe grain boundary attack and internal sulphidation were found in these alloys. DMV310 N showed the best corrosion and oxidation performance. The thermochemical modeling calculations supported the experimental results.

**Keywords:** Flexible generation; Cycling; High temperature corrosion; Oxidation; Thermochemical modeling

# Kurzfassung

Bedingt durch die Zunahme der erneuerbaren Energien im Rahmen der Energiewende sind zunehmend weniger Großkraftwerke erforderlich. Zukünftig erfolgt die Bereitstellung der elektrischen Energie durch dezentrale Energieerzeuger, wie Offshore-Windparks, Solar-Parks sowie die in der Flexibilität gesteigerten konventionellen Kraftwerke. An ein konventionelles Kohlekraftwerk besteht zukünftig der Anspruch einer möglichst flexiblen Fahrweise und die Herausforderung, den bisherigen Dauerbetrieb unter Volllast auf einen Teilbetrieb mit wenigen Betriebsstunden unter Teillast absenken zu können.

Für die nötige flexible Fahrweise sind, neben anderen Faktoren, eine kurze Anfahrdauer, kurze Einsatzzeiten, hochfrequente An- und Abfahrzyklen sowie minimale Stillstandzeiten sehr wichtige Kriterien, um die Betriebsweise dem schwankenden Bedarf optimal angleichen zu können. Diese Kriterien können bisher jedoch nur von Mittel- und Spitzenlastkraftwerken erfüllt werden. Durch die zunehmende Schwankungsbreite der Einspeisung von elektrischer Energie, in Folge des Ausbaus regenerativer Energieerzeugung und dem Abbau von Grundlastkraftwerken, sind zunehmend auch die verbleibenden Grundlastkraftwerke auf eine flexible Fahrweise angewiesen.

Diese Betriebsweise führt in kohlebefeuchten Grundlastkraftwerken zur drastischen Verkürzung der Betriebszeiten durch schneller stattfindende Materialschädigungen, wie beispielsweise Hochtemperaturkorrosion und -oxidation. Um solche Anlagen bei Reduzierung der Betriebskosten für eine flexiblere Fahrweise zu optimieren, ist es notwendig das Korrosionsverhalten der Dampferzeugerwerkstoffe genauer zu untersuchen.

Im Rahmen dieser Arbeit wurden sowohl thermochemische Modellierungen in FactSage<sup>TM</sup> 6.4 als auch experimentelle Untersuchungen durchgeführt. Für die experimentellen Untersuchungen wurden fünf kommerzielle Stähle für den Einsatz in Überhitzern und Zwischenüberhitzern ausgewählt (TP91, VM12-SHC, TP347-HFG, DMV304 HCu und DMV310 N). Diese wurden jeweils für 1000 Stunden unter isothermen sowie thermozyklischen Oxidationsbedingungen bei einer Temperatur von 650°C dem synthetischen Rauchgas ausgesetzt. Das korrosive Rauchgas bestand aus einer Mischung von CO<sub>2</sub>, O<sub>2</sub>, SO<sub>2</sub>, N<sub>2</sub> und H<sub>2</sub>O. Die Materialproben wurden zum Teil mit Flugasche bedeckt, um die Auswirkungen der Ascheablagerungen auf das Korrosions- und Oxidationsverhalten

der Werkstoffe zu untersuchen. Die korrodierten Proben wurden licht- und rasterelektromikroskopisch analysiert (LiMi und REM-EDX). Bei der Charakterisierung von Oxidschicht und Material wurden neben den morphologischen auch die mikrostrukturellen Eigenschaften untersucht.

Bezüglich der Oxidationskinetik (Gewichtsänderungen) zeigten insbesondere die martensitischen Stähle (T91, VM12-SHC) unter thermozyklischen Bedingungen signifikante Oxidwachstumsraten (Gewichtszunahmen). Darüber hinaus konnten metallographische Analysen Oxidschichtabplatzungen in den mit Asche bedeckten Bereichen nachweisen. Hingegen wiesen die austenitischen Stähle (TP347-HFG, DMV310 N), mit Ausnahme von DMV304 HCu, sowohl unter isothermen als auch unter thermozyklischen Bedingungen ein gutes Oxidationsverhalten mit minimalem Oxidschichtwachstum auf. Dennoch konnten Korngrenzenangriffe sowie innere Sulfidbildungen in diesen Legierungen beobachtet werden. Von allen Stählen wies DMV310 N den höchsten Widerstand gegenüber Korrosion und Oxidation auf. Die thermochemische Modellierung bestätigte die experimentellen Ergebnisse.

**Schlagwörter:** Flexible Kraftwerke; Lastwechsel; Hochtemperaturkorrosion; Oxidation; Thermochemische Modellierung

# Acknowledgements

This dissertation would have not been possible without the support and contribution of so many people. I therefore, want to express my sincere gratitude to everyone who supported me. Firstly, I would like to thank Prof. Dr.-Ing. Hans Joachim Krautz (Chair of Power Plant Technology) for inspiring me with distinctive research ideas. I am really grateful for his guidance, support and involvement. His sound advice and suggestions helped me immensely in the development and accomplishment of this study.

I am also sincerely grateful to Prof. Dr.-Ing. habil. Sabine Weiß (Chair of Materials and Physical Metallurgy) for giving me the opportunity to carry out my study under her supervision. Her professionalism, constructive criticism and scientific approach helped me a lot in the completion of this work. Additionally, her interest and dedication as well as her kindness and willingness to help were invaluable.

I would like to especially thank Mr. Patrik Schraven, Salzgitter Mannesmann Stainless Tubes (SMST), Mülheim an der Ruhr and Mr. Frank Weiß, Babcock Borsig Steinmüller GmbH, Peitz for supplying the test materials. I would also like to thank Dr. James Smialek of the Glenn Research Center, NASA, USA for his support with WinCOS. I also wish to thank Dr.-Ing Alexander Lisk for his great deal of support on this project for which I always remain grateful. I also would like to thank Dr.-Ing. Matthias Klatt for his suggestions and contributions. Special thanks to Raimo Kaufmann for the extensive support he offered throughout the experiments. Also, many thanks to Martin Baldzer, Torsten Sanger, Heinz Schallmea, Kristin Schierack, Michelle Grütza, Doris Seifert and Steffen Löffler.

I am also very grateful to the entire team at the Chair of Materials and Physical Metallurgy. Special thanks to Dr.-Ing. Sebastian Bolz for his support with the [SEM](#) analysis and Birgit Kunze for her assistance during the preparation of the test samples and light microscopic analysis. I would also like to thank Dieter Domke, Rainer Konzack, Grit Rodenbeck and Dr.-Ing. Muhammad Naveed. It was much fun to work with them.

Finally, my deepest gratitude goes to my wife Katrin and our sons Arvin and Levin for their moral and psychological support, patience and understanding throughout this study. I also remain highly indebted to my entire family: my mother Esther and grandma Jenny, for the huge sacrifices they made for their children and for providing them with exceptional opportunities for personal and professional development. I also wish to thank my uncle,

Dr. Mathew Abang and aunt Dr. Serah Abang, MD, who have always set the pace for me to follow and are my role models. I acknowledge with thanks the encouragement of all my friends.

# List of Figures

1.1. Gross Electricity Consumption in Germany . . . . .	3
1.2. Gross electricity generation in Germany, 2014 . . . . .	3
1.3. RES share in Germany past and future targets targets . . . . .	4
1.4. Study approach . . . . .	7
2.1. Flexible operation with RES integration . . . . .	10
2.2. Estimated life of baseload unit with and without cycling . . . . .	12
2.3. Effect of part-load operation on steam and steel temperature . . . . .	13
2.4. Effect of weekend shutdown on steam and steel temperatures . . . . .	14
2.5. Plant starts and relative damage caused by cycling . . . . .	15
2.6. Forms of corrosion . . . . .	17
2.7. Ellingham diagram for oxides . . . . .	21
2.8. Gibbs free energy vs composition diagrams . . . . .	22
2.9. Vapour equilibria in the Cr-O system at 1250°C . . . . .	23
2.10. Fe-S-O phase stability diagram at 650 °C . . . . .	25
2.11. Cr-S-O phase stability diagram at 650 °C . . . . .	25
2.12. Nb-S-O phase stability diagram at 650 °C . . . . .	26
2.13. Mn-S-O phase stability diagram at 650 °C . . . . .	26
2.14. Mo-S-O phase stability diagram at 650 °C . . . . .	27
2.15. Fe-Cr-O <sub>2</sub> System at 650 °C . . . . .	27
2.16. Schematic cross-sectional diagram of oxide scale growth . . . . .	28
2.17. Wagner's model on scale formation [44] . . . . .	29
2.18. Hypothetical ways in which oxide scale is damaged . . . . .	31
2.19. Basic rate laws - linear, logarithmic and parabolic relationships [44] . . . . .	33
2.20. Nickel oxide scale with a metal-deficit. [47] . . . . .	34
2.21. Schematic of a p-type oxide growth occurring at the oxide-gas interface . . . . .	34
2.22. Film growth of an n-type anion vacancy oxide on the a metal/oxide interface . . . . .	35
2.23. Growth of a cation interstitial n-type oxide occurring at an oxide/gas interface . . . . .	35
2.24. Fe-O phase diagram . . . . .	36
2.25. Microstructure of alloy B after exposure in air at 550°C . . . . .	37
2.26. Oxide growth model . . . . .	40
2.27. Oxide growth model . . . . .	41

2.28. Effect of chromium in providing corrosion resistance . . . . .	42
2.29. Cross-section morphology of a Ni-6Cr alloy after 40h of oxidation at 900 °C and $pO_2 = 10^{-9}$ Pa . . . . .	43
2.30. Schematic diagram of sulphidation corrosion penetration . . . . .	44
2.31. Regimes of fireside corrosion . . . . .	45
2.32. Typical locations of fouling and slagging in coal-fired boilers . . . . .	47
2.33. Temperature profiles for isothermal and cyclic testing . . . . .	49
2.34. Temperature drop needed to spall 20Cr–25Ni-Nb steel . . . . .	50
2.35. Net specimen weight changes predicted for cyclic oxidation . . . . .	51
2.36. Common equipment problems due to cycling . . . . .	52
2.37. Creep-fatigue curve – effect of introducing two-shifting cycling . . . . .	53
2.38. A generic stress life cycle of stress versus time . . . . .	54
2.39. Membrane waterwall tube damage due to cycling . . . . .	55
3.1. Equilibrium Fugacities of Model Corrosive Gas . . . . .	59
3.2. Stability diagram for the Fe-Cr-O-S system at 650 °C . . . . .	60
3.3. Isothermal section at 650 °C of the $K_2O-Na_2O-SiO_2$ ternary phase diagram	62
3.4. Ternary phase diagram projection at 300 - 1000 °C of $K_2O-Na_2O-SiO_2$ system	63
3.5. $Na_2O-K_2O$ system at 300 - 1000 °C and 1 atm . . . . .	63
3.6. Molten slag phase formation in fly ash . . . . .	64
3.7. TP1 gas–metal phase equilibria . . . . .	65
3.8. VM12-SHC gas–metal phase equilibria . . . . .	67
3.9. TP347-HFG gas–alloy phase equilibria . . . . .	68
3.10. DMV304 HCu gas – alloy phase equilibria . . . . .	69
3.11. DMV310 N gas – alloy phase equilibria . . . . .	70
3.12. Fe–8.75Cr–0.4Ni–0.45Mn alloy with $O_2$ phase diagram (TP91) . . . . .	73
3.13. Fe–12Cr alloy reaction with $SO_2$ phase diagram (VM12-SHC) . . . . .	73
3.14. Fe–18Cr–10Ni alloy reaction with $O_2$ phase diagram (TP347-HFG) . . . . .	74
3.15. Fe-18.4Cr-9.1Ni-Mn- $O_2$ phase diagram (DMV304 HCu) . . . . .	74
3.16. Fe-25.33%Cr-21.05%Ni alloy reaction with $O_2$ phase diagram (DMV310 N)	75
3.17. Fe-Cr-C-O phase diagram at 650 °C and 1 atm . . . . .	75
3.18. Fe-Nb-S-O predominance area diagram at 650 °C and 1 atm . . . . .	76
3.19. Fe-Mn-S-O predominance area diagram at 650 °C and 1 atm . . . . .	76
3.20. Fe-Mo-S-O predominance area diagram at 650 °C and 1 atm . . . . .	77
4.1. Schöffler diagram for stainless steels . . . . .	80
4.2. Microstructure of selected materials, as received . . . . .	83
4.3. Free Cr-content of selected commercial alloys . . . . .	84
4.4. Dimensions of half cylinder machined samples used in the exposure tests .	84
4.5. Schematic diagram of experimental setup . . . . .	86
4.6. Test specimen arrangement in half ceramic shell . . . . .	86



4.7. Temperature distribution in tube furnace . . . . .	87
4.8. Experimental test runs showing (a) isothermal oxidation and (b) thermal cycling . . . . .	87
5.1. Net weight change after 1000 h of exposure at 650 °C under (a) isothermal conditions and (b) thermal cycling conditions . . . . .	92
5.2. Comparison of net wet change of alloys under isothermal and cyclic oxidation	93
5.3. Scale thickness measurements isothermal and thermal cycling . . . . .	94
5.4. Net wet change predicted in WinCOSP and experimental results, isothermal oxidation . . . . .	96
5.5. Total oxygen uptake, metal consumed and weight of retained oxide, isothermal oxidation . . . . .	97
5.6. Net wet change predicted in WinCOSP and experimental results, cyclic oxidation . . . . .	98
5.7. Total oxygen uptake, metal consumed and weight of retained oxide, isothermal oxidation . . . . .	99
5.8. Light optical micrographs of TP91 (isothermal oxidation) . . . . .	100
5.9. Light optical micrographs of VM12 (isothermal oxidation) . . . . .	101
5.10. Light optical micrographs of TP347-HFG (isothermal oxidation) . . . . .	101
5.11. Light optical micrographs of DMV304 HCu (isothermal oxidation) . . . . .	101
5.12. Light optical micrographs of DMV310 N (isothermal oxidation) . . . . .	102
5.13. SEM micrographs with EDS linescans of TP91, isothermal conditions . . . . .	104
5.14. Phase mapping of TP91 isothermal conditions . . . . .	104
5.15. Element mapping of TP91 after 1000 h at 650 °C under isothermal conditions	105
5.16. SEM micrographs with EDS linescans of VM12-SHC, isothermal conditions	107
5.17. Phase mapping of VM12-SHC isothermal conditions . . . . .	107
5.18. Element mapping of VM12-SHC after 1000 h at 650 °C under isothermal conditions . . . . .	108
5.19. SEM micrographs with EDS linescans of TP347-HFG isothermal oxidation .	109
5.20. Phase mapping of TP347-HFG isothermal conditions . . . . .	110
5.21. Element mapping TP347-HFG after 1000 h at 650 °C under isothermal conditions . . . . .	110
5.22. SEM micrographs with EDS linescans of DMV304 HCu, isothermal conditions	112
5.23. Phase mapping of DMV304 HCu isothermal conditions . . . . .	112
5.24. Element mapping of DMV304 HCu after 1000 h at 650 °C, isothermal oxidation . . . . .	113
5.25. SEM micrographs with EDS linescans of DMV310 N isothermal oxidation .	114
5.26. Phase mapping of DMV310 N isothermal conditions . . . . .	114
5.27. Element mapping of DMV310 N after 1000 h at 650 °C under isothermal conditions, . . . . .	115

5.28. Light optical micrographs of TP91 after 1000 <i>h</i> exposure, (cyclic conditions)	116
5.29. Light optical micrographs of VM12-SHC after 1000 <i>h</i> exposure (cyclic conditions)	116
5.30. Light optical micrographs of TP347-HFG after 1000 <i>h</i> exposure (cyclic conditions)	117
5.31. Light optical micrographs of DMV304 HCu after 1000 <i>h</i> exposure (cyclic conditions)	117
5.32. Light optical micrographs of DMV310 HCu after 1000 <i>h</i> exposure (cyclic conditions)	117
5.33. SEM micrographs with EDS linescans of TP91 cyclic conditions	119
5.34. Phase mapping of TP91 cyclic conditions	119
5.35. Element mapping of TP91 after 1000 h at 650 °C under cyclic conditions	120
5.36. SEM micrographs with EDS linescans of VM12-SHC, cyclic conditions	121
5.37. Phase mapping of VM12, cyclic conditions	122
5.38. Element mapping of VM12-SHC after 1000 h at 650 °C under isothermal conditions	122
5.39. SEM micrographs with EDS linescans of TP347-HFG after exposure under cyclic conditions	124
5.40. Phase mapping of TP347, cyclic conditions	124
5.41. Element mapping of TP347-HFG after 1000 h at 650 °C under cyclic conditions	125
5.42. SEM micrographs with EDS linescans of DMV304 HCu after exposure under cyclic conditions	126
5.43. Phase mapping of DMV304 HCu after exposure under cyclic conditions	127
5.44. Element mapping of DMV304-HCu after 1000 h at 650 °C under cyclic conditions	127
5.45. SEM micrographs with EDS linescans of DMV310 N after exposure under cyclic conditions	129
5.46. Phase Mapping of DMV310 N after Exposure under Cyclic Conditions	129
5.47. Element Mapping of DMV310 N after 1000 h at 650 °C under cyclic conditions	130
6.1. Effect of chromium on oxidation rate	132
6.2. Oxide scale comparison between bare metal and ash covered section	136
B.1. Ellingham diagram for selected sulphides	149
B.2. Gross Electricity Generation in Germany 2004 – 2014	150
B.3. Process and Instrumentation Diagram of Gas Mixing Station	150

# List of Tables

1.1. Development of RES in Germany . . . . .	4
1.2. A comparison of coal and gas power plants . . . . .	5
2.1. Oxidizing and reducing environments at high temperature . . . . .	16
2.2. Standard free energies of reactions . . . . .	19
2.3. PB-ratio for common metals . . . . .	31
2.4. Oxidation rate of nickel alloyed with chromium . . . . .	33
2.5. Spinel phases found in alloy oxidation . . . . .	36
2.6. Thermal expansion coefficients of metals and metal oxides . . . . .	38
2.7. Forms of high temperature corrosion in hot flue gases . . . . .	39
3.1. Model flue gas mixture composition . . . . .	59
3.2. Composition of Fly Ash . . . . .	61
3.3. Condensed phases formed from the reaction of gas and deposits on the iron metal oxides, 650 °C, 1 atm . . . . .	71
3.4. Flue gas fugacities from reaction with ash and oxide at 650°C and 1 atm . .	72
4.1. Chemical composition of selected materials . . . . .	80
4.2. Selected material types and dimensions . . . . .	85
4.3. Model flue gas mixture composition . . . . .	85
5.1. Parabolic rate constants, ( $k_p$ ) after 1000 $h$ exposure . . . . .	94
5.2. Possible phases formed in an oxide scale . . . . .	103
A.1. TP91 reaction with corrosive flue gas at 650 °C . . . . .	145



# Nomenclature

## Latin Letters

$A$	surface area	$m^2$
$a, b, c, d$	constant obtained from $\Delta H$ , $\Delta S$ and $\Delta C_p$	
$a_i$	activity of species $i$ , <a href="#">Equation (2.5)</a>	
$A_s$	surface area of sample	$cm^2$
$a, b$	empirical constant, <a href="#">Equation (2.18)</a>	
$dp$	change in pressure	bar
$dT$	change in temperature	bar
$\Delta G^\circ$	Gibb's free energy change at standard state	$kJ/mol$
$\Delta G$	Gibb's free energy change	$kJ/mol$
$\Delta H$	enthalpy change	$kJ/mol$
$K$	equilibrium constant	
$k$	thermal conductivity	$W/K$
$k_e$	logarithmic oxidation rate, <a href="#">Equation (2.18)</a>	
$k_l$	linear rate oxidation, <a href="#">Equation (2.17)</a>	
$k_p$	parabolic oxidation rate, <a href="#">Equation (2.18)</a>	$mg^2/cm^4 \cdot s$
$M_{metal}$	molecular weight of metal	$g/mol$
$M_{oxide}$	molecular weight of oxide	$g/mol$
$M$	metal	
$MO_2$	metal oxide	
$n$	number of metal atoms in oxide molecule	
$n_i$	number of moles of component $i$	$mol$
$p_i$	partial pressure of species $i$ , see <a href="#">Equation (2.5)</a>	$atm$
$p_i^\circ$	partial pressure at standard state of species $i$	$atm$
$q$	heat rate	$W$
$q/A$	heat flux	$W/m^2$
$R$	Gas constant	$8.314 J/mol \cdot K$
$r$	rate exponent	
$\Delta S$	entropy change	$kJ/mol \cdot K$
$t$	oxidation time	$h$

$T_{metal}$	temperature of metal	K
$V_{metal}$	molar volume of metal	cm <sup>3</sup> /mol
$V_{oxide}$	molar volume of oxide	cm <sup>3</sup> /mol
$w$	atomic weight of metal	
$\Delta W$	specific weight change	
$W_f$	final weight of sample	
$W_o$	initial weight of sample	
$X$	mole fraction	
$x$	oxide scale thickness	mm

### Greek Letters

$\alpha, \beta$	two co-existing phases in equilibrium	
$\rho_{metal}$	density of metal	g/cm <sup>3</sup>
$\rho_{oxide}$	density of oxide	g/cm <sup>3</sup>
$\sigma_c$	critical stress value	
$\sigma_{ext}$	external stress	
$\sigma_{ox}$	stress during oxide growth	
$\sigma_{therm}$	thermal stress	
$\mu_A$	chemical potential of component A	kJ/mol·K
$\mu_A^\alpha$	chemical potential of the equilibrium phase $\alpha$	kJ/mol·K
$\mu_A^\beta$	chemical potential of the equilibrium phase $\beta$	kJ/mol·K
$\mu_B$	chemical potential of component B	kJ/mol·K
$\mu_i$	chemical potential of component i	kJ/mol·K
$\chi_{melt}$	oxide thiness of molten sulphate layer	

# Abbreviations

<b>AC</b>	ash covered
<b>AGEE-Stat</b>	Arbeitsgruppe Erneuerbare Energien-Statistik (Working Group on Renewable Energy-Statistics)
<b>BCC</b>	Body Centered Cubic
<b>BDEW</b>	Bundesverband der Energie- und Wasserwirtschaft e.V. (German Federal Association of Energy and Water Management)
<b>BM</b>	bare metal
<b>BMU</b>	Bundesministerium für Umwelt, Naturschutz, Bau und Reaktorsicherheit (German Federal Ministry for the Environment, Nature Conservation, Building and Nuclear Safety)
<b>BMWi</b>	Bundesministerium für Wirtschaft und Energie (German Federal Ministry for Economic Affairs and Energy)
<b>CCGT</b>	Combined-Cycle Gas Turbine
<b>CCP</b>	Combined Cycle Plants
<b>CCT</b>	Cyclic Corrosion Testing
<b>CGS</b>	Coal Generating Station
<b>CHP</b>	Combined Heat and Power
<b>COMPRES700</b>	Component Test Facility for a 700C Power Plant
<b>COSP</b>	Cyclic Oxidation Spalling Program
<b>CSEF</b>	Creep-Strength Enhanced Ferritic
<b>dena</b>	Deutsche Energie Agentur (German Energy Agency)
<b>EDS</b>	Energy Dispersed X-Ray Spectroscopy
<b>EEX</b>	European Energy Exchange

---

<b>EFOR</b>	Equivalent Forced Outage Rate, see <a href="#">appendix C</a> , page 152
<b>ETP</b>	Energy Transition Policy
<b>FATT</b>	Fracture Appearance Transition Temperature
<b>FCC</b>	Face Centered Cubic
<b>FZ</b>	Fusion Zone
<b>GMS</b>	Gas Mixing Station
<b>HAZ</b>	Heat Affected Zone
<b>HRSR</b>	Heat Recovery Steam Generators
<b>HSCC</b>	Hydrogen-induced Stress Corrosion Cracking
<b>ID</b>	Inner Diameter
<b>IRENA</b>	International Renewable Energy Agency
<b>ISO</b>	Independent System Operator
<b>ITDS</b>	Integrated Thermodynamic Database System
<b>LM</b>	Light Microscopy
<b>LOM</b>	Light (Optical) Microscopy
<b>MFC</b>	Mass Flow Controller
<b>MMU</b>	Market Monitoring Unit
<b>NASA</b>	National Aeronautics and Space Administration
<b>OD</b>	Outer Diameter
<b>PB</b>	Pilling-Bedworth
<b>PF</b>	Pulverized Fuel
<b>PSH</b>	Pumped-storage Hydroelectricity
<b>PV</b>	Photovoltaics
<b>RBS</b>	Rutherford Backscattering
<b>RES</b>	Renewable Energy Sources
<b>RWE</b>	Rheinisch-Westfälisches Elektrizitätswerk AG



<b>SC</b>	Supercritical
<b>SCC</b>	Stress Corrosion Cracking
<b>SEM</b>	Scanning Electron Microscopy
<b>SH</b>	Superheater
<b>TSO</b>	Transmission System Operators
<b>USCB</b>	Ultra-Supercritical Coal Boiler
<b>VDEW</b>	Verband der Elektrizitätswirtschaft
<b>VKU</b>	Verband kommunaler Unternehmen e. V.
<b>v-RES</b>	variable Renewable Energy Sources



# Contents

<b>Summary</b>	<b>i</b>
<b>Kurzfassung</b>	<b>iii</b>
<b>Acknowledgements</b>	<b>v</b>
<b>List of Figures</b>	<b>vii</b>
<b>List of Tables</b>	<b>xi</b>
<b>Nomenclature</b>	<b>xiii</b>
<b>Abbreviations</b>	<b>xv</b>
<b>1. Introduction</b>	<b>1</b>
1.1. Background and Motivation	1
1.2. Technical challenges of the <i>Energiewende</i>	2
1.3. Problem Statement	5
1.4. Study Approach	6
<b>2. Literature Review</b>	<b>9</b>
2.1. State of the Art	9
2.2. Cycling of generating units	10
2.2.1. Requirements for conventional coal-fired power plants	13
2.2.2. Damages caused by cycling	14
2.3. High Temperature Corrosion	15
2.3.1. Background	15
2.3.2. Thermodynamic principles	17
2.3.2.1. Standard free energy of formation versus temperature diagrams	18
2.3.2.2. Gibbs free energy vs composition diagrams	20
2.3.2.3. Vapour species diagrams	22
2.3.2.4. Two-dimensional Isothermal stability diagrams	24
2.3.3. Kinetic principles	28
2.3.3.1. Mechanisms of high temperature oxidation	28
	<b>xix</b>

2.3.3.2.	Wagner's theory on high temperature oxidation	29
2.3.3.3.	The Pilling-Bedworth ratio	30
2.3.3.4.	Rate Laws and Micro-mechanisms	31
2.3.4.	Effect of mechanical stresses in oxide scales	37
2.3.5.	High temperature corrosion mechanisms in coal boilers	38
2.3.5.1.	Oxidation	39
2.3.5.2.	Sulphidation	42
2.3.5.3.	Deposit-induced fireside corrosion	43
2.3.5.4.	Carburization	45
2.3.5.5.	Chlorine corrosion	46
2.3.5.6.	Slagging and fouling	46
2.4.	High Temperature Cyclic Oxidation	47
2.4.1.	Background and methods	47
2.4.2.	Important Experimental Parameters for Cyclic Oxidation	48
2.4.3.	Cyclic oxidation kinetics	51
2.4.4.	Damage mechanisms associated with cycling operation	51
2.4.4.1.	Creep-fatigue damage	52
2.4.4.2.	Stress corrosion cracking	53
2.4.4.3.	Furnace Wall Corrosion	54
2.4.4.4.	Fireside corrosion	54
<b>3.</b>	<b>Thermodynamic Modeling of Flue Gas Corrosion</b>	<b>57</b>
3.1.	Description of modeling package – FactSage™	57
3.2.	Gas phase equilibria	58
3.3.	Fly ash behavior	61
3.4.	Gas–Metal Equilibria	62
3.4.1.	TP91	64
3.4.2.	VM12-SHC	66
3.4.3.	TP347-HFG	66
3.4.4.	DMV304 HCu	67
3.4.5.	DMV310 N	70
3.5.	Two phase flow model	71
3.6.	Predominance area diagrams	71
<b>4.</b>	<b>Experimental</b>	<b>79</b>
4.1.	General overview	79
4.2.	Investigated materials	79
4.2.1.	Test sample preparation – shape and size	82
4.3.	Test Procedure	82
4.3.1.	Isothermal oxidation tests	82
4.3.2.	Thermal cycling oxidation tests	86

4.3.3. Experimental Error	87
4.4. Metallographic Investigation Methods	88
4.4.1. Specimen preparation	88
4.4.2. Light (optical) microscopy	89
4.4.3. SEM-EDS microscopy	89
<b>5. Results</b>	<b>91</b>
5.1. Oxidation growth rate kinetics	91
5.1.1. Weight change measurements	91
5.1.2. Parabolic rate kinetics	92
5.2. Kinetic modeling	95
5.3. Isothermal oxidation after 1000 h	100
5.3.1. Light (optical) microscopic analysis	100
5.3.2. Micro-structural (SEM–EDS) analysis of isothermal oxidation	102
5.3.2.1. Isothermal oxidation of TP91	102
5.3.2.2. Isothermal oxidation of VM12-SHC	105
5.3.2.3. Isothermal oxidation of TP347-HFG	108
5.3.2.4. Isothermal oxidation of DMV304 HCu	111
5.3.2.5. Isothermal oxidation of DMV310 N	113
5.4. Cyclic oxidation after 1000 h	115
5.4.1. Light optical microscopy	115
5.4.2. Micro-structural (SEM–EDS) analysis of cyclic oxidation	118
5.4.2.1. Cyclic oxidation of TP91	118
5.4.2.2. Cyclic oxidation of VM12-SHC	120
5.4.2.3. Cyclic oxidation of TP347-HFG	123
5.4.2.4. Cyclic oxidation of DMV304 HCu	125
5.4.2.5. Cyclic oxidation of DMV310 N	128
<b>6. Discussion</b>	<b>131</b>
6.1. Isothermal and cycling oxidation	131
6.1.1. Weight change and parabolic kinetics	131
6.1.2. Effect of Chromium on oxidation rate	132
6.1.3. Effect of minor alloying elements (Ni, Mn, Mo, and Nb)	133
6.1.3.1. Nickel	133
6.1.3.2. Manganese	133
6.1.3.3. Molybdenum	133
6.1.3.4. Niobium	134
6.2. Ferritic-martensitic and austenitic steels oxidation	134
6.2.1. Oxide morphology	134
6.2.1.1. Ferritic–martensitic steels (TP91 and VM12-SHC)	134

---

6.2.1.2. Austenitic steels (TP347-HFG, DMV304 HCu and DMV310 N) . . . . .	135
6.3. Effect of fly ash deposits . . . . .	136
6.3.1. Spallation . . . . .	136
6.4. Comparison of experimental results with thermodynamic modeling . . .	137
<b>7. Conclusion</b>	<b>141</b>
<b>A. Thermochemical Results Table Structure</b>	<b>145</b>
<b>B. Supplementary Figures</b>	<b>149</b>
<b>C. Glossary</b>	<b>151</b>
<b>Bibliography</b>	<b>155</b>
<b>Index</b>	<b>167</b>

# 1. Introduction

## 1.1. Background and Motivation

The goal to reduce energy-related carbon dioxide emissions mainly from fossil fuel combustion has created several challenges for the energy sector worldwide [1]. One of the most important challenges is the integration of renewable energy sources into the power grid and optimizing supply to meet the ever-increasing demand for electricity, heat and transport fuel [2–4]. In the future, there will be an increase in the deployment of intermittent, that is irregular, unpredictable, fluctuating or non-reliable variable Renewable Energy Sources (v-RES) generation from wind and solar power [5, 6]. In Germany, for example, the energy system is in the process of transforming from a nuclear and coal-based system to a more sustainable renewable-based system (an energy policy known as the “Energiewende”, cf. Section 1.2).

Although renewable energy sources RES hold promising benefits for the future to meet the growing energy demand in a more environmentally sound way, it is however required that dispatchable (reliable) power generation units that can be regulated (like baseload coal and nuclear power plants) operate in a highly flexible manner to allow for the smooth integration of variable power into the power grid [2, 3, 5, 6]. High-operational flexibility is therefore a very important prerequisite for coping with intermittent power supply.

High operational flexibility for conventional generating units means an increase in several modes of flexible (cyclic) operation such as increase in load following operations, reducing output to allow for feed-ins from wind or solar, a minimum downtime, two-shifting<sup>1</sup>, frequent unit starts (hot, warm, and cold), increased load and thermal power ramp rates, weekend shutdowns, and long-term plant layup [6, 7].

It is worth mentioning that, cycling is not entirely new to power plants, because demand has always been variable and therefore power units have always been required to cycle. This ‘new’ mode of cycling, especially in the last few years however requires baseload units to operate beyond their nominal design limits. The power ramps and increased thermal cycles are a completely new mode of operating which is not due to changes in demand,

---

<sup>1</sup>Two-shifting is the mode of operation where the plant is started up during the day and shut down at night (cf. Appendix C)

as opposed to the conventional variable power in response to changes in demand that the units are used to (see [Section 2.2](#)) [7–10].

Cycling can have severe irreparable effects on the materials of the vital high-temperature boiler components such as superheater and reheater tubes due to increased temperature transients in the materials [7, 9, 10]. As coal-fired power plants increasingly operate in cycling modes it is essential to understand the corrosion and oxidation risk on the materials of boiler components that are related to increased cycling so as to be able to minimize component damage and reduce operational and maintenance costs. The present study attempts to investigate the impact of increased flexibility (cycling) on coal-based boiler superheater and reheater materials. In [Section 1.2](#) a brief description is given on the German *Energiewende* and the technical difficulties involved – the impact it can have on conventional baseload power generation units.

## 1.2. Technical challenges of the *Energiewende*

The German *Energiewende* – energy transition or turn around, is a regulatory framework to transform Germany’s energy system from a nuclear and coal-based system into a RES-based system [11–13]. In June 2011 the government of Germany decided to completely phase out nuclear power by 2022 following the Fukushima disaster and at the same time also planned to significantly increasing power generation from renewables [6, 11, 12, 14, 15]. It is however, worth mentioning that the *Energiewende* did not start in 2011. It can be traced as far back as in the 1970’s as the result of an anti-nuclear movement (1976) and the search for alternatives during that era [3, 14]. The share of gross electricity consumption from RES has since then increased significantly particularly over the last decade, see [Figure 1.1](#). As of 2014, power from renewables accounted for 25.7% (more than one quarter) of gross electric power generation meanwhile brown coal (lignite) and hard coal summed up to 34.3% with natural gas and nuclear accounting for 9.6% and 15.5% respectively, see [Figure 1.2](#)<sup>2</sup> [16–18]. Also, the German Transmission System Operators (TSO) estimated in 2012 that the shares of onshore and offshore wind will increase to about 45% and PV to about 10% by 2032. Renewable energy shares are expected to rise even further to about 80% by 2050, see [Figure 1.3](#) and [Table 1.1](#) [3, 12, 15, 19, 20].

Today, power generated from RES serves as a kind of baseload and priority is given to renewables over power generated from conventional sources. Nevertheless, unlike baseload power from dispatchable conventional sources, baseload power from variable renewables (wind and solar power) fluctuates and depends highly on the current state of the weather – windy days or longer periods of sunshine [17, 22]. This makes it difficult to be able to actually predict when power from variable renewable sources which is available at any given

---

<sup>2</sup>Also see [Figure B.2](#)



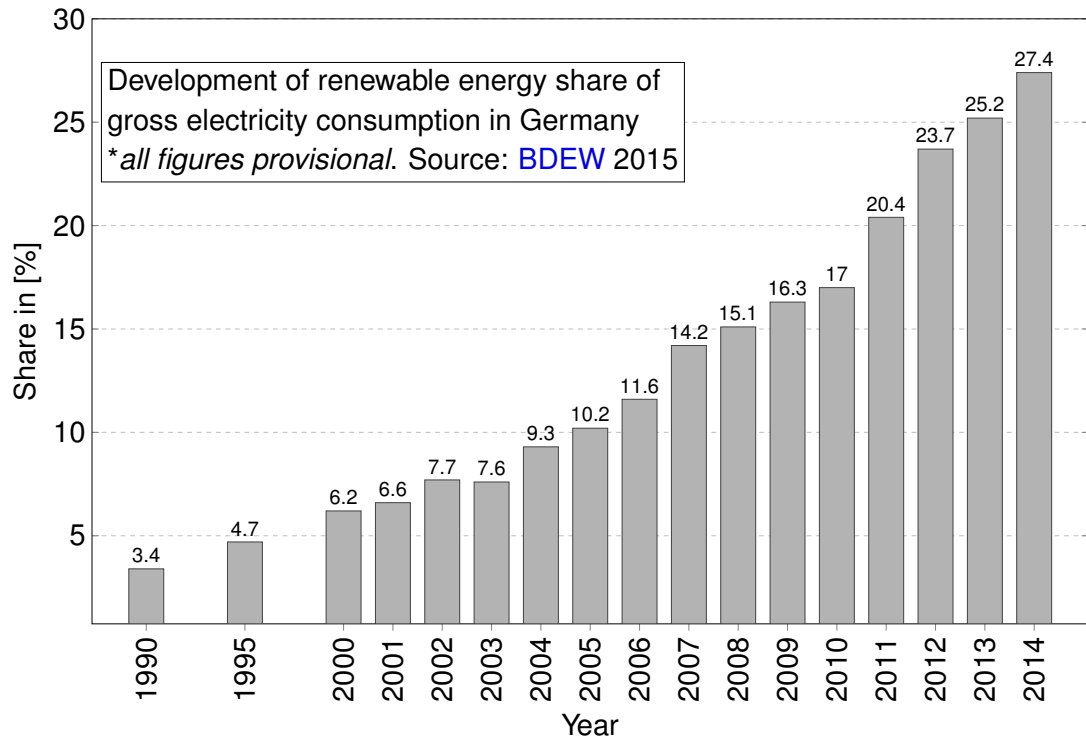
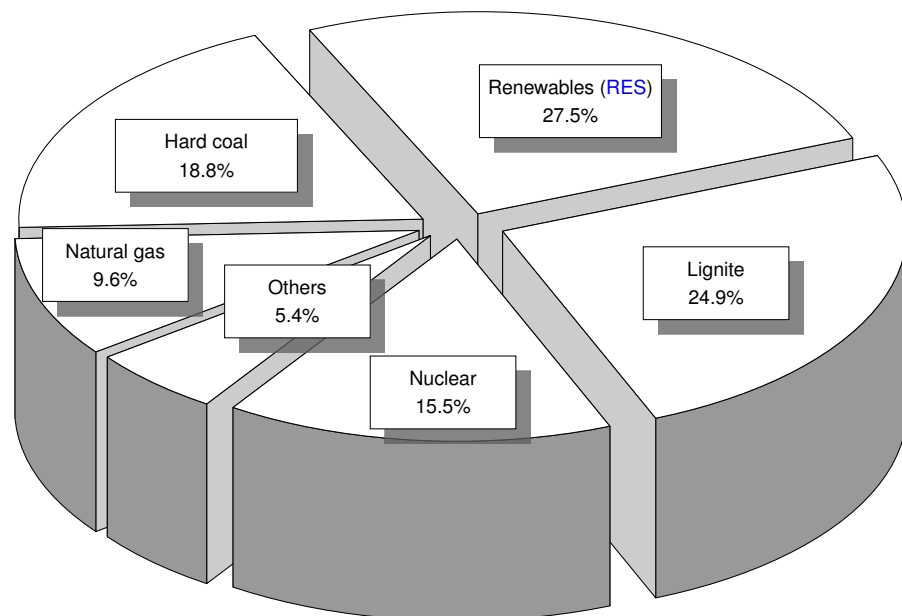
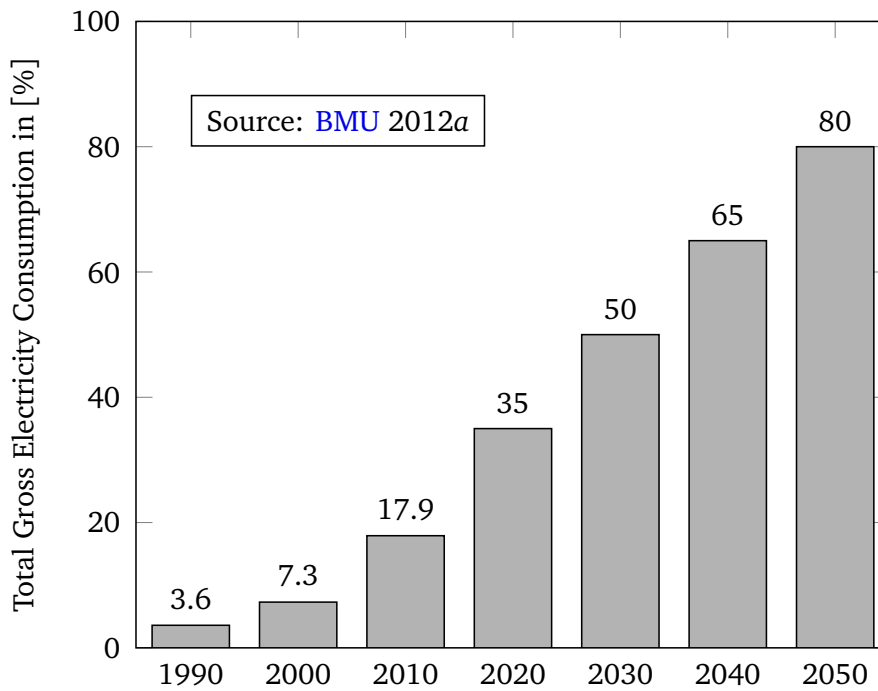


Figure 1.1.: Share of RES Gross Electricity Consumption in Germany, adapted from [21]



Source: adapted from BDEW 2015

Figure 1.2.: Gross electricity generation in Germany, 2014



**Figure 1.3.:** Renewable energy share in Germany past and future targets of the German government [20]

time and therefore making *v-RES* less suitable for grid control and stabilization. This implies that conventional baseload power plants will have to compensate for the variability of wind and solar power (for instance, on a windless or cloudy day) through load cycling operations. Nowadays, this mode of operation is required of all power plants not only mid and peak load plants which are traditionally designed for load cycling operations, but also conventional baseload plants [16, 19, 22, 23].

**Table 1.1.:** Development of *RES* in Germany, [24]

Installed capacities (GW)	<i>RES</i> Integration				
	2010	2020	2030	2040	2050
Hydro (without <i>PSH</i> )	4.8	5.1	5.2	5.2	5.2
Wind onshore	26.8	32.9	35.9	38.0	39.0
Wind offshore	0.2	9.0	23.8	33.5	37.0
Biomass	5.3	7.9	8.5	8.7	8.7
Photovoltaic	10.0	42.0	60.0	70.0	75.0
Geothermal	0.0	0.3	1.0	2.3	5.3
<i>RES</i> direct import	0.0	0.7	7.7	15.8	20.8
<i>RES</i> total	47.1	97.9	142.1	173.5	191.0

The objective of the *Energiewende* to replace coal and nuclear power with renewables is a promising but challenging process for several reasons. As already mentioned [Section 1.1](#) above, nuclear and coal power plants operate as baseload plants throughout the year, that

is they operate for longer periods without interruptions and are only shut down during maintenance. This makes them inflexible and unsuitable for cycling unlike mid and peak load plants such as hard coal and natural gas plants which are flexible [20].

The reasons for conventional baseload inflexibility include lower operating costs, their large unit sizes and material-related problems. Load following operations or power ramps increases thermal stress or creep strains which can reduce the life expectancy of the material [20, 25, 26]. Cycling baseload power plants might also lead to safety issues from increased human errors, low efficiency as well as negative environmental effects [20].

Furthermore, the start up time from a cold state (cold start) for baseload plants can take several hours and even days to reach full load, see Table 1.2. Therefore, load following operations can be very slow which again makes baseload plants unsuitable for cycling [20, 27]. However, according to Deutsche Energie Agentur (German Energy Agency) (dena) [19], increased flexibility of conventional power plants can be achieved through retrofits of existing plants or the construction of new, highly flexible power plants.

**Table 1.2.:** A comparison of coal and gas power plants, [27]

		Coal power plant		Gas power plant
		Brown coal	Hard coal	(combined cycle)
Electrical efficiency in [%]	actual	43	46	58
	future	50	50	60
Start-up duration in [h]	cold start	4		2 – 3
	warm start	2 – 3		1 – 1.5
	hot start	1 – 2		0.5 – 1
Load rate of change, [%NP <sup>a</sup> per min.]		2 – 5	3 – 5	7
Minimum load, [%NP]	existing plants	40 – 50	35 – 40	30 – 50
	new plants	25	25	20 – 40

<sup>a</sup>NP =nominal power, cf. Appendix C

### 1.3. Problem Statement

As already discussed in Section 1.1 above, the rapid growth of renewable energy sources in the generation mix require conventional power plant to operate on a more flexible basis (cyclic mode) to compensate for the variable supply from wind and solar power. Older plants traditionally designed for baseload operations are required to adjust to increased cycling. Furthermore, fewer baseload plants will be needed for the future as they are being replaced by more modern and more flexible ones [28, 29]. Also, as already mentioned in Section 1.2 there are several technical difficulties associated with the increase of RES

especially from variable renewables such as wind and solar power into the generation mix. Increased flexibility means baseload power plants will have to increase the number of load following operations, part load operations, numerous starts and stop, reduce minimal, shorter periods offline, longer plants layups and ramping up and down. These mode of operations which are new for conventional plants can greatly affect or reduce the estimated life of the plants from material damage of important plant components (cf. [Section 2.2](#)).

Material problems that can result from increase cyclic operation include creep-fatigue damage, fireside corrosion of superheater and reheater tubings as well as membrane waterwall tubings, stress cracking corrosion among others. Furthermore, an increased rate in cycling operation on high-temperature components of existing plants can lead to an increase in wear-and-tear of the materials through fouling and slagging from the action of coal deposits on the materials (see [Section 2.4.4](#)). All these lead to a decrease in thermal efficiency and an increase in operating costs from repeated unit starts making it less profitable for these plants to stay in business.

Most studies on the impact of [RES](#) on conventional baseload plants often tend to neglect the material degradation aspects from corrosion and oxidation. Therefore, extensive research is needed in this area. As baseload coal-fired power plants increasingly operate in cycling modes it is important to understand the consequences of increased cycling on vital plant components such as superheaters and reheaters to minimize component damage and reduce operational and maintenance costs [[7](#), [9](#), [10](#)].

## 1.4. Study Approach

The goal of the present study is to investigate the corrosion and cyclic oxidation effects on coal-fired power plant materials which may arise from increased cycling. For this purpose, five commercial coal boiler superheater materials, namely: T91, VM12-SHC, TP347-HFG, DMV304 HCu and DMV310 N were selected for investigation. The materials were exposed to a model corrosive flue gas atmosphere under well controlled isothermal and cyclic oxidation conditions for 1000 h each at 650 °C. The corrosive gas used was a synthetic flue gas mixture consisting of CO<sub>2</sub>, O<sub>2</sub>, SO<sub>2</sub> at 500 ppmv, N<sub>2</sub> and H<sub>2</sub>O. The materials were also partly covered in coal boiler fly ash to investigated the impact it has on oxidation.

The weight change of the materials were measured at different time intervals to obtain information on the oxide scale growth and spallation. The results were fitted with kinetic modeling results from [COSP](#) – a Windows-based kinetic modeling software package to predict oxidation and spallation. The materials were analyzed metallographically using Light (Optical) Microscopy ([LOM](#)) and Scanning Electron Microscopy ([SEM](#)) together with Energy Dispersed X-Ray Spectroscopy ([EDS](#)), for scale morphology, oxide scale thickness and corrosion products.

Thermo-chemical computer-aided calculations were also performed to better understand the oxidation behavior of the test materials. The thermo-chemical software package FactSage™ version 6.4 – an Integrated Thermodynamic Database System (ITDS) with a compound (pure substances) database and a solution database (oxides, salts, metallic alloys etc.) was used to study the reaction of the synthetic flue gas and the fly ash with the tested alloys. In the next section (Section 1.4) the study approach and structure of the this study are outlined.

Figure 1.4 illustrates the structure of the current study which is divided into seven chapters. In Chapter 1 the reader is introduced to the problem and the goals and objectives of the study are presented. A critical review of available literature on high temperature cyclic oxidation and corrosion is given in Chapter 2. Thermo-chemical modeling calculations of flue gas corrosion are presented in Chapter 3. Chapter 4 provides the experimental work on isothermal and cyclic oxidation carried out in this study and the oxidation results are presented in Chapter 5 together with kinetic modeling results. In Chapter 6 the results obtained from the entire study are discussed while Chapter 7 gives a summary as well as suggestions and prospects for future studies.

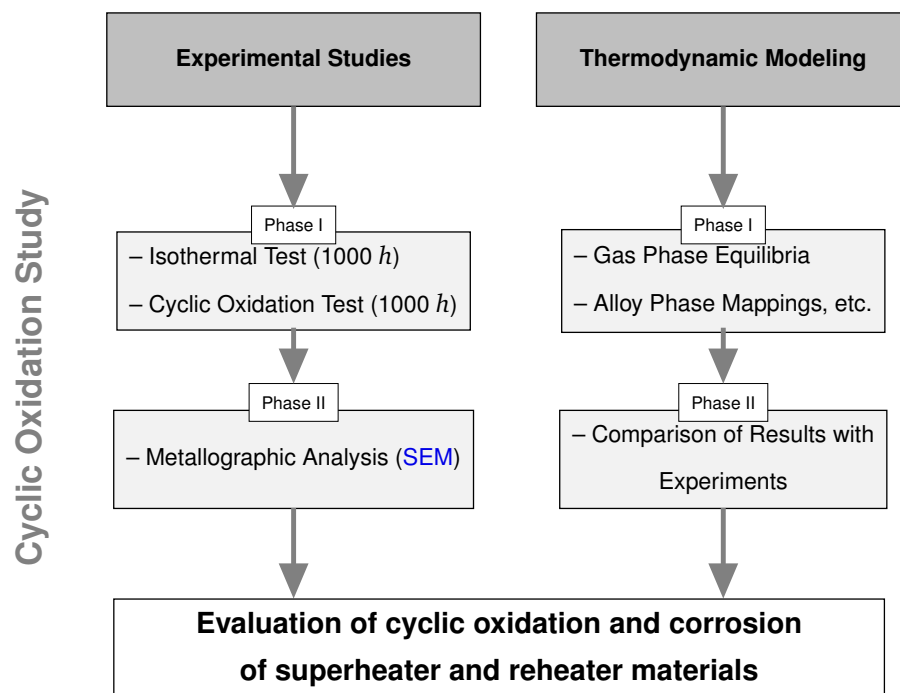


Figure 1.4.: Study approach



## 2. Literature Review

### 2.1. State of the Art

As already discussed in [Section 1.1](#), one of the main challenges facing energy systems worldwide is coping with the rapid growth of renewables in the generation mix. The main problem for conventional baseload power plants is that they are required to increase cycling which is different from the traditional mode of operation. This means load following operations, power ramps within short time intervals during periods of low wind or no sunshine and reducing generation at other times when there is a rise in wind power generation.

This trend is projected to continue and increase even further in the future. For example, in Germany, flexibility (i.e. dealing with power ramps within a few hours) was expected to increase from 30 GW of flexibility in 2009 to about 50 GW by 2020. This means more flexibility (20 GW) is required in the future. It is therefore necessary to look for ways of dealing with the increased load ramps [5]. At the moment the flexibility of coal power plants is estimated at about 2 GW for brown coal (lignite) and 1.5 GW for hard coal (including Combined Heat and Power (CHP)) plants at an installed capacity of 22 GW and 30 GW respectively. This means only about 5% of the installed capacities of both brown coal and hard coal can be used for flexibility operations corresponding to load gradient of 2 – 3 % per minute [5].

Renewable Energy Sources (RES) and especially variable Renewable Energy Sources (v-RES) such wind and solar power differ greatly from conventional baseload power in several aspects. Baseload power plants are dispatchable meaning they can be regulated, meanwhile variable energy sources are non-dispatchable and their hourly generation fluctuates or varies greatly, depending on the current state of the weather (windy or sunny) and the time of the day. Therefore, an increase of variable power in the generation mix can greatly affect the residual load<sup>1</sup> which could lead to brief situations where there is a surplus of variable power but at the same there is also a shortage in power. As a result, the integration of variable energies must take into account others important aspects such

---

<sup>1</sup>Residual load is the difference between actual power demand and feed-in from variable sources such as wind and solar [17]. cf. [Appendix C](#)

as energy storage systems, highly flexible thermal power plants as backups, expansion of the network among others [15].

Figure 2.1 shows a common load cycling operation of a conventional coal-based power unit with variable feed-ins from wind and PV, for the 16<sup>th</sup> of March 2012 [16]. As can be seen on the diagram this was a day with intense sunshine. Feed-in from PV increased from between 08:00 AM and 01:00 PM with about 16 GW and then started to drop between 02:00 PM and 06:00 PM.

Coal and gas power plants had to be ramped-up to cover for the high demand in the morning periods and then ramped-down during midday to give way for the temporary feed-ins from solar and to be able to also cover evening periods when demand is high again with full load operations. Thus, the coal and gas plants were briefly switched to partial load operations. This way separate grids are not needed for each feed-in [16].

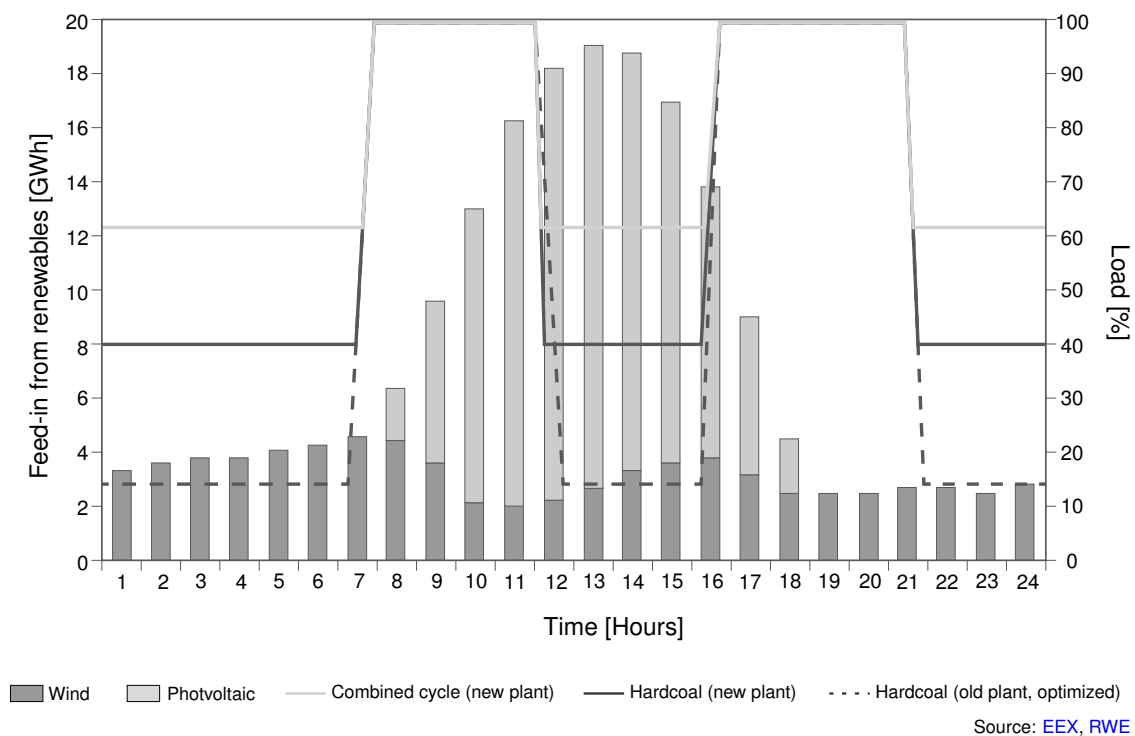


Figure 2.1.: Flexible operation with RES integration [16]

## 2.2. Cycling of generating units

Cycling is defined as a variety of operations which alters a plant's output. These include among others start ups and shut downs, ramping up or down and part load operations [9, 30, 31]. Cycling can also be referred to as sudden changes (i.e. an increase or a decrease) in the generation output of a plant. There are several reasons for cycling in power plants and these may be for servicing or maintenance, component failure, rapid load size changes



or more recently allowing for variable renewable generation. As already mentioned, the integration of intermittent v-RES into the power grid requires the increased cycling of both coal-based and natural gas units to make way for wind and solar power [28, 32, 33]. Mid and peak load power units such as gas turbines (natural gas combustion) and Combined Cycle Plants (CCP) are specifically designed for cycling operations. Baseload power units are less responsive to load changes than their load-cycling counterparts [5, 23, 34]. The minimum load for lignite and hard coal power plants is around 40 – 50% of the plants nominal output<sup>2</sup>, but newer or refurbished plants can have as low as 25 – 30% of nominal output [5].

As mentioned previously in Section 1.1, cycling is not new to power plants. Demand has always been variable and power system operators have always in the past been forced to vary generation to meet a highly predictable consumer demand on a daily, weekly or seasonal basis. Over the years, three different generators with different modes of operation were designed to balance electrical power output with consumer demand; these include: baseload, mid load (load-cycling) and peak load (also for load cycling). Baseload plants are traditionally large units that operate regularly at almost maximum power output, and are shut down a few times in a year during maintenance. This enables them to run for comparably longer periods without failure or equipment loss. Load cycling (mid load and peak load) plants on the other hand are specifically used as system reserves and they normally operate during periods of high demand to balance power output with consumer demand. Usually, brown coal (lignite) plants and nuclear power plants operate as baseload plants [20, 26].

Formerly, in a centralized power system, baseload plants operated only within their technical design limits throughout their lifetime with only brief periods of load cycling, peaking or use as system reserves before they were decommissioned. Nowadays, in a decentralized power system and also with the rapid increase of v-RES from solar and wind power, there has been a sudden change in the way baseload plants are required to operate. Power fluctuations are not only demand-driven as it previously was (determined by consumers) but also generation-driven which is determined by the availability of power from variable renewable sources [5]. The demand-driven fluctuation was more or less well defined, but variable power fluctuations are completely unpredictable. These kind of power fluctuations are completely new to conventional plants. Therefore, baseload load plants have to compete with medium and peak load cycling plants by increasing cycling operations (off-design operations) in order to maintain the price at which they sell power instead of operating within their design limits. Furthermore, feed-in priority is given to variable sources which forces conventional power plants out of merit. As a result, baseload plants have to increasingly operate in cycling modes which cause severe repercussions such as rapid age-

---

<sup>2</sup>Nominal power, output, or capacity, is the maximum potential full load capacity of a plant which is not necessarily the same as the actual full load output of the plant (cf. Appendix C).

ing, an increase in the cost of operation and a reduced lifespan (see Figure 2.2). [23, 34].

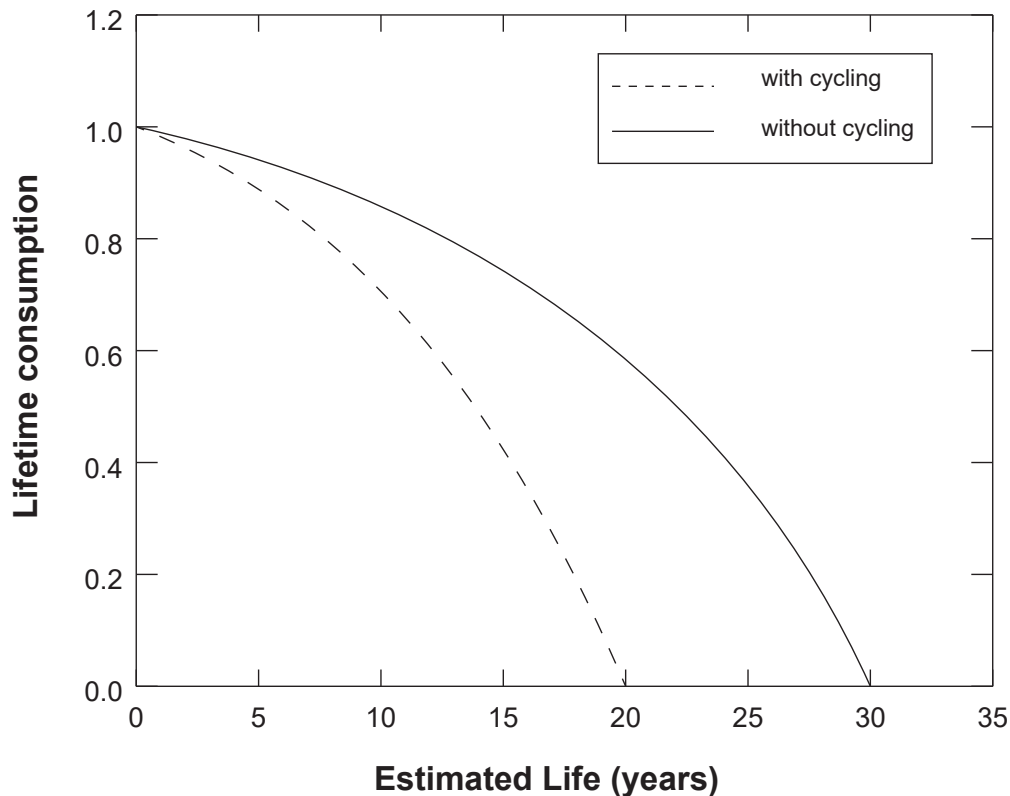


**Figure 2.2.:** Estimated life of baseload unit with and without cycling, adapted from [35]

Modern Combined-Cycle Gas Turbine (CCGT) are manufactured taking into consideration the new order of the day – increased cycling. They are designed to efficiently cope with variable nature of operation and still be able to minimize damage. Although large conventional units manage to cope with increase flexible operation, it still does not change the fact that these plants have an average design life between 25 – 40 years meaning existing baseload power plants will operate in increased cycling modes for most or the remainder of their service life. Studies on RES integration have often neglected the engineering impacts as well as the cost of increased cycling on baseload units [5, 34].

Material related issues (creep, fatigue or corrosion damage) which may result from off-design operating modes are of particular relevance to plant operators and owners of generation units as these have a significant impact on the service life of these plants [23, 34]. Cycling a plant leads to high temperature gradients and pressure stress on the boiler, the turbine as well as auxiliary equipment resulting in the damage of these components. Damage builds-up over time and ultimately leads to accelerated equipment breakdowns and forced outages which increases a plant's unreliability<sup>3</sup> [26]. It is also important to mention

<sup>3</sup>cf. Equivalent Forced Outage Rate (EFOR), Appendix C

that cycling or changing a units output once its on and running has little damaging effects. However, frequent starts ups and shut downs can be very damaging due to the large thermal transients. Figures 2.3 and 2.4 show the effect of part load operation and weekend shutdown on steam and metal temperatures. It is clear from the diagrams that shut downs and start ups cause a huge temperature change in both steam and steel temperatures than the part load operation at one-third of the full load.

Besides material damage caused by operating in cycling mode, cycling can also be very costly for baseload plants. According to Gutierrez-Martin *et al.*, [23] cycling increases the heat rate of generating units i.e. the amount of fuel used per unit of output, because more fuel is needed to bring the unit from say a cold state to steady operation state. This means less MWh generated for a similar amount of fuel.

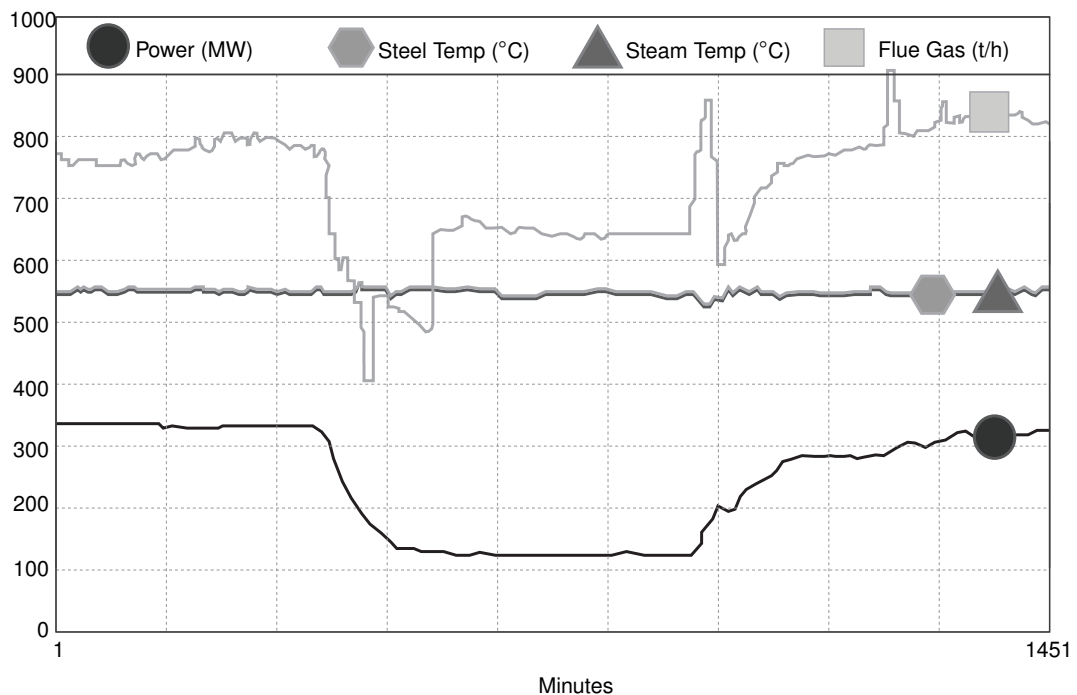


**Figure 2.3.:** Effect of part-load operation on steam and steel temperature [36]

### 2.2.1. Requirements for conventional coal-fired power plants

As variable energy feed-in continue to increase, the technical requirements for conventional baseload units have also increased. Some of the most essential of these requirements include: increased number of starts and stops, faster startups, a minimum downtime, brief operational periods, increase in part-load operations and load following operations, two-shifting, week shutdowns or long periods of standstills [29, 37, 38]. On the contrary, conventional power plants are designed for longer periods of operation at full load, and they have longer start-up times which could be disadvantageous for high operational flexibility. Nevertheless, the above mentioned requirements are a must today and

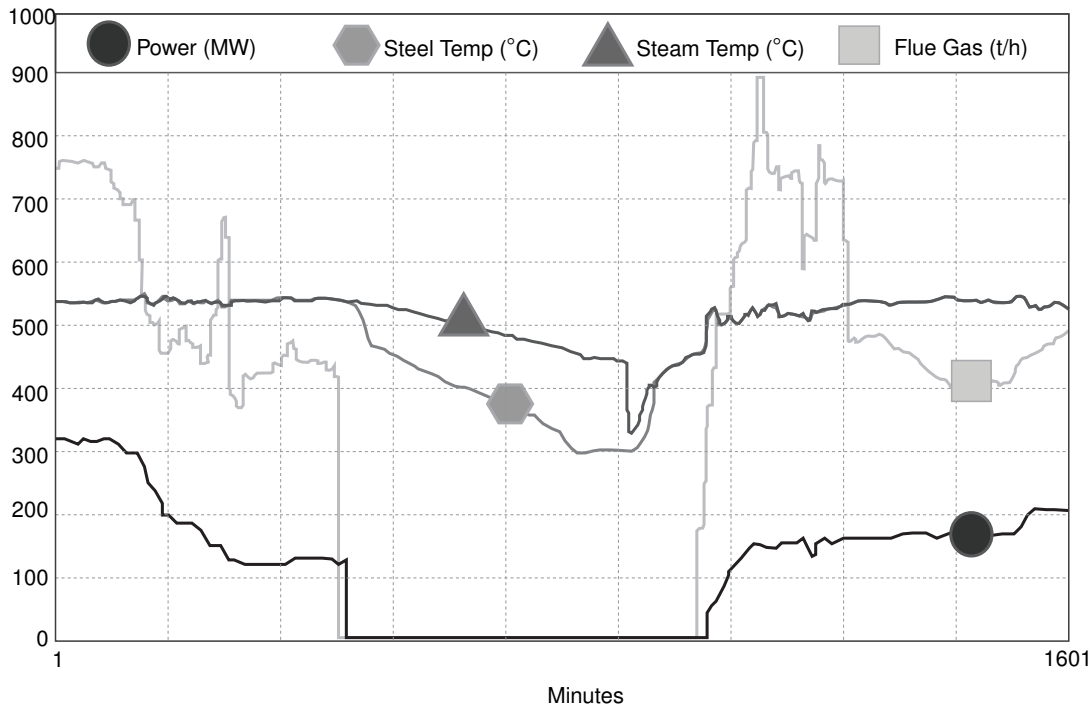


**Figure 2.4.:** Effect of weekend shutdown on steam and steel temperatures [36]

plants are required to have maximum output under a short period of time, minimum loads, frequent starts, increased rate of load change, shorter offline periods. This means existing conventional plants have to switch from baseload to more flexible load-cycling generation units [39,40].

### 2.2.2. Damages caused by cycling

Cycling can have damaging effects on coal-based power plant units as stated previously in [Section 2.2](#). Varying output leads to strains and stresses in the materials of plant components as the components undergo enormous changes in thermal and pressure stresses, for instance, during start up and shut down. This can result in accelerated equipment damage and unplanned outages. Start ups and shut downs are more damaging than load following operations. Wear and tear<sup>4</sup> on plant components can be increased from creep-fatigue interaction [28]. [Figure 2.5](#) shows the damage related with cycling (cold, warm and hot start) for a generation unit. The different damage mechanisms that may result from increased plant cycling are discussed in detail in [Section 2.4.4](#).

<sup>4</sup>see [Appendix C](#)

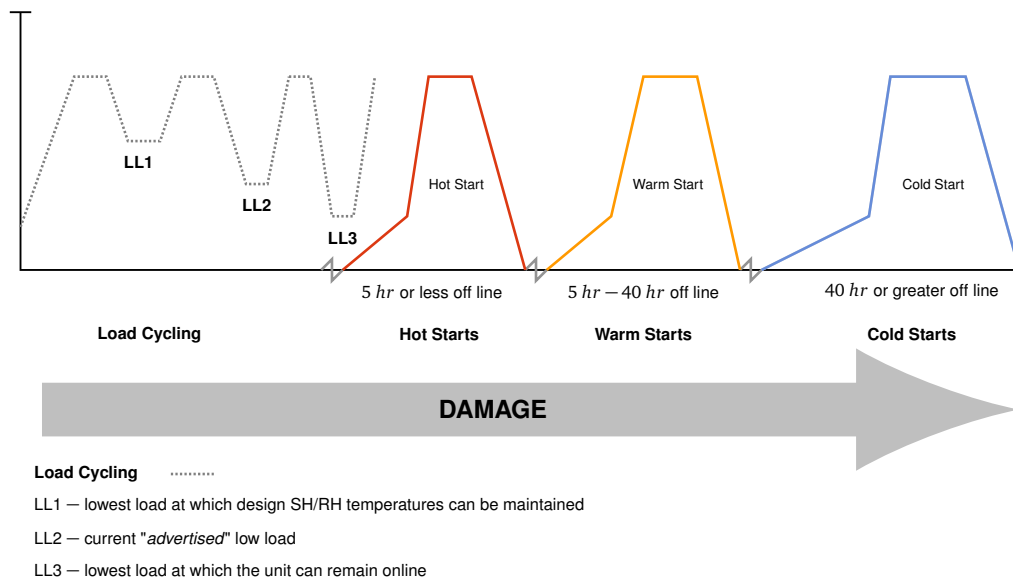


**Figure 2.5.:** Plant starts and relative damage caused by cycling (adapted from [10])

## 2.3. High Temperature Corrosion

### 2.3.1. Background

High temperature corrosion can be defined as the reaction of a metal with its environment at high temperatures in the absence of a liquid electrolyte [41–43]. It is also referred to as *scaling* or *dry corrosion*. Oxidation can sometimes be ambiguous because it can either refer to the formation of oxides or the oxidation of a metal (i.e. a change from a lower valence metallic state to a higher valence state). However, it is only one type of high temperature corrosion as shall be discussed in the next sections. It is, worth noting that oxidation is the most vital form of high temperature corrosion because alloys rely on this reaction to form protective scales for resistance against corrosion attack such as carburization, sulphidation or other forms of high temperature corrosion [42, 43]. The oxidation resistance of a metal is also dependent on other important properties of the high temperature oxide scale formed, and these include; the micro-structure, the thermodynamic stability of the scale, as well as the ionic defect structure [42] since all metals oxides and sulphides are ionic in structure [44].

Oxide scale formation is limited in reducing environments (see Table 2.1) which are characterized by low oxygen activities unlike in oxidizing conditions with high oxygen activities. Therefore, industrial reducing atmospheres are more corrosive than the oxidizing environments. At elevated temperatures, metals are able to *directly* react with the gaseous environment to form oxides or sulphides but electrochemical reactions remains the basic channel of high temperature corrosion [45, 46].

High temperature environment	
Oxidizing	Reducing
Oxygen	Hydrogen
Sulphur dioxide	Ammonia
Sulphur trioxide	Hydrogen sulfide
Water (steam)	Sulfur
Chlorine	Carbon
Carbon dioxide	Carbon monoxide
Molten salts	

**Table 2.1.:** Oxidizing and reducing environments at high temperature

Corrosion in general can take several forms as summarized in [Figure 2.6](#). The first group shows forms of corrosion which can be identified when visually inspected. *Uniform corrosion* or general corrosion is the form of corrosion where metal loss is regular or even; *Localized corrosion* (pitting, crevice) is the type where metal loss is found at distinct parts; *Galvanized corrosion* which is the damage that occurs when two dissimilar metals contact in the presence of an electrolyte.

The second group includes corrosion forms which may need additional means of identification. Flow related damages include *erosion* at high velocities; *cavitation* occurs at even higher velocities by bubbles at low pressure areas in the path of a flowing stream, *fretting* from friction of two surface in contact, and *intergranular corrosion* (grain boundary attack) occurring at the grain boundaries of metal structures; *exfoliation* involves preferential attack of a metal at or near grain boundaries. *dealloying* is damage where one or more alloying elements are selectively removed.

The last group are those types which must be identified by microscopic means. *Cracking* involves corrosion fatigue (cf. [Section 2.4.4.1](#)) due to mechanical stress in corrosive environments where a ductile material becomes brittle (e.g. Stress Corrosion Cracking (SCC)) High temperature (or gaseous, dry) corrosion e.g. scaling, internal attack as discussed above. There is also micro-biologically induced corrosion from the metabolic process of bacteria or microbes producing corrosive species in usually harmless environments.

High temperature corrosion remains an important problem in several industries, such as conventional power generations units like coal-based and nuclear power plants, natural gas combustion turbines, petrochemical and refineries, pulp and paper, chemical processing industries waste incineration and many others [42]. In the next sections, the thermodynamic ([Section 2.3.2](#)) and kinetic ([Section 2.3.3](#)) fundamentals necessary to understand gas-metal high temperature corrosion reactions are discussed and some examples are also given on the high temperature corrosion mechanisms peculiar to coal-fired generation plants ([Section 2.3.5](#)).

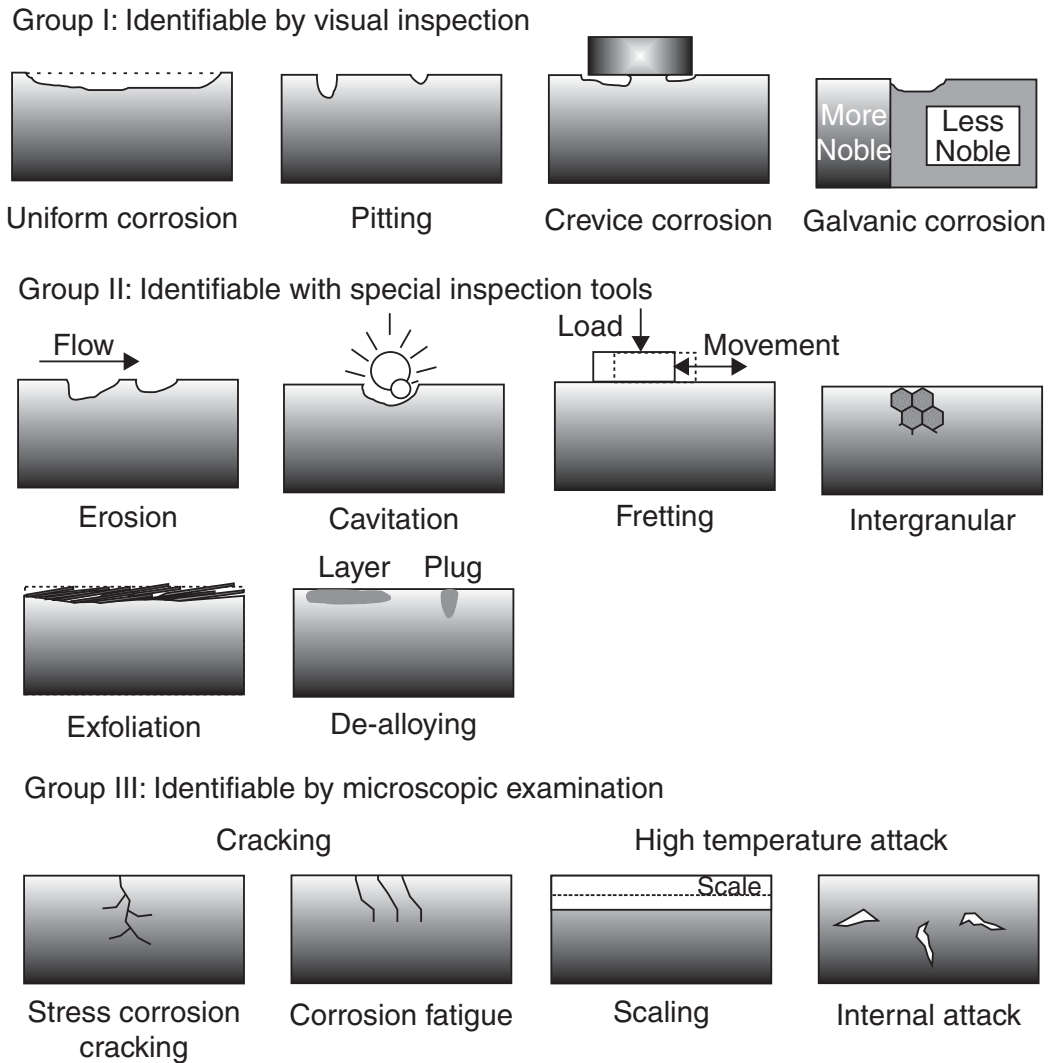


Figure 2.6.: Forms of corrosion [47]

### 2.3.2. Thermodynamic principles

A good knowledge of high-temperature corrosion reactions means one is able to predict whether a given metal or alloy component will react with a given gas phase component in its environment and then make an attempt to justify the corrosion products. However, in practice, corrosion related problems are more complex, and often involves multi-component systems i.e. one or more alloys reacting with gas mixtures made up of several components. The presence of liquid or solid particles that form by either condensation in the vapor or collision of particulate matter make the problem even worse [44].

One way of analyzing such problems is through equilibrium thermodynamics. Although not predictive, equilibrium thermodynamics allows one to verify the whether or not a given species will evaporate or condense significantly, the reaction products that may form, under which conditions a given reaction product will react with a condensed phase and many

other possibilities [42,44,46,47]. These analysis are conveniently represented in graphical form. A selected few of the various types of diagrams used are discussed below.

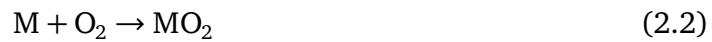
### 2.3.2.1. Standard free energy of formation versus temperature diagrams

It is often of interest to predict the possibilities under which a certain corrosion product (oxide, sulphide etc.) will form (for example, the selective oxidation of alloys). This information can be obtained by verifying which oxide is the most stable. The stability of a system at constant temperature and pressure is determined by its Gibbs free energy [46] which is the driving force of the reaction between a metal and a gaseous component [48]. It is defined by the second law of thermodynamics as shown in Equation (2.1):

$$\Delta G = \Delta H - T \Delta S \quad (2.1)$$

where  $\Delta H$  is the enthalpy change,  $\Delta S$  the entropy change of the reaction and  $T$  is the absolute temperature in Kelvins.

Considering a chemical reaction such as the oxidation of a metal Equation (2.2):



or for one mole of molecular oxygen Equation (2.3):



the Gibbs energy under standard temperature and pressure conditions is given as Equation (2.4):

$$\Delta G_{O_2/MO} = \Delta G_{O_2/MO}^{\circ} + RT \ln \frac{a_{M_xO_y}^{2/y}}{(a_M^{2x/y})(a_{O_2})} \quad (2.4)$$

where  $\Delta G$  is the Gibbs free energy of the system,  $\Delta G^{\circ}$  the free energy change of all species in their standard states,  $R$  the universal gas constant,  $T$  the temperature and  $a$  the thermodynamic activity which indicates the deviation from the standard state for a given species<sup>5</sup> [44, 48, 50]. The activity is given in Equation (2.5) as:

$$a_i = \frac{p_i}{p_i^{\circ}} \quad (2.5)$$

where  $p_i$  is the partial pressure of a gaseous species or the vapor pressure of a condensed species and  $p_i^{\circ}$  is the partial pressure at standard state of species  $i$  which is usually chosen as unity (1 atm) for convenience [46]. When  $\Delta G < 0$ , the reaction is spontaneous;  $\Delta G = 0$ , means thermodynamic equilibrium and when  $\Delta G > 0$ , the process is thermodynamically

<sup>5</sup>Activity can also be defined as the ratio of the fugacity of a species  $i$  at a given state to the fugacity of the same species at standard state i.e.  $a_i = f_i/f_i^{\circ}$  (relative fugacity). Fugacity is an effective pressure and is defined as the pressure at which the chemical potential of an ideal gas is the same as that of the real gas cf. [49].



impossible. At equilibrium conditions when the change in temperature and pressure are both equal to zero i.e.  $dT = 0 = dp$  ( $\Delta G = 0$ ), Equation (2.4) becomes Equation (2.6):

$$\Delta G_{\text{O}_2/\text{MO}}^0 = -RT \ln \frac{a_{\text{M}_x\text{O}_y}^{2/y}}{(a_{\text{M}}^{2x/y})(a_{\text{O}_2})} = -RT \ln K \quad (2.6)$$

where  $K$  is the equilibrium constant which describes the equilibrium state of the system. The standard free energy of a selected reactions of interest are given in Table 2.2.

**Table 2.2.:** Standard free energies of reactions [46, 51]

Reaction	$\Delta G^0 = A + BT^a$ ( $\text{J} \cdot \text{mol}^{-1}$ )	
	A	B
$\frac{2}{3}\text{Al} + \frac{1}{2}\text{O}_2 \rightarrow \frac{1}{3}\text{Al}_2\text{O}_3$	-565,900	128
$\frac{1}{2}\text{Si} + \frac{1}{2}\text{O}_2 \rightarrow \frac{1}{2}\text{SiO}_2$	-451,040	86.8
$\text{Mn} + \frac{1}{2}\text{O}_2 \rightarrow \text{MnO}$	-412,304	72.8
$\frac{2}{3}\text{Cr} + \frac{1}{2}\text{O}_2 \rightarrow \frac{1}{3}\text{Cr}_2\text{O}_3$	-373,420	86
$\frac{23}{6}\text{Cr} + \text{C} \rightarrow \frac{1}{6}\text{Cr}_{23}\text{C}_6$	-68,533	-6.45
$\text{Fe} + \frac{1}{2}\text{O}_2 \rightarrow \text{FeO}$	-264,890	65.4
$3\text{FeO} + \frac{1}{2}\text{O}_2 \rightarrow \text{Fe}_3\text{O}_4$	-312,210	125.1
$2\text{Fe}_3\text{O}_4 + \frac{1}{2}\text{O}_2 \rightarrow 3\text{Fe}_2\text{O}_3$	-249,450	140.7
$\text{Fe} + \frac{1}{2}\text{S}_2 \rightarrow \text{FeS}$	-150,247	52.6
$3\text{Fe} + \text{C} \rightarrow \text{Fe}_3\text{C}$	-29,037	-28.0
$\text{Co} + \frac{1}{2}\text{O}_2 \rightarrow \text{CoO}$	-233,886	70.7
$3\text{CoO} + \frac{1}{2}\text{O}_2 \rightarrow \text{Co}_3\text{O}_4$	-183,260	148.1
$\text{Ni} + \frac{1}{2}\text{O}_2 \rightarrow \text{NiO}$	-234,345	84.3

<sup>a</sup>where  $A$  is the temperature-independent standard enthalpy change of the reaction ( $\Delta H^0$ ),  $B$  is the temperature-independent standard entropy change of the reaction ( $S^0$ ) and  $T$  is the temperature in  $[K]$

*Ellingham diagrams* or *Ellingham-Richardson diagrams* [41, 46] are standard Gibbs free energy of formation ( $\Delta G^0$ ) which are used to compare the relative stability of each product as well as estimate the conditions under which a metal is oxidized or the circumstances

where a metal oxide is reduced [42, 44, 45, 52–56]. The values of  $\Delta G^\circ$  are represented in kilojoules [kJ] per mole of  $O_2$ . This is to normalize the scale as well as making it possible to do a direct comparison of the stability of these oxides. Figure 2.7 illustrates Ellingham diagram for the stability of oxides<sup>6</sup>. The lower the position of a line (lower standard free energy) on the diagram, the more stable is the oxide, sulphide etc in question. [42].

Reconsidering the reaction for the oxidation of metals (Equation (2.2)), and assuming that the metal and its oxide have unit activities, the oxygen partial pressure can be represented as given in Equation (2.7) or in its logarithmic form as given in Equation (2.8). Equation (2.7) indicates the oxygen partial pressure at which both metal and oxide coexist (i.e., the dissociation pressure of the oxide) [42, 44, 47].

$$p_{O_2}^{M/MO_2} = \exp\left(\frac{\Delta G^\circ}{RT}\right) \quad (2.7)$$

$$\log p_{O_2}^{M/MO_2} = \frac{\Delta G^\circ}{RT} \quad (2.8)$$

### 2.3.2.2. Gibbs free energy vs composition diagrams

The equilibrium state at constant temperature and pressure is described by the Gibbs free energy minimization i.e. a minimum in the Gibbs free energy of the system. The Gibbs free energy is given by Equation (2.9):

$$G = \sum_i \mu_i n_i \quad (2.9)$$

where:  $\mu_i$  is the chemical potential and  $n_i$  the number of moles of component  $i$ . At chemical equilibrium i.e. when the change in temperature and pressure are both equal to zero ( $dT = 0 = dp$ ) the Gibbs energy equation becomes Equation (2.10).

$$\sum_i \mu_i n_i = 0 \quad (2.10)$$

For a binary system the Gibbs energy is given by Equation (2.11):

$$G = (1 - X)\mu_A + X\mu_B \quad (2.11)$$

where  $\mu_A$  and  $\mu_B$  are the chemical potentials of the components A and B while  $(1 - X)$  and  $X$  are the mole fractions of A and B respectively. For a multi-component system with multiple phases the minimum energy represents the stability of the chemical potential ( $\mu$ ), of each component in the system.

From Equation (2.11) the chemical potentials ( $\mu_A$ ) and ( $\mu_B$ ) can be derived as given in Equation (2.12) and Equation (2.13) respectively.

$$\mu_A = G - X \frac{dG}{dX} \quad (2.12)$$

<sup>6</sup>The Ellingham diagram for sulphides is given in Figure B.1

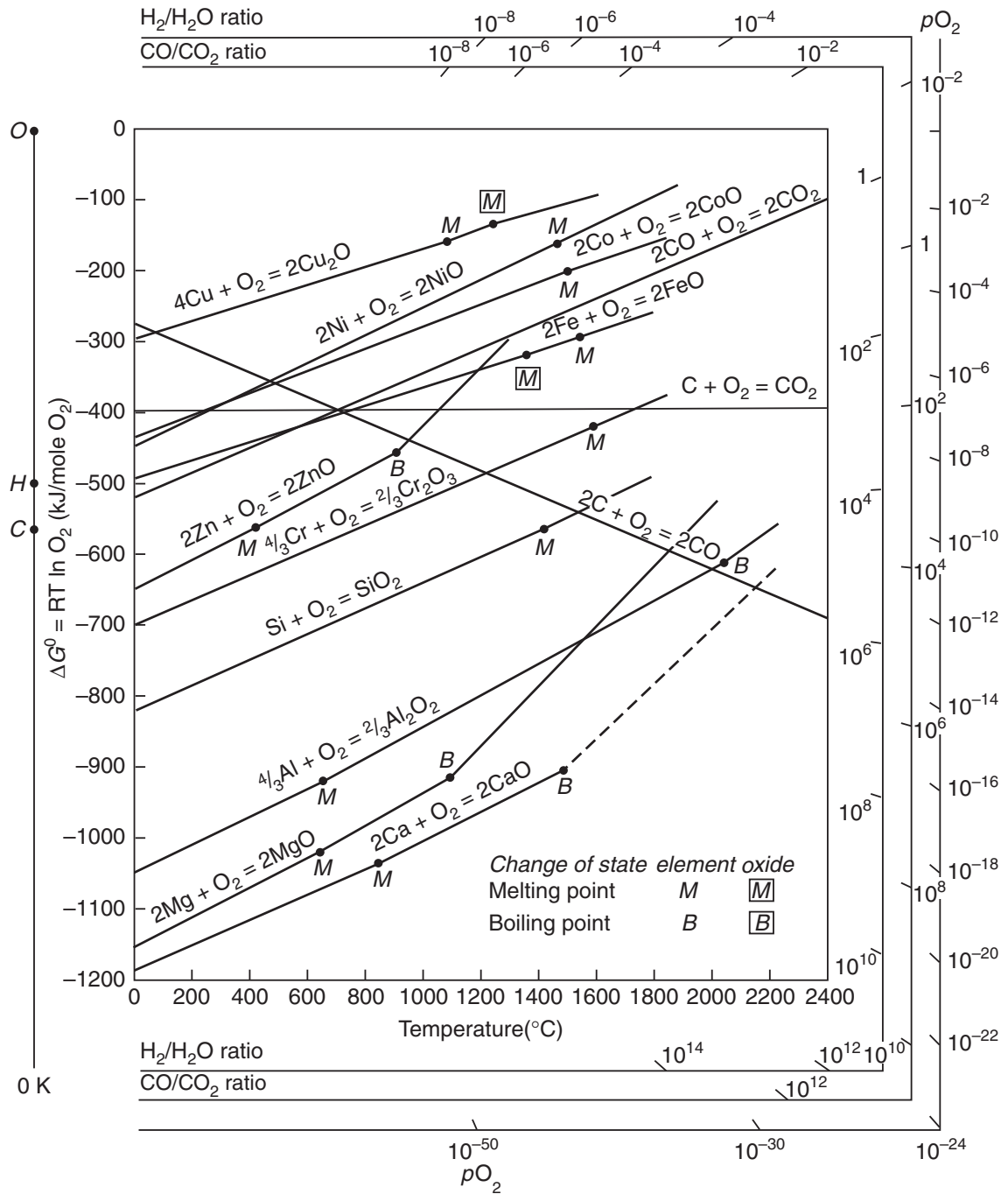


**Figure 2.7.:** Ellingham diagram for oxides formation at standard states: pure elements, pure oxides and gases at 1 amt. [43]

$$\mu_A = G - (1 - X) \frac{dG}{dX} \tag{2.13}$$

Figure 2.8 illustrates a plot of Gibbs energy versus composition for a single phase and two co-existing phases. From Figure 2.8a a tangent drawn to the free-energy curve intercepts the  $y$  - axis at  $X = 0$  and  $X = 1$  which corresponds to the chemical potentials of A and B, respectively. From Figure 2.8b, it is seen that, the two phases cross each other at lower temperatures and the standard free energy is minimized by separating the two phases. A

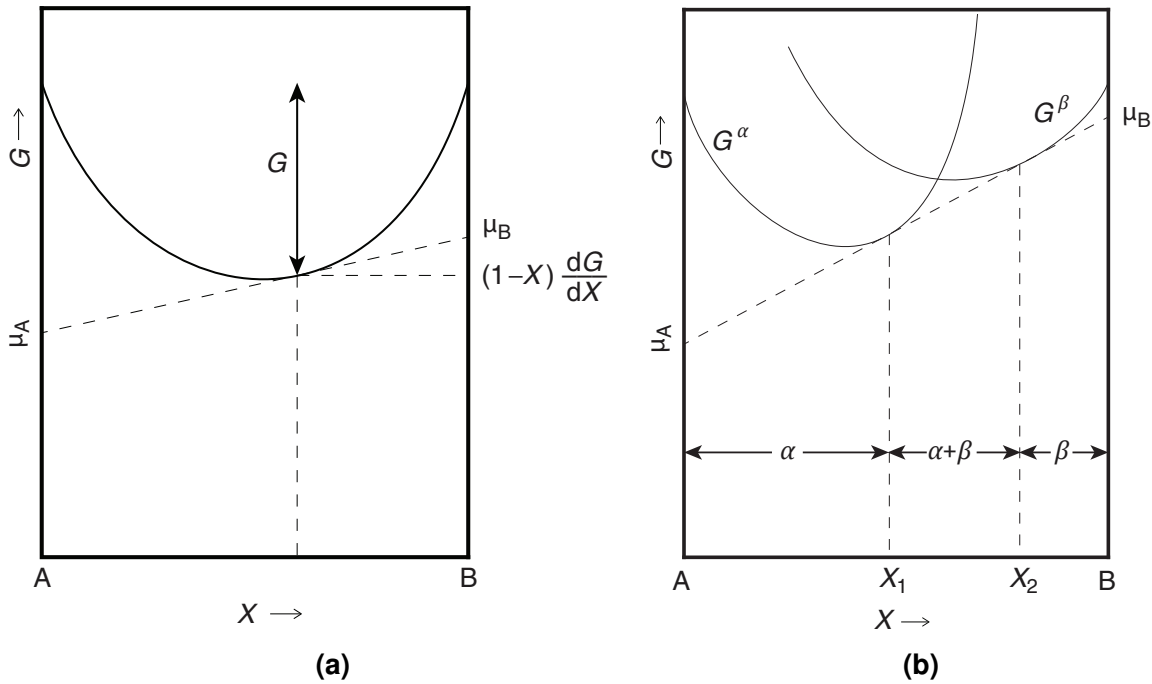


**Figure 2.8.:** Gibbs free energy vs composition diagrams for (a) single phase and (b) two co-existing phases (adapted from [44])

common tangent drawn between the two individual Gibbs energy curves with intercepts at  $X = 0$  and  $X = 1$  indicates that  $X_1$  and  $X_2$  are the equilibrium compositions of the two co-existing phases and also the equality of the chemical potentials i.e.  $\mu_A^\alpha = \mu_A^\beta$  and  $\mu_B^\alpha = \mu_B^\beta$  in the composition range  $X_1$  to  $X_2$  with two co-existing phases  $\alpha + \beta$  [44]. Isothermal horizontal lines (on a temperature vs composition diagram) that connect two co-existing phases throughout the two-phase region are called *tie lines* [57].

Other diagrams used for graphical representation of high temperature corrosion systems, e.g. oxides, sulphides, etc. are activity vs composition diagrams that are useful to explain corrosion products or particulate matter formed on the metal [44].

### 2.3.2.3. Vapour species diagrams

According to Birks *et al.*, [44] and Roberge, [42, 47] vapor species formed during high temperature corrosion can strongly affect the corrosion rate. The formation of volatile vapor species significantly accelerate the rate of attack. As cited in [42] it has been shown by Gulbransen and Jansson that the metal and volatile oxide species play an important role in the kinetics of high-temperature oxidation of chromium, molybdenum, carbon and silicon. Some six important facts of high temperature oxidation that have been deduced include [44]:

1. Oxygen and metal species diffuse through a compact oxide film at low temperatures,

2. Oxide films form and evaporate at medium and high temperatures,
3. Volatile metal and oxide species form at the metal-oxide interface and move through the oxide layer and mechanically form cracks in the oxide layer at moderate and high temperatures,
4. Volatile oxide gases directly form at moderate and high temperatures,
5. Gaseous oxygen diffuse through a barrier oxide layer that has been volatilized at high temperatures, and
6. *Spallation* or the breaking off of metal and oxide particles occur at high temperatures.

Vapour pressures in oxide systems are usually represented in  $\text{Log}(p_{M_xO_y})$  (i.e. the log of the metal oxide partial pressures) versus  $\text{Log}(p_{O_2})$  (i.e. the log oxygen partial pressures) at constant temperature, (cf. Figure 2.9). Another diagram used is the Arrhenius diagram which is a  $\text{Log}(p_{M_xO_y})$  versus  $1/T$  (with T in K) at a constant oxygen pressure. It can be seen from Figure 2.9 that high Cr(g) vapor pressures are formed at low-oxygen partial pressures and high-oxygen partial pressures produce a much larger  $\text{CrO}_3(\text{g})$  pressure. This high pressure of  $\text{CrO}_3(\text{g})$  can lead to the thinning of protective chromia ( $\text{Cr}_2\text{O}_3$ ) scales [42]. Also, for this Cr-O system at high temperatures only one condensed

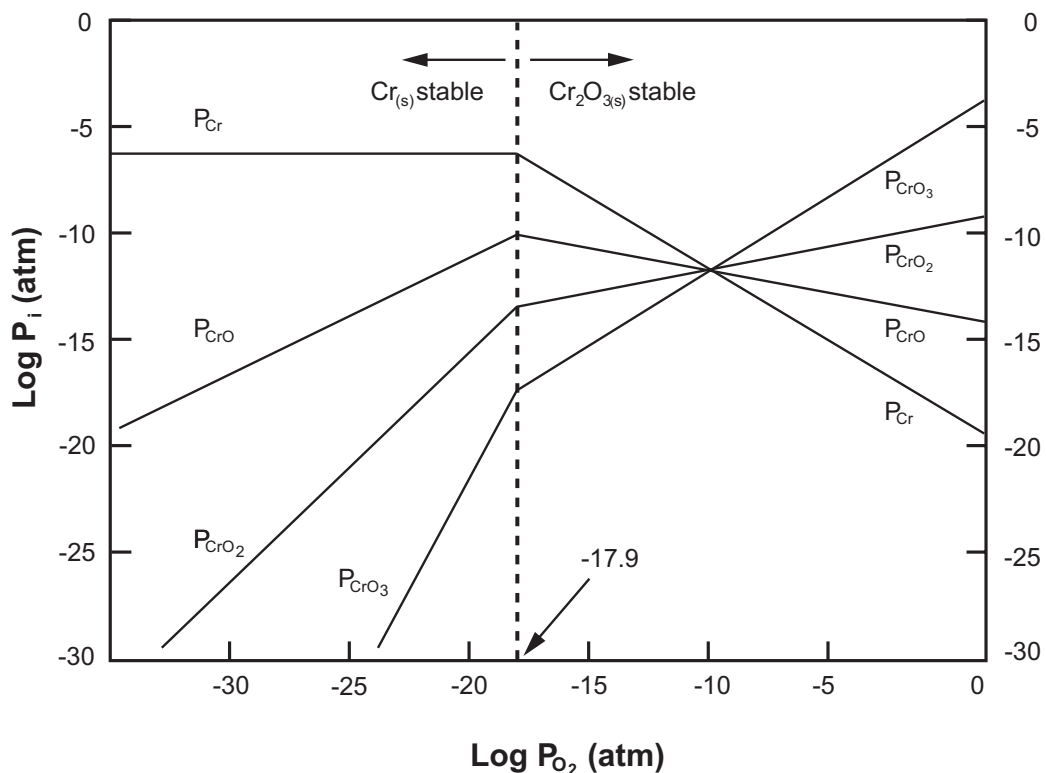


Figure 2.9.: Vapour equilibria in the Cr-O system at 1250 °C [42]

#### 2.3.2.4. Two-dimensional Isothermal stability diagrams

During the reaction of a metal with a gas system consisting of two or more oxidants different phases are formed that depend on thermodynamic and kinetic considerations. The phases during such reactions are best represented graphically using classical *two-dimensional isothermal stability diagrams*. They offer a simpler way of analysing the different condensed phases during oxidation, sulphidation or carburization etc. reactions. They are commonly plotted as the log of the activities or the log partial pressures of two non-metallic components (usually  $O_2$ ,  $SO_2$ , etc.) or sometimes as the log of the partial pressures of one non-metallic component against the composition ratio of two metallic components (e.g. Fe-Cr-O system).

Some of the properties of the diagram are: the diagram is divided into areas that are labelled with the predominant (stable) phase under the specified conditions of temperature or pressure – hence the name *predominance area diagrams* is also used to refer to these diagrams. However, more than one phase may be stable in an area but the other phases are only in smaller quantities. Secondly, the line separating two phases indicate conditions of equilibrium between the two phases [58].

Phase stability diagrams assume that all the species have an activity of one which corresponds to standard state [42, 44, 46]. Small deviations from unity in the activities indicate only minor instability while large deviations imply that particular phase is not likely to form [59]. There are also three-dimensional phase diagrams for reactions that illustrate two metallic components reacting with two non-metallic components [44].

#### Limitations of phase stability diagrams

The assumption of unit activity limits the use of phase stability diagrams. The limitations of stability diagrams include [48, 58]:

- The diagrams often only indicate the main components while leaving out important impurities that are commonly found in industrial atmospheres.
- As already noted above, the diagrams assume unit activities i.e. equilibrium conditions. Equilibrium can often be reached quite rapidly in high temperature oxidation settings. However, when the metal or material is cooled-down equilibrium conditions are not re-established.
- Another important limitation of phase stability diagrams is that they are based entirely on thermodynamic data but they do not give any information on the kinetics (i.e. the rate of oxidation).

- Finally, gases in cracks or voids (*micro-environments*) can lead to a phase other than expected from the overall reaction reaction.

Figures 2.10 to 2.15 show some examples of interest of two dimensional phase stability diagrams calculated with the thermodynamic modeling software FactSage™.

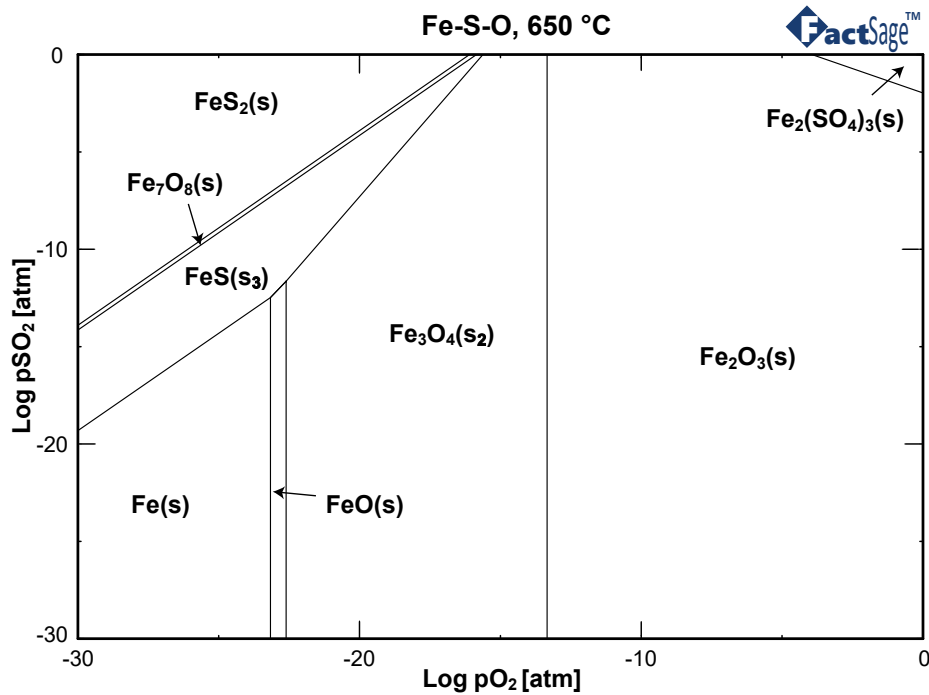


Figure 2.10.: Fe-S-O phase stability diagram at 650 °C

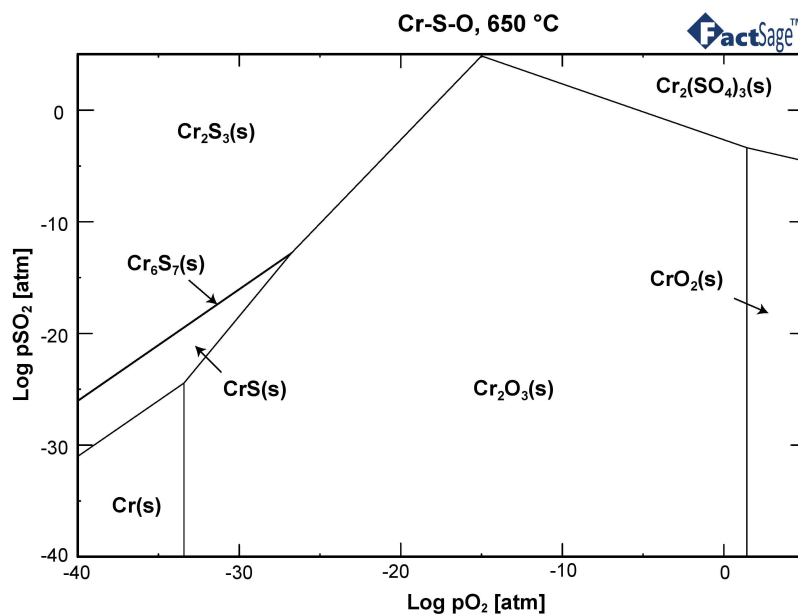


Figure 2.11.: Cr-S-O phase stability diagram at 650 °C

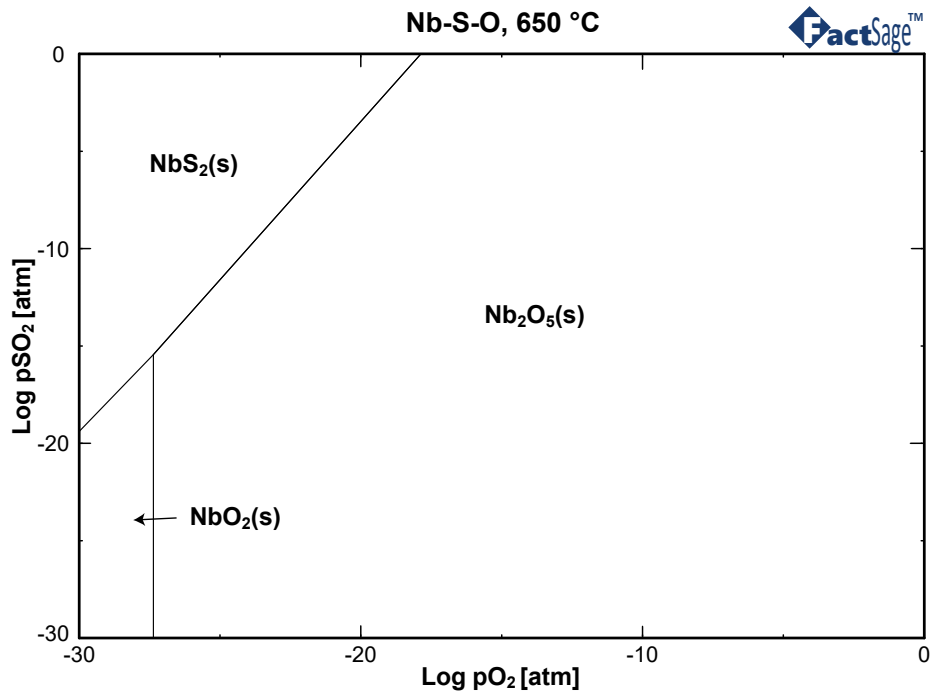


Figure 2.12.: Nb-S-O phase stability diagram at 650 °C

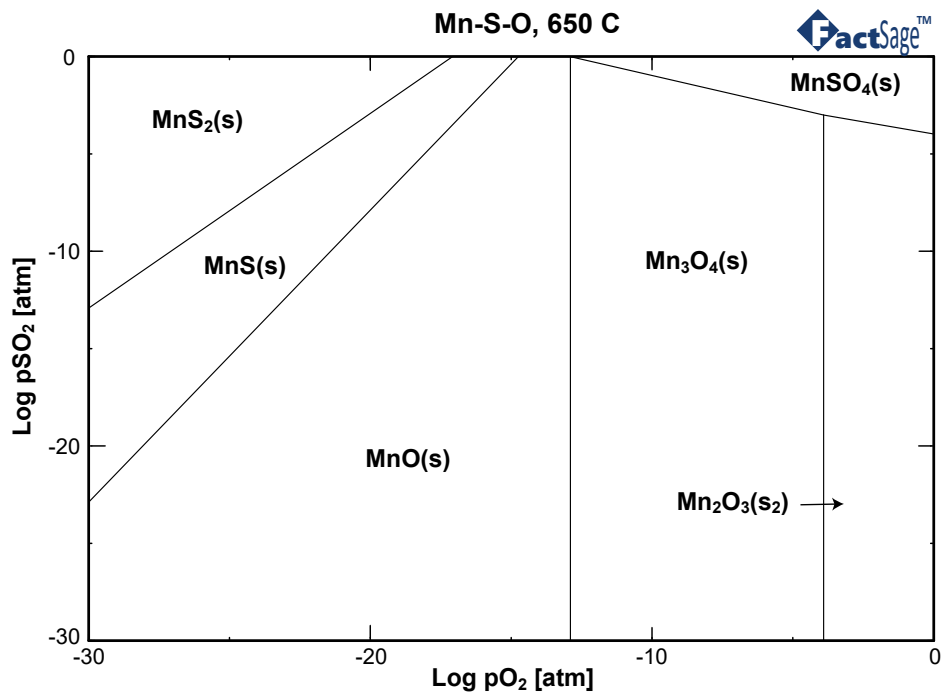


Figure 2.13.: Mn-S-O phase stability diagram at 650 °C



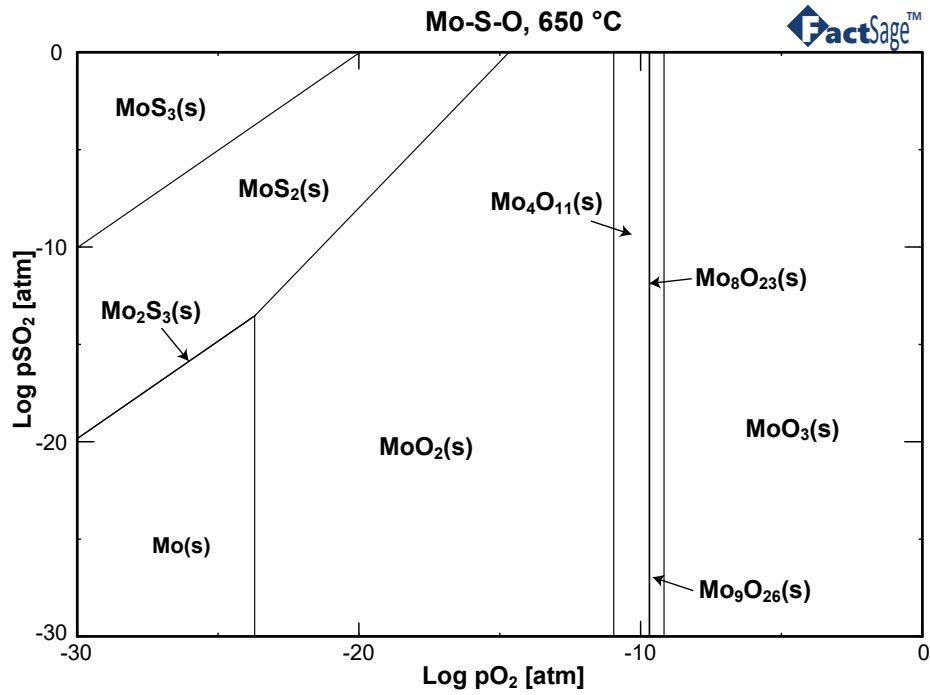


Figure 2.14.: Mo-S-O phase stability diagram at 650 °C

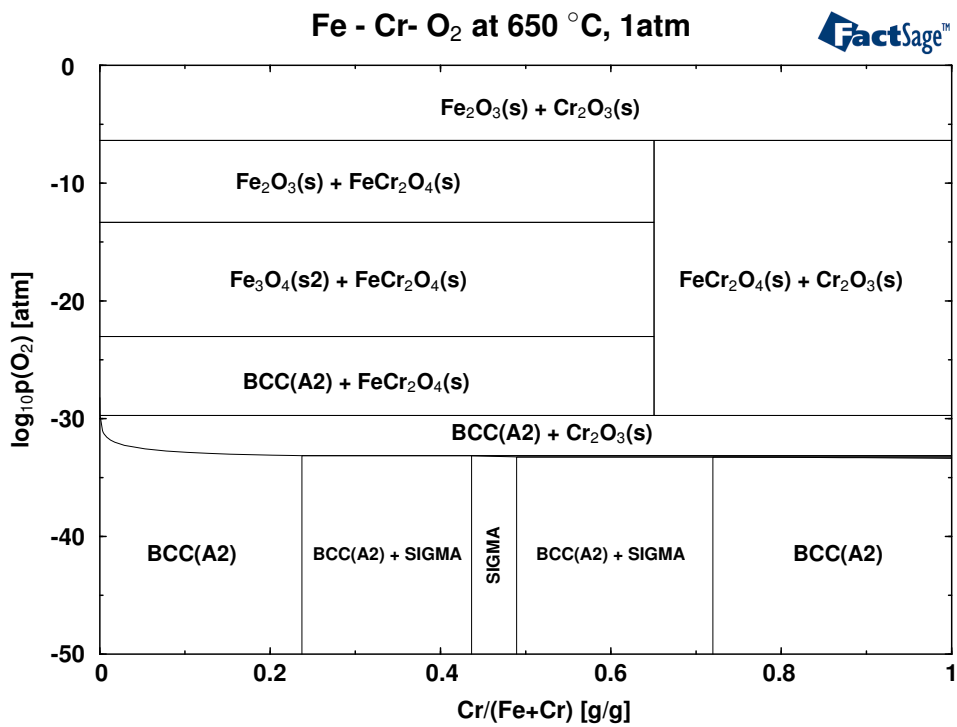


Figure 2.15.: Fe-Cr-O<sub>2</sub> System at 650 °C

### 2.3.3. Kinetic principles

#### 2.3.3.1. Mechanisms of high temperature oxidation

Considering the reaction of a metal with oxygen to form an oxide Equation (2.14):



the solid metal oxide (MO) product that forms from the reaction separates the two reactants as shown in Figure 2.16. The metal oxide product formed may be a solid, liquid or a gas. For instance, chromium, vanadium and molybdenum oxidizes to  $Cr_2O_3$  (solid),  $V_2O_5$  (liquid) and  $MoO_3$  (gaseous). Therefore, for such a case only chromium oxide will not corrode easily and could act as a protective barrier [47].

The overall oxidation process can be summarized into a series of steps as follows: First, there is mass transfer of oxygen to the metal surface where it is adsorbed. Next, the reacting metal is transferred to the metal-scale boundary where it assimilates into the scale. Further growth occurs by the movement of metal and or oxygen through the oxide layer [46]. The formation of defects such a voids or macro-cracks as the scale grows can reduce the protectiveness of the oxide film because such defects facilitate the movement of oxygen to the metal substrate to cause further oxidation [42]. There are several theories in the literature used to explain the transport mechanisms especially at low temperatures or at the early phase of high temperature oxidation where logarithmic growth rate prevails [44, 48].

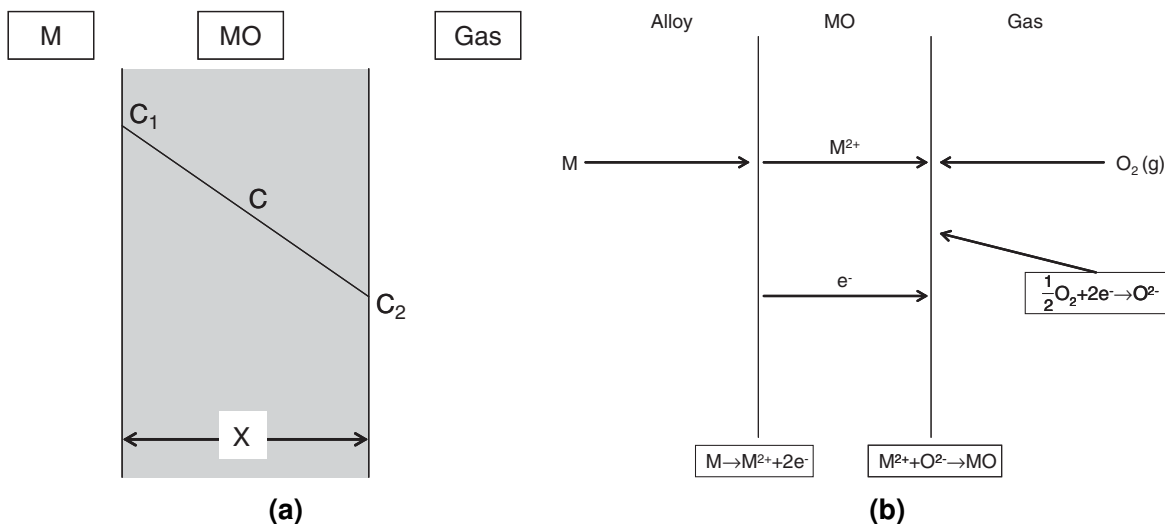


**Figure 2.16.:** Schematic cross-sectional diagram of oxide scale growth, (a) showing scale thickness and (b) transport processes and reactions occurring during oxide scale growth [46]

### 2.3.3.2. Wagner's theory on high temperature oxidation

Wagner's model attempts to explain the the behavior of high temperature oxidation where the diffusion of ions determines the rate of oxidation as is illustrated in Figure 2.17. For an oxidation process to progress in such a case as shown in Figure 2.17, Wagner assumes that (as cited in [44]):

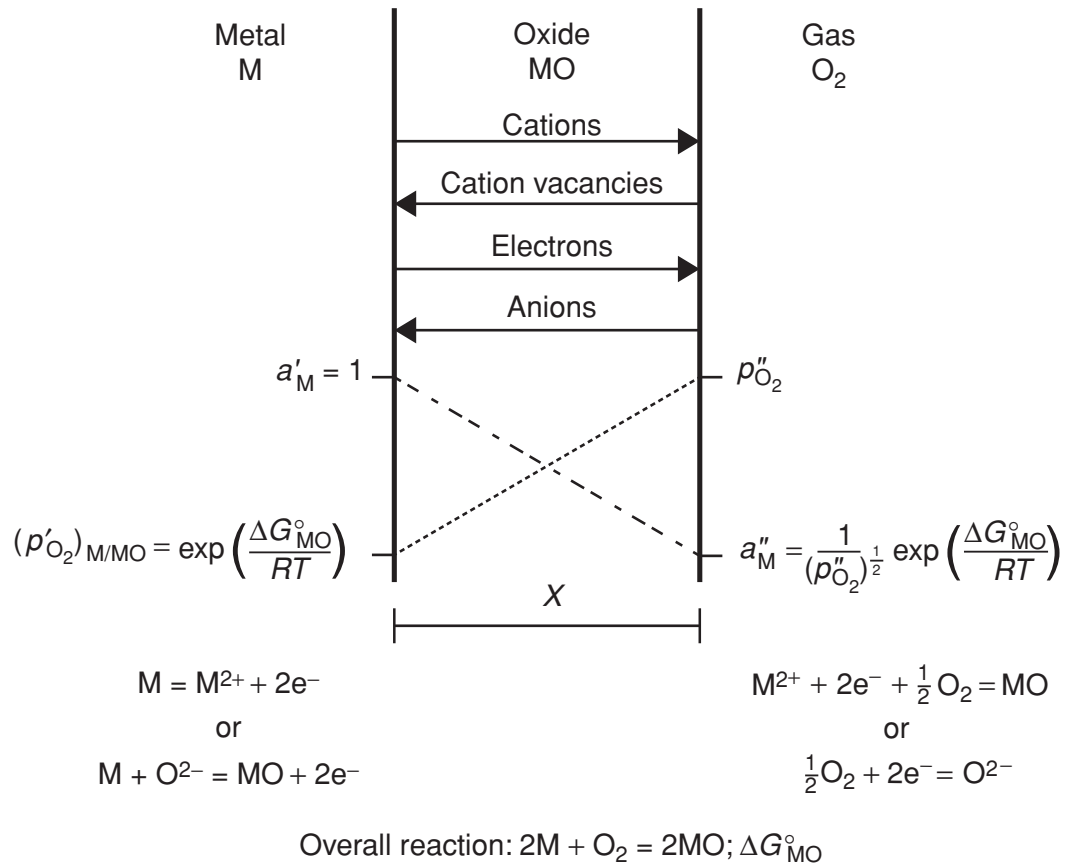


**Figure 2.17.:** Wagner's model on scale formation [44]

- the metal oxide scale is compact and perfectly adherent.
- the movement of electrons or ions across the scale is what controls the rate of the oxidation process.
- thermodynamic equilibrium exist at both the metal–scale and scale–gas interfaces.
- the oxide layer indicates only small variations from stoichiometry (i.e. the metal to non-metal ratio as given by the chemical formula) which therefore means that the movement of ions do not depend on their position within the scale.
- thermodynamic equilibrium also exist locally throughout the oxide scale.

- the thickness of the oxide layer can be compared with the distance where the electrical double layer (i.e. two parallel layers with opposite electric charges) takes place
- the solubility of oxygen in the metal is not considered.

With the assumption of thermodynamic equilibrium conditions at both the metal–scale and scale–gas interfaces, it can be concluded that activity gradients also exist across the scale for both the metal and non-metal (oxygen, sulphur, etc.). As a result, metal and oxide ions are inclined to migrate in opposite directions across the oxide scale. Due to this back and forth movements of ions, the net of charge transfer is zero (balanced).

### 2.3.3.3. The Pilling-Bedworth ratio

A useful parameter that is used in describing the protectiveness of an oxide scale is the Pilling-Bedworth ratio, which is the ratio of the volume of oxide produced to the volume of oxide consumed cf. Equation (2.15). The volumes of the oxides and metals are calculated from the atomic and molecular weights as well as the densities of the phases. If the volume of oxide produced is relatively high, this could break the binding force between the metal and the oxide. On the other hand, when the volume of oxide produced is comparatively low, this could lead to higher tensile stress in the oxide layer which can eventually result in cracks [42, 52]. Table 2.3 shows the PB–ratio for a selected number of oxides.

$$PB = \frac{V_{\text{oxide}}}{V_{\text{metal}}} = \frac{M_{\text{oxide}} \cdot \rho_{\text{metal}}}{n \cdot \rho_{\text{oxide}} \cdot M_{\text{metal}}} \quad (2.15)$$

$V_{\text{metal}}$  is the molar volume of the metal,  $M_{\text{oxide}}$  is the molecular weight of the oxide,  $\rho_{\text{oxide}}$  is the oxide density,  $n$  the number of metal atoms in the oxide molecule,  $\rho_{\text{metal}}$  the density of the metal and  $M_{\text{metal}}$  is the atomic weight of the metal.

The following applies for the PB ratio: a PB ratio moderately greater than 1 (like the case for Fe, Ni, Cr, Si, Co, Al and their alloys) implies good protection (most desired situation) because in this case only very little compressive stresses are produced in the oxide scale. If the ratio is greater than two (like the case for niobium, Nb and tungsten, W), large compressive stresses often occur during oxide growth which can cause cracks and eventually spalling thereby exposing the metal to further oxidation. Figure 2.18 shows some of the ways in which oxide layers are damaged. For a PB ratio less than 1, this directly implies the scale is non-protective. This is the case for porous scales on metals such as Mg, Ca, Na and K where tensile stresses can cause cracks and therefore offer no barrier against gas penetration to the surface of the metal. However, it is also worth mentioning that PB ratios have been found to offer poor evidence of the actual protectiveness of oxide scales for various reasons explained in [42, 52].

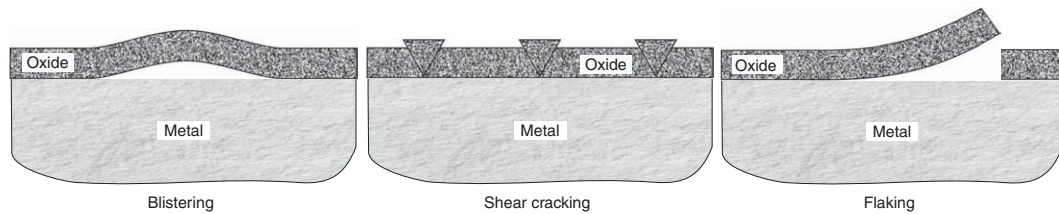


**Figure 2.18.:** Hypothetical ways in which an oxide scale is damaged [47]

Oxide	Oxide/Metal Volume Ratio
$\text{Al}_2\text{O}_3$	1.28
NiO	1.65
FeO (on $\alpha$ -Fe)	1.68
$\text{TiO}_2$	1.70 – 1.78
CoO	1.86
$\text{Cr}_2\text{O}_3$	2.07
$\text{Fe}_3\text{O}_4$ (on $\alpha$ -Fe)	2.10
$\text{Fe}_2\text{O}_3$ (on $\alpha$ -Fe)	2.14
$\text{Nb}_2\text{O}_5$	2.68

**Table 2.3.:** PB–ratio for common metals

#### 2.3.3.4. Rate Laws and Micro-mechanisms

There are three basic kinetic laws that have been used to explain rate of oxidation of pure metals which depend on quite simple oxidation models. It worth noting that in practice, oxidation problems and oxide layer properties are more sophisticated than these simple models.

##### Linear kinetics

Linear oxidation rate occurs in the case where the oxide scale is porous or there are cracks in the scale such that the corrosive gas easily and continuously penetrates the scale and reacts with the base metal in a disastrous way. Thus, no protection against corrosive gas is available and the corrosion rate is determined basically by the amount of corrosive gas available. In this instance the rate does change with time (it is more or less constant as time proceeds) [47]. The linear oxidation rate is given in Equation (2.16) as:

$$\frac{dx}{dt} = k_l \quad (2.16)$$

which upon integrating gives Equation (2.17):

$$x = k_l t \quad (2.17)$$

where  $x$  is the oxide scale thickness,  $t$  is the time of oxidation and  $k_l$  is the linear rate constant [48]. Figure 2.19 shows the linear relationship between oxide scale and time.

### Logarithmic kinetics

The logarithmic relationship is based on empirical relations with no underlying mechanisms. As mentioned in [Section 2.3.3.1](#), this behavior is seen to take place in the early stages of oxidation or at low temperatures where the oxide films are thin. This therefore restricts their use for high temperature corrosion problems [47, 52].

It takes the form [Equation \(2.18\)](#):

$$x = k_e \cdot \log(at + b) \quad (2.18)$$

where  $k_e$  is the rate constant and  $a$  and  $b$  are empirical constants for the test condition in question. [Figure 2.19](#) also shows the logarithmic behavior.

### Parabolic kinetics

If the oxide scale formed on the metal is a continuous and adherent scale which prevents the corrosive gas from reacting with the base metal, the protection of the metal increases as the scale grows. In this situation the amount of corrosive gas available is not what determines the oxidation or attack rate but the diffusion of ions is the rate controlling step of the oxidation process. The diffusion distance increases as the scales grows which therefore slows down the oxidation rate. The rate ( $dx/dt$ ) is thus inversely proportional to the scale thickness ( $x$ ) as shown in [Equation \(2.19\)](#) [47, 52]:

$$\frac{dx}{dt} = \frac{k_p}{x} \quad (2.19)$$

which after integrating gives [Equation \(2.20\)](#):

$$x^2 = 2k_p \cdot t \quad (2.20)$$

where  $k_p$  is the parabolic rate constant and  $x$  the oxide scale thickness and  $t$  oxidation time. The parabolic rate behavior is also shown in [Figure 2.19](#).

The parabolic oxidation rate constant  $k_p$  is the most useful parameter for determining oxidation resistance. A low  $k_p$  value indicates an overall low oxidation rate which implies the metal is consumed at a very slow rate which is common for protective oxidation. On the other hand, a high  $k_p$  value signifies that the metal is consumed at a higher rate and therefore there is no protection against oxidation [60].

### Micro-mechanisms

On a sub-molecular level, the diffusion of gases and metals across the oxide layer takes place by the movement of atoms. This movement is made easier by the presence of vacancies in the oxide ionic structures as shown in [Figure 2.20](#) for the case of NiO. From

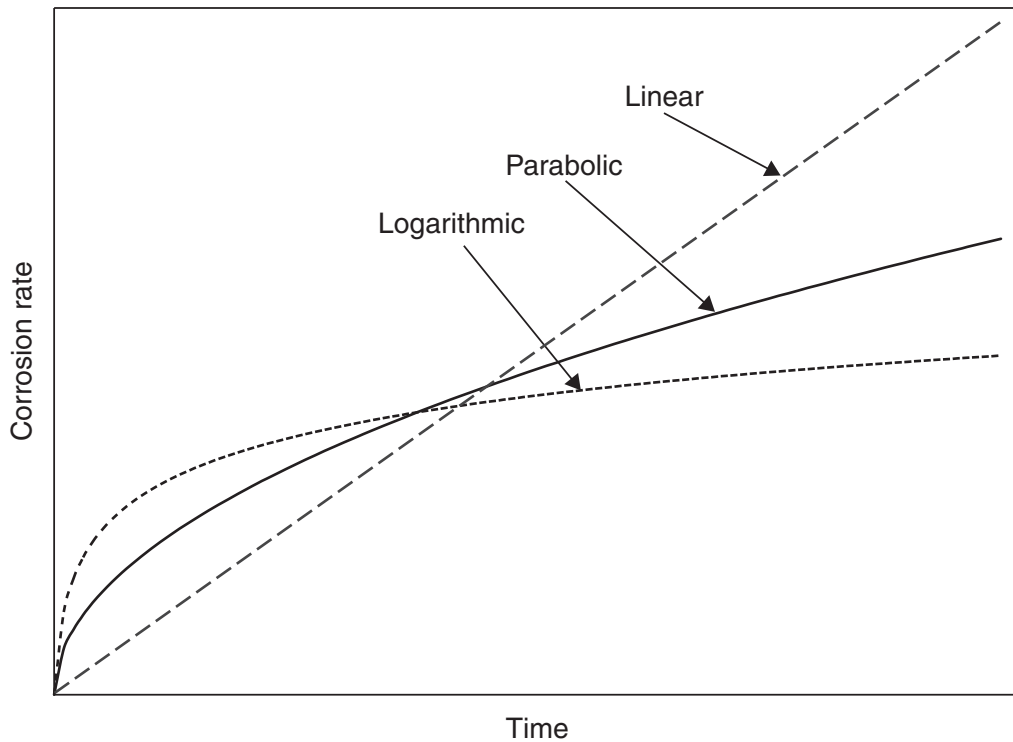


**Figure 2.19.:** Basic rate laws - linear, logarithmic and parabolic relationships [44]

Figure 2.20 it is seen that a few  $\text{Ni}^{+3}$  sites are present together with the  $\text{Ni}^{+2}$  and for every two  $\text{Ni}^{+3}$  there is a vacant  $\text{Ni}^{+2}$  site. The density of the vacancies increases when only a small quantity of a foreign metal is present e.g.  $\text{Cr}^{+3}$  (considered an impurity) and the rate of oxidation increases [45]. This kind of metal-deficit oxide is known as a *p-type* oxide<sup>7</sup> [42, 47] see Figure 2.21. Table 2.4 shows the effect of adding chromium on the oxidation of nickel.

**Table 2.4.:** Oxidation rate of nickel alloyed with chromium at 1000 °C and 1 atm [45]

Weight percent Cr	Parabolic rate constant $k_p$ [ $\text{g}^2\text{cm}^4\text{s}^{-1}$ ]
0	$3.1 \cdot 10^{-10}$
0.3	$14 \cdot 10^{-10}$
1.0	$26 \cdot 10^{-10}$
3.0	$31 \cdot 10^{-10}$
10.0	$1.5 \cdot 10^{-10}$

<sup>7</sup>For a p-type oxide with significant cation vacancies, the growth of the oxide lattice (layer) takes place at the gas/scale interface while metal consumption occurs at the scale/substrate interface [61].

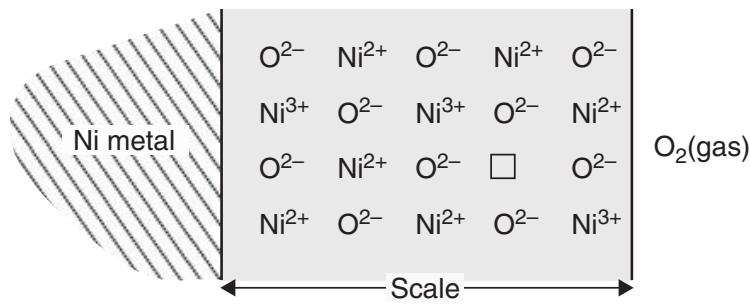


Figure 2.20.: Nickel oxide scale with a metal-deficit. [47]

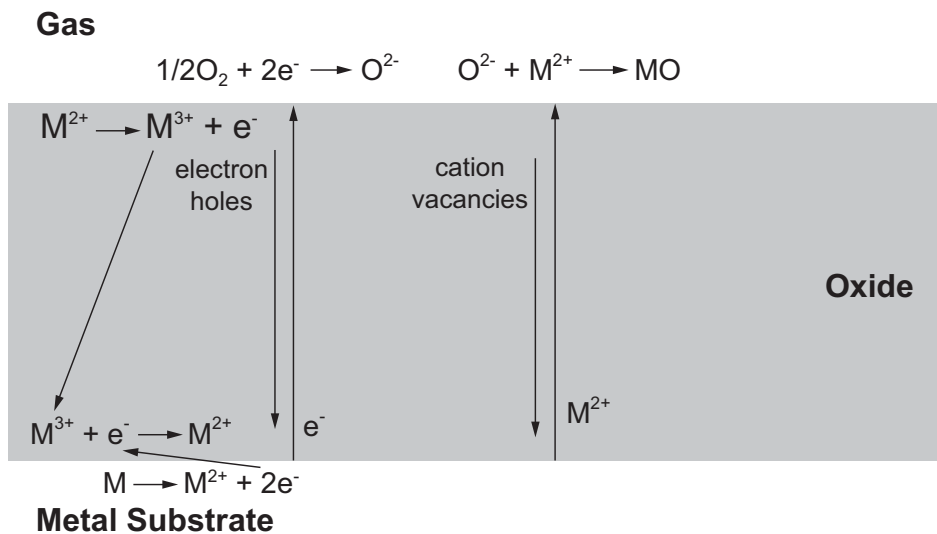


Figure 2.21.: Schematic diagram of a p-type oxide growth occurring at the oxide/gas interface showing cathodic reaction [42]

On the contrary, an oxide with a metal-excess is known as an *n-type*<sup>8</sup> oxide where extra metal ions occupy positions within the oxide scale. The growth of n-type oxides are illustrated in Figure 2.22 and Figure 2.23. Here also the presence of a metal will also affect the vacancies. For the case of zinc, a lower valence metal will lead to a metal excess which is a desired effect while the presence of a higher valence metal will cause a decrease in the number of zinc ions and consequently the oxidation rate of zinc [42,47]. An elaborate explanation of these defects can be found in Birks *et al.* [44].

In the case of metals that form more than one oxide, e.g. iron which can form FeO, Fe<sub>2</sub>O<sub>3</sub> and Fe<sub>3</sub>O<sub>4</sub> scales, all the three oxides will form simultaneously depending on available oxygen on the surface of the metal. The oxide which requires the most oxygen, in this

<sup>8</sup>For n-type oxides, the oxide layer growth and metal consumption occur simultaneously at the oxide/metal interface [61]. There are two forms of the *n-type* oxide: (1) an n-type cation interstitial metal-excess oxide which consists of interstitial cations plus other cations and (2) an n-type anion oxide which consist of oxygen anion vacancies [42].



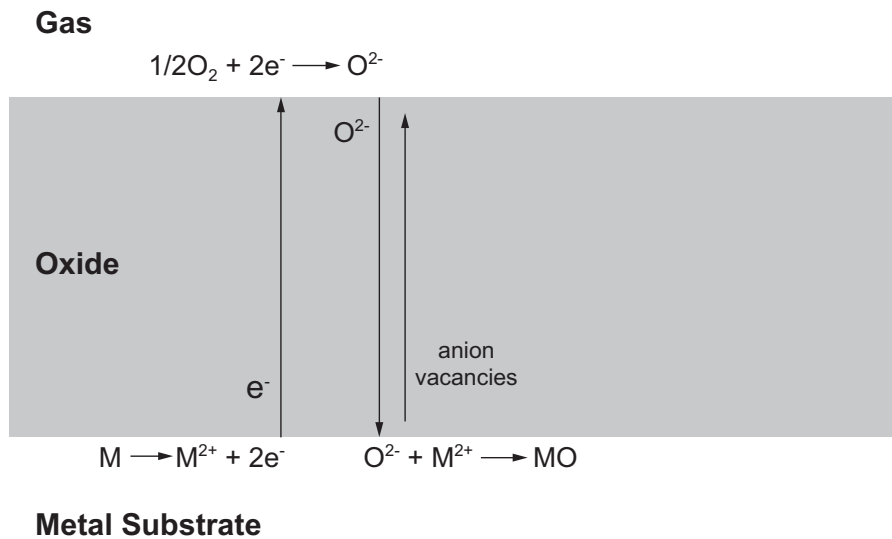


**Figure 2.22.:** Film growth of an n-type anion vacancy oxide on the metal/oxide interface [42]

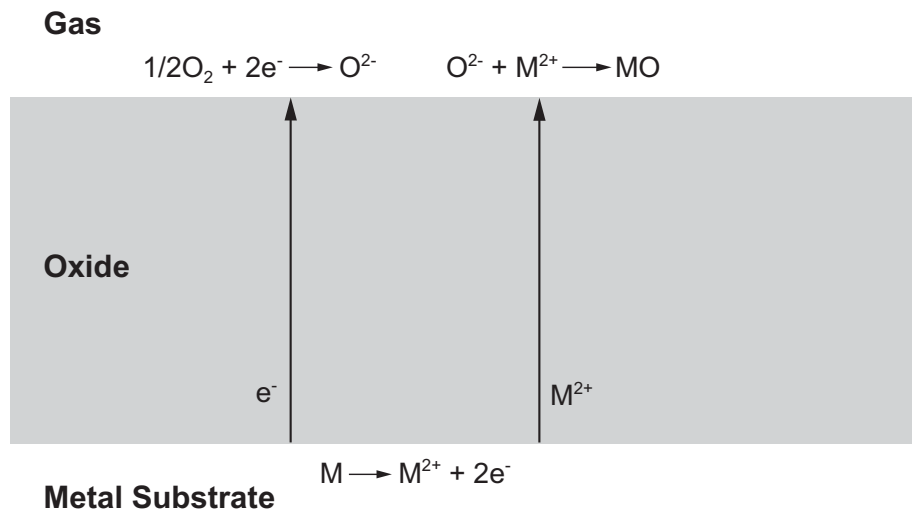


**Figure 2.23.:** Growth of a cation interstitial n-type oxide occurring at an oxide/gas interface [42]

case  $\text{Fe}_2\text{O}_3$  will be formed on the outer scale while  $\text{FeO}$  which requires the least amount of oxygen will form on the inside next to the metal substrate and  $\text{Fe}_3\text{O}_4$  will form in the middle with well-defined boundaries for each oxide. If the oxide layers are not damaged they will grow further at parabolic rate as discussed above [42, 47, 62]. Wustite ( $\text{FeO}$ ), which is stable at temperatures above  $570^\circ\text{C}$ , is a simple (cubic cation vacant) p-type oxide. Here,  $\text{Fe}^{2+}$  is the only mobile species but it can diffuse quite greatly. In the case of magnetite ( $\text{FeO}\cdot\text{Fe}_2\text{O}_3$ , commonly written as  $\text{Fe}_3\text{O}_4$  [48]) an inverse spinel, iron will act in both divalent and trivalent forms. Here,  $\text{Fe}^{2+}$ ,  $\text{Fe}^{3+}$  and  $\text{O}^{2-}$  are the mobile species. Lastly, hematite ( $\text{Fe}_2\text{O}_3$ ) which consists of both cation interstitials and anion vacancies is a rhombohedral n-type oxide. The amount of defects are much lesser than those in  $\text{FeO}$  and  $\text{Fe}_3\text{O}_4$ . The mobile species in this case are  $\text{Fe}^{+3}$  and  $\text{O}^{2-}$  [63]. Figure 2.24 shows

the iron-oxygen (Fe–O) phase diagram. Trindade et al., [64] obtained similar multi-layer

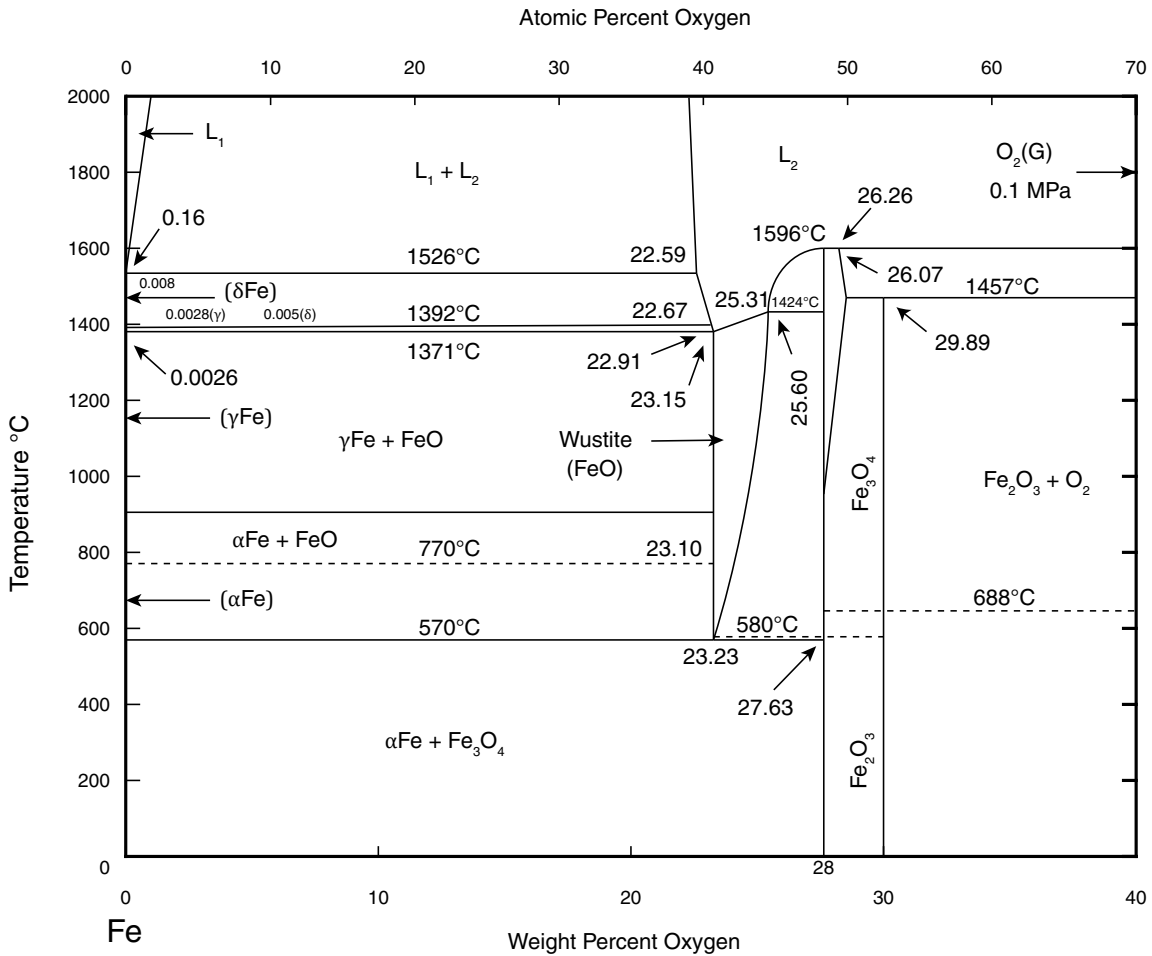


Figure 2.24.: Fe-O phase diagram, adapted from [44, 57]

oxide arrangements after exposing a low Cr-alloy (Alloy B) at high temperatures (550 °C) see Figure 2.25. Table 2.5 shows some common spinel phases found in alloy oxidation.

Table 2.5.: Spinel phases found in alloy oxidation [65]

<i>n</i> -type	MgFe <sub>2</sub> O <sub>4</sub>	ZnCo <sub>2</sub> O <sub>4</sub>
	NiFe <sub>2</sub> O <sub>4</sub>	MgAl <sub>2</sub> O <sub>4</sub>
	ZnFe <sub>2</sub> O <sub>4</sub>	ZnAl <sub>2</sub> O <sub>4</sub>
<i>p</i> -type	MgCr <sub>2</sub> O <sub>4</sub>	ZnCr <sub>2</sub> O <sub>4</sub>
	FeCr <sub>2</sub> O <sub>4</sub>	CoAl <sub>2</sub> O <sub>4</sub>
	CoCr <sub>2</sub> O <sub>4</sub>	NiAl <sub>2</sub> O <sub>4</sub>

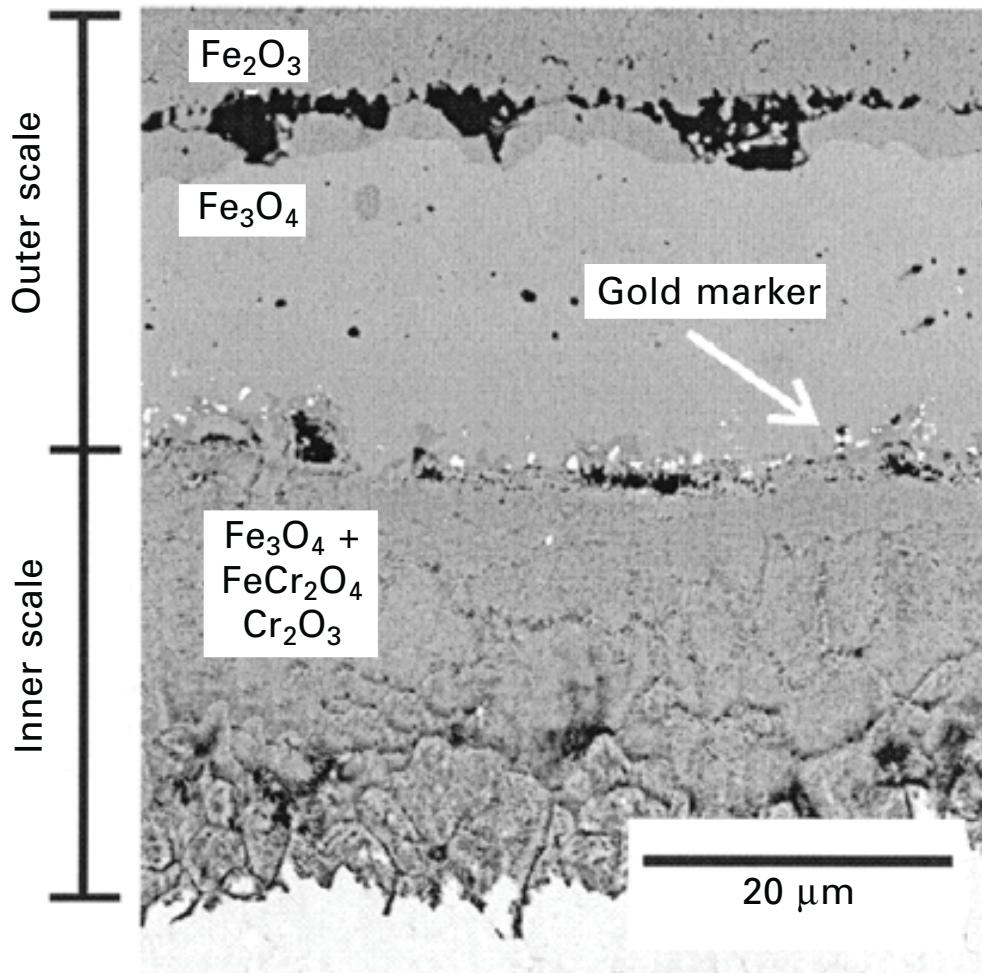


Figure 2.25.: Microstructure of alloy B after exposure in air at 550°C [64]

#### 2.3.4. Effect of mechanical stresses in oxide scales

Another important factor of interest that affects oxide scale growth are mechanical stresses during oxidation. Mechanical stresses are important because if they are high enough, they can deform or even break the scale and eventually damages the protectiveness of the scale. It is important to determine such effects in order to design more resistant scale-retaining alloys. Normally, a compressive stress in the scale is countered with a balanced tensile stress in the metal. i.e. in the absence of external stresses [46].

There are mainly three types of stress that have been examined [52] and these include: mechanical stresses that occur during oxide growth or oxidation or corrosion process ( $\sigma_{ox}$ ), external stresses from operation ( $\sigma_{ext}$ ) and stress induced by a temperature change ( $\sigma_{therm}$ ). The sum of the three stress describes the mechanical failure mechanism. For instance, if the sum is greater than or equal to a given critical value ( $\sigma_c$ ), then spalling or cracking of the protective scales can occur. There are several methods available to measure and calculate stresses in order to determine if failure will occur or not [46,52].

**Table 2.6.:** Thermal expansion coefficients ( $\alpha$ ) of metals and their oxides [46]

Material	$10^6 \alpha$ [ $K^{-1}$ ]	$T$ [ $^{\circ}C$ ]
Fe	15.3	0 – 900
FeO	15.0	400 – 800
FeO	12.2	100 – 1000
Fe <sub>2</sub> O <sub>3</sub>	14.9	20 – 900
Ni	17.6	0 – 1000
NiO	17.1	20 – 1000
Co	14.0	25 – 350
CoO	15.0	20 – 900
Cr	9.5	0 – 1000
Cr <sub>2</sub> O <sub>3</sub>	7.3	100 – 1000
Cr <sub>2</sub> O <sub>3</sub>	8.5	400 – 800
Alloy 800	16.2–19.2	20 – 1000

The stresses during oxide growth are as a result of volume change which depending on the shape, size or composition of the material could lead to deformations in the oxide. Thermally induced stresses, as the name implies depend on the extent of the temperature change as well as the thermal expansion coefficients of both the oxide and the metal. Generally, metals have a higher thermal expansion coefficient than their respective oxides, as can be seen from Table 2.6 for a selected list of materials and their coefficients of thermal expansion. Cooling an oxidized metal quickly will cause compression in the oxide scale such that if the stress is too high, the scale may undergo mechanical break down. Scale damage is less common in nickel and cobalt oxide scales but common in chromium oxide scales as seen in austenitic materials that form chroma scales [46].

### 2.3.5. High temperature corrosion mechanisms in coal boilers

High temperature corrosion problems in coal-fired power plants has always been of importance to plant operators and engineers ever since coal was used as a fuel for the generation of electricity. Such problems include, fireside (gas-side) corrosion of boiler water wall, superheaters and reheaters tubings from the combustion products, steam-side oxidation, *hot* corrosion, slagging and fouling among others.

In a nutshell, coal contains sufficiently high levels of sulphur and alkali metals (sodium and potassium) which are extremely damaging as they have been found to be the main sources of corrosive attack in boiler and superheater tubes. This is as a result of complex chemical reactions which involve sulfur and alkali metals (Na, K) to form alkali sulphates. The alkali sulphates, together with sulphur tri-oxide (SO<sub>3</sub>), react with the protective iron oxide scale breaking it down to form more complex alkali iron sulphates deposits. The deposits can flake off at temperatures between 425 – 480 °C, such as for water wall tubes, thereby

exposing the bare metal to more attack known as *fireside corrosion*. With increasing temperatures between 565 – 705 °C, as is the case for superheater and reheater tubes, these complex iron alkali sulphates can melt into a liquid form (*molten slag*) and directly attack the tubes leading to a phenomena known as *hot corrosion* [48]. There is also *steam-side oxidation* which occurs on the inner surfaces of superheaters and reheaters from superheated steam which behaves similarly to oxygen at high temperatures above 570 °C [48,53,66].

These problems constitute the main reason why steam temperatures were maintained at 540°C over the last few decades. It is apparent that increasing the steam temperature also increases efficiency however, this could have catastrophic effects on vital plant components through high temperature corrosion. Some of the main forms of high temperature corrosion peculiar to coal boilers are discussed below.

There are several forms of high temperature corrosion affecting coal-fired boilers which can be broadly grouped into three main types: oxidation, sulphidation and carburization. The names basically describe the most prevalent product of corrosions: oxidation for oxides, sulphidation for sulphides, carburization for carbides etc. [43]. There is also chlorine-induced and deposit induced forms of high temperature corrosion which will also be discussed in the next sections below. Nitridation which is also another form of high temperature corrosion is more common in ammonia production plants and shall not be treated here. Table 2.7 shows the main forms of high temperature corrosion in hot flue gases.

**Table 2.7.:** Forms of high temperature corrosion in hot flue gases [67]

Corrosion mechanism	Species responsible
Oxidation	O <sub>2</sub> , H <sub>2</sub> O, CO <sub>2</sub> /CO
Sulphidation	H <sub>2</sub> S
Oxidation/Sulphidation	SO <sub>2</sub>
Carburization	CO
Oxidation/carburization	CO <sub>2</sub>
Hydrogen corrosion	H <sub>2</sub>
Oxidation and hydrogen action	H <sub>2</sub> O
Nitridation	N <sub>2</sub> , NH <sub>3</sub>
Chlorine-induced	Cl <sub>2</sub>
Deposit-induced	alkali sulphates, oxides

### 2.3.5.1. Oxidation

As mentioned previously in Section 2.3.1 oxidation is the reaction of a metal with oxygen to form an oxide or a scale on the surface of the metal. It is the most important and

common form of high temperature corrosion as heat resistant materials depend on the formation of an oxide film to resist against attack from the corrosive gas. Viswanathan *et al.*, [66] suggest the oxidation of ferritic steels to take the form Equation (2.21):

$$x = kt^r \quad (2.21)$$

where,  $x$  is the oxide scale thickness,  $k$  is a proportionality coefficient that depends on the temperature, oxygen partial pressure, alloy composition, geometry (radius of curvature) and stress level,  $t$  is the oxidation time and  $r$  is the rate exponent. Figure 2.26 shows the oxidation of metals under high temperature conditions.

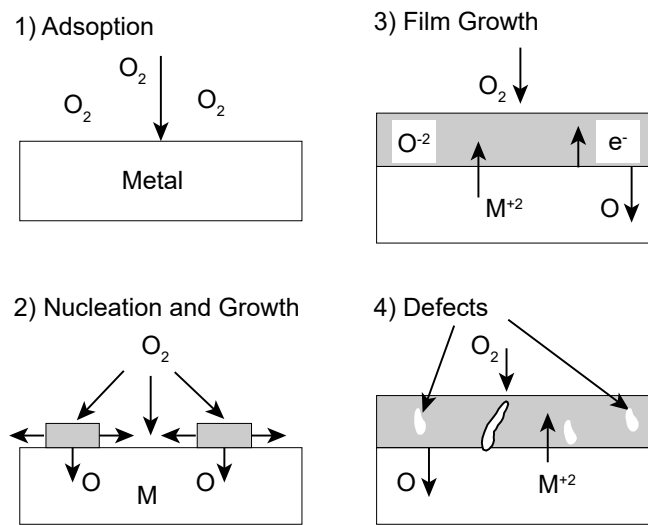


**Figure 2.26.:** Oxide growth model, adapted from [68]

The operating temperature of the boiler is critical in the oxidation rate of materials. Viswanathan *et al.* [66] found out that parabolic kinetics briefly prevails for a short period of about 6 months below temperatures of 700 °C, and that above this temperature (>700 °C) there is a change to linear kinetics which increases the oxidation rate. This implies an increase in temperature is associated with an increase in the oxidation rate. For example, chromia scales which are generally preferred and used to reduce oxidation attack, provide less protection at higher temperatures. For instance, low-chromium alloys (with about 2–3% Cr) used in boiler tubes are restricted to temperatures of about 565°C to 600°C due to increased oxidation from fireside corrosion attack. Figure 2.27 shows the effect of temperature on the penetration of common alloys.

As previously mentioned, chromium oxide ( $Cr_2O_3$  or chromia) is very important in reducing oxidation attack as it provides a protective oxide film. Generally, austenitic stainless steels with relatively high amounts of chromium are comparably robust at high temperatures than ferritic stainless steels. This effect is depicted in Figure 2.28. Also, according to Viswanathan *et al.*, [66] ferritic-martensitic alloys with about 9–12 Cr% such as HCM12,

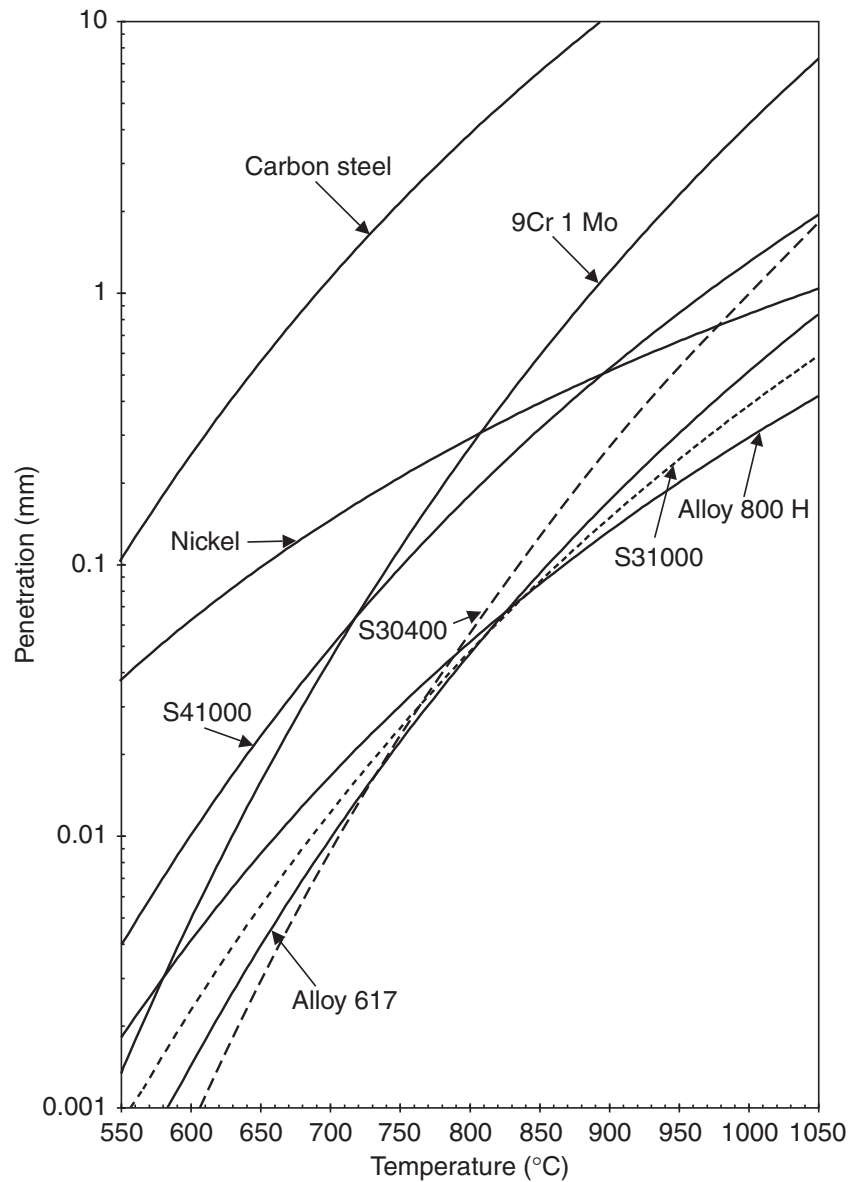


**Figure 2.27.:** Effect of temperature on penetration of common alloys [47]

TP91 and TP92 have shown to offer favorable resistance for temperatures up to 620°C while their advanced counterparts like VM12 and T122 can withstand temperatures above 620°C.

The grain size also plays an important role during oxidation. Trindade *et al.*, [64] also reported the formation of a slow growing chromia scale on the high-Cr alloy steel TP347 with smaller grain size which they attributed to the high density of grain boundaries causing chromium to diffuse outward at a faster rate along the grain boundaries. For similar alloy with larger grain boundaries they obtained a complex scale mixture consisting of the oxides of Fe, Cr, Ni and Mn.

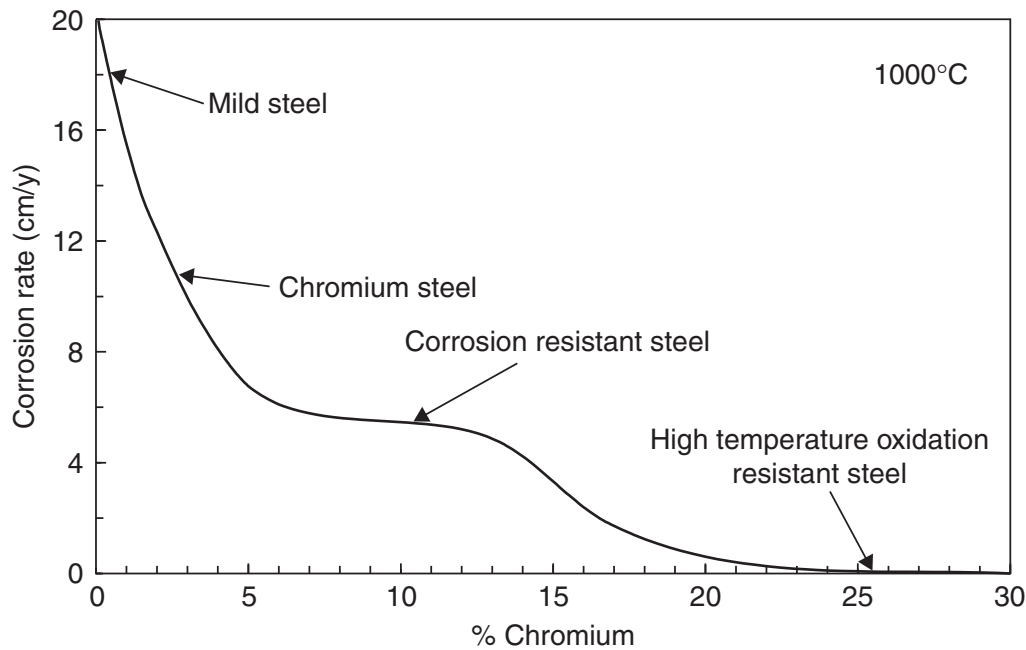


**Figure 2.28.:** Effect of chromium in providing corrosion resistance [47]

### Internal oxidation

*Internal oxidation* is defined as the process where oxygen diffuses into an alloy and reacts with one or more alloying elements causing a sub-surface precipitation of the oxide of the respective metals [44]. In other words, when oxygen dissolves and diffuses inward into an alloy when exposed to high temperature conditions, causing oxygen to react with the less noble metals (that are less resistant to oxidation) to form oxide scales within the alloy, internal oxidation can be said to have occurred. The reverse situation where oxygen and metal atoms diffuse in opposite directions to form an oxide layer on the surface of the material is known as *external oxidation* [44, 61]. A similar situation can also occur when the reacting gas is sulphur or carbon etc. It is important to note that, the resistance of alloys to high temperature corrosion depends on the formation of stable and slow growing external oxide scale such as chromia ( $\text{Cr}_2\text{O}_3$ ) and alumina ( $\text{Al}_2\text{O}_3$ ). Internal oxidation negatively alters (damages) the mechanical properties of the alloy, thus it is undesired although according to Gao and Li, [61] can be sometimes used under suitable conditions to produce oxide dispersion strength. Figure 2.29 shows the internal oxidation on a Ni-9Cr alloy after 40 h of exposure at 900 °C.

#### 2.3.5.2. Sulphidation

Sulphidation can simply be defined as contamination or corrosion caused by the presence of sulphur or its compounds [42]. This form of corrosion is catastrophic as it has been found to penetrate the base material, see Figure 2.30. Previously,  $\text{Cr}_2\text{O}_3$  scales were used to prevent this form of attack however, this led to an accelerated form of corrosion (*hot*



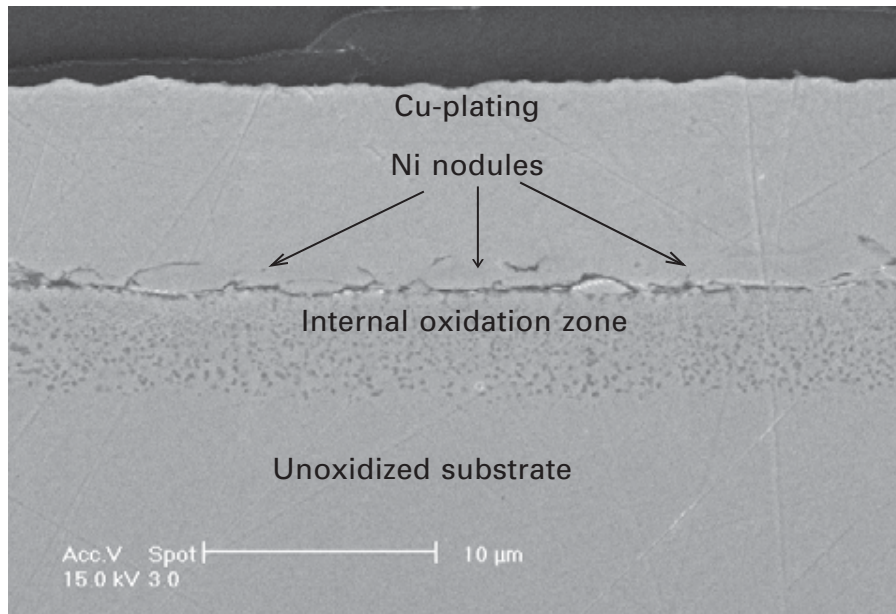


**Figure 2.29.:** Cross-section morphology of a Ni-6Cr alloy after 40h of oxidation at 900 °C and  $pO_2 = 10^{-9}$  Pa [61]

*corrosion*<sup>9)</sup> which has been linked to alkali sulphates deposits on the surface of the material [69].

Furthermore, the sulphidation of common metals is much faster than their oxidation [44, 70]. For instance, Cr which offers good oxidation resistance, sulphidizes about a million times faster than it oxidizes [71] and alloys that depend on the formation of a chromia scale for resistance against high temperature oxidation are susceptible to sulphides formation in mixed gases with substantially high sulphur partial pressures ( $pS_2$ ) and low oxygen partial pressures ( $pO_2$ ) [72].

### 2.3.5.3. Deposit-induced fireside corrosion

Generally, *fireside corrosion* in coal-fired boilers can loosely be divided into two types based on the location. These are; (1) waterwall corrosion which occurs in the lower part of the furnace and (2) fuel ash corrosion of superheaters/reheaters in the upper region of the furnace). There are different corrosion mechanisms involved which determines the nature of corrosion such as; the gas and metal temperature, the composition of the boiler tube materials and the local chemistry of the combustion and ash deposits [73].

<sup>9)</sup>There are two types of hot corrosion: Type I (or high temperature hot corrosion, 900 °C [46]) and Type II (or low temperature hot corrosion, 650 – 670 °C [46]). In Type 1 sulphur compounds are usually involved whereas in Type II sulphides are not often present in the metal closer to the corrosion products. Here, the partial pressure of  $SO_3$  determines whether sulphides will form. Also, some alloy rich in Ni can form sulphides [44].

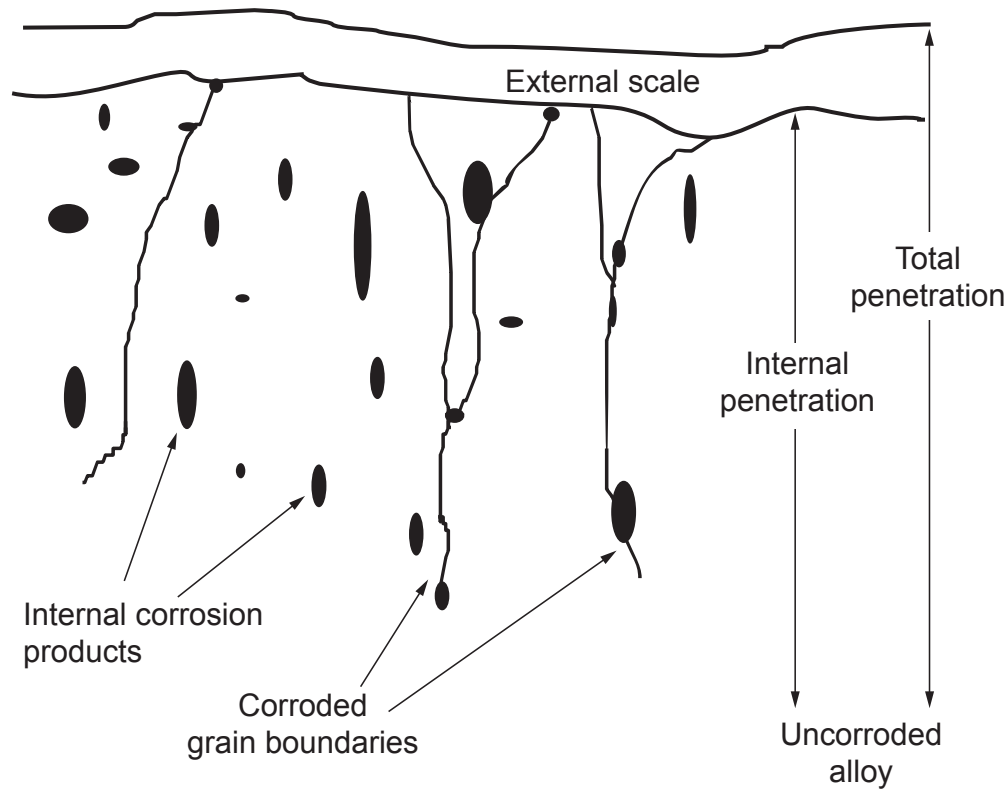
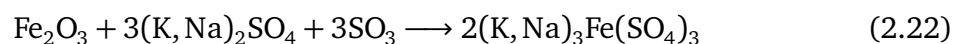


**Figure 2.30.:** Schematic diagram of sulphidation corrosion penetration [42]

Fireside corrosion is caused either by gas-phase oxidation or liquid-phase (coal-ash) corrosion also known as *hot corrosion*. Gas-phase oxidation can be minimized by using materials that are resistant to oxidation [42, 74, 75] however, liquid phase deposit-induced corrosion on the other hand poses serious problems due to its accelerated form of attack resulting from a molten slag layer (between 593 to 760 °C). The mechanisms involved in liquid-phase deposit-induced corrosion in the superheater/reheater region of coal-fired boilers can be summarized as follows [76]; alkali sulphates containing deposits build-up on the surface of superheater/reheater tubes which becomes sticky as a result of an increasing temperature gradient. This then facilitates any fly ash particles from the flue gas to be easily captured which eventually increases the amount of potassium and sodium sulphate that build up on the metal surface typically between temperatures of 593 to 760 °C. The alkali sulphate compounds are then thermally dissociated and SO<sub>2</sub> is catalyzed by Fe<sub>2</sub>O<sub>3</sub> in the flue gas to form SO<sub>3</sub>. It is the reaction of SO<sub>3</sub> together with Fe<sub>2</sub>O<sub>3</sub> and alkali sulphates in the deposits that leads to the formation of molten alkali-iron tri-sulphates at the metal interface as shown in Equation (2.22). Finally, the molten alkali sulphates moves through the protective oxide scales (Cr, Ni, Mo, Fe) onto the surface of the material where it directly reacts with the metal causing accelerated *oxidation* and *sulphidation*. Equation (2.22) shows the various regimes of fireside corrosion.



A quantitative method has also been derived to describe the effect of temperature on the corrosion rate [77, 78]. The thickness of the molten sulphate can be obtained as shown in Equation (2.23):

$$X_{\text{melt}} = \frac{k_{\text{SO}_4^{2-}} \left[ T_{\text{decomp}} - \left( \frac{\chi_{\text{oxide}} \left( \frac{q}{A} \right)}{k_{\text{oxide}}} \right) + T_{\text{metal}} \right]}{\left( \frac{q}{A} \right)} \quad (2.23)$$

where,  $X_{\text{melt}}$  is the thickness of the molten sulphate layer,  $\chi_{\text{oxide}}$  is the thickness of the oxide,  $T_{\text{decomp}}$  is the decomposition temperature of the sulphate layer,  $T_{\text{metal}}$  is the metal surface temperature,  $k_{\text{SO}_4^{2-}}$  is the thermal conductivity of the sulphate layer,  $k_{\text{oxide}}$  is the thermal conductivity of the oxide layer and  $(q/A)$  is the heat flux through the scale.

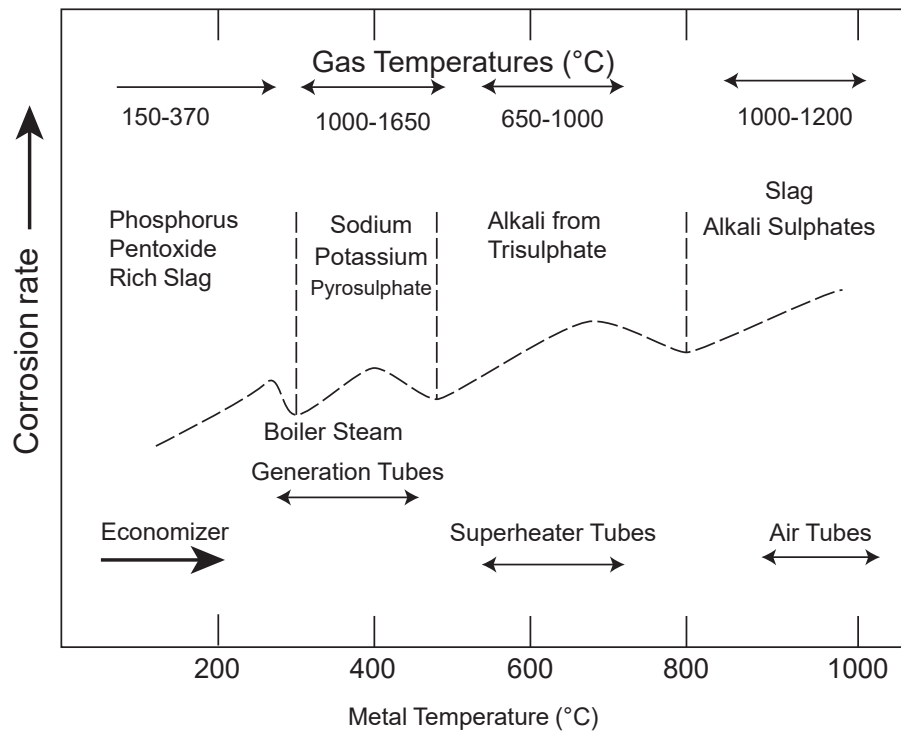


Figure 2.31.: Regimes of fireside corrosion; adapted from [74]

#### 2.3.5.4. Carburization

Carburization is the absorption of carbon atoms into a metal surface at high temperatures to form chromium carbides products, which decrease the protectiveness of the oxide scales previously formed [79]. In coal-based boilers superheaters and reheaters, this form of attack is commonly found in boiler materials that are exposed to coal, CO, CH<sub>4</sub>, soot, or other hydrocarbons at high temperatures greater than 800 °C. This form of attack takes place when carbon fluxes through the oxide scale layer to the oxide/metal interface as

CO or other carbon-containing species [42, 80]. Furnaces rich in carbonate deposits have been found to experience high rates of carburization. In one study by Nava [81], the author reported that the presence of carbon together with sodium sulphate ( $\text{NaSO}_4$ ) could cause  $\text{NaSO}_4$  to become unstable, thereby producing  $\text{Na}_2\text{S}$  and  $\text{CO}_2$ . The  $\text{CO}_2$  reacts with the leftover C to form CO which is seen as the major cause of carburization. Furthermore, Lopez-Lopez *et al.* [82] indicated that carburization has been found on the surfaces of tubings facing the flue gas flow (i.e. the path of combustion gas).

#### 2.3.5.5. Chlorine corrosion

The major reason advocated for the reduced corrosion resistance from halogens (such as chlorine and fluorine) is that they form volatile corrosion products which are non-protective [42, 47]. According to Khanna, [53], 75% of chlorine is found in the residuals after flue gas cleaning (to remove dust particles etc.) while some 25% is also found in the filter dust. It is difficult to determine the role of chlorine on fireside corrosion in oxidizing conditions, but in reducing atmospheres HCl and NaCl render the protective oxides ineffective by either inducing a crack on the oxides or by reacting with the metal oxides or base metal to form volatiles species [53].

Kung [83] have shown that found that chlorine may have some benefits in sub stoichiometric sulphidizing environments. The author reported that at 371 °C chlorine found in reducing/sulphidizing gas mixtures had little or no effect on the corrosion behaviour of the several commercial alloys that were investigated. An even more beneficial effect was found at 482°C where the presence of HCl prevented sulphidation attack from  $\text{H}_2\text{S}$  again under certain sub-stoichiometric combustion conditions.

#### 2.3.5.6. Slagging and fouling

Slagging and fouling are basically processes that lead to deposition of ash particles on the heat transfer surfaces of coal-fired boilers. *Slagging* is defined as the deposition of ash deposits on regions of the furnace that are directly in contact with the radiant heat from coal combustion, particularly in the lower region of the furnace. On the other hand *fouling* is the collection of ash deposits on heat transfer surfaces which are not in contact with the combustion flame, i.e. the upper region of the furnace where heat transfer is by convection (the closely spaced tubing's in pulverized fuel (PF) boiler). Slagging and fouling in coal boilers is common in water walls tubes, pendant super-heaters as well as burner quarls<sup>10</sup>. Most often, the ash deposit is in a molten state and either flows from the initial point of deposition or is highly fused [84]. Figure 2.32 shows some typical locations slagging and fouling in a coal boilers.

<sup>10</sup>Burner quarls, tiles or tunnels are holes on furnace walls used for air and fuel injection

The impact of slagging and fouling for a plant can be detrimental causing loss in efficiency, unplanned outages, huge financial penalties as well as posing a problem for safety. Another issue with slagging and fouling which makes the problem complicated is that coals that have been identified as high and low risk fuels have all had severe slagging and fouling impacts. Fuel mixtures (coal blends) could therefore make the problem worse. Changes in the boiler operation parameters due to load variations or component failure from the malfunction of equipment could also lead to slagging and fouling [84].

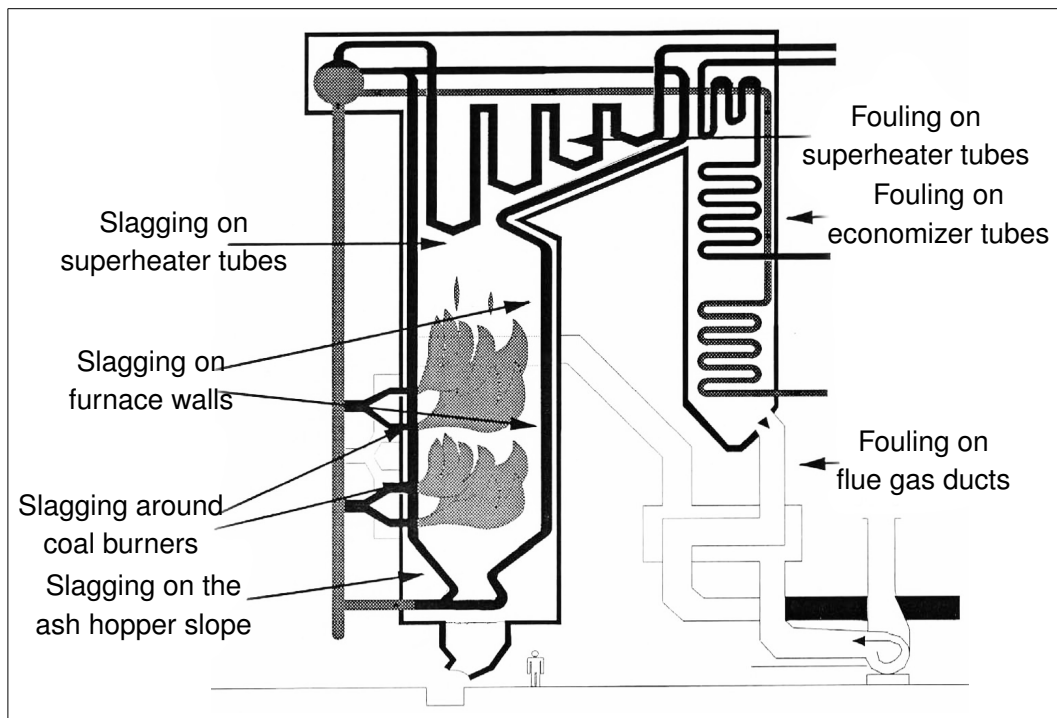


**Figure 2.32.:** Typical locations of fouling and slagging in coal-fired boilers [84]

## 2.4. High Temperature Cyclic Oxidation

### 2.4.1. Background and methods

High temperature alloys are usually prone to duty cycles that differ widely from one application to another. This could be for instance, very brief periods of operation such as those of propulsion engines or weeks, months or even years of operation such as in power generation systems and chemical industries. Whatever the case may be, the operation mode includes start ups and shutdowns with complex interactions from temperature changes that causes stress in otherwise protective oxide layers. In the absence of any stress relief, the thermally induced stresses could lead to an increase in scale thickness [46, 85]. In the case where the oxide film is too thin to withstand the temperature change and there is a

thermal mismatch between the metal and the oxide, a sufficient increase in the size of the oxide could lead to spalling of the oxide [46].

These factors are what determines if a component will fail prematurely or show long-term resistance. This also sets an upper service temperature limit for materials which can of course have a direct influence on the efficiency as well as economical and ecological implications [85].

Thermal cycling oxidation tests are usually weight-change versus time measurements which are followed by microscopic examination of the exposed material samples. They are regularly applied to estimate damage to materials which can result from oxidation. Usually, these test simulate industrial situations for a given period of time, often for quite shorter periods than in real operating situations to draw useful conclusions on the oxidation the materials in that particular industrial environment. There are several standards used for cyclic oxidation tests. The ISO technical committee 156 (cited in [86]) have defined several test methods which are widely used for high temperature cyclic oxidation testing. These methods include:

1. *Thermogravimetric testing* which is in-situ weight change measurements at high temperatures on a single test sample without intermediate cooling in between of the sample.
2. *Continuous isothermal exposure testing* (ISO/TC 156CD21608) which is a single *post-exposure* weight change measurements on a number of test samples without intermediate cooling (Figure 2.33a).
3. *Discontinuous isothermal exposure testing* (ISO/TC 1561122) which is a series of weight change measurements on a single test sample with intermediate cooling at predefined time intervals which must not necessarily be regular (Figure 2.33b).
4. *Cyclic oxidation testing* (ISO/TC 15 NWIP) which is a number of weight change measurements on a single test sample with frequent, regularly controlled temperature cycles (Figure 2.33c).

### 2.4.2. Important Experimental Parameters for Cyclic Oxidation

There are several experimental variables which might be of no significance in isothermal oxidation experiments but can be very crucial for cyclic oxidation tests. These include; the extent of the temperature change (i.e. how large is the temperature change,  $\Delta T$ ), the number of cycles (frequency), the heating and the cooling rate as well as the exposure time or duration [46].

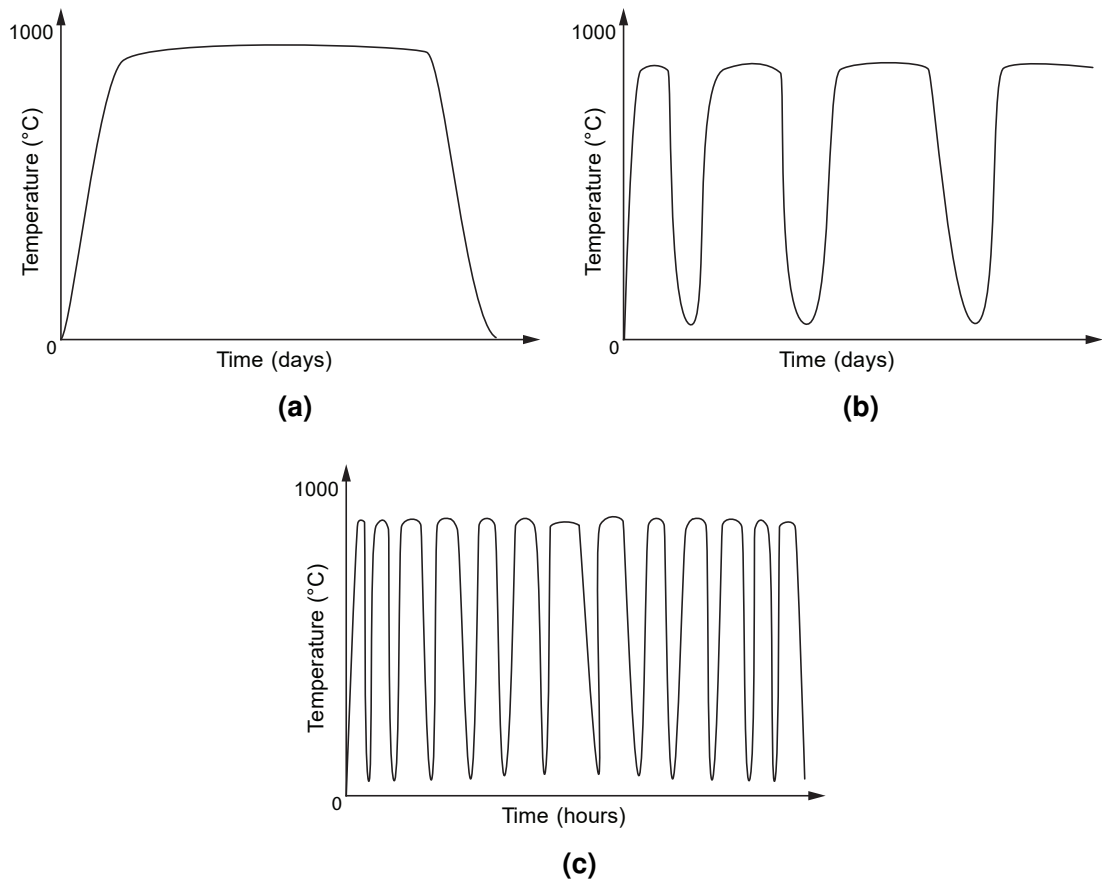


**Figure 2.33.:** Temperature profiles for isothermal and cyclic testing (a) continuous isothermal testing (b) discontinuous isothermal testing (c) thermal oxidation cycling testing [86]

### Temperature and cycling duration (frequency)

Cyclic oxidation experiments usually involves heating the test specimen to a desired temperature and cooling it down at room temperature which can provide enough thermal stress to break off any oxides at high temperatures. However, if the oxidation rates at lower temperatures are slow this implies the scale formed is capable of resisting thermal cycling for much longer periods. The effect is shown in Figure 2.34 for a 20Cr–25Ni–Nb stainless steel alloy.

The thermally induced stress can only be detrimental to the oxide lattice if there are no stress relief mechanisms<sup>11</sup> present which could lead to damage of the oxide scale. This is typically the case when the cooling rate is very rapid but if slow could lead to creep in the metal which can reduce the stress in the oxide scale [46].

<sup>11</sup>Examples of stress relief mechanisms include: porosity in the oxide as it grows, cracking of oxide, double layer formation and decohesion, reducing oxidation rates and selective oxidation [52]. The presence of vacancies within the oxide lattice (porosity) can however also lead to stresses in the metal substrate and thus causes creep [44, 87].

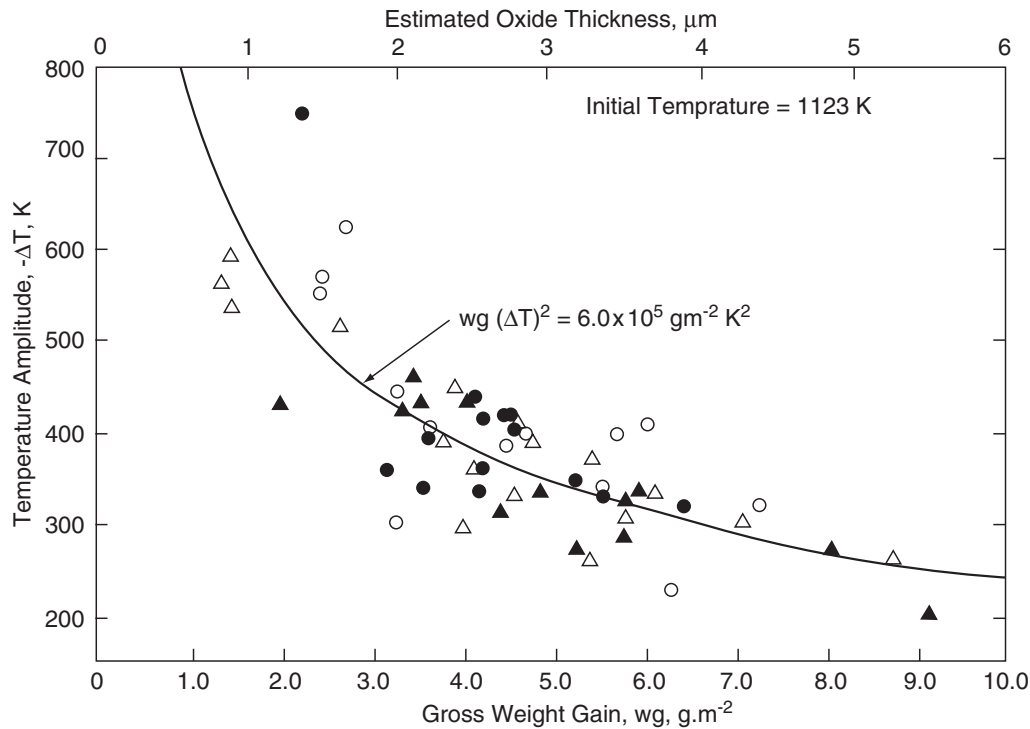


**Figure 2.34.:** Temperature drop needed to spall 20Cr–25Ni–Nb steel [46]

The frequency of cycling also plays an important role during high temperature cyclic oxidation and its effect has also been studied extensively. The results in the literature show that short and more frequent cycles increase spallation of the metal oxides and Smialek (cited in [46]) have reported that longer cycles lead to a more faster weight loss. Figure 2.35 shows the weight change vs number of cycles.

### Corrosive environment

The presence of water vapor and carbon dioxide which is found in the flue gas of fossil fuel combustion plants have been found to increase the reaction rates of steels and other metals substantially. Water vapor in particular which is found in almost all high temperature engineering applications has been found to have detrimental effects on oxidation. One of the most damaging effects of water vapor is that it increases the rate of spalling of chromia ( $Cr_2O_3$ ) and alumina ( $Al_2O_3$ ) scales [44]. This has been found in the alumina-forming superalloy CMSX-4. Water vapor reduces the fracture toughness of the alloy–oxide scale boundary. In sulphidizing environments, sulphide scales which are formed tend to have poor adherence due to the fact that most of such scales grow by outward cation diffusion which can bring about the formation of voids around the scale/metal boundary [44].



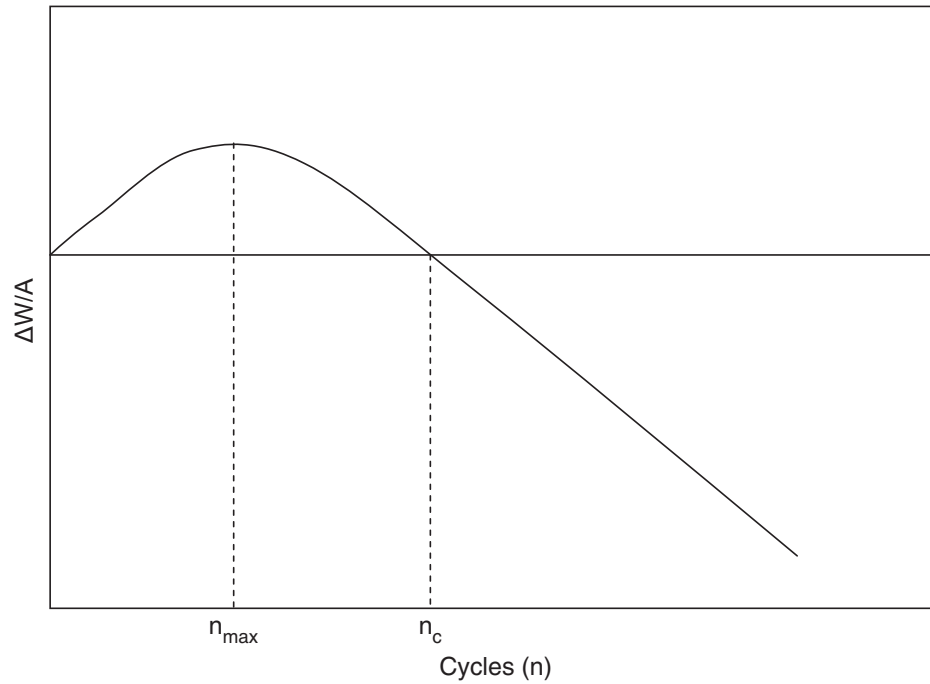


Figure 2.35.: Net specimen weight changes predicted for cyclic oxidation

### 2.4.3. Cyclic oxidation kinetics

According to Smialek [88], in most cases of high temperature cyclic oxidation, parabolic rate kinetics prevails and deviations from parabolic growth law are usually very small or require that the oxidation duration be extended in order to become noticeable.

### 2.4.4. Damage mechanisms associated with cycling operation

As coal-fired energy generation plants continue to operate in cyclic modes, the level of component damage might increase and reduced overall performance [10,89]. It has been seen that about 60 – 80% of all plant failures are as a result of cycling [10]. Figure 2.36 shows the common equipment problems that are related to cycling.

Critical plant components that might be affected or damaged from increased cycling include superheater and reheater tubes, water wall tubes, plant start-up components, economizer inlet, minor system related components such as valves, generator windings etc.

As already mentioned Section 2.4.2, the magnitude of the temperature gradient and ramp rates are useful indicators of creep and fatigue damage that might result from cycling. The above mentioned variables are what determine how serious cycling a unit can be. This data can also be used to troubleshoot a unit cycling operation conditions such as setting a temperature ramp rate limit e.g. for superheater, economizers during start-up and shut down or cooling in order to minimize damage and increase the life of the components,

reduce maintenance costs as well as improve reliability of the plant [34, 90]. Some of the main damage mechanisms that might occur from cycling are discussed below.

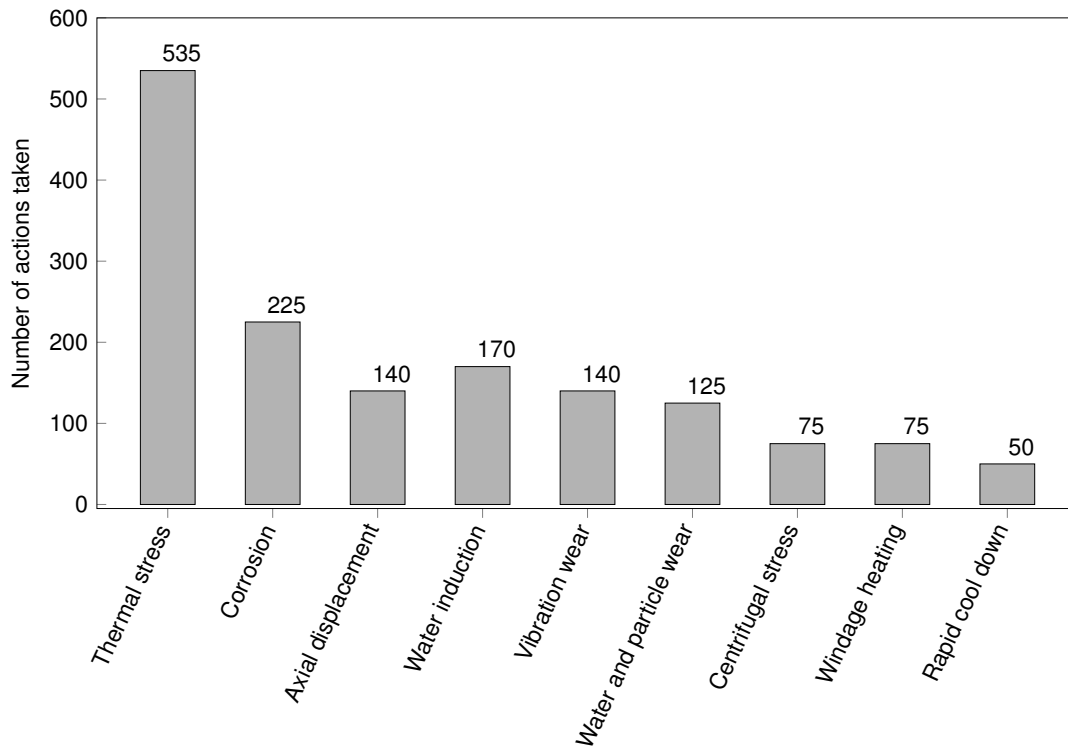


**Figure 2.36.:** Common equipment problems due to cycling [10]

#### 2.4.4.1. Creep-fatigue damage

*Creep* can be defined as the change in the shape or size of a material resulting from stresses on the material over time. Baseload units that are usually operated over a long period of time are commonly faced with such problems.

*Fatigue* is defined as the damage to a material which occurs when a material is exposed to cyclical or fluctuating (repeated and varying levels) of stress which can lead to fractures and failures. Therefore, fatigue is more likely to occur during cycling operations where there are large thermal and pressure gradients [26]. Frequent starts and stops of the boiler cause thermal stresses which lead to fatigue, cracks in the base materials or welds [91].

Creep and fatigue go hand in hand. According to Denny and O'Malley [26], a plant component that has already reached half of its creep damage life can fail with only about 10% of fatigue. Therefore, older baseload units which have been operated for a number years are very vulnerable to component failure.

Creep-fatigue interaction is of great importance to component failure. Creep and fatigue can act together to cause premature failure. Figure 2.37a shows the creep-fatigue interaction for a 2.25Cr-1Mo alloy. The solid line (or limit line) indicates the design limit which

is expressed as a fraction of the creep and fatigue life of the material [92]. This line is used to determine the effect of combining fatigue and creep and different materials have different creep-fatigue curves.

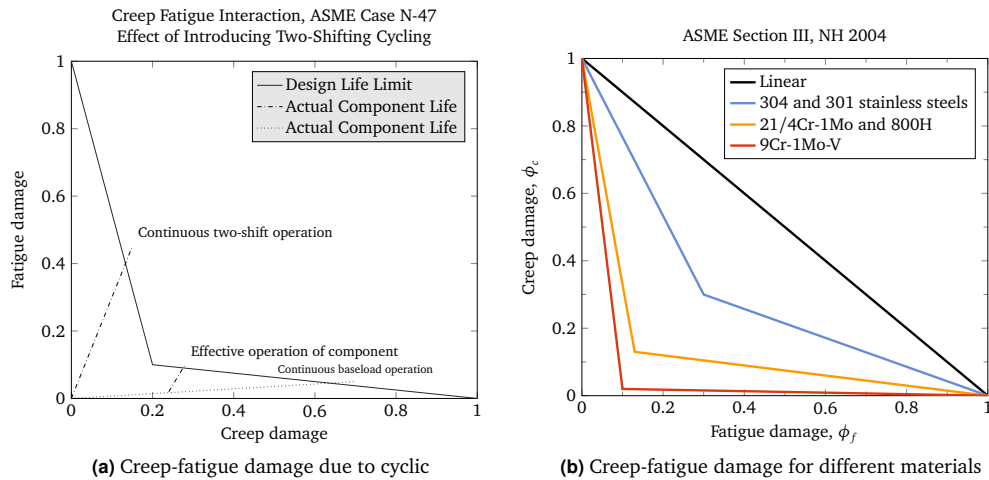


**Figure 2.37.:** Creep-fatigue curve – effect of introducing two-shifting cycling [92]

The dotted line's length determines the relative life of components subjected to fatigue and creep i.e. components exposed to only one type of damage mechanism tend to have a longer life whereas those exposed to both types of stress damage are prone to fail faster [92]. Baseload power plant components often are exposed to more creep than fatigue and this can be seen on the graph. But when a plant component is introduced to fatigue for part of its life as a result of cycling, the component is expected to fail sooner. Plant components for creep-fatigue interaction that are of importance include: superheater and reheater, feedwater heaters and economizers among others [92]. Figure 2.37b shows the creep-fatigue damage for different materials.

#### 2.4.4.2. Stress corrosion cracking

Stress Corrosion Cracking (SCC) is generally found to occur in waterwall tubes particularly at attachments such as corner tubes, wall box openings etc. SCC in the waterwall tubes at the buckstay attachments used to resist the internal pressure of the furnace occurs by non-uniform thermal stresses cycles which by definition go from a minimum to maximum to complete one cycle for a given time period [10]. Figure 2.38 shows the typical stress life cycle of stress vs time.

Changes in plant load during load following operations involve rapid changes in temperatures (increase and decrease) leading to large thermal stresses. This could have numerous undesired effects such as coal mills or pulverizers going off, or the velocities of steam and flue gas changing, furnace temperature and heat profiles are being altered to name a few. This causes a plant to operate out of its design limits [10].

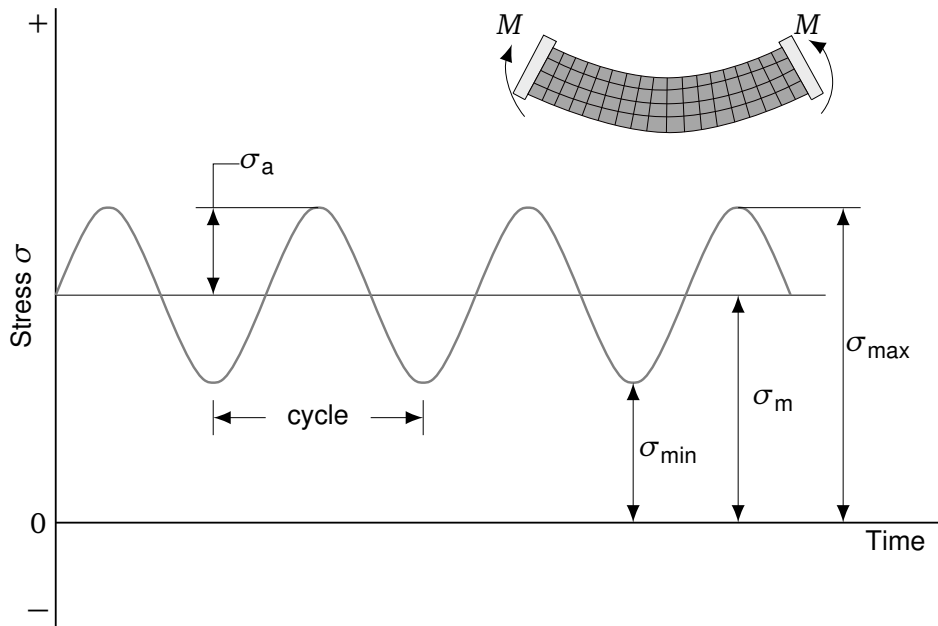


**Figure 2.38.:** A generic stress life cycle of stress versus time, where  $M$  = bending moment,  $\sigma_a$  = stress amplitude,  $\sigma_{max}$  = maximum tensile stress,  $\sigma_{min}$  = minimum tensile stress,  $\sigma_m$  = mean stress i.e.  $(\sigma_{max} + \sigma_{min})/2$ .

#### 2.4.4.3. Furnace Wall Corrosion

Furnace wall corrosion problems result from the combined effect of oxidation and sulphidation. Sulphidation as already discussed in [Section 2.3.5.2](#) increases the rate of attack where sulphide scales can form underneath the protective oxide scales and sulphidation being faster than oxidation could lead to severe material damage.

Another problem of concern is that of thermal creep and fatigue in furnace wall (water wall) tubes which lead to “elephant skin” cracking of the water wall tubes. This type of cracking is generally difficult to identify due to layers of ash deposits or slag covering the parts affected [92]. [Figure 2.39](#) shows furnace wall corrosion problems related to cycling.

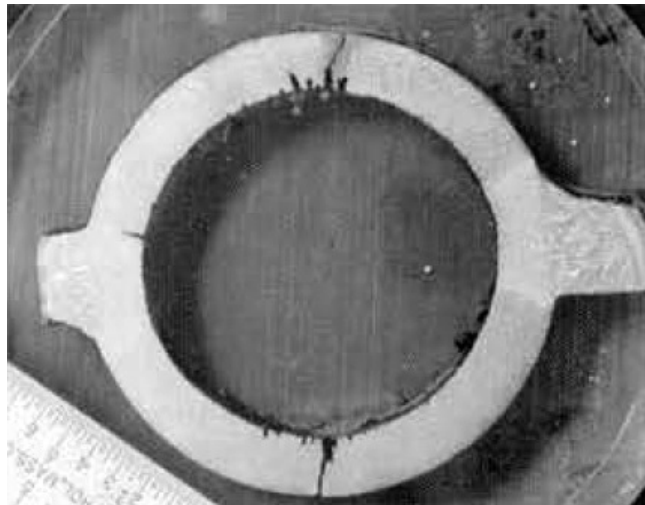
#### 2.4.4.4. Fireside corrosion

As previously described in [Section 2.3.5.3](#) fire-side corrosion is the damage mechanism which result from the chemical reaction of the boiler materials with the coal ash deposits (forming molten alkali-iron tri-sulphate) at high temperatures. Elements such as sulphur and chloride found in coal which are released during combustion can react with the otherwise protective oxide scales and greatly reduce the oxidation resistance of the metals which therefore increase oxidation attack of the materials [93]. Again as mentioned earlier, the metal surface temperature which increase with steam temperatures and the flue gas (combustion) temperatures also affect the corrosion. Components affected here are

superheater/reheater and also water wall (furnace) tubes [94]. Serious fireside corrosion has been reported by plants where steam temperatures are above 565 °C [92]. Below about 550 °C, the alkali iron trisulphates are solid, but dissociate above 780 °C.



(a) Leakage tubes caused by thermal transients, [7]



(b) Corrosion fatigue on waterwall tube, [95]

**Figure 2.39.:** Membrane waterwall tube damage due to cycling



# 3. Thermodynamic Modeling of Flue Gas Corrosion

## 3.1. Description of modeling package – FactSage™

Thermodynamic modeling of high temperature corrosion or oxidation processes is a useful way of analyzing the corrosion behavior of high temperature materials in flue gas atmospheres [50, 59, 67, 96]. As already discussed in Section 2.3.5, the corrosion behavior of the high temperature materials is affected by the constituents of the flue gas (oxygen, sulphur etc.) whose reaction with the metal or material (ferritic-martensitic, austenitic etc.) can conveniently be studied using a complex thermodynamic modeling approach or thermochemical calculations, to be able to describe the corrosion and oxidation behavior of the materials [59, 67, 96].

These calculations are based on the Gibbs energy minimization principle from which under normal standard conditions could be used to derive the oxygen partial pressure at which both the metal and its oxide will co-exist (see Section 2.3.2). Therefore, for a given state, the stability regions of the metal oxide can be determined depending on the oxygen partial pressure [67, 97]. For a pure substance e.g. a gas species or an element or even a stoichiometric compound like  $\text{Al}_2\text{O}_3$ , the Gibbs energy depends mainly on the temperature i.e. if the pressure is neglected such that  $G = G(T)$ . For a non-ideal system such as solid metal matrix phases like the BCC, FCC, intermetallic phases like SIGMA or LAVES phase, solid salts ( $\text{K}_2(\text{SO}_4, \text{CrO}_4)$ ), solid oxide solution phases such as *wustite* – FeO or corundum –  $(\text{Al, Cr, Fe})_2\text{O}_3$ , the Gibbs energy depends on both the temperature and the composition (again neglecting the effect of pressure) i.e.  $G = G(T, x_i)$ . Mathematical methods or calculations could be used to obtain activities, phase amounts, equilibrium constants etc. from the Gibbs energy of the various phases [59]. The dependence of Gibbs energy on temperature is as follows Equation (3.1) [50, 97]:

$$G = a + bT + cT \ln T + \sum d_n T^n \quad (3.1)$$

The coefficients,  $a$ ,  $b$ ,  $c$ , and  $d$  are obtained from the heat capacities, enthalpies and entropies at a reference state (298 K and 1 bar) and are directly used in determining the Gibbs energy. This information is then used to obtain stability phase area diagrams [50]. In this

respect, the thermochemical modeling software package FactSage™, version 6.4 was used to carry out complex equilibria calculations to study the oxidation and corrosion behavior of the commercial alloys experimentally investigated in this study. A brief description of the software package follows in the next section [Section 3.1](#).

FactSage™™ is a Windows-based thermodynamic modeling software package and an Integrated Thermodynamic Database System (ITDS) consisting of a *compound or pure substances database* (elements, gas species, condensed phases, intermetallic compounds etc.) and a *solution database* (oxides, salts, metallic alloys etc.). It implements the Gibbs energy minimization method and has various modules for point calculations, complex equilibria (i.e. multi-phase, multi-component systems), phase diagrams, predominance area diagrams and many others [59, 98, 99]. The database stores thermochemical data for each compound at a given state and temperature range such as; standard enthalpy of formation ( $\Delta H^\circ$ ), absolute or standard entropy of change ( $S^\circ$ ), and temperature dependent heat capacities ( $c_p(T)$ ) [59, 98–100].

The results obtained show the equilibrium state of a phase (i.e. the equilibrium amounts or activities) or in case of a solution phase the equilibrium amounts of the internal phase constituents are also given. The activities indicate how far away a phase is from equilibrium. The smaller the activity the less likely that such a phase will form as already stated in [Section 2.3.2.1](#).

It is worth noting some important limitations of the software package: limited number of phase selection per calculation run. With the numerous amounts of phases that might form in a high temperature reaction system such as those in a coal combustion flue gas environment, only a limited number of solutions, with limited  $c_p$  ranges can be selected per calculation run. Selecting therefore the possible number of phases which might form can be difficult. Secondly, as already mentioned in [Section 2.3.2.4](#), the use of thermodynamic databases to obtain phase stability diagrams provides no information on the kinetics or oxidation rate and therefore the kinetics cannot be studied.

## 3.2. Gas phase equilibria

The thermochemical behavior of the flue gas – the composition, the partial pressure of individual gas components during high temperature corrosion is important as this determine what phases will be formed in equilibrium. The simulation of the modeled flue gas mixture ([Table 3.1](#)) used in this study is vital to establish the composition of the individual gas species at equilibrium as a function of temperature i.e. how the flue gas changes with respect to temperature. The calculations for the gas phase calculations were carried out in the Equilib module using the FactPS database for pure substances. The calculation results



of the model flue gas mixture are shown in Figure 3.1 as the fugacity (effective partial pressure) change with respect to temperature.

**Table 3.1.:** Model flue gas mixture composition

Gas species	CO <sub>2</sub>	O <sub>2</sub>	N <sub>2</sub>	SO <sub>2</sub>	H <sub>2</sub> O
[vol%]	14.29	3.34	65.72	0.05	16.60

It can be seen from Figure 3.1 that, for the given flue gas model in Table 3.1, the fugacities of N<sub>2</sub>, H<sub>2</sub>O, O<sub>2</sub> and CO<sub>2</sub> are relatively higher compared to the other gas species and their fugacities do not change with temperature (they are more or less constant). CO and H<sub>2</sub> have quite low fugacities but their fugacities increase greatly with temperature. Not shown on the diagram is S<sub>2</sub> with even much lower partial pressures in the range;  $-69.91 < \log p(S_2) < -29.76$  for temperatures between 300 – 1000 °C,  $pS_2$  also increases with temperature. The corrosive species SO<sub>2</sub> and SO<sub>3</sub> have moderately high fugacities. The partial pressures of SO<sub>2</sub> increases with temperature while that of SO<sub>3</sub> decreases with temperature.

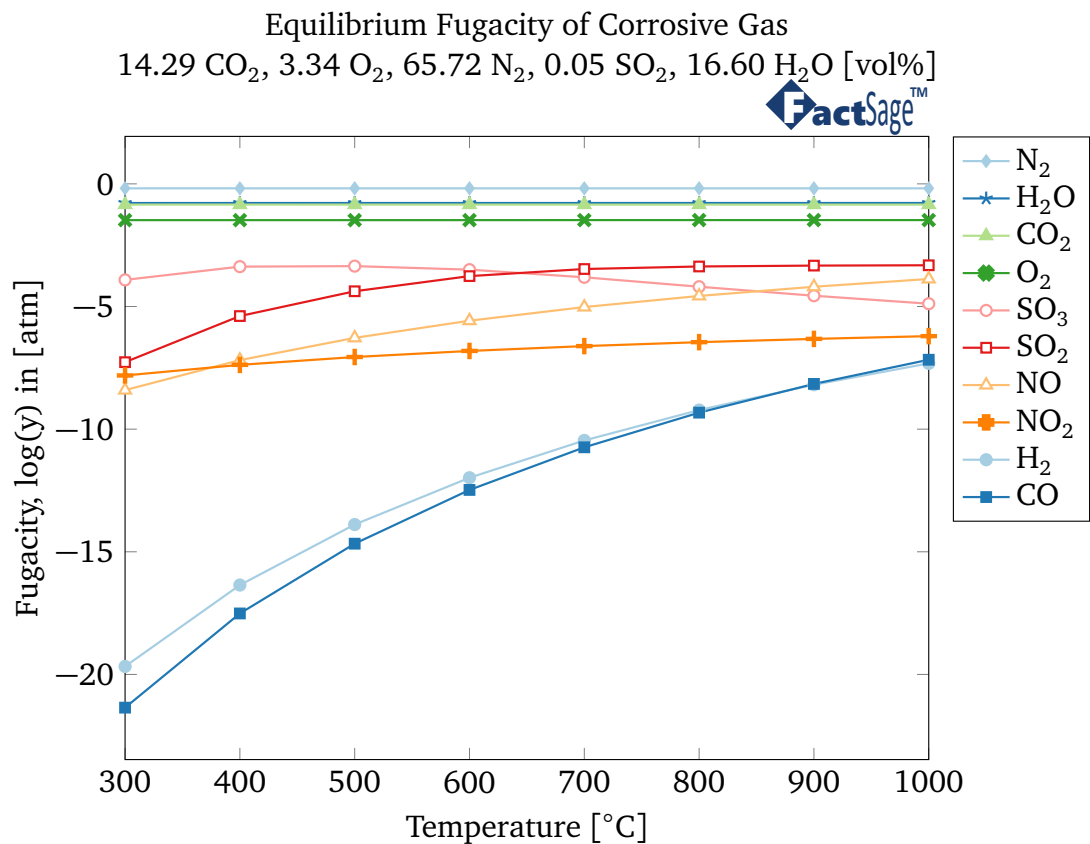


**Figure 3.1.:** Equilibrium Fugacities of Model Corrosive Gas

This information is needed to establish the position of the flue gas in a phase stability diagram (cf. Section 2.3.2.4). For example, in the Fe-Cr-O-S phase stability diagram at 650 °C and 1 atm shown in Figure 3.2, where Fe + Cr represent the typical components found in coal power plant materials and O + S representing gas species found in the combustion gas, the equilibrium position of the model flue gas can be identified for this system using the results obtained from gas phase calculations. This is represented by the gray sphere shape in the diagram. This point corresponds to the partial pressures of  $\text{SO}_2$  and  $\text{O}_2$  as obtained from the flue gas calculations at 650 °C and 1 atm, where the ordinate  $\log p(\text{SO}_2) = -3.582$  and the abscissa  $\log p(\text{O}_2) = -1.478$ . At that position, hematite ( $\text{Fe}_2\text{O}_3$ ) and chromia ( $\text{Cr}_2\text{O}_3$ ) are the phases that are in equilibrium with the flue gas model. Therefore, any change in equilibrium i.e. an increase or a decrease in temperature or the partial pressure of either  $\text{O}_2$  or  $\text{SO}_2$  will lead to a corresponding shift in the equilibrium position to a different region on the phase diagram. For instance, a decrease in  $p(\text{O}_2)$  and high  $p(\text{SO}_2)$  will result in the formation of the corrosive products  $\text{FeS}_2$  and  $\text{Cr}_2\text{S}_3$ .

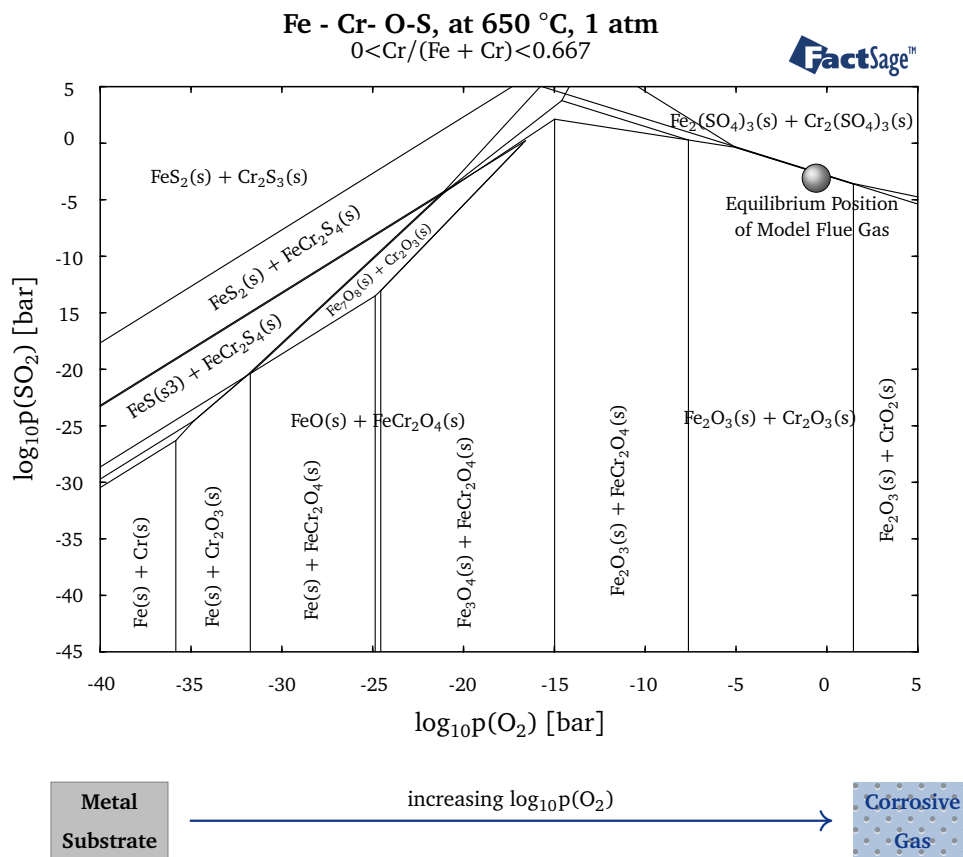


**Figure 3.2.:** Stability diagram for the Fe-Cr-O-S system at 650 °C

Furthermore, it can also be depicted from Figure 3.2 that the oxide layer sequence changes with increasing partial pressure of oxygen i.e. from the metal substrate or alloy (Fe, Cr) at low oxygen partial pressures to  $\text{Fe}_2\text{O}_3$  and  $\text{Cr}_2\text{O}_3$  at high oxygen partial pressures. This

sequence is expected in reality for Fe-Cr alloys assuming of course that  $pSO_2 = 0$ .

### 3.3. Fly ash behavior

Coal ash particles deposited on boiler materials during coal combustion play a very important role on the corrosion of those materials. On the one hand, they act as protective barriers against the corrosive flue gas preventing further corrosion but on the other hand they also reduce the corrosion resistance of the materials through chemical reactions from particles in the deposits with the material [50, 101]. The reaction is aggravated in the case where the ash is in a molten state as discussed in Section 2.3.5.3. It is also therefore of interest to examine the behavior of the fly ash at the given test temperature of 650 °C for this study, using thermochemical modeling approach. The composition of the fly ash used in the experiments is given in Table 3.2.

**Table 3.2.:** Composition of Fly Ash

Element	Concentration	Normalized
	[wt%]	[wt%]
Na <sub>2</sub> O	0.32	0.34
MgO	3.53	3.71
Al <sub>2</sub> O <sub>3</sub>	12.16	12.77
SiO <sub>2</sub>	43.69	45.90
K <sub>2</sub> O	1.44	1.51
CaO	17.01	17.87
Fe <sub>2</sub> O <sub>3</sub>	17.04	17.90
<b>Sum</b>	<b>95.19</b>	<b>100.00</b>

For the simulation of the fly ash, two slag phases (Slag#1 and Slag#2) which consist basically of the constituents of the fly ash are modeled at the test temperature of 650 °C to determine the melting behavior of the ash. The alkali metal oxides K<sub>2</sub>O and Na<sub>2</sub>O are known to influence the melting behavior of ash. Figure 3.3 shows the isothermal section of the K<sub>2</sub>O–Na<sub>2</sub>O–SiO<sub>2</sub> ternary system at 650 °C with the various slag phases for different concentrations of K<sub>2</sub>O, Na<sub>2</sub>O and SiO<sub>2</sub>.

Additionally, a projection of the fly ash melting behavior is carried out in the temperature range 300 – 1000 °C for the K<sub>2</sub>O–Na<sub>2</sub>O–SiO<sub>2</sub> ternary system. This result is presented in Figure 3.4. It can be seen from the diagram that a liquid slag will form only above 800 °C and at high of K<sub>2</sub>O concentrations. This is also confirmed in Figure 3.5 and Figure 3.6 showing the melting behavior for different concentrations of K<sub>2</sub>O and Na<sub>2</sub>O at different temperatures. From the results of simulation of fly ash, it is clear that at low K<sub>2</sub>O and

$\text{Na}_2\text{O}$  concentrations a corresponding molten phase eutectic can only be attained above 800 °C and therefore such liquid slag phases for the given fly ash composition will have little or no effect on the corrosion attack of the materials. The results obtained here agree with that of Meyer and Gutte [50].

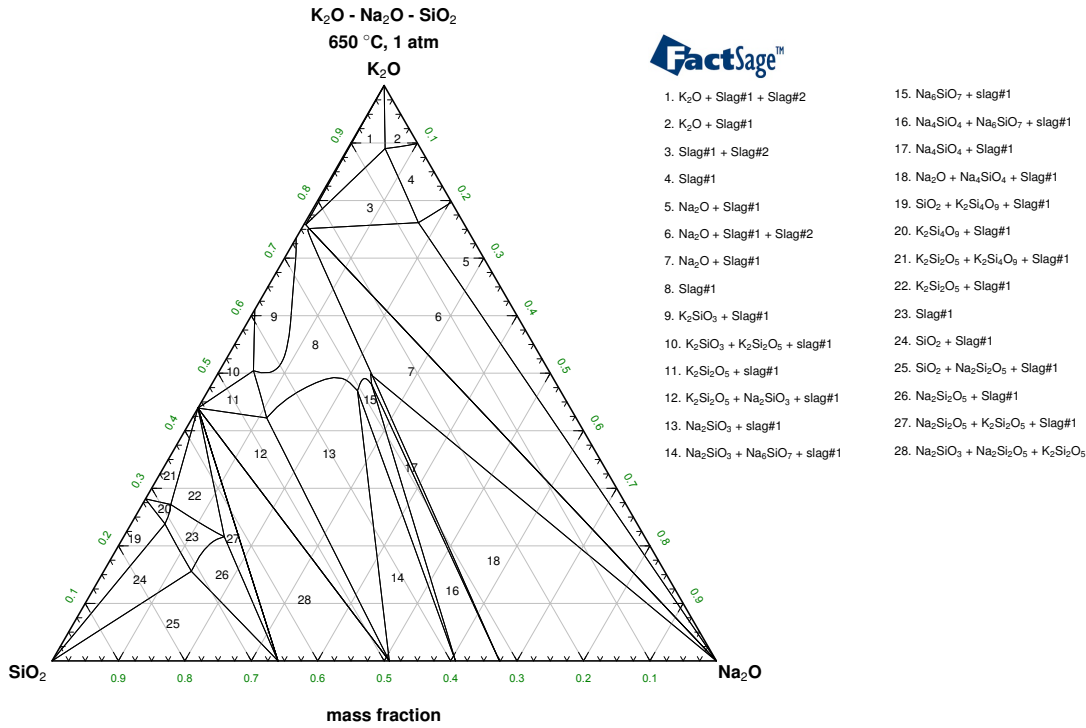


**Figure 3.3.:** Isothermal section at 650 °C of the  $\text{K}_2\text{O}$ – $\text{Na}_2\text{O}$ – $\text{SiO}_2$  ternary phase diagram

### 3.4. Gas–Metal Equilibria

For the gas–metal equilibria the reaction of flue gas with the commercial alloys are simulated. It is important to note that, the equilibrium phase diagrams derived from these calculations do not present the complete picture of the reaction owing firstly to the fact that not all the components of the alloy system will take part in the reaction with the flue gas [59] and also due to the limitations mentioned in Section 3.1. Therefore, only a limited numbers of possible phases that can occur are selected for the equilibrium calculations. To obtain of possible phases that might form from the reaction of the alloy system with the flue gas, non-isothermal stability diagrams (so called one–dimensional alloy phase mappings) were simulated as a function of temperature.

The calculations were performed in the Equilib module (for complex equilibria), making use of the FactPS database for pure substances for the gas phase, the FT-Oxid database for all pure oxides and oxide solutions and the FS-Stel database for alloy systems. The results of the gas – metal equilibration for the investigated commercial alloys are presented and discussed below. It should be noted that particular attention is paid here to the ‘gas phase’

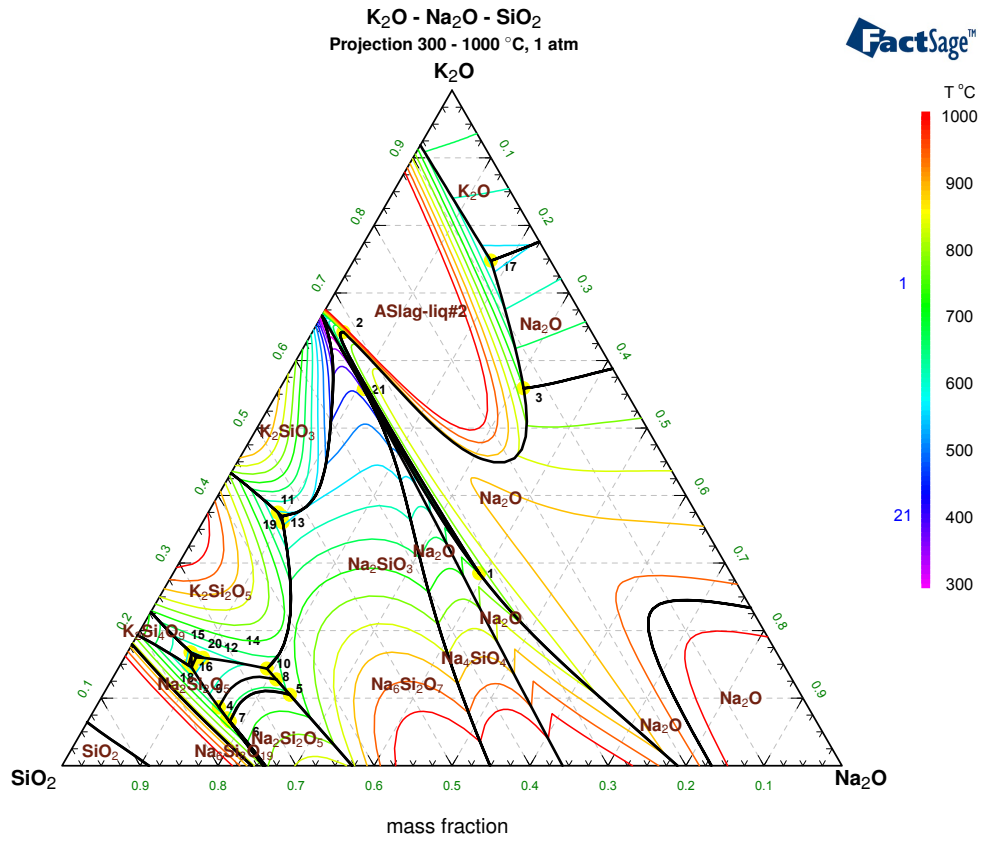


Figure 3.4.: Ternary phase diagram projection at 300 - 1000 °C of  $K_2O$ - $Na_2O$ - $SiO_2$  system

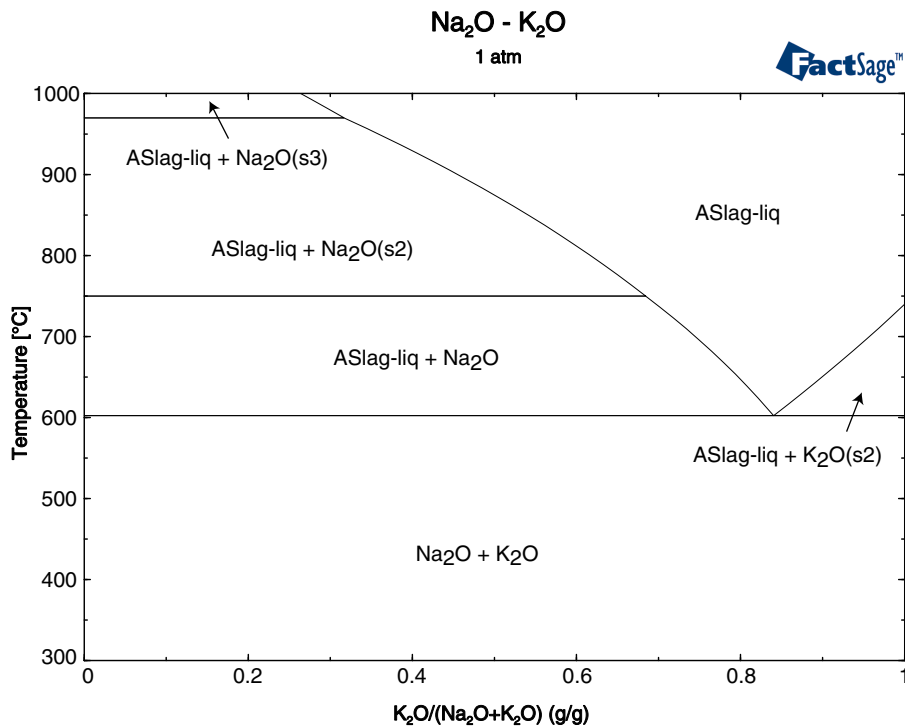
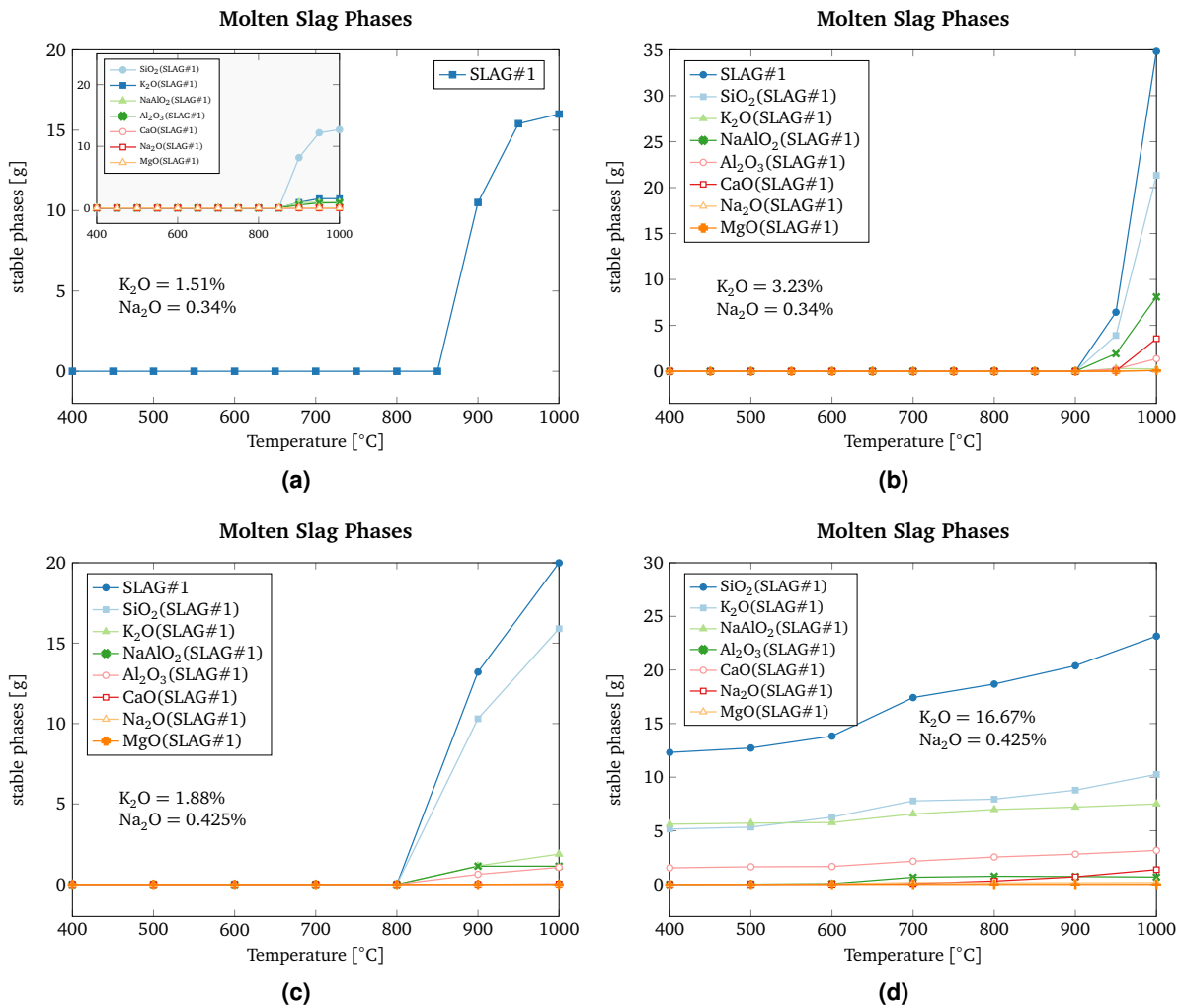


Figure 3.5.:  $Na_2O$ - $K_2O$  system at 300 - 1000 °C and 1 atm



**Figure 3.6.:** Molten slag phase formation in fly ash

of the flue gas only. Deposits are not considered in the calculations. A two phase flow (gas + ash deposits) model is presented in [Section 3.5](#).

### 3.4.1. TP91

The gas – alloy phase equilibria results for TP91 are presented in [Figure 3.7](#). The results shows the typical BCC phase which is very common of ferritic steels [59]. The precipitate phase  $M_{23}C_6$  is also seen to be constant throughout the temperature range reaching a maximum at about 600 °C. The  $M_{23}C_6$  phase is normally expected for ferritic-martensitic steels with < 12% Cr. It is said to be stable up to temperatures of about 800 °C and dissolves in the matrix between 900 – 1000 °C as can be seen from the diagram [50]. The main components of the  $M_{23}C_6$  phase are  $Fe_{23}Mo_3C$  with about 4g and  $Fe_{23}C_6$  with about 1g. This phase is important because inter-crystalline corrosion of ferritic and austenitic steels is caused by the depletion of Cr in the base metal. Grain boundary attack is enhanced through the precipitation of Cr-rich metal carbide phases such as  $M_{23}C_6$  as well as  $M_7C_3$  and

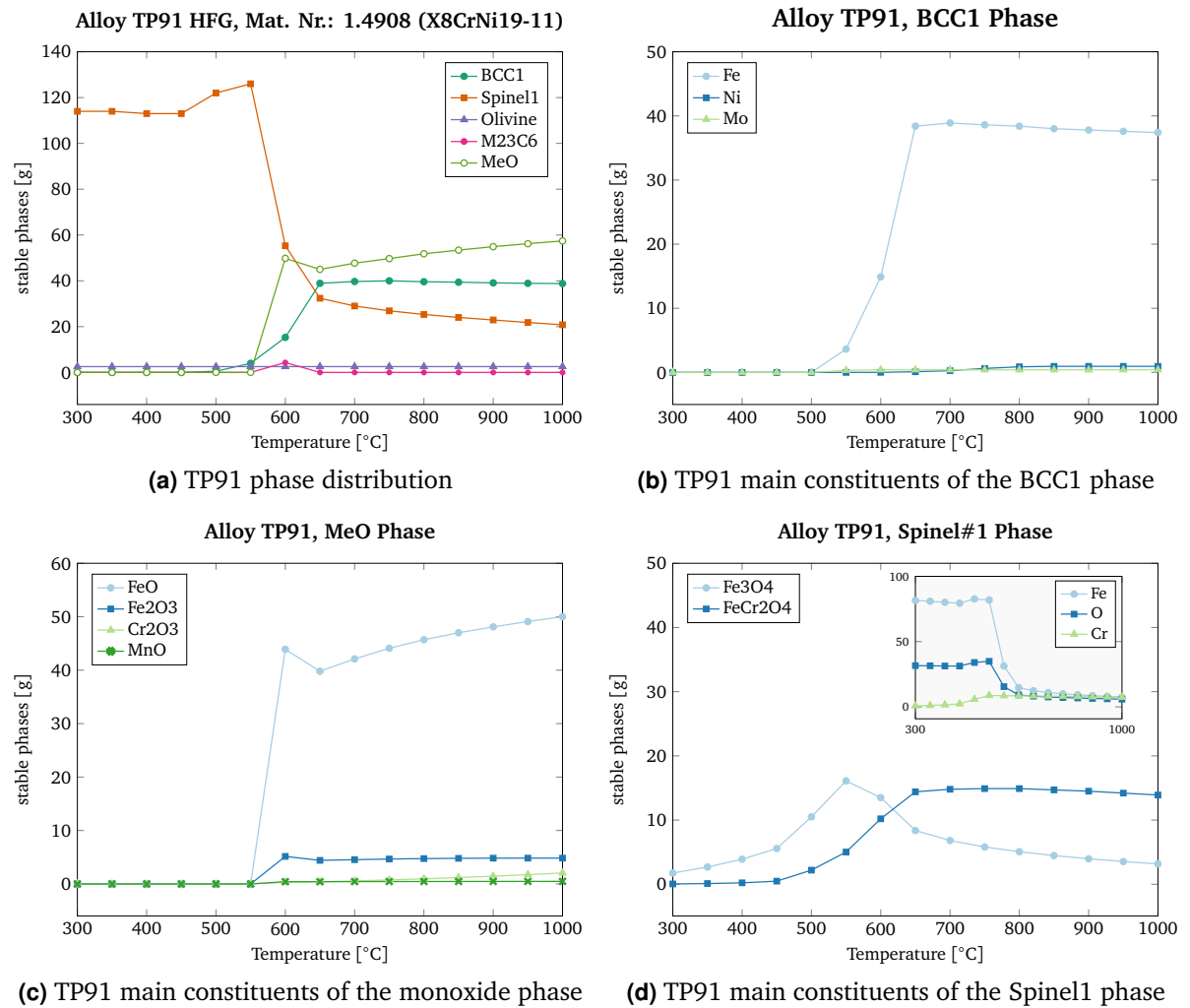


Figure 3.7.: TP1 gas–metal phase equilibria

M<sub>6</sub>C<sub>6</sub> and even nitrides such Cr<sub>2</sub>N [50]. According to Hald cited in [50], the metal carbide phase M<sub>23</sub>C<sub>6</sub> is the most important phase for 9 – 12 %Cr steels. The carbides can form also in austenitic steels. During formation, on the grain boundaries, they are responsible for depleting Cr in the vicinity of the grain boundary. If the metal is heated to about 900 °C, the M<sub>23</sub>C<sub>6</sub> phase eventually dissolves. Conversely, during cooling of the metal, this leads to the precipitation of the carbide phase. This could lead to embrittlement and inter-crystalline corrosion. This effect is worse for ferritic steels than for austenitic steels due a high diffusion rate and low dissolution.

The spinel phase (Spinel1) is seen to be dominant at low temperatures up to about 550 °C and is overlapped by the MeO (metal oxide) phase and BCC phase at higher temperatures above 650 °C. The main constituents of the Spinel1 phase are the inverse spinel magnetite (Fe<sub>3</sub>O<sub>4</sub>) and the Fe-Cr spinel FeCr<sub>2</sub>O<sub>4</sub>. The spinel phase formed is also important because the oxidation of steel materials may leads to the formation of a protective single phase at the surface such as magnetite Fe<sub>3</sub>O<sub>4</sub> [65]. The spinel lattice is relevant with respect

to the protection it provides the alloy and the spinel structure may occur with different stoichiometry continually as a 'double oxide' phase. Such a phase may offer a good kinetic barrier to prevent further oxidation. An example of such spinel is  $\text{NiO}\cdot\text{Cr}_2\text{O}_3$  spinel in Cr-Ni-Fe alloys (cf. Table 2.5). The structure of the spinel is therefore vital on the corrosion behavior of steel alloys. It should be noted that a second spinel phase might form, but that is not represented on the diagram.

The MeO (metal oxide) phase which is the most dominant phase above 600 °C is composed of mainly FeO,  $\text{Fe}_2\text{O}_3$ ,  $\text{Cr}_2\text{O}_3$  and some MnO. Finally, the Olivine phase is also quite constant throughout the temperature range. Olivine, with the general form  $\text{M}_2\text{SiO}_4$  (where  $\text{M} = \text{Mg}, \text{Fe}$ ) is an orthosilicate and they are susceptible to mechanical and chemical breakdown [102]. The main constituents of the olivine phase from the calculation is  $\text{Fe}_2\text{SiO}_4$  (fayalite).

**Pure solids:** Not represented on the phase equilibria diagrams for clarity purposes are pure solids that might form. The pure solids include small quantities (< 2 g) of  $\text{Nb}_2\text{O}_5$ , the spinel  $\text{FeV}_2\text{O}_4$ , which occur throughout the temperature range;  $\text{MoS}_2$ , which might form up to about 850 °C and FeS between 800 and 900 °C with a maximum at 850 °C.

### 3.4.2. VM12-SHC

The ferritic-martensitic alloy VM12-SHC also shows quite a similar equilibria (see Figure 3.8) to TP91 with a classical BCC matrix which is dominant above 650 °C. The precipitate carbide phase  $\text{M}_{23}\text{C}_6$  (with mainly  $\text{Fe}_{20}\text{Mo}_3\text{C}_6$  and small amounts of  $\text{Fe}_{23}\text{C}_6$ ) is constant throughout the temperature range. A precipitate sulphide phase, (Fe-Mn)S composing of mainly FeS and MnS is also found to be present in the equilibria in small amounts and is expected throughout the temperature range as well. The metal oxide phase MeO which is superimposed by the BCC phase also has similar constituents as in TP91 i.e. FeO,  $\text{Fe}_2\text{O}_3$ ,  $\text{Cr}_2\text{O}_3$  and MnO. The 'low' temperature (below 650 °C) dominant Spinel1 phase also has magnetite and Fe-Cr spinel as main components. The HCP phase, which is a hexagonal metallic structure with C and N might also form.

**Pure solids:** The pure solids expected here are also in small amounts < 2g and include; MoO – at low temperatures up 500 °C, MoC – between 450 °C and 700 °C,  $\text{MoS}_2$  – up to 800 °C,  $\text{Cu}_2\text{S}$  and the spinel  $\text{FeV}_2\text{O}_4$  which is constant through the entire temperature range.

### 3.4.3. TP347-HFG

The austenitic alloy TP347-HFG shows the typical FCC phase common in austenitic materials. The phase equilibria diagrams are shown in Figure 3.9. It can be seen here that the spinel phase is the most dominant throughout the temperature range. It is quite high



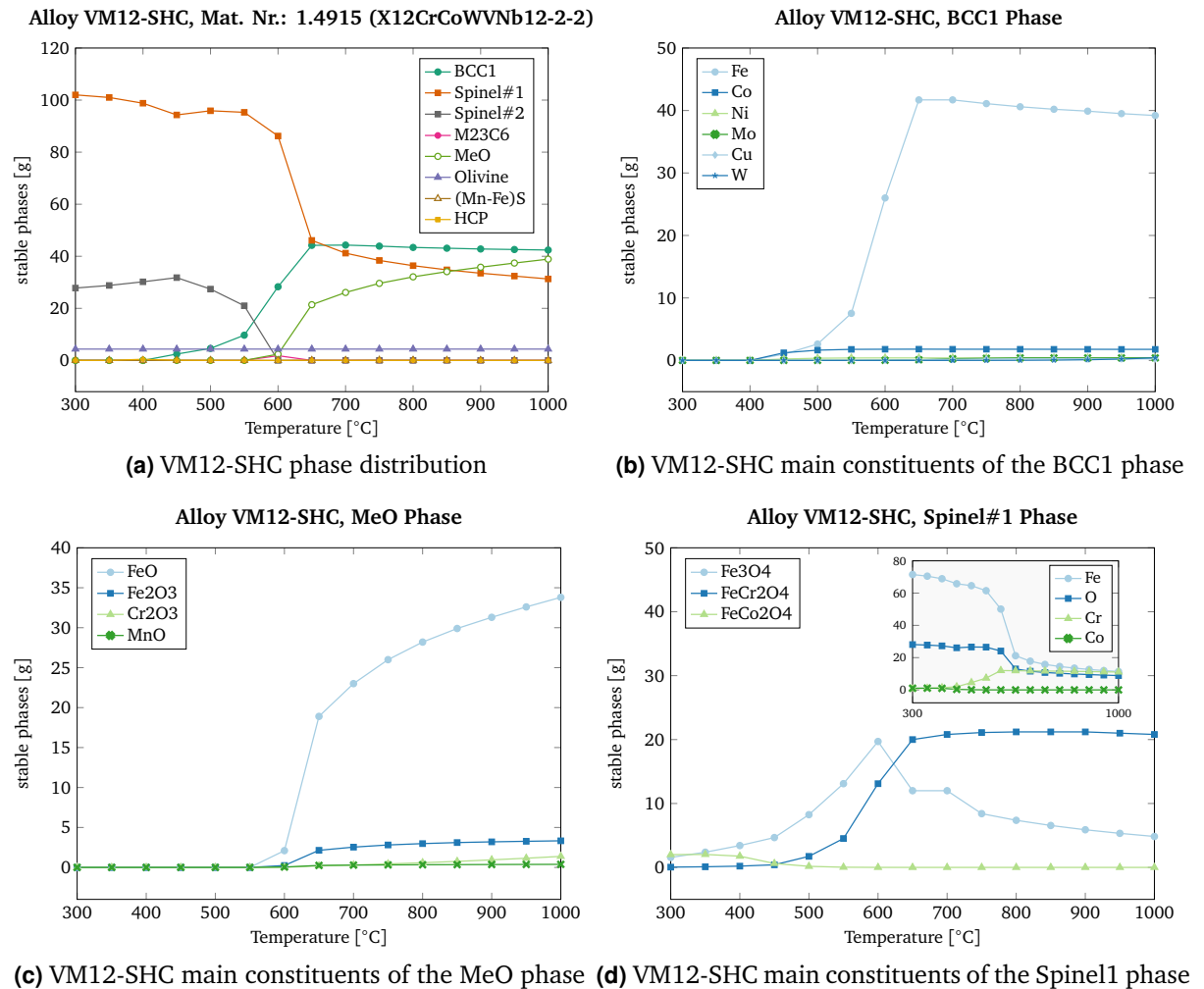


**Figure 3.8.:** VM12-SHC gas–metal phase equilibria

at low temperatures and slightly decreases with increasing temperature. The main components for the Spinel1 phase are the inverse spinel magnetite ( $\text{Fe}_3\text{O}_4$ ) and Fe-Cr spinel ( $\text{FeCr}_2\text{O}_4$ ).  $\text{M}_{23}\text{C}_6$  was not found to be stable for this equilibration. The precipitate (Mn-Fe)S is present in smaller quantities throughout the temperature range. Olivine phase with main constituents  $\text{MnFeSiO}_4$ ,  $\text{Mn}_2\text{SiO}_4$  and  $\text{Fe}_2\text{SiO}_4$  is also expected to form most likely above 400 °C. The MeO phase might also form above 550 °C with main components being FeO,  $\text{Fe}_2\text{O}_3$ , MnO and some  $\text{Cr}_2\text{O}_3$ .

**Pure solids:** The pure solids which might form here also in small quantities (< 2g) are  $\text{Nb}_2\text{O}_5$  which is constant throughout the temperature range and  $\text{Ni}_3\text{S}_2$  which might occur at low temperatures up to 500 °C.

### 3.4.4. DMV304 HCu

The phase equilibria for the austenitic alloy DMV304 HCu is given in Figure 3.10. The alloy also shows the FCC matrix common in austenitic alloy. It can also be seen that corundum

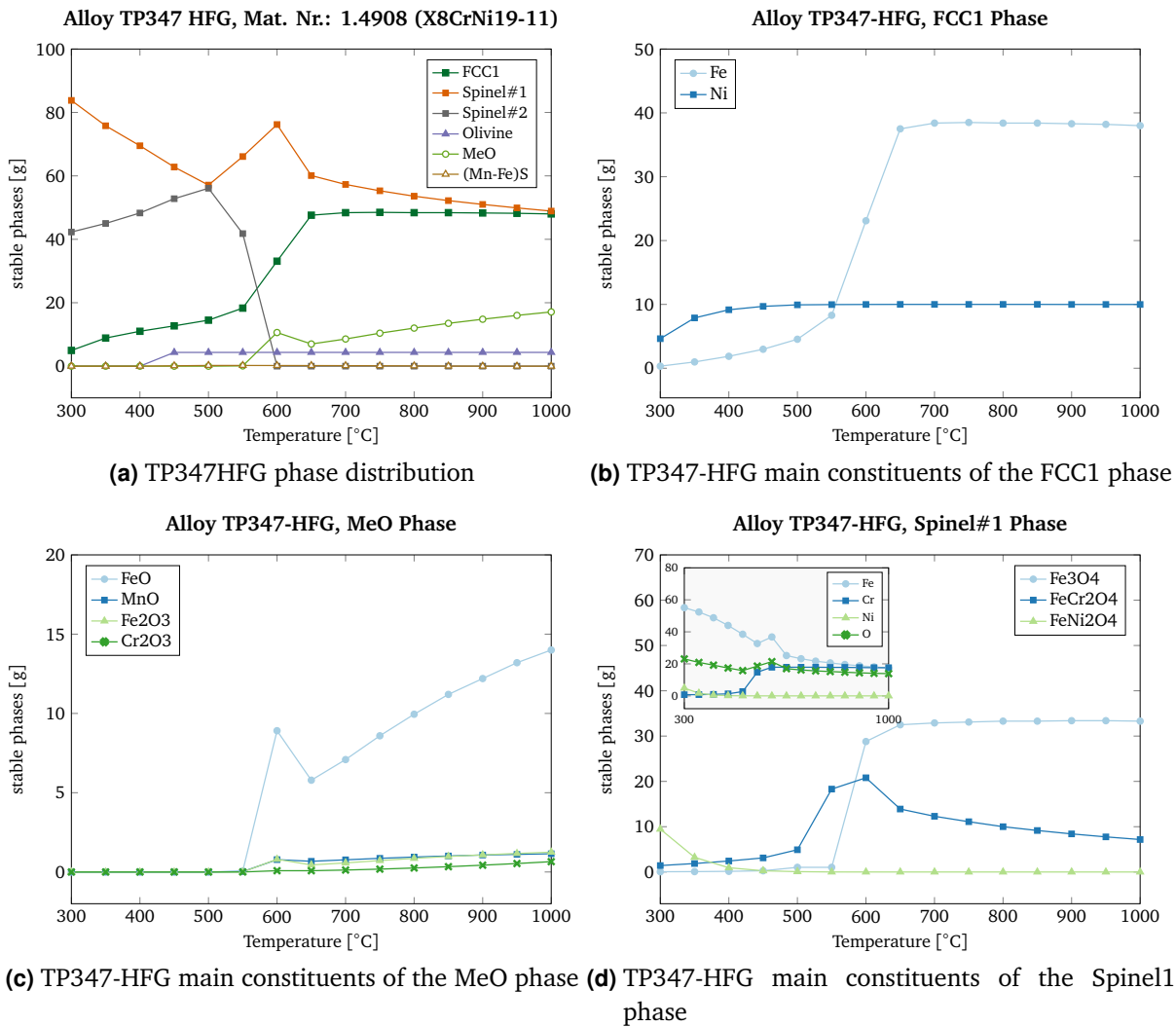
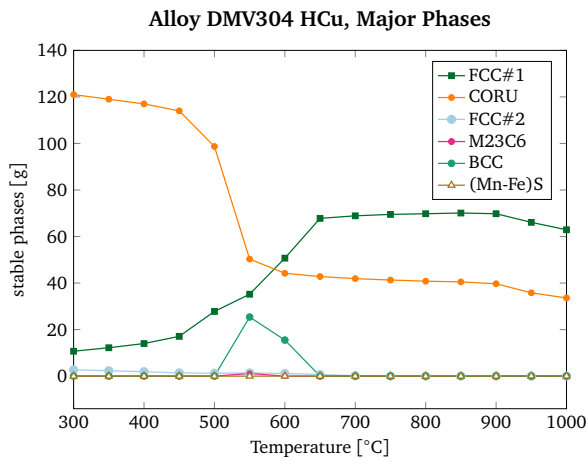


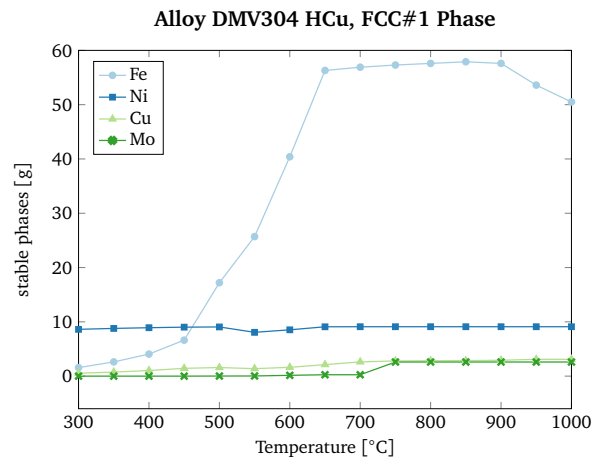
**Figure 3.9.:** TP347-HFG gas–alloy phase equilibria

with main components being  $\text{Cr}_2\text{O}_3$  and  $\text{Fe}_2\text{O}_3$  is dominant at low temperatures but it is overlapped by the FCC phase above 600 °C. The precipitate phase  $\text{M}_{23}\text{C}_6$  with main constituents being  $\text{Fe}_{20}\text{Mo}_3\text{C}_6$  is expected throughout the temperature range. The BCC phase is found for this equilibration and it is expected for such complex Fe-Cr-Ni alloys with high amounts of the three main components. The (Mn-Fe)S precipitate is also expected throughout the temperature range.

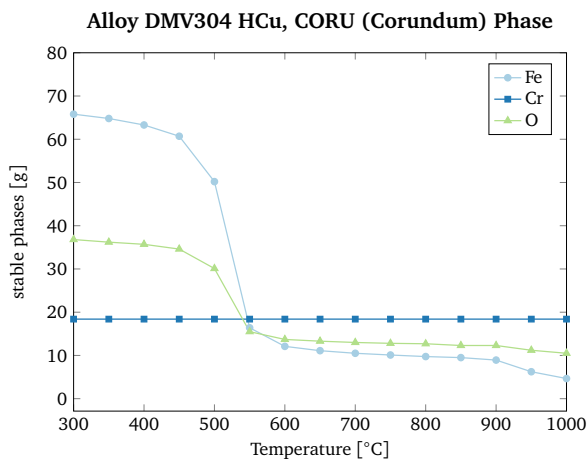
**Pure solids:** The stable pure solids expected are  $\text{MoO}_2$  up to 650 °C,  $\text{Cu}_2\text{S}$  up to 950 °C, and  $\text{Nb}_2\text{O}_5$  constant for the entire temperature range. The oxides of Mn i.e. MnO and  $\text{MnO}_2$  are closer to equilibrium with activities of 0.7 and 0.9 respectively. This implies they are likely to form. MnS also has activity of 0.6.



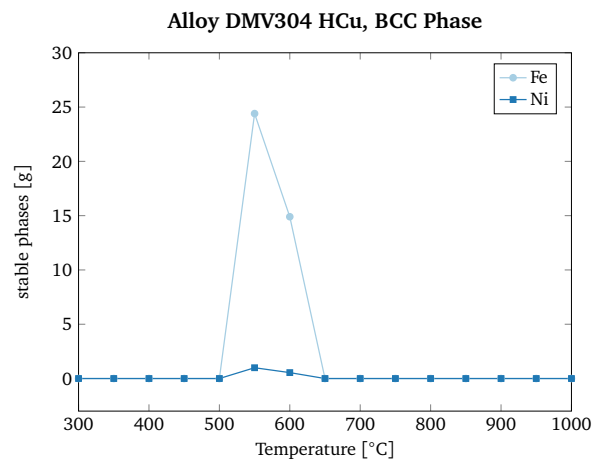
(a) DMV304 HCu phase distribution



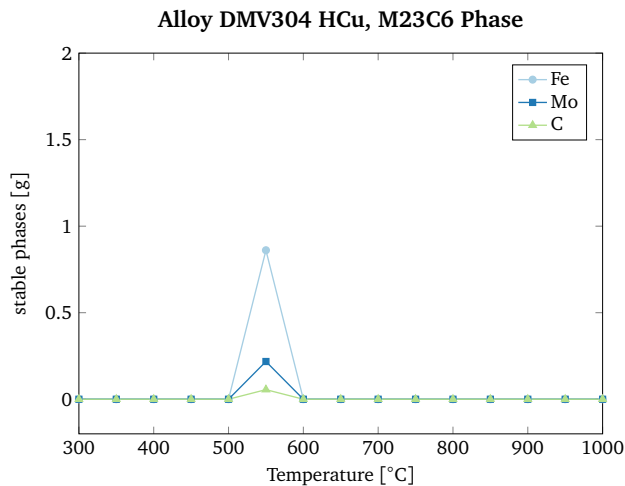
(b) DMV304 HCu main constituents of the FCC#1 phase



(c) DMV304 HCu main constituents of the CORU (corundum) phase



(d) DMV304 HCu main constituents of the BCC phase



(e) DMV304 HCu main constituents of the M23C6 phase

Figure 3.10.: DMV304 HCu gas – alloy phase equilibria

### 3.4.5. DMV310 N

The complex austenitic Fe-Cr-Ni based alloy shows the typical FCC phase which is dominant at high temperatures above 550 °C and the corundum phase which is dominant at low temperatures below 550 °C but superimposed by the FCC phase at high temperatures (see Figure 3.11). Also, the precipitate phase (Mn-Fe)S with mainly MnS might form. As can be seen from the corundum phase (Figure 3.11c), chromia prevails over hematite above 550 °C, which in practice if the chromia layer is dense will shield the material from corrosion.

**Pure solids:** Similar to TP347 HFG, Nb<sub>2</sub>O<sub>5</sub> (for the entire temperature range) and Ni<sub>3</sub>S<sub>2</sub> (below 450 °C) are the pure solids expected to form in small amounts.

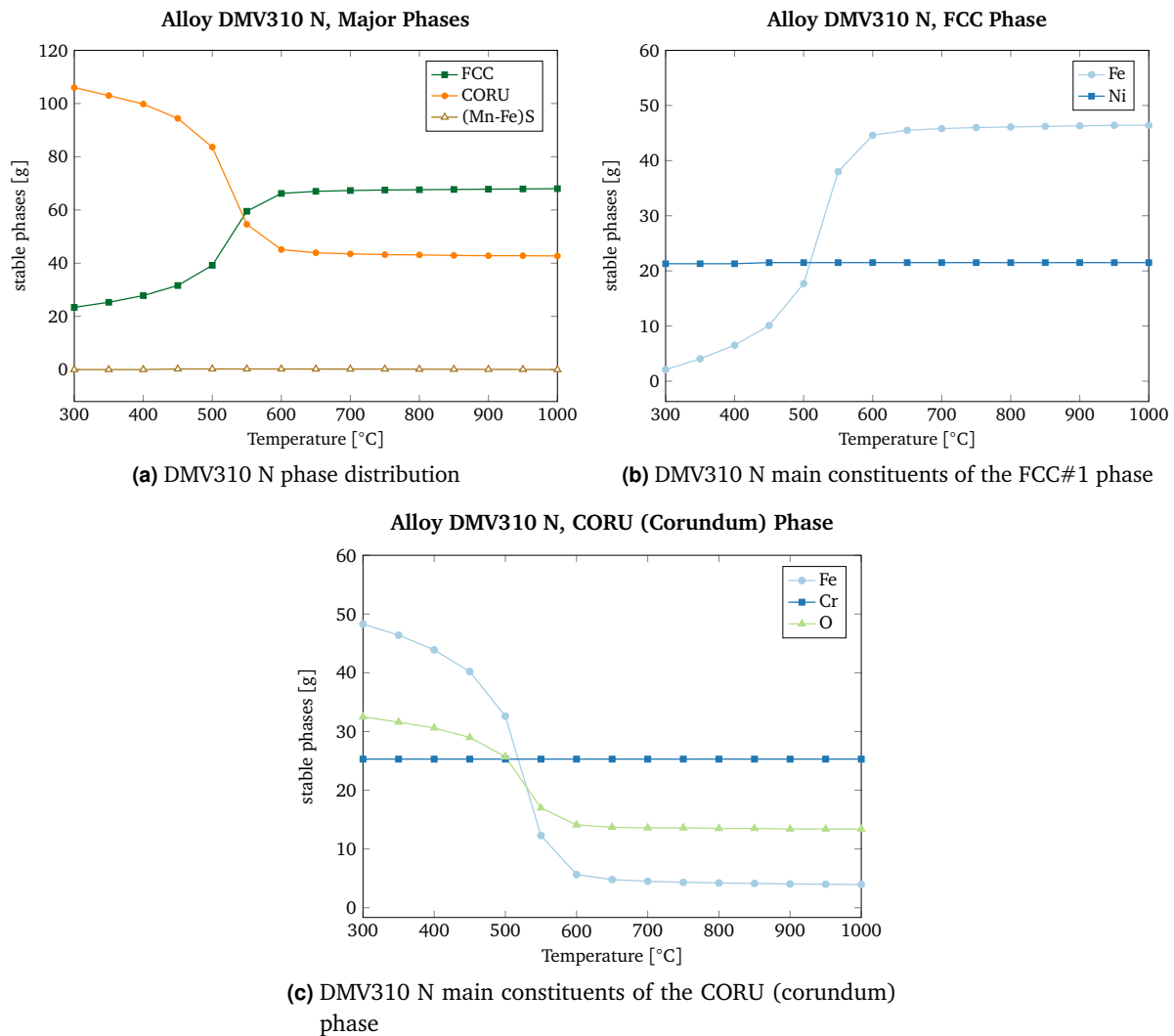


Figure 3.11.: DMV310 N gas – alloy phase equilibria

**Table 3.3.:** Condensed phases formed from the reaction of gas and deposits on the iron metal oxides, 650 °C, 1 atm

Condensed phase	Amount [g]	Activity
Fe <sub>2</sub> O <sub>3</sub> , hematite	1.0040E+02	1
CaAl <sub>2</sub> Si <sub>2</sub> O <sub>8</sub> , anorthite	2.8858E+01	1
Ca <sub>3</sub> Fe <sub>2</sub> Si <sub>3</sub> O <sub>12</sub> , andradite	2.0816E+01	1
CaMgSi <sub>2</sub> O <sub>6</sub> , diopside	1.9933E+01	1
Fe <sub>2</sub> SiO <sub>4</sub> , fayalite	1.9565E+01	1
KAlSi <sub>2</sub> O <sub>6</sub> , leucite	6.9972E+00	1
SiO <sub>2</sub> , quartz	3.3908E+00	1
NaAlSi <sub>3</sub> O <sub>8</sub> , high-albite	2.8770E+00	1

### 3.5. Two phase flow model

The flue gas in coal-fired combustion chambers contains both gases plus ash particles (aerosols). It is therefore important to determine the reaction of the aerosol particles in fly ash deposits with the oxides formed on the metal surface. In this section, an attempt is made to estimate under which conditions the ash deposits will react with and damage the oxides formed on the material surfaces, i.e. the condensed phases which might form from such a reaction. The fugacities of the flue gas species used correspond to those given in Section 3.2 and the ash deposits composition are those given in Table 3.2. Since the deposits found on superheater materials in coal fired boilers are low in Cl-content [50], the effect of chlorine was not considered for this calculation. The oxides used were those of iron (Fe<sub>2</sub>O<sub>3</sub> 40 g, Fe<sub>3</sub>O<sub>4</sub> 30 g and FeO 30g). Table 3.3 shows the condensed phases formed from the reaction of the gas, ash deposits and iron oxides at 650 °C and 1 atm. These are the condensed species that are expected to form on the walls of the superheater/reheater materials at the calculated temperature.

As it can be seen from Table 3.4, the reaction of the flue gas with the ash deposits leads to decreasing oxygen partial pressures,  $p(O_2)$  and an increase in the partial pressures of sulphur dioxide,  $p(SO_2)$  (cf. Section 3.2) which could alter the stoichiometry of the oxide layer.

### 3.6. Predominance area diagrams

As discussed in Section 2.3.2.4, predominance area diagrams can be divided into two categories: in the first type the partial pressure of a corrosive gas component is plotted against the composition of one alloy component. This is particular useful when investigating the

**Table 3.4.:** Flue gas fugacities from reaction with ash and oxide at 650 °C and 1 atm

Gas species	Equil. amount	Fugacity, $p(X_i)$ [atm]	$\log p(X_i)$ [atm]
N <sub>2</sub>	1.31E+02	5.15E-01	-0.29
H <sub>2</sub> O	6.59E+01	2.60E-01	-0.59
CO <sub>2</sub>	5.68E+01	2.24E-01	-0.65
SO <sub>2</sub>	1.89E-01	7.46E-04	-3.13
H <sub>2</sub>	7.79E-02	3.07E-04	-3.51
CO	3.24E-02	1.28E-04	-3.89
H <sub>2</sub> S	1.16E-02	4.58E-05	-4.34
S <sub>2</sub>	4.82E-05	1.90E-07	-6.72
SO <sub>3</sub>	5.62E-09	2.22E-11	-10.65
O <sub>2</sub>	9.55E-15	3.76E-17	-16.42

effect of the alloy composition on the reaction system [59]. In the second category the log partial pressure of one corrosive gas component is plotted against the log partial pressure of another component of the corrosive gas. Here, the alloy composition is kept constant to investigate the role of the various corrosive gas species.

It is worth noting the difference between the predominance area diagrams and the alloy phase equilibria performed in Section 3.4. For the predominance area diagrams, the few selected alloy components for calculation are considered to react with the corrosive gas which leads to a change in their compositions or amounts whereas for the alloy phase equilibria the total alloy composition is used for calculation to obtain component activities and thus their compositions of the individual components do no change [59]. The phase stability diagrams for various systems representing the commercial alloys investigated in the experiments and the various phases that might form were calculated and are presented Figures 3.12 to 3.20.

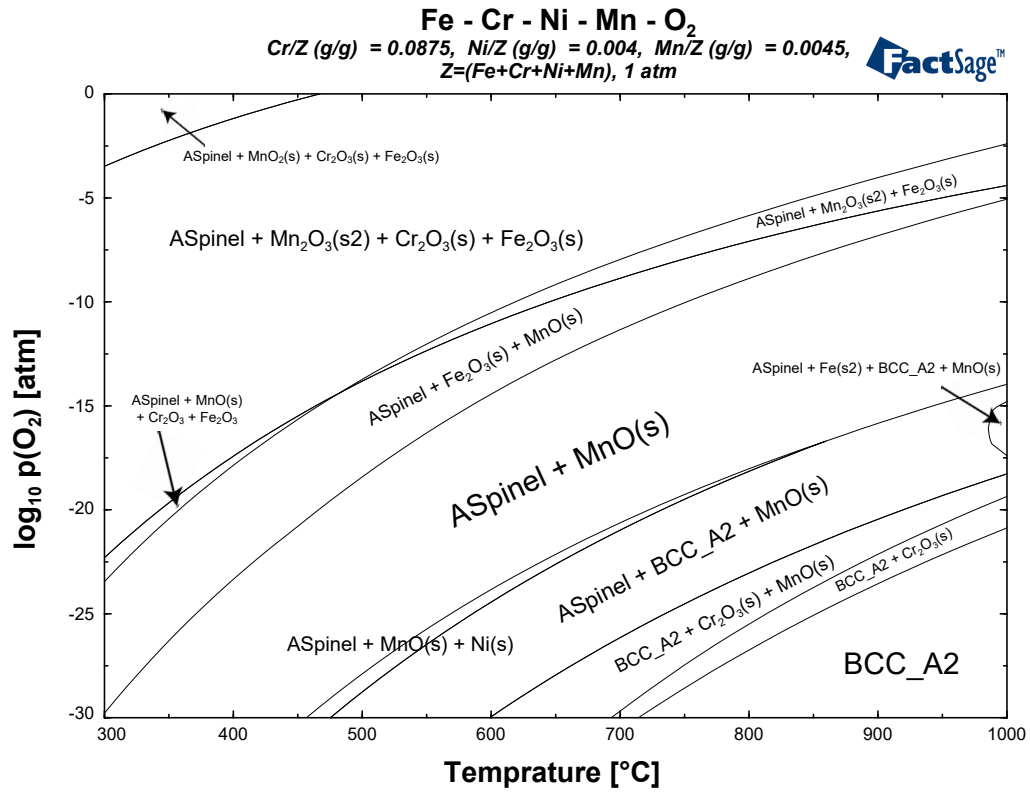


Figure 3.12.: Fe–8.75Cr–0.4Ni–0.45Mn alloy with O<sub>2</sub> phase diagram (TP91)

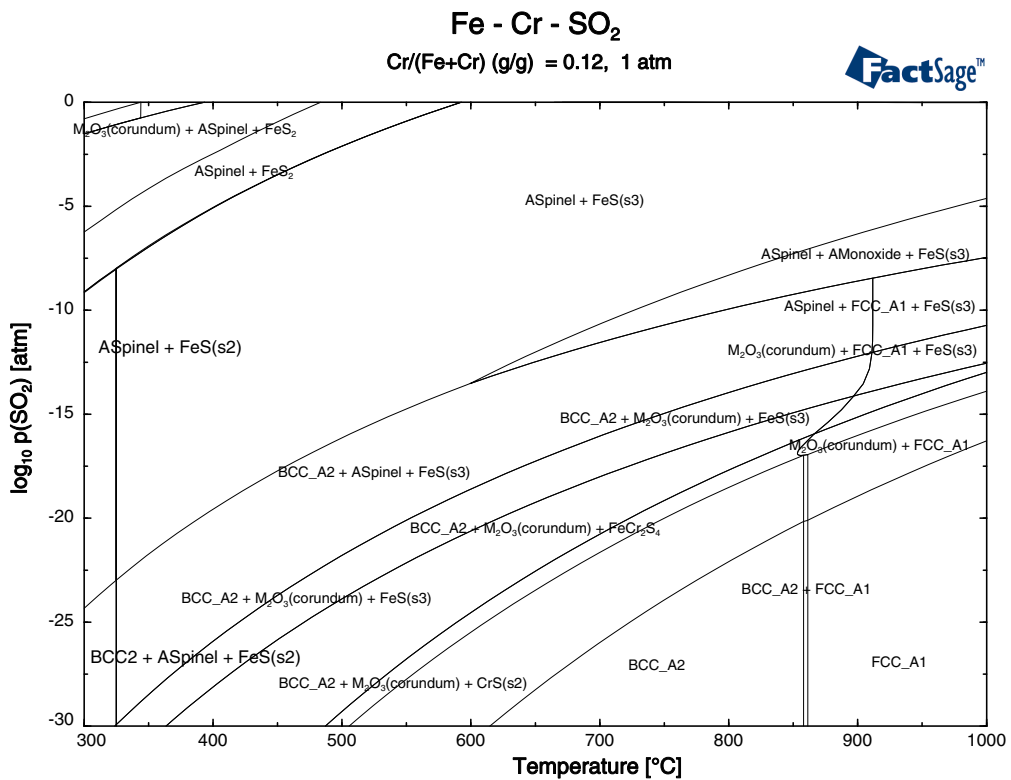
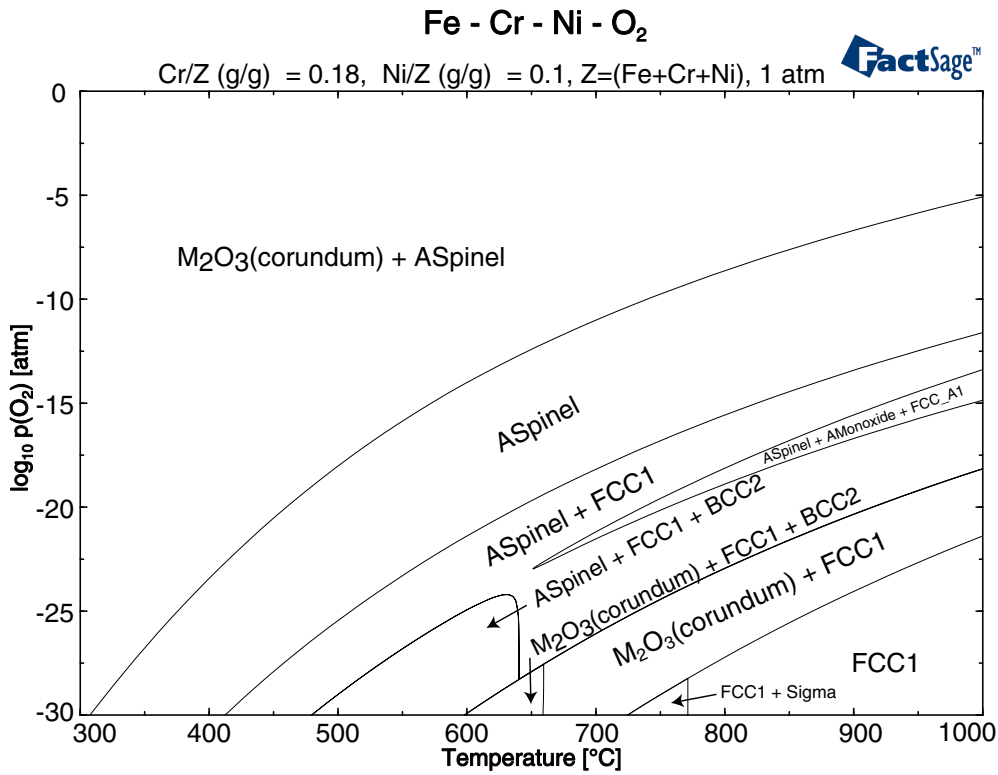
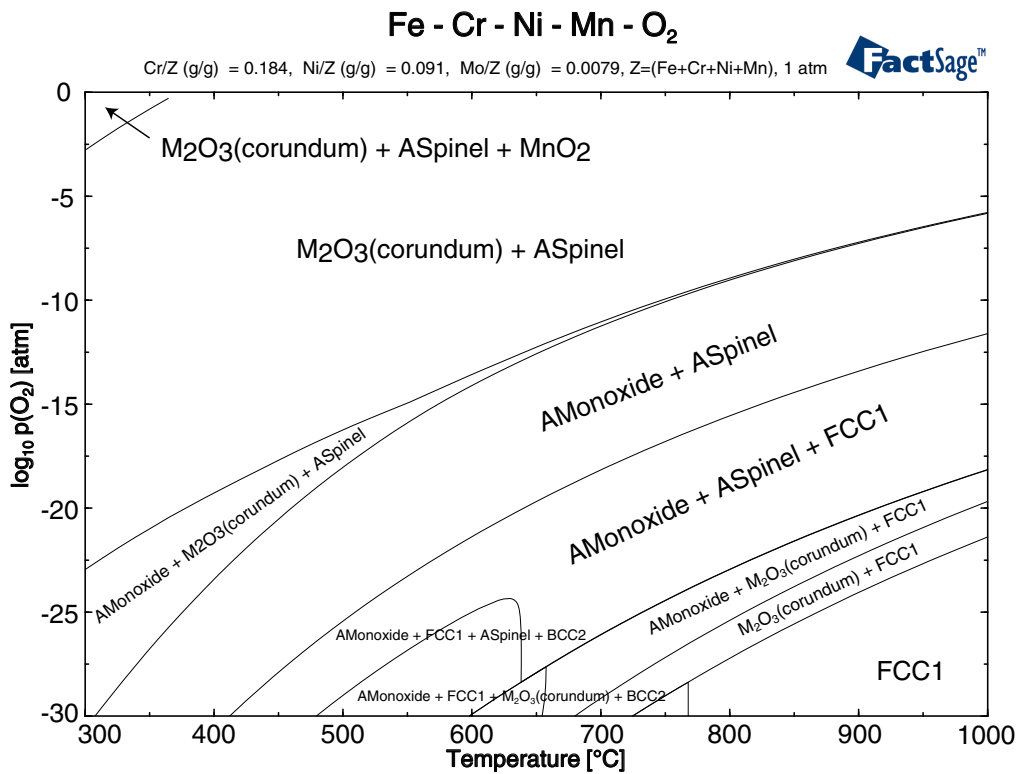


Figure 3.13.: Fe–12Cr alloy reaction with SO<sub>2</sub> phase diagram (VM12-SHC)



**Figure 3.14.:** Fe-18Cr-10Ni alloy reaction with O<sub>2</sub> phase diagram (TP347-HFG)



**Figure 3.15.:** Fe-18.4Cr-9.1Ni-Mn-O<sub>2</sub> phase diagram (DMV304 HCu)



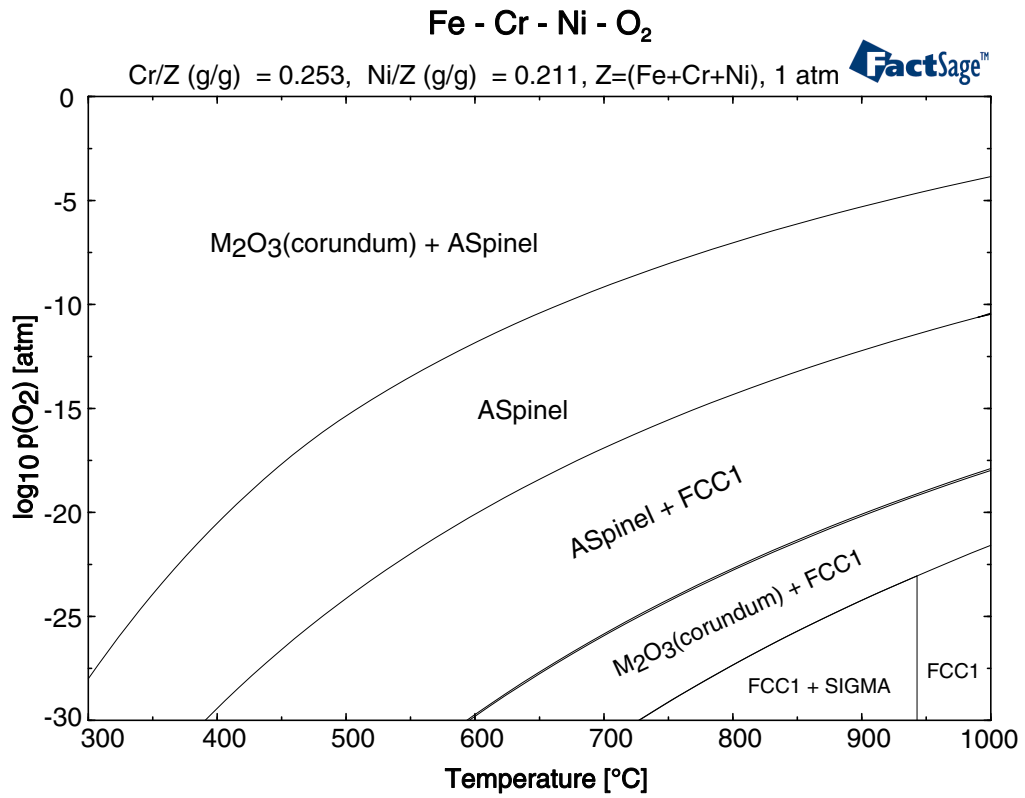


Figure 3.16.: Fe-25.33%Cr-21.05%Ni alloy reaction with O<sub>2</sub> phase diagram (DMV310 N)

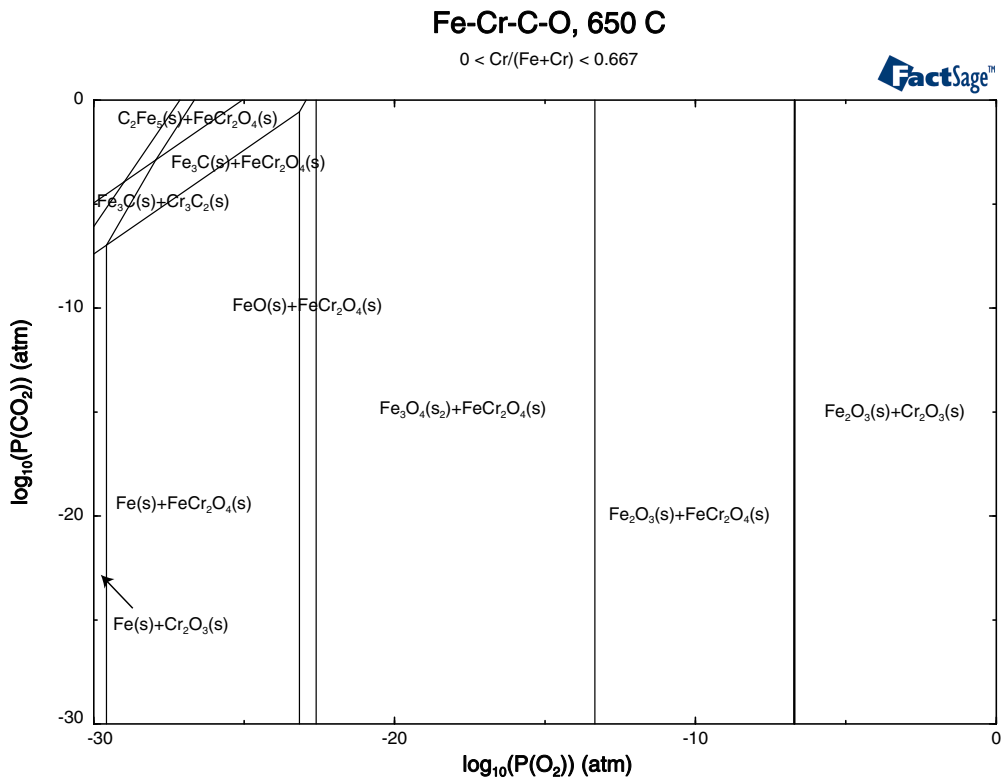


Figure 3.17.: Fe-Cr-C-O phase diagram at 650 °C and 1 atm

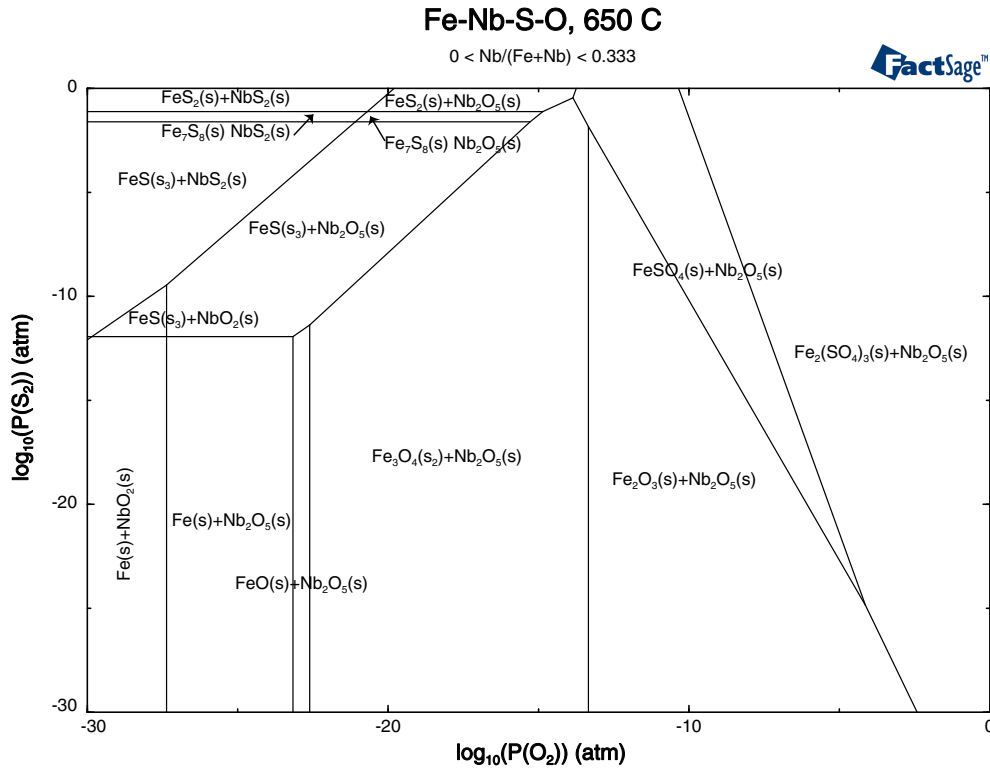


Figure 3.18.: Fe-Nb-S-O predominance area diagram at 650 °C and 1 atm

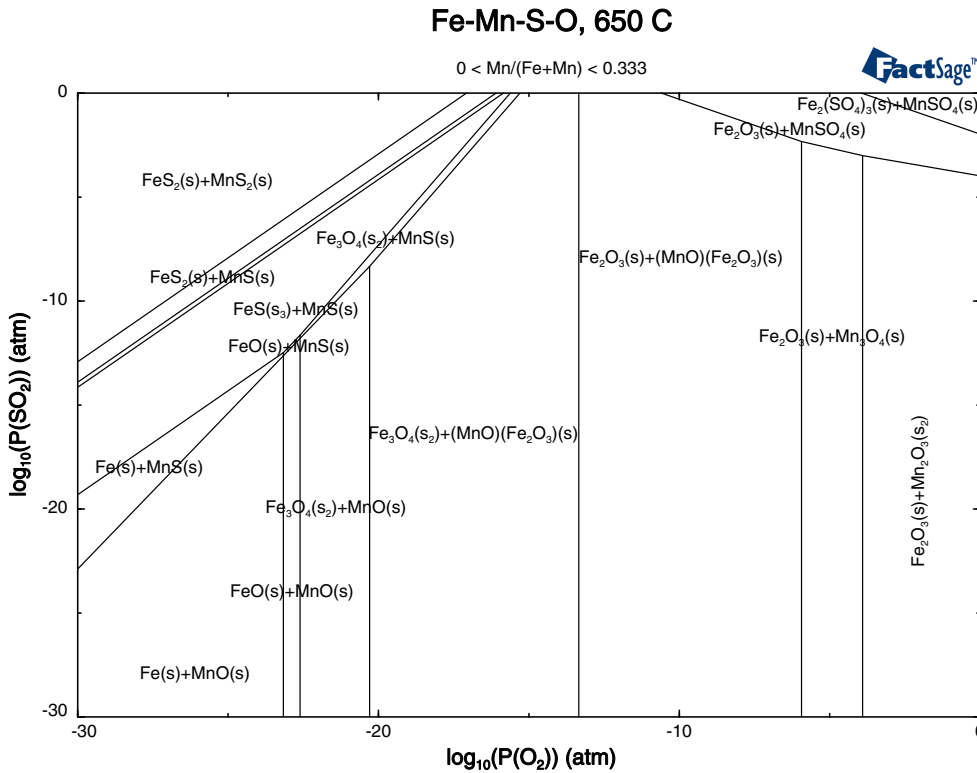
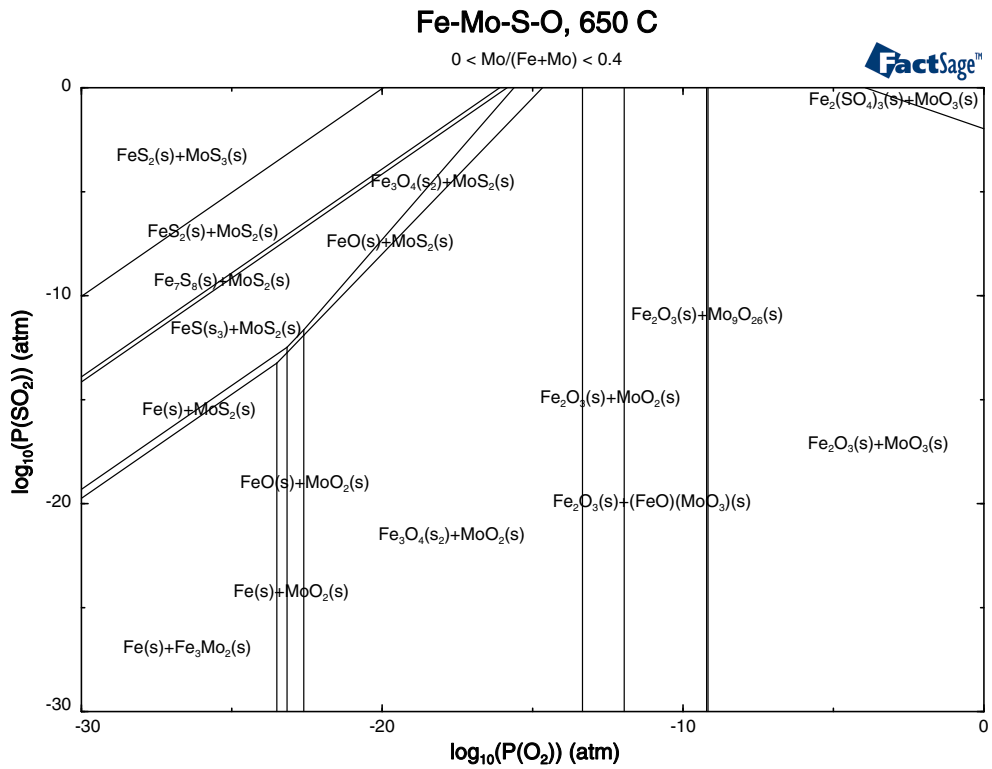


Figure 3.19.: Fe-Mn-S-O predominance area diagram at 650 °C and 1 atm



**Figure 3.20.:** Fe-Mo-S-O predominance area diagram at 650 °C and 1 atm



## 4. Experimental

### 4.1. General overview

As discussed in [Section 2.4.1](#) high temperature oxidation or corrosion tests usually involve weight-change measurements over time followed by metallographic analysis of the exposed or corroded materials to obtain information on the oxidation behavior and damage mechanisms of the materials in a given environment. There are several approaches to these, and these include: continuous thermogravimetric testing, continuous isothermal testing, discontinuous isothermal testing and thermal cycling oxidation testing. The cycling oxidation tests are widely used [85] (cf. [Section 2.4.1](#)).

The net weight change of the materials is taken to be equal to the net weight of oxygen absorbed as a result of scaling or oxide formation. Assuming uniform and compact oxide formation, the specific weights i.e. mass change divided by the surface area of the test sample will correspond approximately to the oxide scale thickness. This approach is widely used in practice because it is precise, less tedious and also economical than measuring the oxide scale thickness at regular time intervals. In this study, discontinuous isothermal oxidation and thermal cycling oxidation tests were carried out to evaluate the effect of increased cycling on commercial boiler materials. This chapter presents the experimental work carried out and the analytical methods used on the corroded test materials to evaluate the impact of increased cycling on the materials.

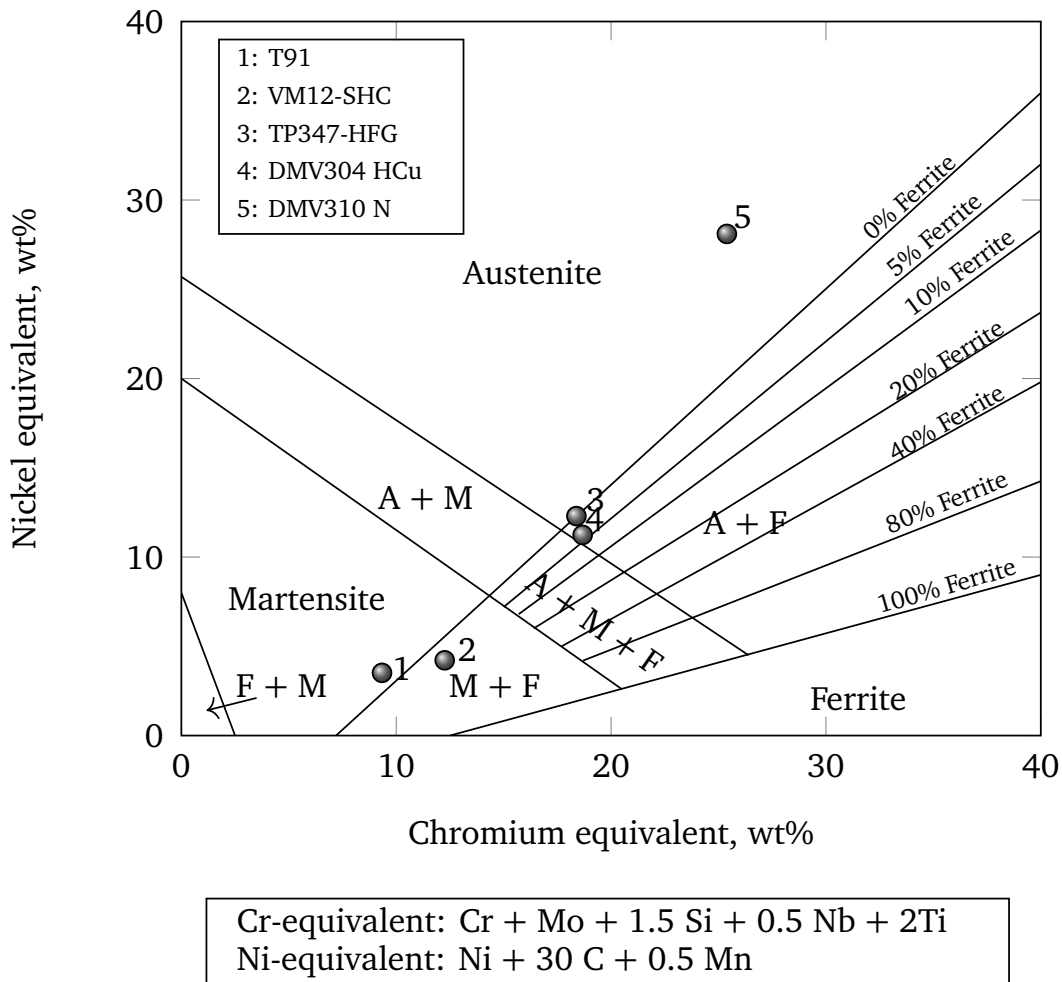
### 4.2. Investigated materials

A total of five commercial coal boiler (superheater and reheater) alloys were selected for isothermal and cyclic corrosion testing. These included: T91, VM12-SHC, TP347-HFG, DMV304 HCu and DMV310 N; The microstructure of the materials are shown on the Schaeffler diagram given in [Figure 4.1](#). Their chemical compositions are given in [Table 4.1](#). A brief description of the materials is given below.

**TP 91:** TP91 alloy is a martensitic ASTM steel grade used in the furnace waterwalls and superheater and reheaters in fossil fuel and nuclear power plants. It is used for both tubular

**Table 4.1.:** Chemical composition of selected materials

Alloy	Fe	Cr	Ni	C	Mo	Mn	Si	Others
TP91	Bal	8.75	0.4	0.105	0.95	0.45	0.35	V0.22
VM12-SHC	Bal	12	0.40	0.14	0.40	0.45	0.60	Cu 0.25; W 1.7; V 0.30; Co 1.8
TP347HFG	Bal	18.0	10.0	0.08	-	1.6	0.60	Nb 0.8
DMV304HCu	Bal	18.4	9.1	0.087	0.26	0.79	0.23	Cu 3.1; Nb 0.44; N 0.11
DMV310N	Bal	25.33	21.05	0.058	-	1.2	0.39	Nb 0.445; N 0.255

**Schäffler diagram for stainless steels****Figure 4.1.:** Schäffler diagram for stainless steels, adapted from [103]

or tubes (T) and pipes (P) with varying wall thicknesses, hence the name TP91. It was developed in the USA at the beginning of the 1980. The material is a modified form of P9 i.e. a 9Cr–1Mo steel, and has higher allowable stress than P22. This property allowed thinner

wall pipes to be designed thereby saving material cost in manufacturing as well as installations. Also, the welding and preheating of this steel grade requires less energy [104]. TP91 falls in the category of 9 – 12 %Cr alloys which are given the collective name Creep-Strength Enhanced Ferritic (CSEF) [105, 106]. It is an advance chromium-molybdenum steel (9CrMoV) used in coal-fired plants for the manufacture of boilers components as already mentioned above and can be operated for temperatures up to about 650°C [107].

**VM12-SHC:** VM12-SHC (with SHC meaning super high corrosion resistant) is a 12Cr–1.6Co–1.5W–B ferritic-martensitic steel developed by Vallourec Group for use in coal boilers and Heat Recovery Steam Generators (HRSG) plants. It is also used to replace the grade X20CrMoV11-1 in existing power plants [108]. It has good creep resistance and steam-side oxidation behavior. It can be used for working temperatures up to 620 °C [109]. VM12-SHC bridges the gap between 12% Cr steels, X20CrMoV12-1 and austenitic steels used in the hot boiler-tube regions for temperatures up to 620 °C. Seamless tubes of VM12-SHC coal boiler are usually normalized and tempered for thin wall components and about 12 mm thick for several applications [110].

**TP347-HFG:** TP347-HFG alloy is an austenitic heat-resistant steel, used in the fabrication of superheater and reheater tubings in advanced coal boilers. It is an 18%Cr–9%Ni–0.7Nb alloy with higher allowable stress and creep rupture strength compared to the grades TP304, TP321H and TP316H [111]. However, according to Chi *et al.*, [111] this steel grade has poor high temperature performance in Ultra-Supercritical Coal Boiler (USCB) power plants. The heat treatment<sup>1</sup> involves solution treated at high temperatures between 1150 – 1200 °C, followed by water quenching to stop the precipitation of new phases during cooling [111]. The material has a finer grain size which affects the material properties (corrosion resistance) during service. This is beneficial for creep resistance during service which is the main reason for alloying the material with niobium unlike its predecessor TP347 H [112, 113].

**DMV304 HCu:** DMV304 HCu is an 18Cr-8Ni austenitic stainless steel alloyed with copper and boron to improve the creep strength. It is produced by adding ~3 wt% of copper, some niobium and nitrogen to the traditional 18Cr-8Ni steel grade (304 steel), and also increasing the carbon content to enhance creep and high temperature properties. Nitrogen also strengthens the solid solution of the material which gives the material higher allowable tensile stresses. Additionally, chromium diffuses to the surface faster to form a dense and adherent chromia (Cr<sub>2</sub>O<sub>3</sub>) scale. The material is best suited for tube applications in the temperature range 600 – 650 °C [114]. It has also been found that the steel grade

---

<sup>1</sup>Heat treatment is the process or the combination of processes which involve heating and cooling a metal or an alloy in its solid state to obtain a desired property or condition. These include; annealing, hardening, quenching, normalizing, patenting, spheroidizing and tempering etc. See Appendix C for a description of the heat treatment methods.

DMV304 HCu has shown coarsening of the Cu-rich phases which occurs in long-term service conditions and therefore could be less protective in the case where the coarsening rate is faster. [114].

**DMV310 N:** DMV310 N is a 25Cr–20Ni austenitic steel alloyed with nitrogen. It has good creep and high temperature corrosion resistance for temperatures between 600 °C to 670 °C [115] compared to the grades 304 and 347. It is suited for use in the most advanced coal-based power plants (Supercritical (SC) and USCB vessels) for steam temperatures up to 620°C. The good high temperature corrosion and creep resistance is attributed to the addition of niobium and nitrogen which gives a solid-solution strengthening from nitrogen as well as the precipitation hardening by fine and stable NbCrN. Nevertheless, DMV310 N is susceptible to form coarse sigma and Cr<sub>2</sub>N phases which could reduce the strength and embrittle the material. This is the reason why the micro-structure is stabilized with nickel, nitrogen and niobium which makes this alloy particularly suitable for boiler superheater materials. [116].

Figure 4.2 shows the micro-structures of the alloys as received. It is generally found that the corrosion resistance of high temperature materials is approximately determined by the amount of free chromium in the alloy as shown by the relation in Equation (4.1) [50, 117, 118]:

$$Cr_{\text{free}} = Cr\% - 14.54C\% \quad (4.1)$$

The free Cr-contents of the selected candidate materials are presented in Figure 4.3. A description of sample preparation and test procedure follows.

#### 4.2.1. Test sample preparation – shape and size

The candidate materials were received as 1m long seamless tubes with varying outer diameters and wall thicknesses, between 4 – 8 mm (Table 4.2) from which 2 sets of 20 mm half cylinders were machined (Figure 4.4) – for isothermal and thermal cycling testing respectively. The sample sizes were designed and machined for easy handling and operation during the exposure tests (weight measurements). Furthermore, they were tested 'as received' without any additional modifications.

### 4.3. Test Procedure

#### 4.3.1. Isothermal oxidation tests

As mentioned previously, discontinuous isothermal oxidation tests according to ISO/TC 1561122 were performed for 1000 h at 650 °C. Figure 4.5 shows the arrangement of



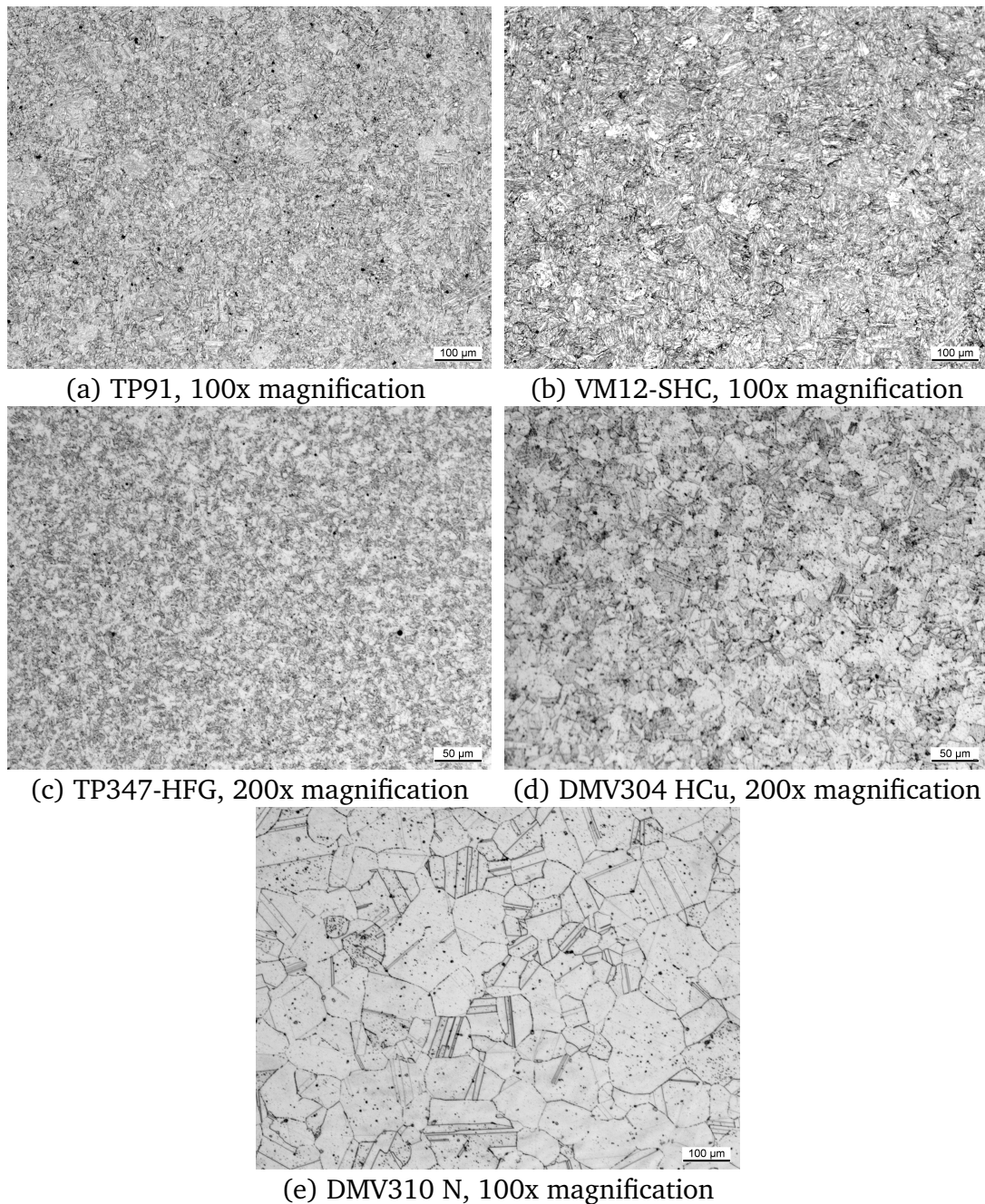


**Figure 4.2.:** Microstructure of selected materials, as received

the experimental setup for the oxidation tests. The experiments were carried out in a horizontal test tube furnace that included a heat resistant mullite ceramic working tube measuring 1200 mm x 75 mm x 86 mm (L x ID x OD). The test samples were placed on a ceramic shell with both ends of the half cylinder partially covered in coal fly ash<sup>2</sup> (Figure 4.6) to simulate the action of deposits on the heat transfer surface in real boilers conditions. The region of the tube furnace with uniform temperature distribution was used for testing. The temperature profile of the tube furnace is shown in Figure 4.7. A type K

<sup>2</sup>Fly ash was obtained from the brown coal (lignite) power plant in Jänschwalde, Peitz burning lignite from the Lusatian (Lausitz) region in Germany. The composition of the fly ash is given in Table 3.2

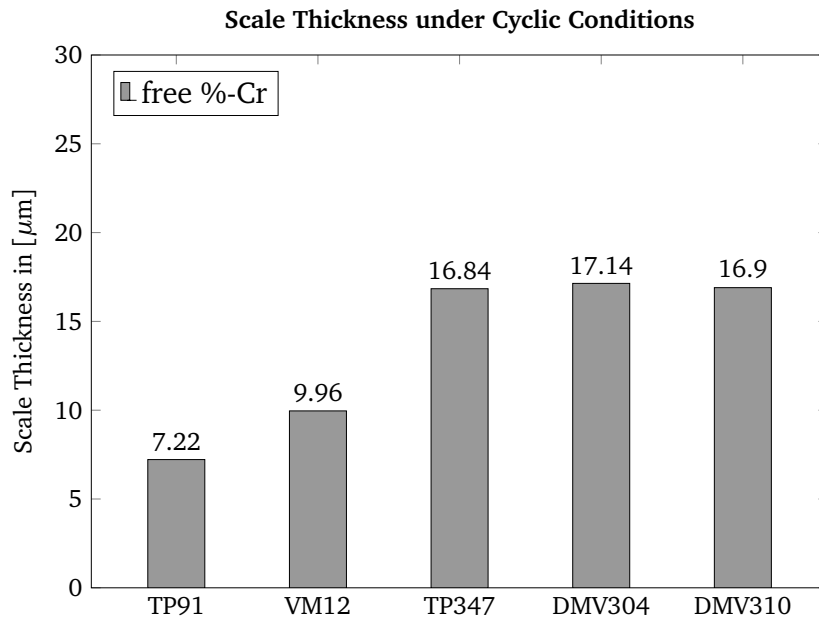


**Figure 4.3.:** Free Cr-content of selected commercial alloys

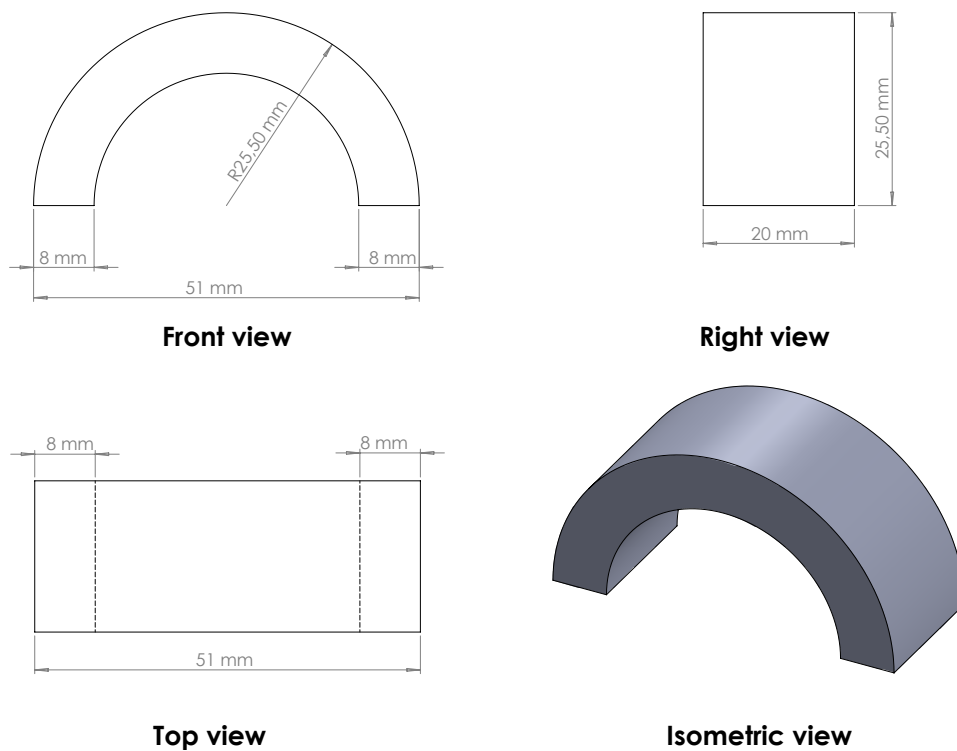


**Figure 4.4.:** Dimensions of half cylinder machined samples used in the exposure tests

thermocouple (NiCr-Ni) was inserted close to the samples within  $\pm 3$  °C in the vicinity of the samples to monitor local temperatures. A synthetic flue gas mixture ( $\text{SO}_2$  at 500 ppmv) preheated to 110 °C was fed through a gas mixing station (GMS600 see Figure B.3) with a mass flow controller (MFC) over the test samples at 1000 mL/min. The composition and

**Table 4.2.:** Selected material types and dimensions

Material	DIN	Mat. Nr.	Type	OD	Wall thickness
				[mm]	[mm]
TP 91	X10CrMoVNb9-1	1.4903	Martensitic	51	4.20
VM12-SHC	X12CrCoWVNb12-2-2	1.4915	Martensitic	50	4.10
TP347-HFG	X8CrNi19-11	1.4908	Austenitic	51	7.10
DMV304HCu	X10CrNiCu Nb 18-9-3	1.4907	Austenitic	51	7.50
DMV310N	X6CrNiNbN 25-20	1.4952	Austenitic	51	8.00

the volumetric flow rates of the gas mixture can be taken from [Table 4.3](#).

**Table 4.3.:** Model flue gas mixture composition

Gas species	Composition	Flow rate
	[vol%]	L/min
CO <sub>2</sub>	14.29	1.429
O <sub>2</sub>	3.34	0.334
N <sub>2</sub>	65.72	7.880
SO <sub>2</sub>	0.05	0.005
H <sub>2</sub> O	16.60	0.352
<b>Sum</b>	<b>100</b>	<b>10</b>

The isothermal oxidation tests were interrupted at regular intervals (every 200 h), the test samples were allowed to cool, carefully cleaned of any ash deposits with a soft brush, their weights recorded and then reinserted back into the furnace with a fresh ash deposit. At the end of each cycle, the materials were visually inspected with the naked eye for any surface change i.e. if the sample is wrinkled, cracked, flaked (spalled), or if there is any corrosion on the edges.

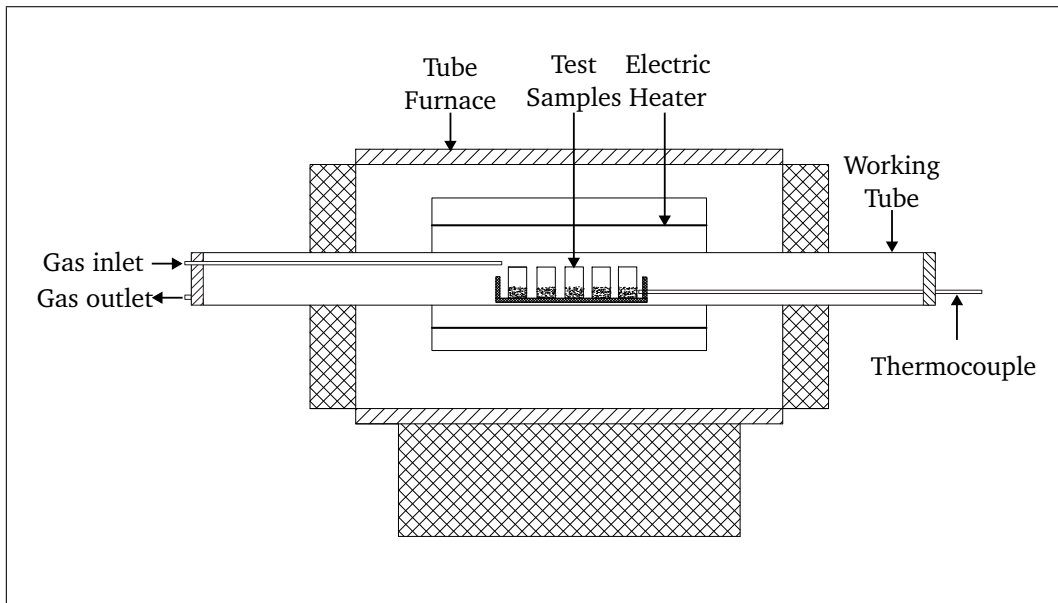


**Figure 4.5.:** Schematic diagram of experimental setup



**Figure 4.6.:** Test specimen arrangement in half ceramic shell

### 4.3.2. Thermal cycling oxidation tests

The thermal cycling tests were equally performed for 1000 h at 650 °C. The experimental setup, flue gas mixture and fly ash used in the isothermal oxidation tests were also used for the thermal cycling tests without any modifications. The total number of cycles was 50 i.e. 20 h per cycle. To reproduce near realistic thermal gradients in boiler settings, each cycle consisted of a heating phase where the test samples were slowly heated at 5 K/min to 300 °C and then holding this temperature for 2 hours. The temperature was then ramped up to the maximum test temperature of 650 °C at a faster heat rate of 20 K/min. This temperature was maintained for 10 h before cooling the samples down to 150 °C in the furnace and the process was repeated. The experiment was stopped at regular intervals (after 5 complete cycles) to measure the weight change of the materials. The cycling

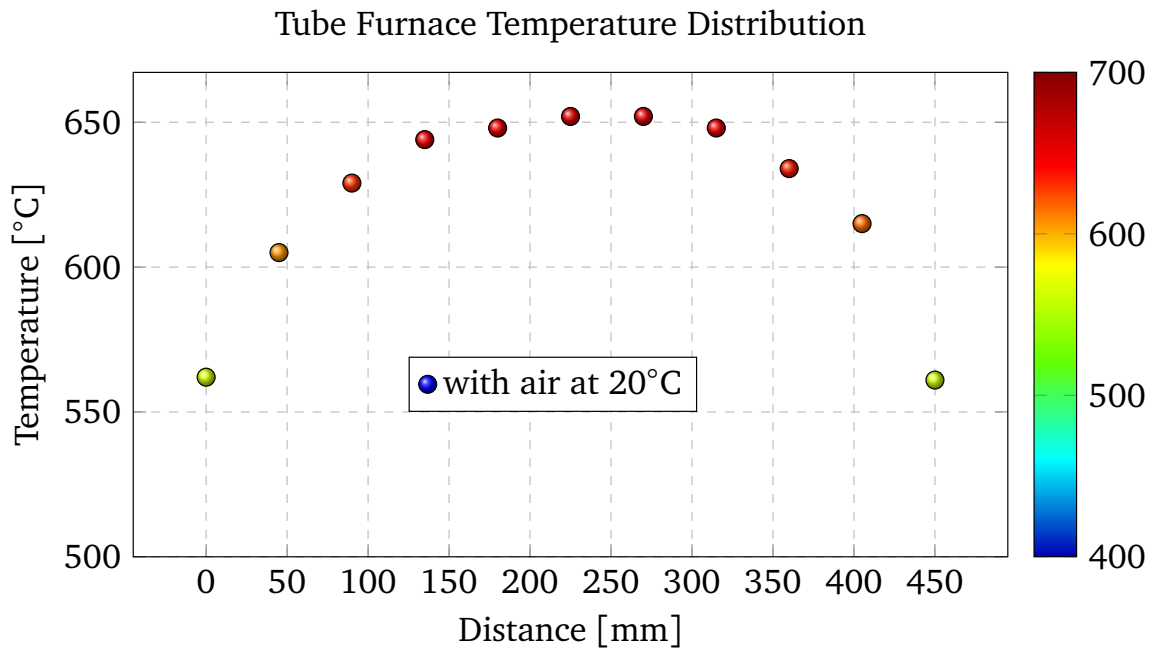


**Figure 4.7.:** Temperature distribution in tube furnace

process was programmed and carried out automatically in the furnace. The temperature profiles for both the isothermal oxidation and thermal cycling test are shown in [Figure 4.8](#).

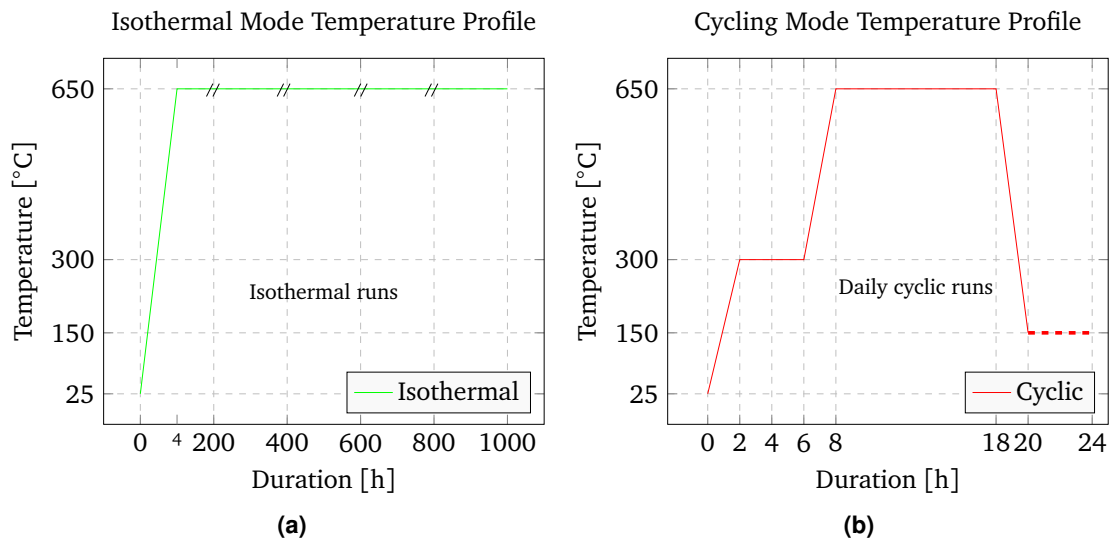


**Figure 4.8.:** Experimental test runs showing (a) isothermal oxidation and (b) thermal cycling

### 4.3.3. Experimental Error

As already mentioned above, the temperature variation in the furnace was in the range  $\pm 3\text{K}$ . Also, the oxidation time or duration was recorded only under steady state opera-

tions of the furnace, this means any periods during unstable conditions (repairs) were not accounted for. The experimental error for the weight change measurements was around  $\pm 0.05\text{mg}$  and the different sizes of the materials were measured with an accuracy of  $\pm 0.02\text{mm}$ . The accuracy of the specific weights calculations was in the range  $\pm 0.5\text{mg} \cdot \text{cm}^{-2}$ . The scale thickness measurement errors were taken to be around  $\pm 2\mu\text{m}$  for the ferritic steels TP91 and VM12-SHC with even oxide scales and approximately  $\pm 0.5\mu\text{m}$  for TP347 HFG, DMV304 HCu and DMV310 N with minor scales. Due to poor adhesion and poor edge retention of epoxy mount on the austenitic alloys this leads to gaps between the materials and the epoxy mounts damaging the scales. It was quite difficult to accurately measure the scale thickness for the austenitic alloys especially TP347-HFG and DMV310 N.

## 4.4. Metallographic Investigation Methods

The analytical techniques used included: light (optical) microscopy (LOM) as a first step to inspect the microstructures of the materials and Scanning Electron Microscopy (SEM) coupled with Energy Dispersed X-Ray Spectroscopy (EDS) was used to obtain the surface morphology and compositional analysis of the products of corrosion. The preparation of the samples for metallographic analysis is given below in (Section 4.4.1).

### 4.4.1. Specimen preparation

**Mounting, sectioning, grinding, and polishing:** After completion of the experiments, the material samples were weighed as usual and immediately placed in a desiccator for subsequent metallographic preparation. The test samples (half cylinders) were then mounted in epoxy resin (EpoFix) for 12 hours. The mounted specimens were then sectioned longitudinally in two halves. They were then ground using different grades of silicon carbide papers (P240-coarse – P4000-fine) with a force of about 20N, then cloth polished in a vibration polisher (VibroMet2) for 24 h. After removal from the polisher, the specimens were immediately cleaned, sprayed with alcohol and followed by drying with warm air to remove any remaining moisture.

**Etching:** To reveal grain structures under the optical microscope, the specimens were etched accordingly.

- *Etchant 1* (used for the ferritic-martensitic steels TP91 and VM12-SHC): 100 ml 4% picral (picric acid) + 5 ml 37% hydrochloric acid (HCl). Etched by swabbing at room temperature for about 10 – 15 seconds. Then rinsed with water and alcohol and dried with hot air.

- *Etchant 2*: used for the austenitic steels (TP347 HFG, DMV304 HCu and DMV310 N): 200 ml distilled water (H<sub>2</sub>O), 200 ml 32% hydrochloric acid (HCl) and 20 ml 65% nitric acid (HNO<sub>3</sub>) heated to about 65°C. Etched by immersion for 60 – 70 seconds and immediately cleaned with water and alcohol and then dried with hot air.

**Conductive coating for SEM:** to minimize distortions and improve image quality the SEM specimens were preferentially sputtered with gold.

#### 4.4.2. Light (optical) microscopy

Light (optical) microscopy (LOM) was used to obtain cross-sectional micro-structures of the commercial alloys before and after exposure to isothermal and cycling conditions. The Carl Zeiss - AxioTech 100 HD of using an Olympus BX60M, with magnifications up to 500X was used.

#### 4.4.3. SEM-EDS microscopy

Scanning Electron Microscopy (SEM) which has much higher magnifications than optical microscopes was used together with Energy Dispersed X-Ray Spectroscopy (EDS) for detailed analysis of the materials to check surface morphology, type of attack and depth of attack (internal oxidation, sulphidation etc.), oxide formation, and chemical composition of corrosion products. An SEM system MIRA II XMH (Tescan, Brno, Czech Republic) combined with an EDS system Inca (Oxford Instruments, Wiesbaden, Germany) was used for the analysis.





# 5. Results

## 5.1. Oxidation growth rate kinetics

### 5.1.1. Weight change measurements

The weight change of the samples after oxidation exposure testing are presented as a function of time. The specific weight change was determined by subtracting the initial weight before oxidation from the weight measured after oxidation and then normalized with the initial surface area of the sample as shown in [Equation \(5.1\)](#).

$$\Delta W_{\text{net}} = \frac{W_f - W_o}{A} \quad (5.1)$$

where:  $\Delta W_{\text{net}}$  is the net weight change in [ $\text{mg} \cdot \text{cm}^{-2}$ ],  $W_f$  and  $W_o$  the final and initial weights in [ $\text{mg}$ ], and  $A$  the area in [ $\text{cm}^2$ ]. [Figures 5.1a](#) and [5.1b](#) show the kinetic data obtained from isothermal and thermal cycling oxidation testing of all candidate alloys after 1000  $h$  of exposure at 650 °C. A comparative evaluation of the individual alloys under both test conditions is illustrated in [Figures 5.2a](#) and [5.2e](#).

The net weight change data revealed positive weight gains after 1000  $h$  of exposure at 650 °C for all candidate alloys, under both isothermal and cycling modes. However, the weight gain during thermal cycling oxidation exposure was significantly higher than under isothermal oxidation conditions, especially for the martensitic steels TP91 and VM12-SHC. The austenitic alloys showed no significant increase in weight from isothermal to thermo-cyclic oxidation. The austenitic alloys TP347-HFG and DMV310 N showed the least weight gain under both isothermal as well as thermo-cyclic oxidation while DMV304 HCu was the only austenitic alloy with substantial weight gain under both test conditions. As can be seen from [Figures 5.2c](#) to [5.2e](#), the austenitic steels showed a slight decrease in weight change after about 400  $h$  especially DMV310 N. From visual inspection light spallation (flaking) was found on both the martensitic and austenitic materials during thermo-cycling testing. The excessive weight gain of the martensitic steels during thermal cycling indicate the adverse effect on these materials.

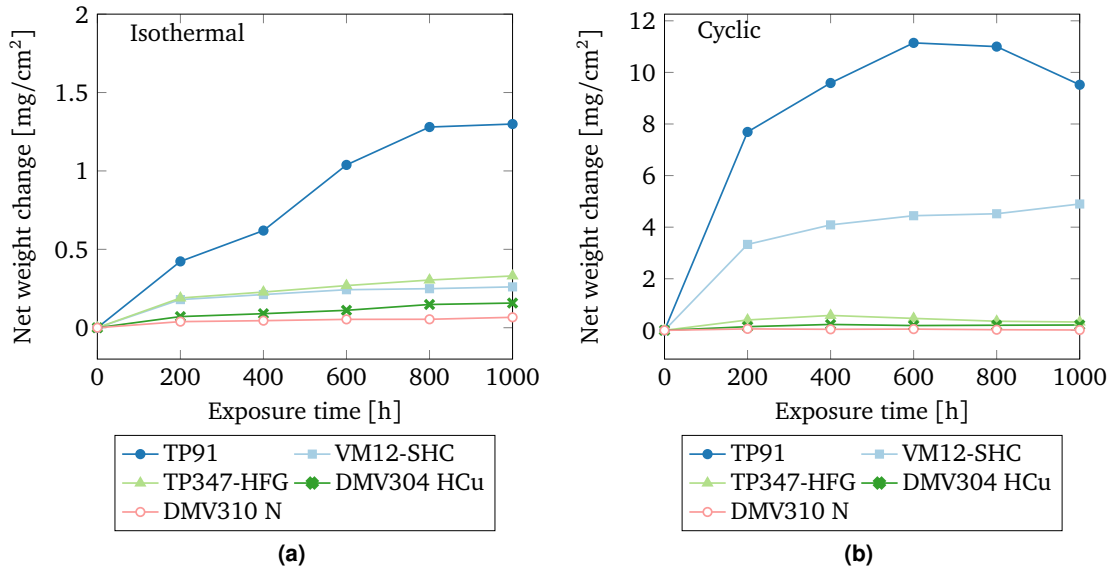


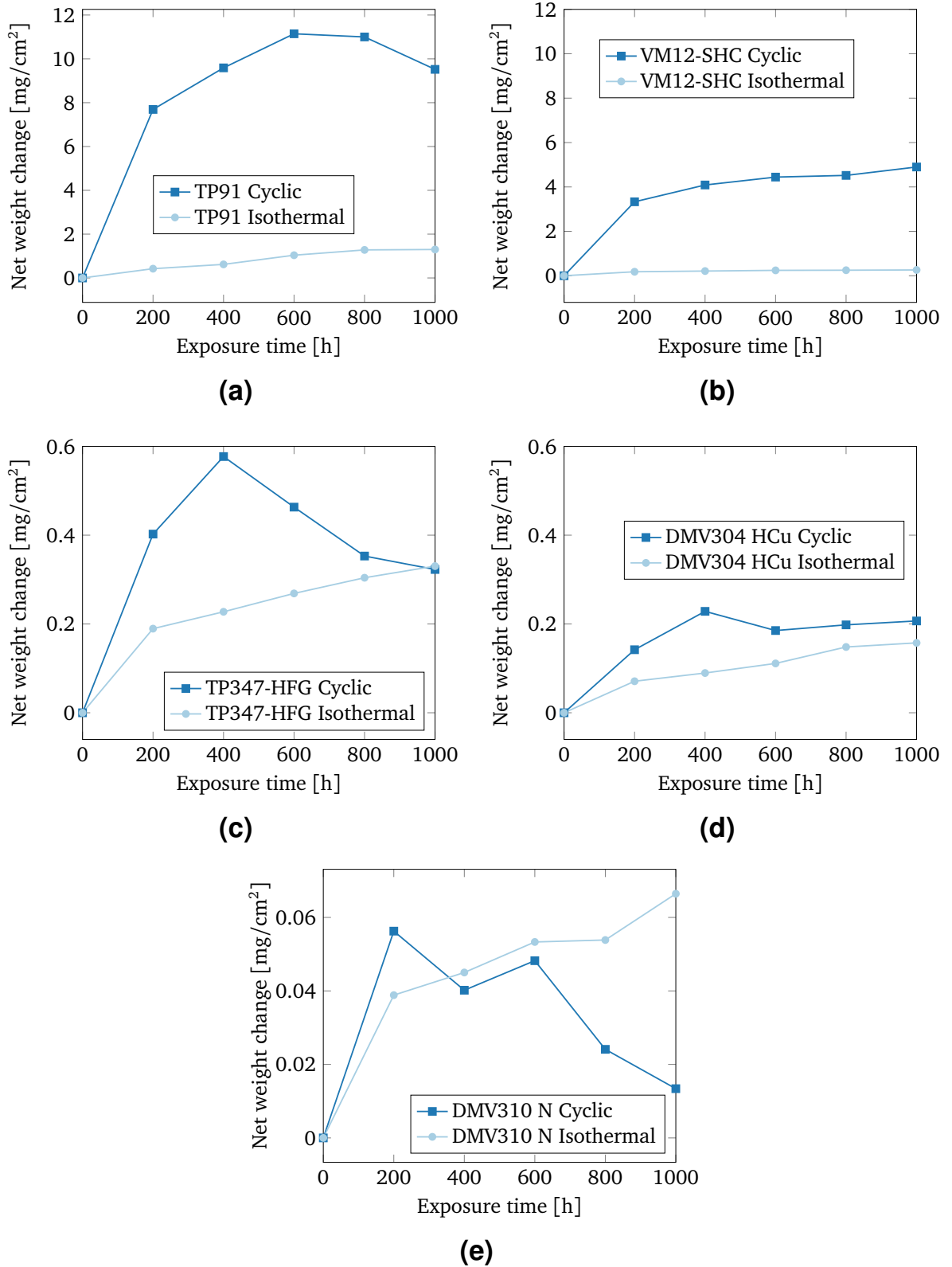
**Figure 5.1.:** Net weight change after 1000 h of exposure at 650 °C under (a) isothermal conditions and (b) thermal cycling conditions

### 5.1.2. Parabolic rate kinetics

The alloys followed parabolic rate kinetics after 1000 h of exposure under isothermal and cyclic conditions. The parabolic rate constants,  $k_p$  in  $[\text{mg}^2 \cdot \text{cm}^{-4} \cdot \text{s}^{-1}]$  were calculated using the relation given in Equation (5.2) and the results are presented in Table 5.1.

$$\left(\frac{\Delta W}{A_s}\right)^2 = k_p \cdot t \quad (5.2)$$

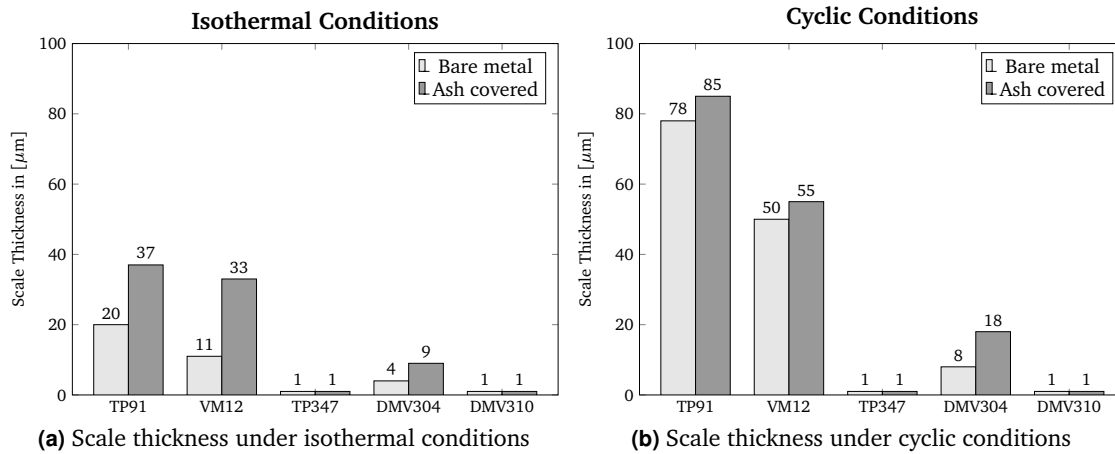
where  $\Delta W$  is the weight change in [mg],  $A_s$  the surface area of the sample in  $[\text{cm}^2]$  and  $t$  the time in [s]. As discussed in Section 2.3.3.4, the low  $k_p$  values for the austenitic steels especially DMV310 under both isothermal oxidation and cyclic oxidation conditions indicate good oxidation resistance. Conversely, the high  $k_p$  values for the ferritic-martensitic alloys, especially TP91 signify poor protection against oxidation especially under thermo-cyclic conditions for these materials. The scale thickness measurements are given in Figure 5.3.



**Figure 5.2.:** Comparison of net wet change of alloys under isothermal and cyclic oxidation

**Table 5.1.:** Parabolic rate constants, ( $k_p$ ) after 1000  $h$  exposure

Material	$(k_p)$ [ $\text{mg}^2\text{cm}^4\text{s}^{-1}$ ]	
	Isothermal	Cyclic
TP91	$4.69 \cdot 10^{-7}$	$2.52 \cdot 10^{-5}$
VM12-SHC	$1.89 \cdot 10^{-8}$	$6.67 \cdot 10^{-6}$
TP 347 HFG	$3.03 \cdot 10^{-8}$	$2.89 \cdot 10^{-8}$
DMV 304 HCu	$6.88 \cdot 10^{-9}$	$1.19 \cdot 10^{-8}$
DMV 310 N	$1.23 \cdot 10^{-9}$	$4.99 \cdot 10^{-11}$

**Figure 5.3.:** Scale thickness measurements isothermal and thermal cycling

## 5.2. Kinetic modeling

Kinetic modeling was performed in **COSP** and fitted to the experimental results. **COSP** (i.e. Cyclic Oxidation Spalling Program) is a windows based software package used to model cyclic oxidation weight gain and spallation. The input parameters include: selecting an oxidation growth model or law (logarithmic, parabolic, etc.) and a spalling geometry, the oxide involved, the growth rate, the spall constant, the cycle frequency and exposure time parameters. The output of the model includes: weight change results, the total amount of metal consumed and oxygen uptake, the retained and spalled oxide amounts and much more. Detailed explanation of the software package can be found in [88, 119].

**Model development:** For modeling, the hematite ( $\text{Fe}_2\text{O}_3$ ) oxide layer with a stoichiometric constant of 3.3270 was assumed to form. The parabolic growth law was selected and the parabolic rate constants obtained from the experiments were implemented in the model and adjusted where necessary. Furthermore, a uniform growth or oxide thickness was assumed with no spallation under isothermal conditions (i.e. a spall constant of zero,  $Q_0 = 0$ ) and varying spall constants under cyclic conditions. The results from modeling for both the isothermal and cyclic case fitted with the experimental results are given in Figures 5.4 and 5.6. The total oxygen uptake, metal consumed and weight of retained oxide were also calculated and are presented in Figures 5.5 and 5.7. The experimental results show good fitting with the **COSP** model, showing a positive weight gain for all candidate materials under isothermal and cyclic conditions. The ferritic-martensitic materials showed a particular good fit with the model while the austenitic materials showed small deviations from the model probably due to minimal weight gain in these materials.

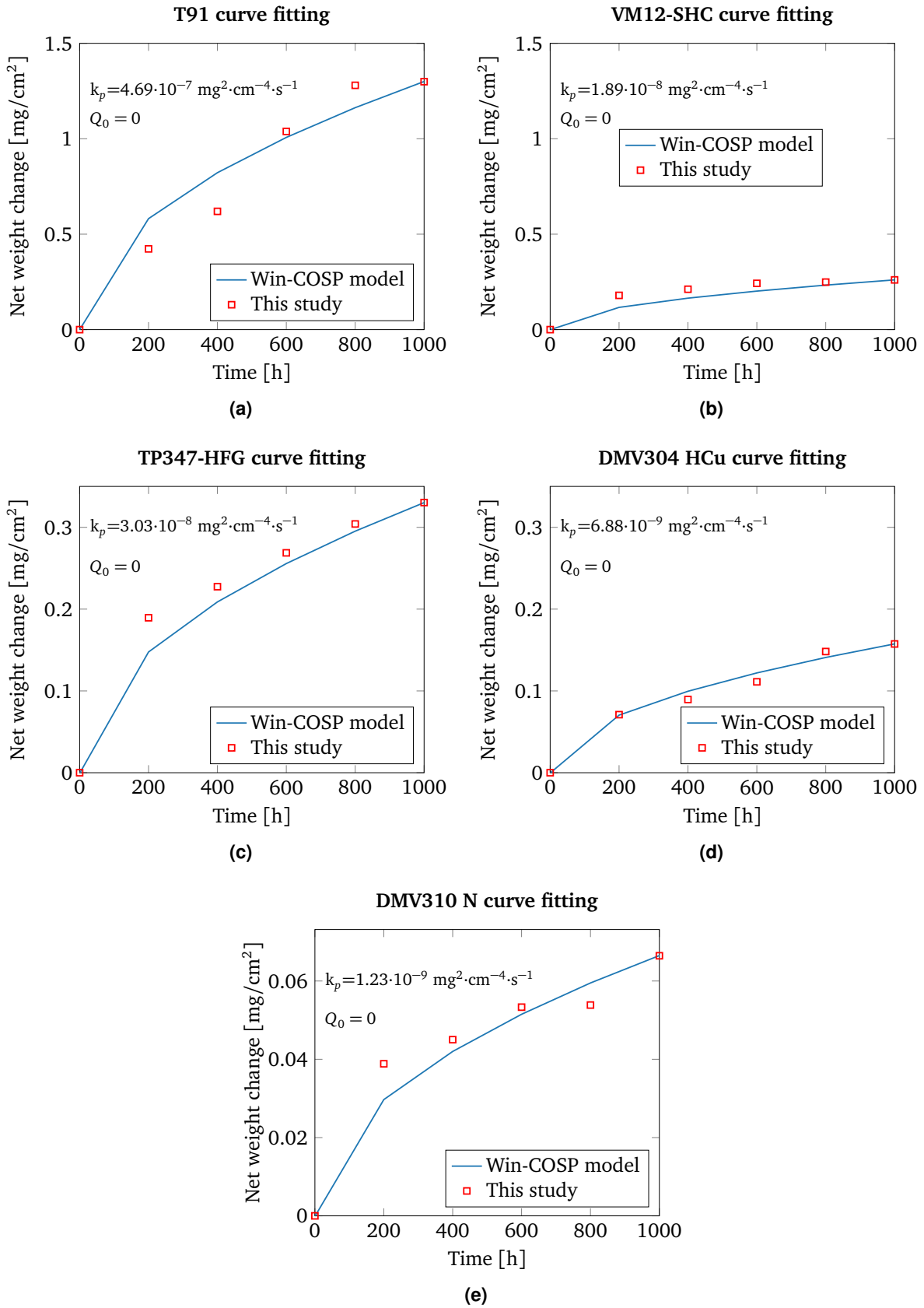


**Figure 5.4.:** Net wet change predicted in WinCOSP and experimental results, isothermal oxidation

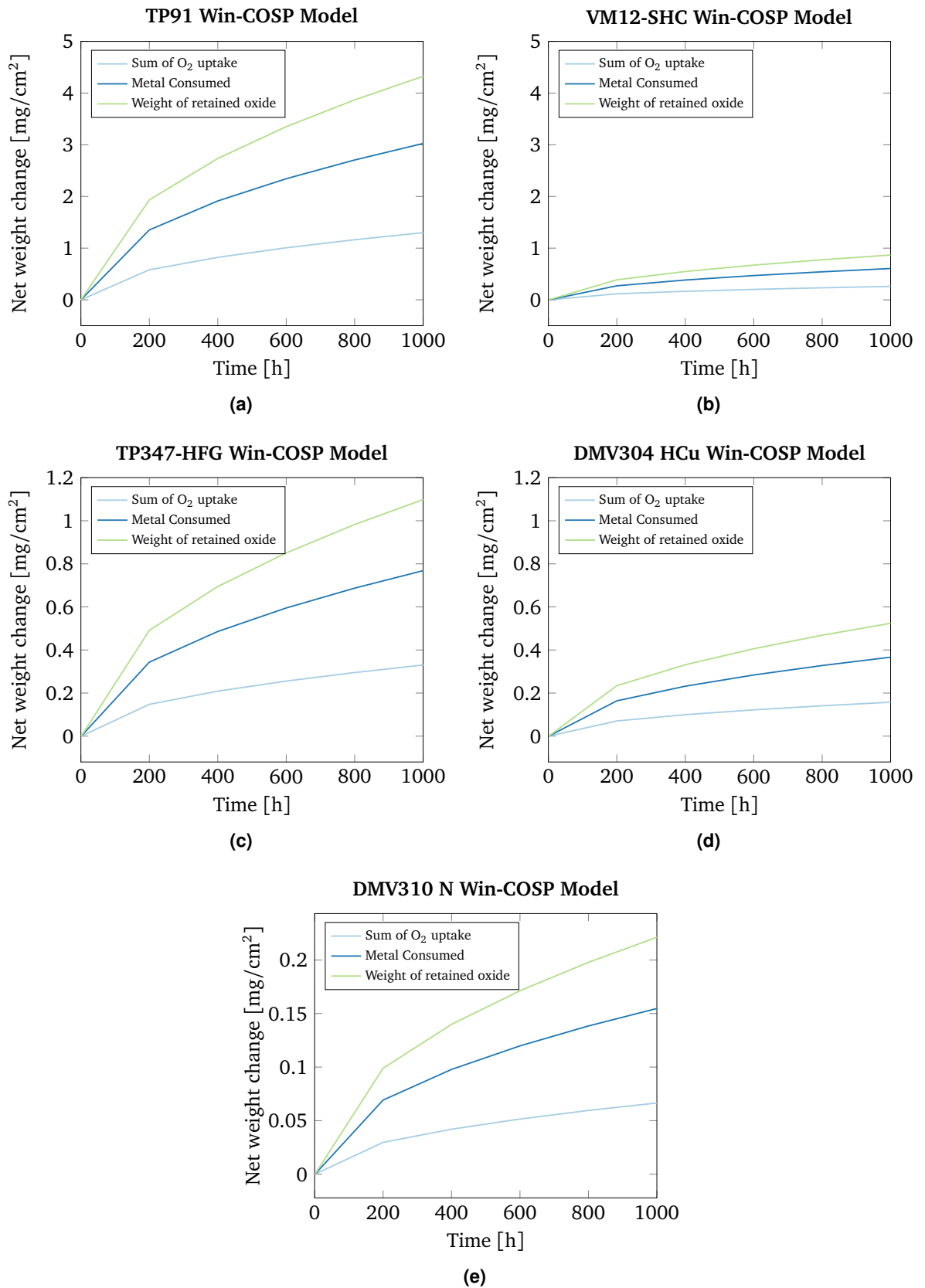


**Figure 5.5.:** Total oxygen uptake, metal consumed and weight of retained oxide, isothermal oxidation

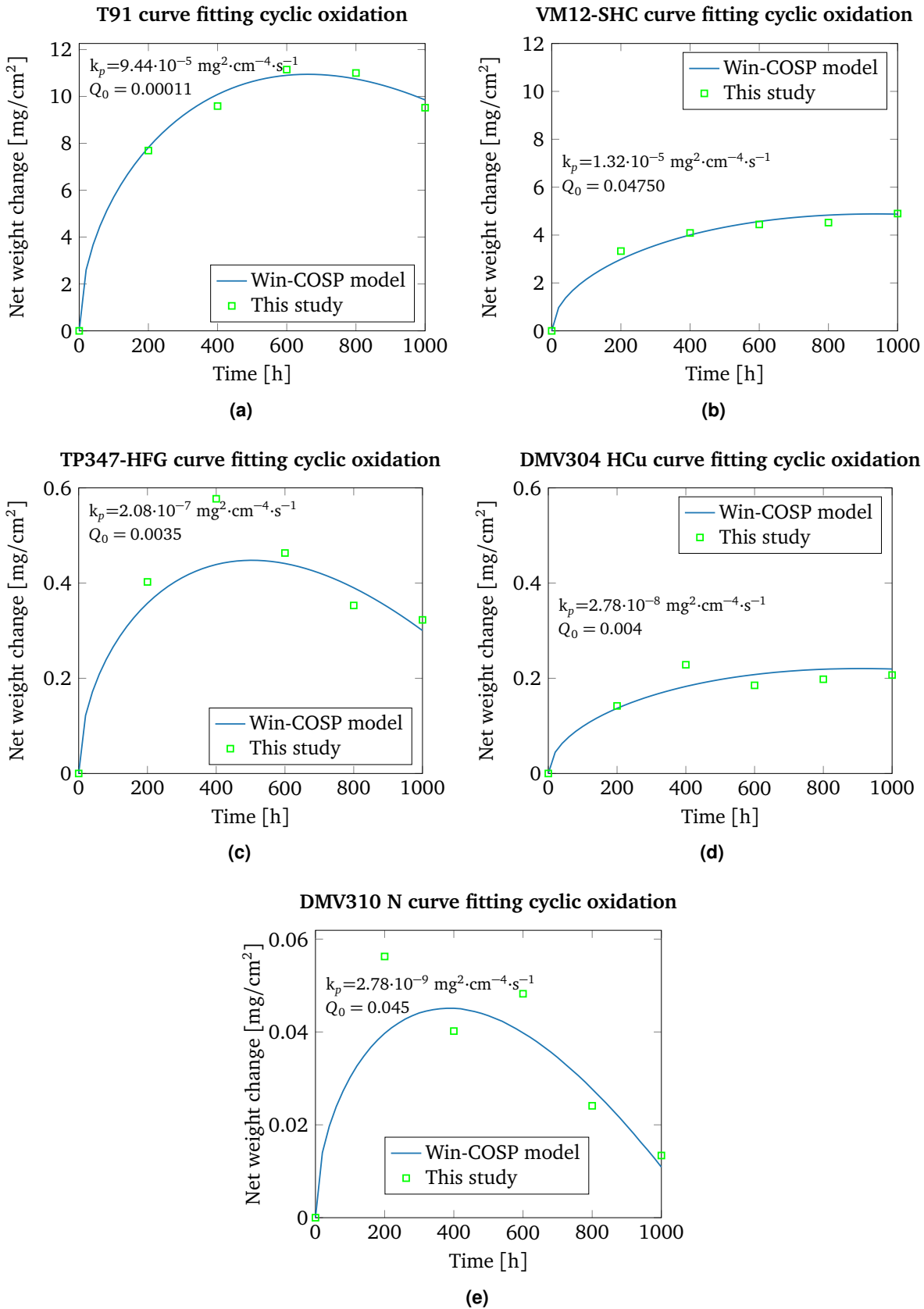
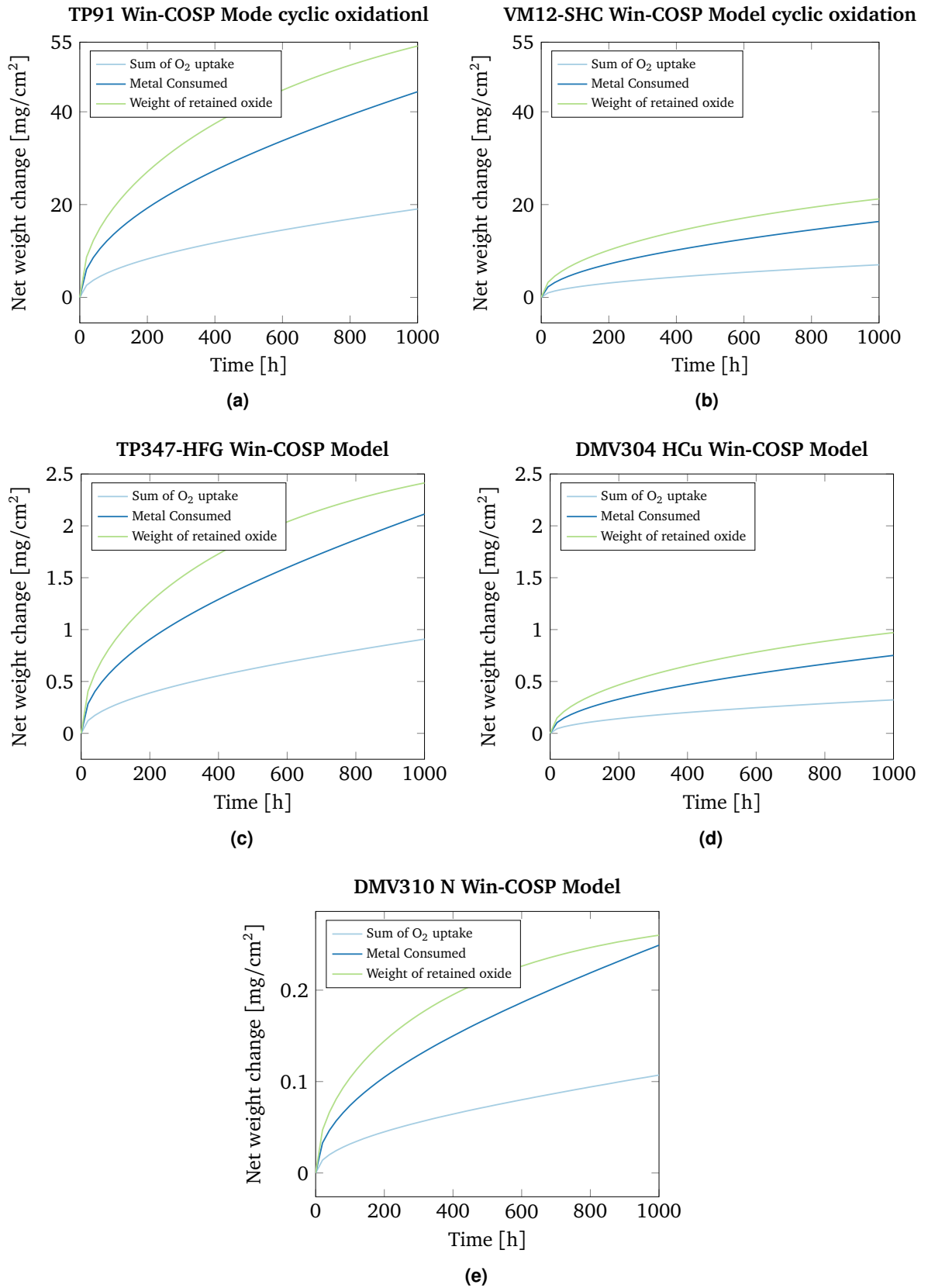


Figure 5.6.: Net wet change predicted in WinCOSP and experimental results, cyclic oxidation





**Figure 5.7.:** Total oxygen uptake, metal consumed and weight of retained oxide, isothermal oxidation

### 5.3. Isothermal oxidation after 1000 h

The results from metallographic analysis (LOM and SEM-EDS) of the exposed materials after 1000 h of exposure at 650 °C under isothermal oxidation conditions are presented in the section. As mentioned in Section 4.3, the test samples were partly covered with ash to allow an estimation of the influence of coal ash on the materials oxidation behavior by drawing a comparison between the bare metal (BM) and the ash covered (AC) regions as will be discussed here.

#### 5.3.1. Light (optical) microscopic analysis

The LOM images, at low magnifications (200x), of all exposed alloys under isothermal conditions for both ash covered section (AC) and bare metal (BM), are shown in Figures 5.8 to 5.12. The micrographs show that the corrosion rate (scale growth) was uniform for the ferritic-martensitic steels TP91 and VM12-SHC (Figures 5.8 and 5.9). The austenitic materials showed minimal scale growth, especially TP347 HFG and DMV310 N (see Figures 5.10 and 5.12). The tainted areas in DMV310 N (Figure 5.12 a) are results of staining from the etchant during preparation and not a product of oxidation or corrosion. Oxide scale growth on DMV304 HCu was inconsistent and uneven as only selected locations of the sample were oxidized, some more than the others. This effect is even more pronounced in the section of the material covered with ash (AC) as can be depicted from Figure 5.11.

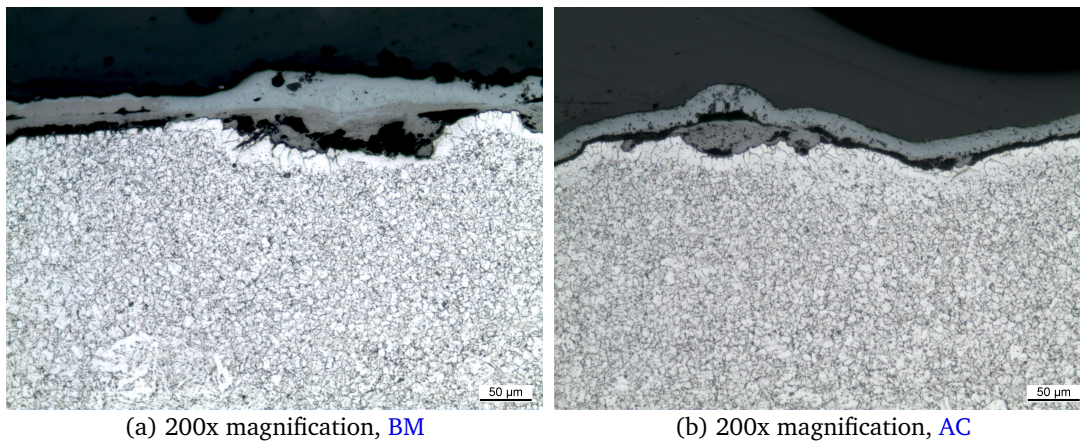


**Figure 5.8.:** Light optical micrographs of TP91 (isothermal oxidation)

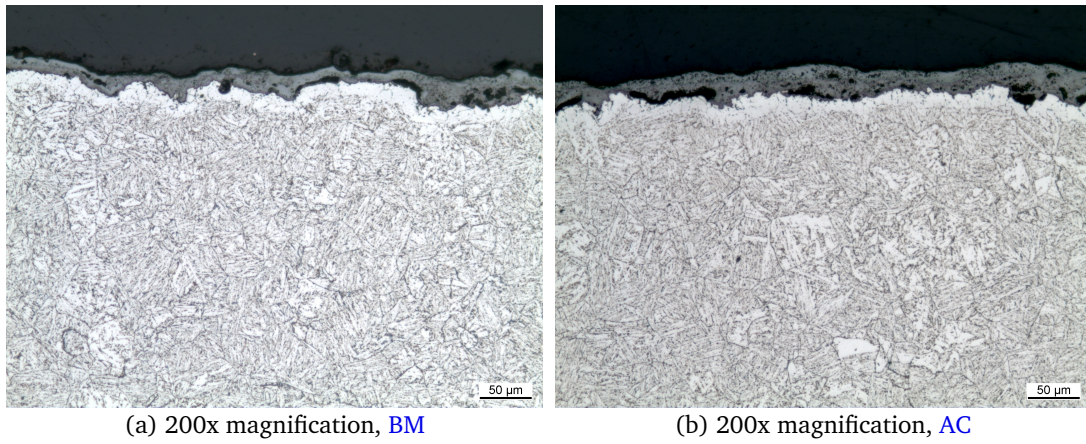


**Figure 5.9.:** Light optical micrographs of VM12 (isothermal oxidation)

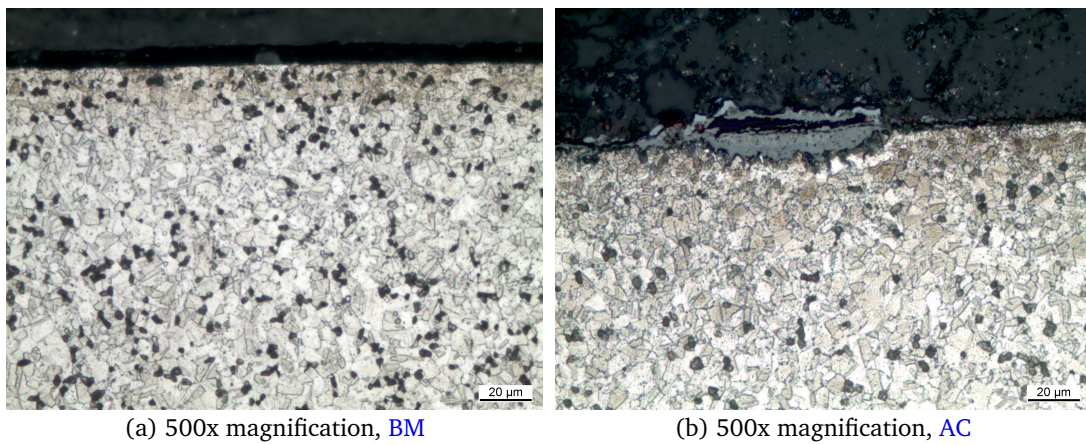


**Figure 5.10.:** Light optical micrographs of TP347-HFG (isothermal oxidation)

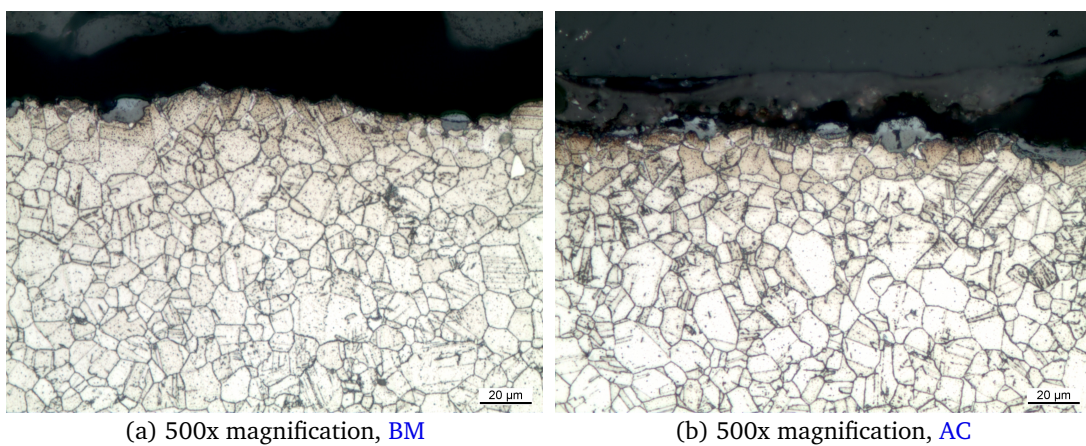


**Figure 5.11.:** Light optical micrographs of DMV304 HCu (isothermal oxidation)

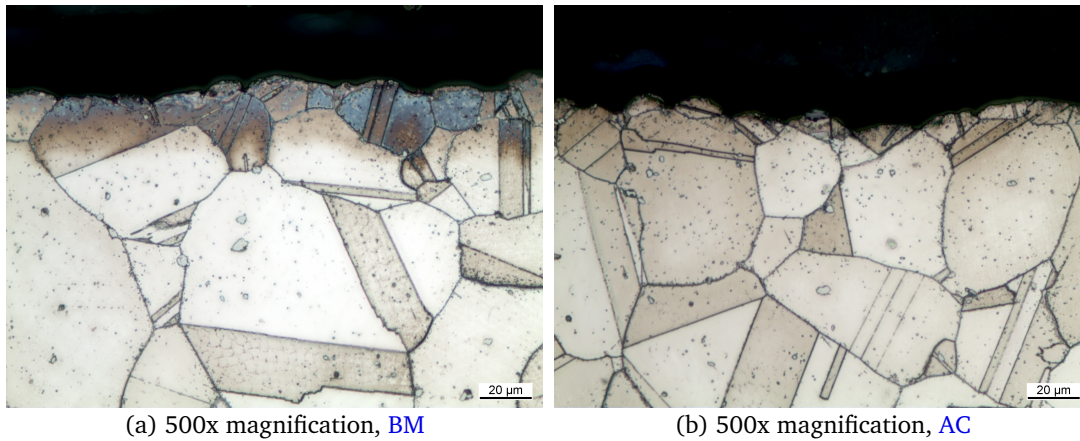


**Figure 5.12.:** Light optical micrographs of DMV310 N (isothermal oxidation)

### 5.3.2. Micro-structural (SEM–EDS) analysis of isothermal oxidation

#### 5.3.2.1. Isothermal oxidation of TP91

Figure 5.13 shows the SEM cross-section micrographs and EDS linescans of TP91 for the ash covered (AC) and bare metal (BM). TP91 was severely oxidized with the formation of spongy, porous and poorly adhesive oxide scales. The average scale thickness<sup>1</sup> measured at several points on the sample were approximately  $20\mu m$  for the bare metal section and  $37\mu m$  for the ash covered section (Figure 5.3a). The oxide scales were duplex in nature (Figure 5.14) with two distinctive layers: an outer (epitactic) and an inner (topotactic) oxide layer on both the bare metal and the ash covered sections of the sample. This is typical and was expected for the ferritic-martensitic steels. From the EDS line scans (Figure 5.13b and d), it can be estimated that the layers consist of alternating Fe-rich and Cr-rich oxides. The elemental distribution is given in Figures 5.15a and 5.15b.

On the bare alloy section (Figure 5.14a), EDS compositional analysis revealed that Fe and O contents in the outer epitactic oxide layer (about  $14\mu m$  thick) were around 40 and 60 at% respectively. Following from Table 5.2 this corresponds approximately to hematite ( $Fe_2O_3$ ) formation which was the most dominant oxide formed. The inner oxide layer (about  $9\mu m$  thick) with decreasing Fe content (between 27 – 29 at%) and increasing Cr-content of about 24 – 25 at% indicate the possibility of a magnetite layer together with the spinel  $FeCr_2O_4$ . This is common and was expected for oxide scales formed on the ferritic-martensitic steel – with an oxygen rich hematite layer forming outwards, an intermediate magnetite layer and an iron rich (wustite) oxide layer forming close to the base material. From the elemental mappings shown in Figure 5.15a it can also be depicted that the innermost layer consists of a manganese oxide and also a thin chromium oxide

<sup>1</sup>Note: The scale thickness measurement given here is an average obtained from various measurement points from the whole sample.

scale close to the metal. The base metal was depleted of chromium. This is confirmed not only by the mappings but also by the EDS linescans given in Figure 5.13b.

at%	$\text{Fe}_2\text{O}_3$	$\text{Fe}_3\text{O}_4$	$\text{Cr}_2\text{O}_3$	Spinel $\text{FeCr}_2\text{O}_4$	$\text{Fe}_3\text{O}_4 \cdot \text{FeCr}_2\text{O}_4$	$\text{FeO} \cdot \text{FeCr}_2\text{O}_4$	$2\text{Fe}_3\text{O}_4 \cdot \text{FeCr}_2\text{O}_4$
Fe	40	43	0	14	29	22	10
Cr	0	0	40	29	14	22	34
O	60	57	60	57	57	56	57

**Table 5.2.:** Possible phases formed in an oxide scale, [120]

For the ash covered section of the sample (Figure 5.14b), a distinctively unique layer (with about 34  $\mu\text{m}$  maximum thickness) was formed outwards. The epitactic outer layer has an oxygen content of about 60 at% and an Fe-content of about 40 at% which signifies a possible hematite scale. The inner layer is characterized by alternating Fe-rich and Cr-rich oxides as can be seen from the line scans. It was estimated that this layer could possibly be made up of a magnetite and  $\text{FeCr}_2\text{O}_4$  spinel. The elemental mappings (Figure 5.15b) show a thin chromium oxide layer adjacent to the metal (metal/oxide interface). Manganese oxide can also be depicted in the inner lower layer. The base material was depleted of both chromium and manganese. Some traces of molybdenum oxide are also found in the lower layer. Furthermore, a brittle ash layer with cracks was found in this section (AC) separating the two oxide scales at various points of the sample as can be seen on the phase mappings given in Figure 5.14. Such a porous layer facilitates the outward diffusion of iron leading to higher rates of oxidation. No inward diffusion of sulphur was noticed in the material. It is also important to note that the ash deposits on the alloy TP91 were quite sticky and difficult to remove from the surface during soft brushing after only 100 hours of the experiment.

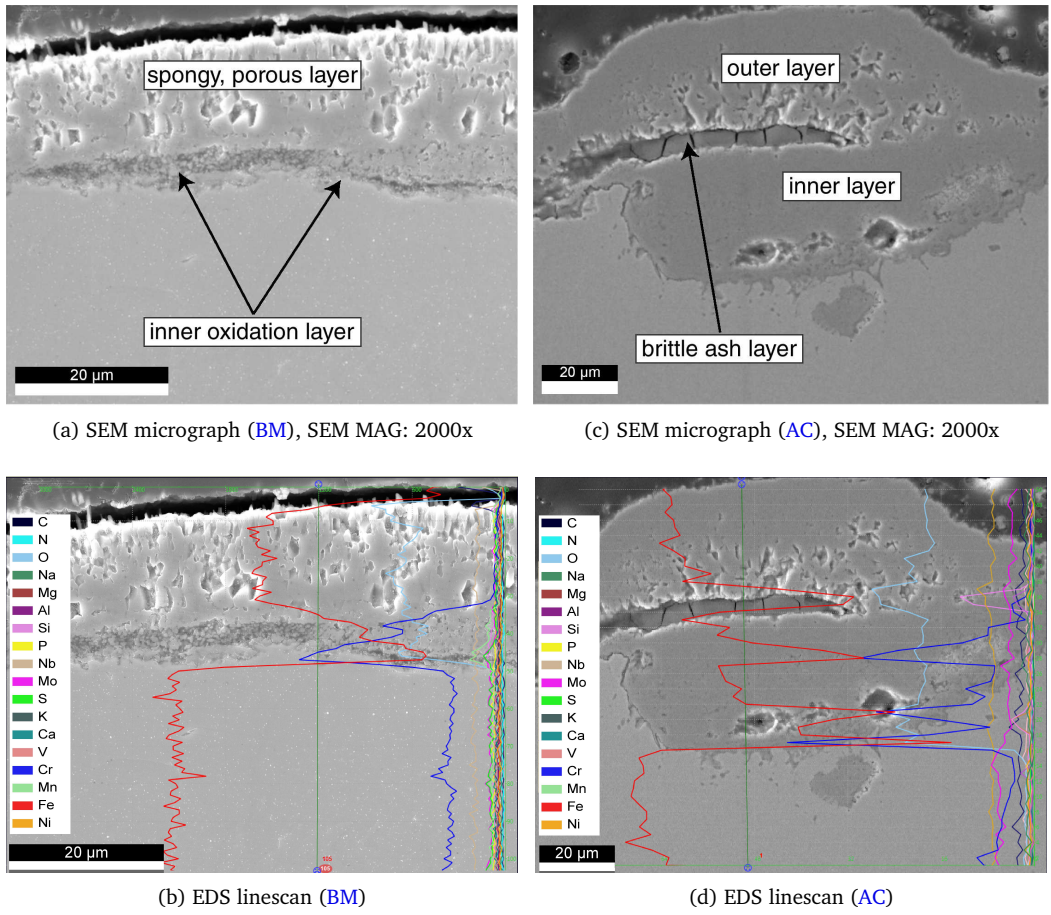


**Figure 5.13.:** SEM micrographs with EDS linescans of TP91 after 1000 h at 650 °C, isothermal conditions

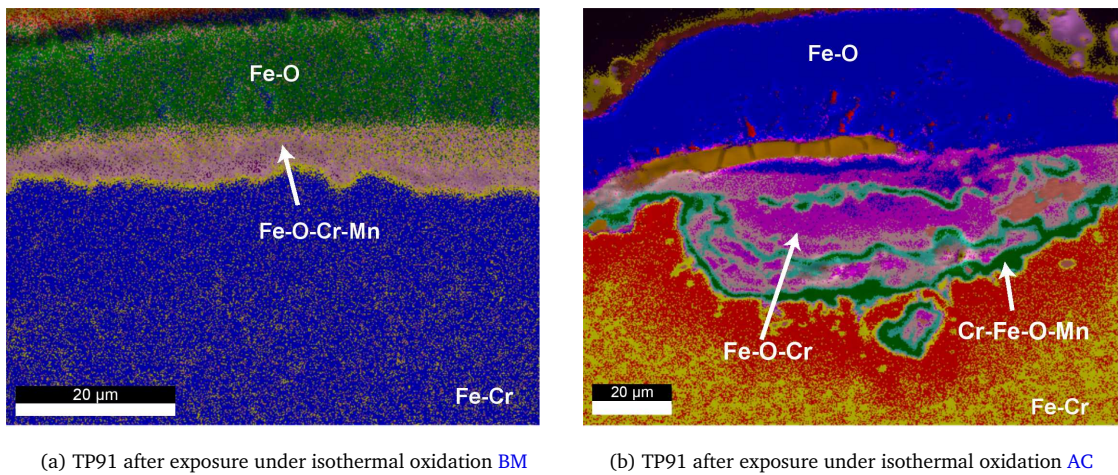
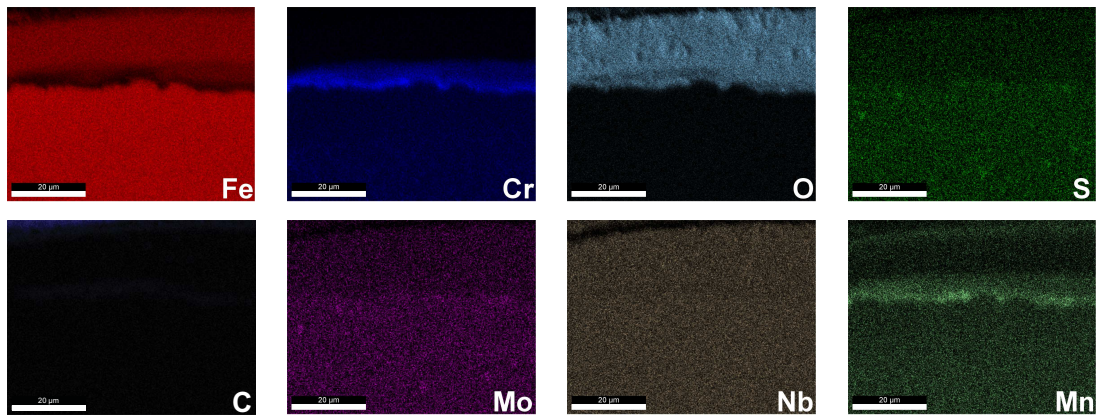
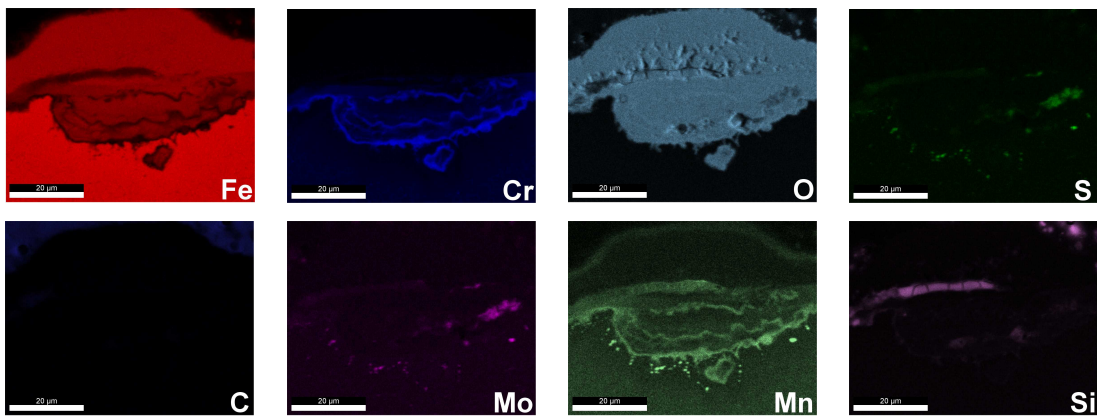


**Figure 5.14.:** Phase mapping of TP91 after 1000 h at 650 °C under isothermal conditions



(a) Element mapping of TP91 after 1000 h at 650 °C under isothermal conditions (BM)



(b) Element mapping of TP91 after 1000 h at 650 °C under isothermal conditions (AC)

**Figure 5.15.:** Element mapping of TP91 after 1000 h at 650 °C under isothermal conditions

### 5.3.2.2. Isothermal oxidation of VM12-SHC

The SEM cross-sectional micrographs and EDS linescans of the ferritic–martensitic alloy VM12-SHC are presented in Figure 5.16. The oxide scale formed on the sample was also sample was porous and poorly adhesive similar to the case of the ferritic steel TP91. The scale was characterized by several layers; an outermost oxide layer, an intermediate and a thin innermost layer. The average scale thickness according to measurements at different points on the entire sample gave an average of  $11\mu\text{m}$  for the bare metal section (BM) and approximately  $33\mu\text{m}$  for the ash covered section (AC), see (Figure 5.3a). From the EDS line scans (Figure 5.16 b and d), it becomes obvious that the layers are composed of alternating Fe-rich and Cr-rich oxide layers similar to TP91.

The bare metal section of the sample (Figure 5.17a) revealed an outermost oxide layer (maximum thickness of  $14\mu\text{m}$  and minimum of  $3\mu\text{m}$ ) with about 40 at% Fe and 60 at% O which according to Table 5.2 suggests the possibility of a hematite oxide layer. The inner

oxide layer showed slightly reduced oxygen amount ( $\sim 54$  at%) and an Fe and Cr content of 28 at% and 18 at% respectively indicate a magnetite and Fe-Cr spinel layer, too. The innermost oxide layer with an increased Cr content indicates possible chromia ( $\text{Cr}_2\text{O}_3$ ) formation at the metal/oxide interface and the base material was depleted of chromium. This layer contains small amounts of Mn and Fe as available from the elemental distribution mappings given in Figures 5.18a and 5.18b. Some traces of a molybdenum sulphide can be seen at the oxide/metal interface.

The ash covered section of the test sample (see Figure 5.17b) portrayed oxide layers similar in structure to the bare metal section. The outer epitaxial layer – with a scale thickness of about  $11 \mu\text{m}$ , was found to have roughly 60 at% O and 40 at% Fe layer suggesting a hematite ( $\text{Fe}_2\text{O}_3$ ). The inner topotaxial layer was found to consist of Fe-O-Cr compound which can be estimated to be a combination of magnetite and  $\text{FeCr}_2\text{O}_4$  spinel. The innermost layer was rich in Cr and consisted of Cr-O-Fe-Mn which suggest a possible chromia scale with an oxide of manganese. Again the base material was depleted of chromium. This is confirmed by the elemental mappings shown in Figure 5.18b, too. There was an increase in silicon in the inner oxide layer as can be seen from the elemental mappings. Similarly, like in the bare metal section, the elemental mapping revealed some traces (in very small amounts) of molybdenum sulphide at the oxide–alloy interface.



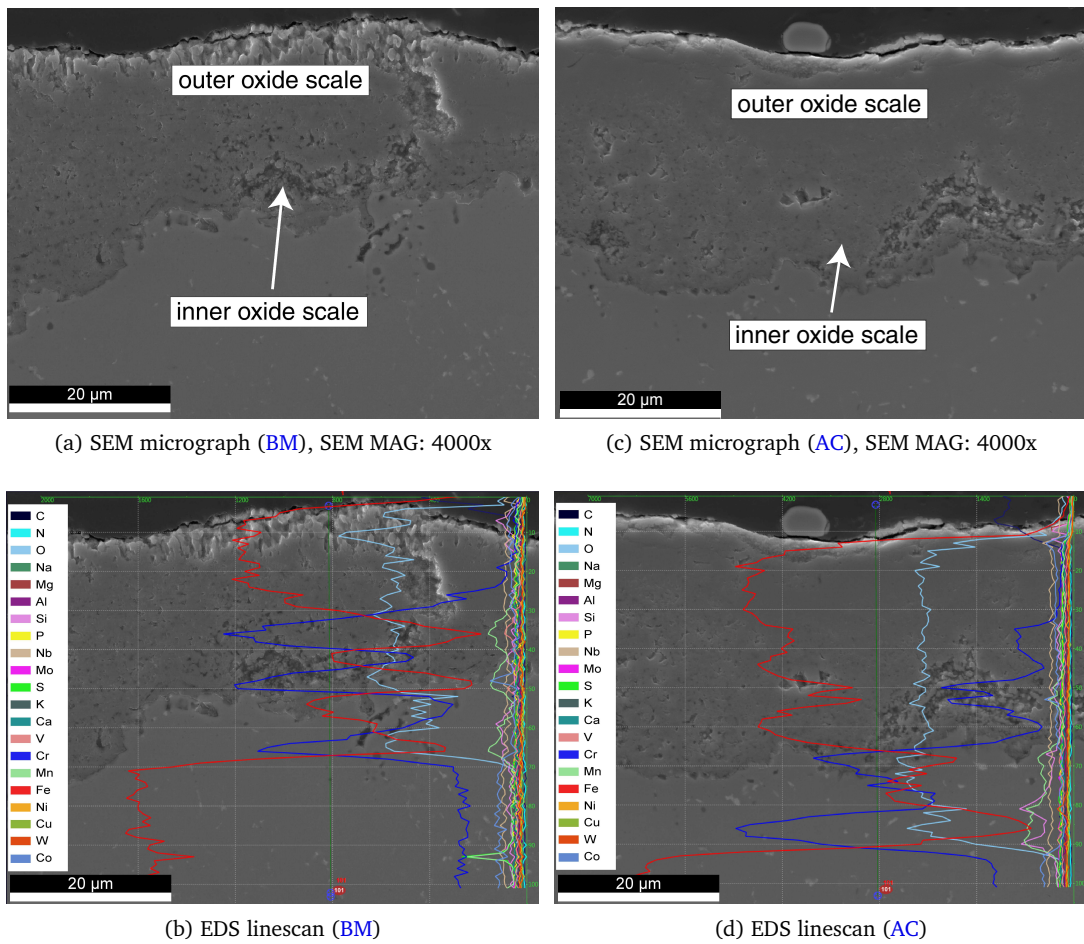


**Figure 5.16.:** SEM micrographs with EDS linescans of VM12-SHC after 1000 h at 650 °C, isothermal conditions

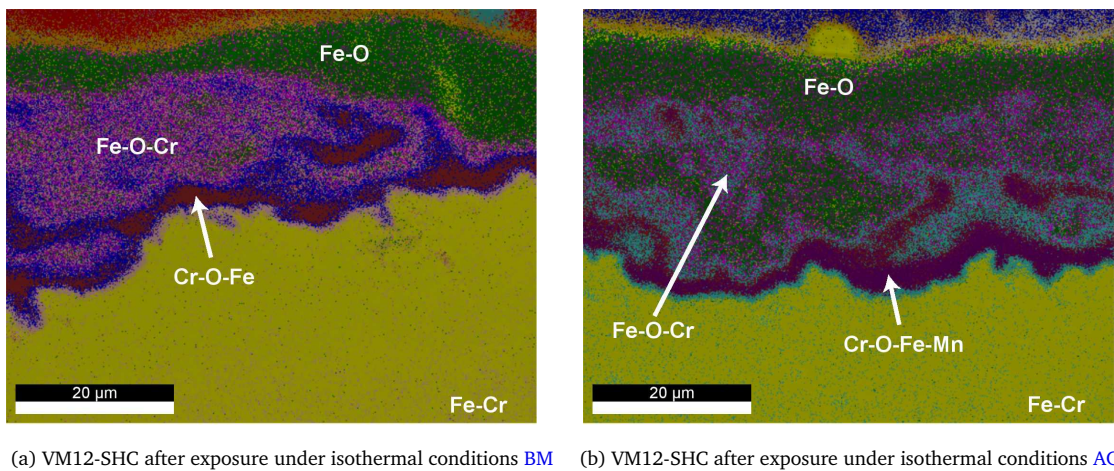
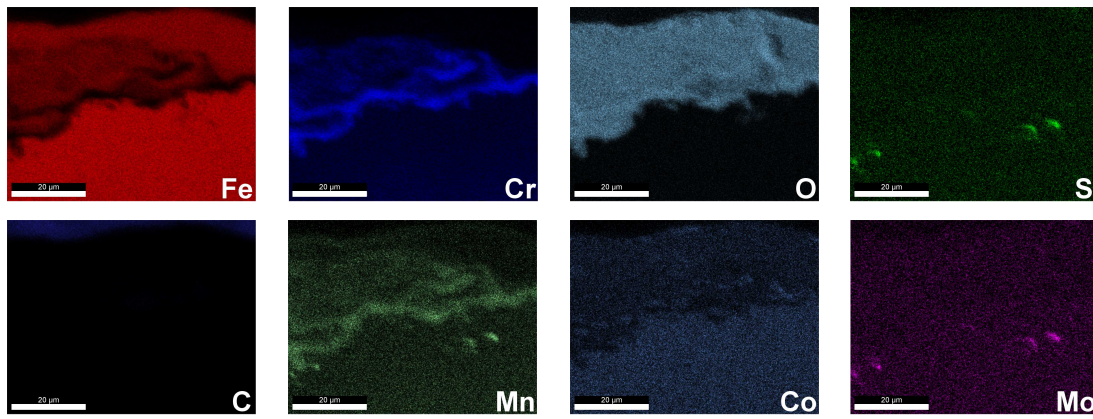
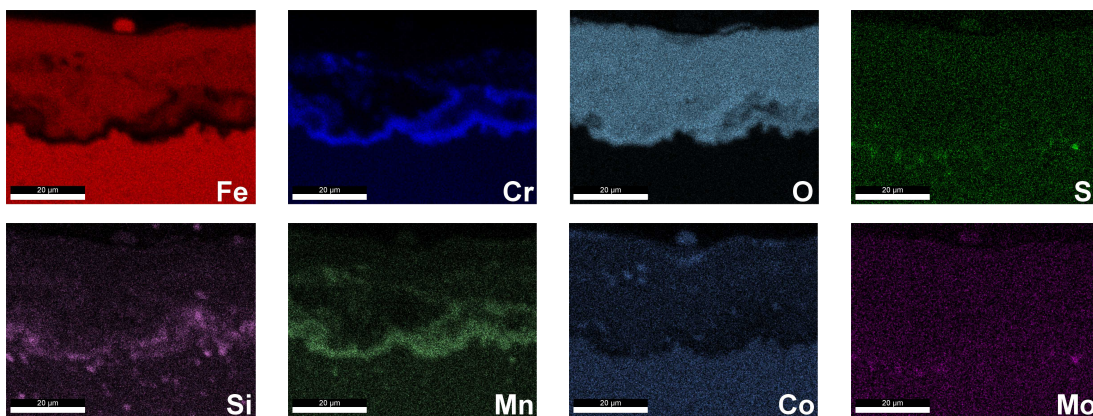


**Figure 5.17.:** Phase mapping of VM12-SHC after 1000 h at 650 °C under isothermal conditions



(a) Element mapping VM12-SHC after 1000 h at 650 °C under isothermal conditions (BM)



(b) Element mapping of VM12-SHC after 1000 h at 650 °C under isothermal conditions (AC)

**Figure 5.18.:** Element mapping of VM12-SHC after 1000 h at 650 °C under isothermal conditions

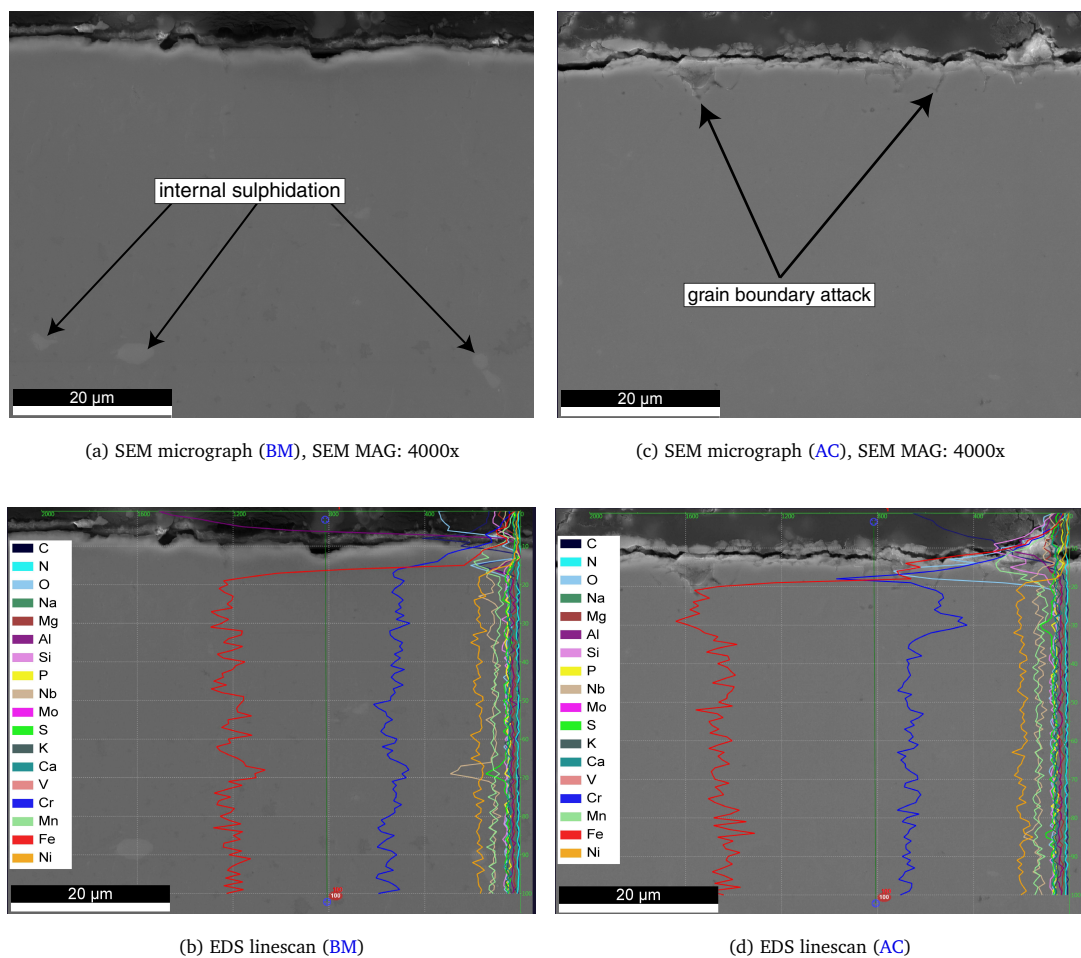
### 5.3.2.3. Isothermal oxidation of TP347-HFG

Figure 5.19 shows the cross-sectional SEM micrographs and EDS linescans of the oxide scale developed on the austenitic alloy TP347 HFG after 1000 h at 650 °C under isothermal conditions. Firstly, as mentioned in Section 4.3.3, it is worth noting that the oxides formed on the austenitic steels were partially damaged during metallographic preparation due to poor adhesion and poor edge retention of epoxy mount causing wide gaps and consequently erroneous scale thickness measurements and hindering accurate determination of the phase compositions. Nevertheless, the alloy TP347-HFG showed good corrosion resistance on both the bare metal and ash covered section. Average scale thickness on the entire sample was approximately 1 – 2 microns.

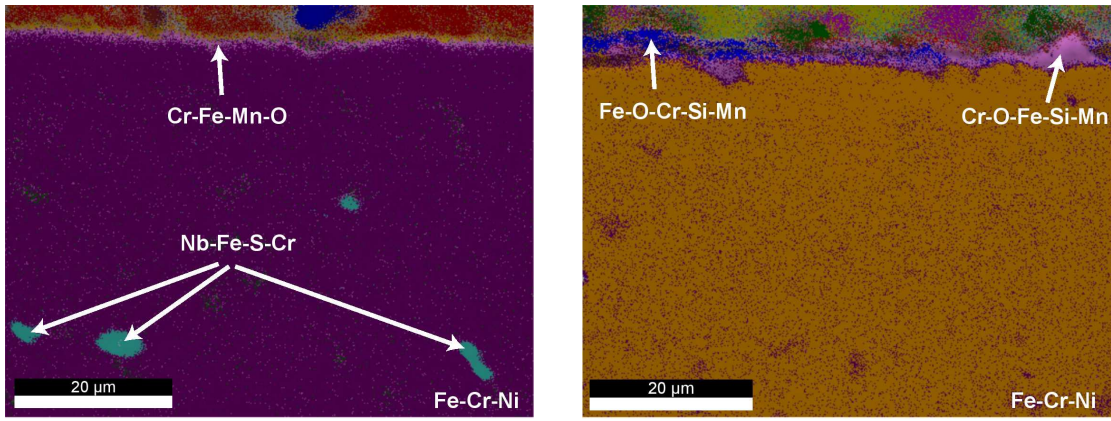
The very thin oxide scale ( $\sim 1\mu m$ ) formed on the bare metal section (Figure 5.20a) was made up of Cr-Fe-Mn-O with very low oxygen contents (in the range 22 – 24 at%) with high

chromium content of about 48 at% and low Fe and Mn contents. The elemental mappings (Figure 5.21a) reveal that the base material was almost depleted of Cr. This indicates the possibility of a protective chromia scale formation. Most importantly, there was significant internal sulphidation (with a penetration depth ranging from 22 – 38  $\mu\text{m}$ ) found on the bare metal section. The phase mapping image (Figure 5.20a) indicates the formation of Nb, Fe and Cr sulphides in the base metal, confirmed by the elemental mapping too. Some manganese enrichment towards the surface of the metal suggest the formation of a manganese oxide.

The ash covered section with an average oxide thickness of about 2 microns revealed a much more oxygen rich layer of more than 60 at% with correspondingly low Fe and Cr contents (14 and 20 at% respectively). This indicates the formation of magnetite together with Fe-Cr spinel ( $\text{FeCr}_2\text{O}_4$ ). However, grain boundary attack was found on the ash covered section. The elemental distributions are given in Figures 5.21a and 5.21b. Similar to the bare metal alloy section manganese was found to be present in the oxide layer which probably means that a manganese oxide was also formed, too.

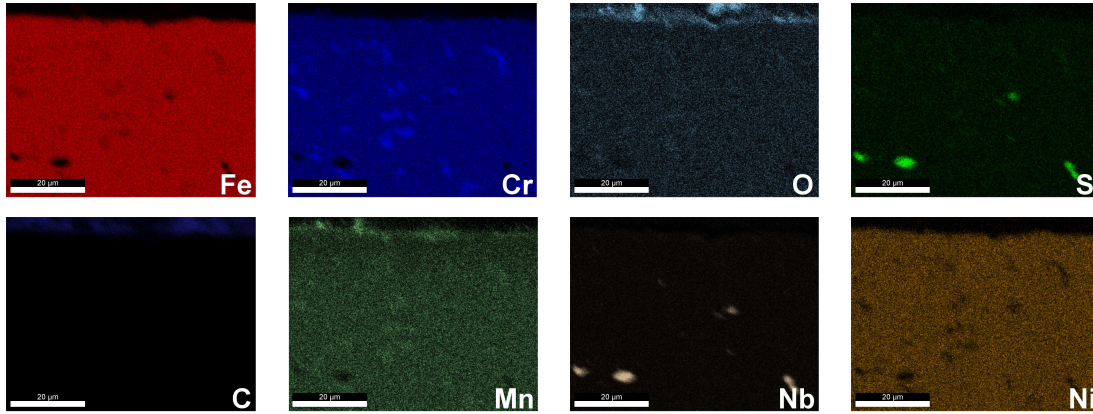


**Figure 5.19.:** SEM micrographs with EDS linescans of TP347-HFG after 1000 h at 650 °C, isothermal oxidation

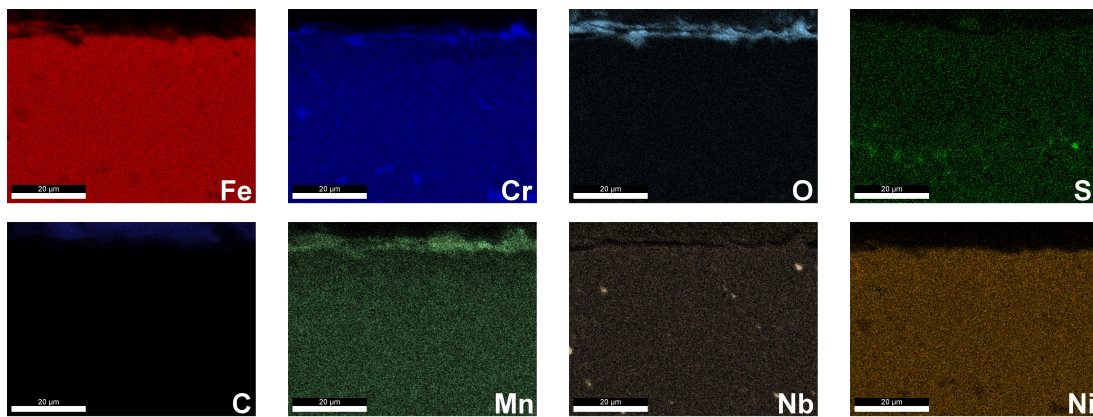


(a) TP347-HFG after exposure under isothermal conditions **BM** (b) TP347-HFG after exposure under isothermal conditions **AC**

**Figure 5.20.:** Phase mapping of TP347-HFG after 1000 h at 650 °C under isothermal conditions



(a) Element mapping of TP347-HFG after 1000 h at 650 °C under isothermal conditions (**BM**)



(b) Element mapping of TP347-HFG after 1000 h at 650 °C under isothermal conditions (**AC**)

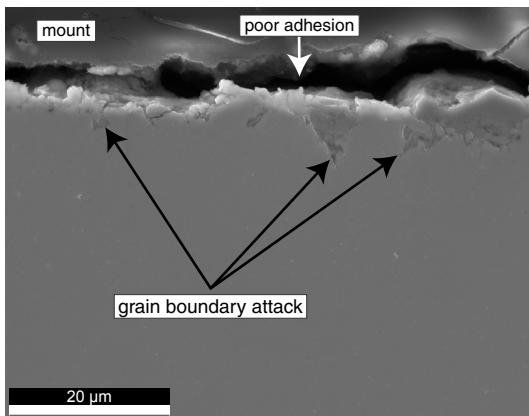
**Figure 5.21.:** Element mapping TP347-HFG after 1000 h at 650 °C under isothermal conditions

#### 5.3.2.4. Isothermal oxidation of DMV304 HCu

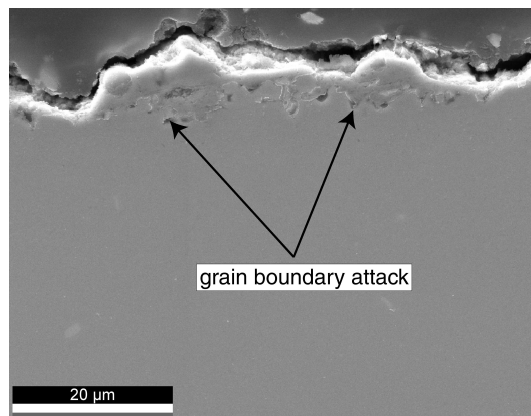
The SEM cross-section images of the surface morphologies and EDS linescans of the austenitic alloy DMV304 HCu are given in Figure 5.22 and the phase mappings in Figure 5.23, respectively. As already highlighted in Section 5.3.1 the oxide layer formed on the entire metal was uneven with corrosion appearing stronger in some areas than others. The average scale thickness on the entire sample was measured to be around 4  $\mu\text{m}$  in the bare metal section and 9  $\mu\text{m}$  in the ash covered section, cf. Figure 5.3a. The oxide layer was partly destroyed during preparation due to poor adhesion of epoxy mount which could affect measurements and compositional analysis.

The oxides formed on the bare metal section measured between 8 – 10  $\mu\text{m}$  on the surface of the material as can be seen in Figure 5.23a. From EDS compositional analysis of the different phases, the partially damaged oxide layer consisted of more than 60 at% O and 38 at% Fe which probably implies a hematite scale was formed. The sub-surface grain boundary attack layer (with an average depth of 9 microns) was caused by the oxides of Cr, Fe and Mn, with oxygen contents of about 47at% and iron and chromium contents of roughly 23 at% and 30 at% respectively, while Mn was negligibly less than 1 at%. The elemental mappings of the bare alloy section are given in Figure 5.24a. No inward diffusion of sulphur was noticed here.

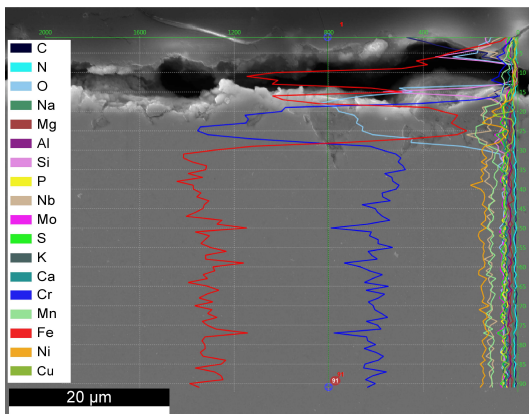
On the ash covered section with also partially damaged oxide layers, some form of localized oxidation of certain areas was found. Oxide layer measurements revealed between 8 – 12  $\mu\text{m}$  together with some grain boundary attack. Similar to the scale on the bare metal section, the ash covered region showed a duplex oxidation layer: an outer iron rich and an inner chromium rich layer. The surface oxide layer indicated the formation of hematite (40 at% Fe and 60 at% O). The inner layer revealed 30 at% Fe, 17 at% Cr and 53% O and some small amounts of Mn. Worth noting internal diffusion of sulphur into the base material (Figure 5.24b) takes place. The elemental mappings revealed the possibility of Mo and Nb sulphide formation.



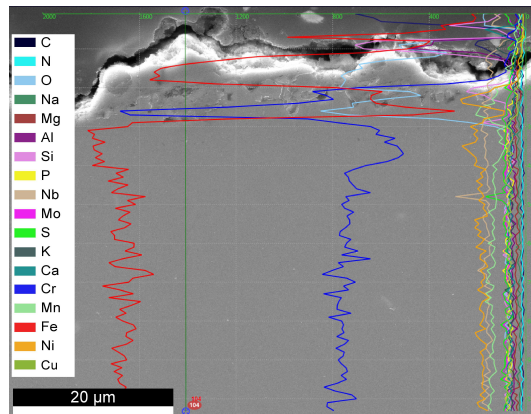
(a) SEM micrograph (BM), SEM MAG: 4000x



(c) SEM micrograph (AC), SEM MAG: 4000x

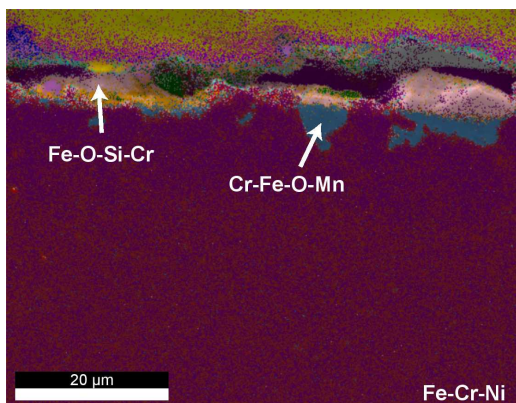


(b) EDS linescans (BM)

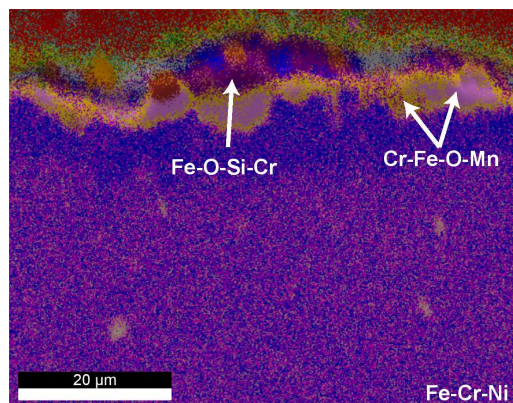


(d) EDS linescans (AC)

**Figure 5.22.:** SEM micrographs with EDS linescans of DMV304 HCu after 1000 h at 650 °C, isothermal conditions

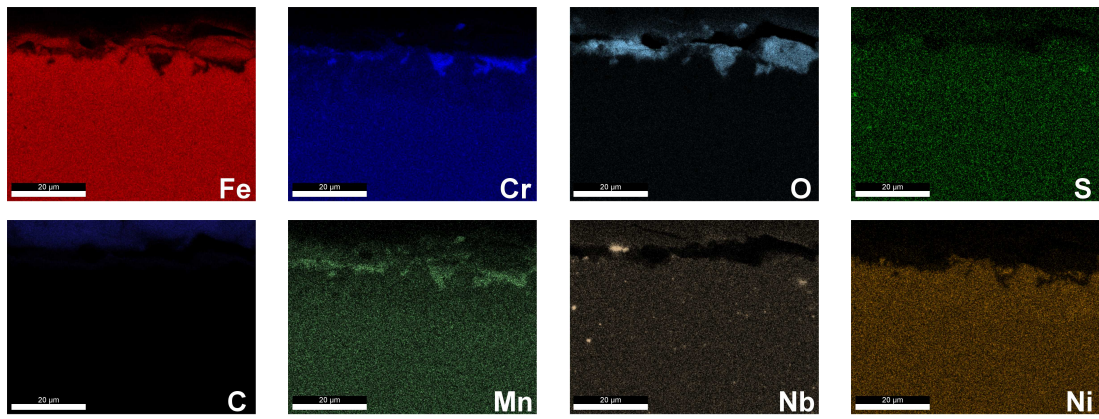


(a) DMV304 HCu after exposure under isothermal conditions BM

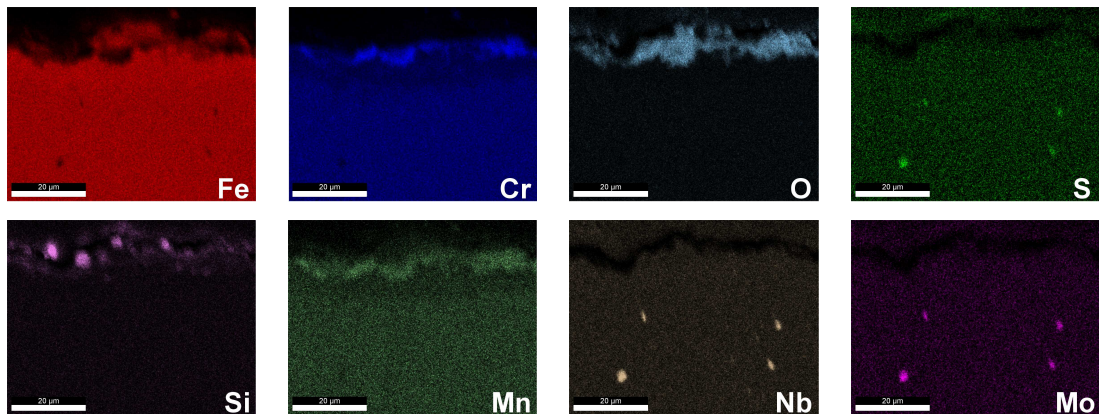


(b) DMV304 HCu after exposure under isothermal conditions AC

**Figure 5.23.:** Phase mapping of DMV304 HCu after 1000 h at 650 °C, isothermal conditions



(a) Element mapping DMV304 HCu after 1000 h at 650 °C, isothermal oxidation, [BM](#)



(b) Element mapping of DMV304 HCu after 1000 h at 650 °C, isothermal conditions, [AC](#)

**Figure 5.24.:** Element mapping of DMV304 HCu after 1000 h at 650 °C, isothermal oxidation

### 5.3.2.5. Isothermal oxidation of DMV310 N

The austenitic alloy DMV310 N has the best oxidation performance under isothermal conditions after 1000 h of exposure at 650 °C. As can be depicted from the [SEM](#) cross-sectional micrographs and [EDS](#) linescans shown in [Figure 5.25](#), oxidation was at its minimum with less than 1  $\mu\text{m}$  oxide scale thickness. However, as already stated, the scales formed on the austenitic alloys were damaged and therefore difficult to measure accurately measuring. This was particularly the case for the ash covered section as no trace of oxide was found, therefore scale thickness and phase composition of the ash covered section will be omitted in the subsequent discussion.

According to the phase mapping in the bare metal section a Cr-Fe-Ni-Mn-Nb oxides were formed. The Cr and O rich layer corresponding 26 at% and 64 % with a small amount of 10 at% Fe gives a rough approximation of magnetite ( $\text{Fe}_3\text{O}_4$ ) and  $\text{FeCr}_2\text{O}_4$  spinel ([Table 5.2](#)). The increasing chromium content close to the metal indicates the formation of a protective Cr-layer. Some light form of pitting indicating localized attack occurred on the

entire sample. Similar to the other austenitic materials, some grain boundary attack was noticed on the ash covered section of the sample. The elemental mappings are shown in Figures 5.27a and 5.27b.

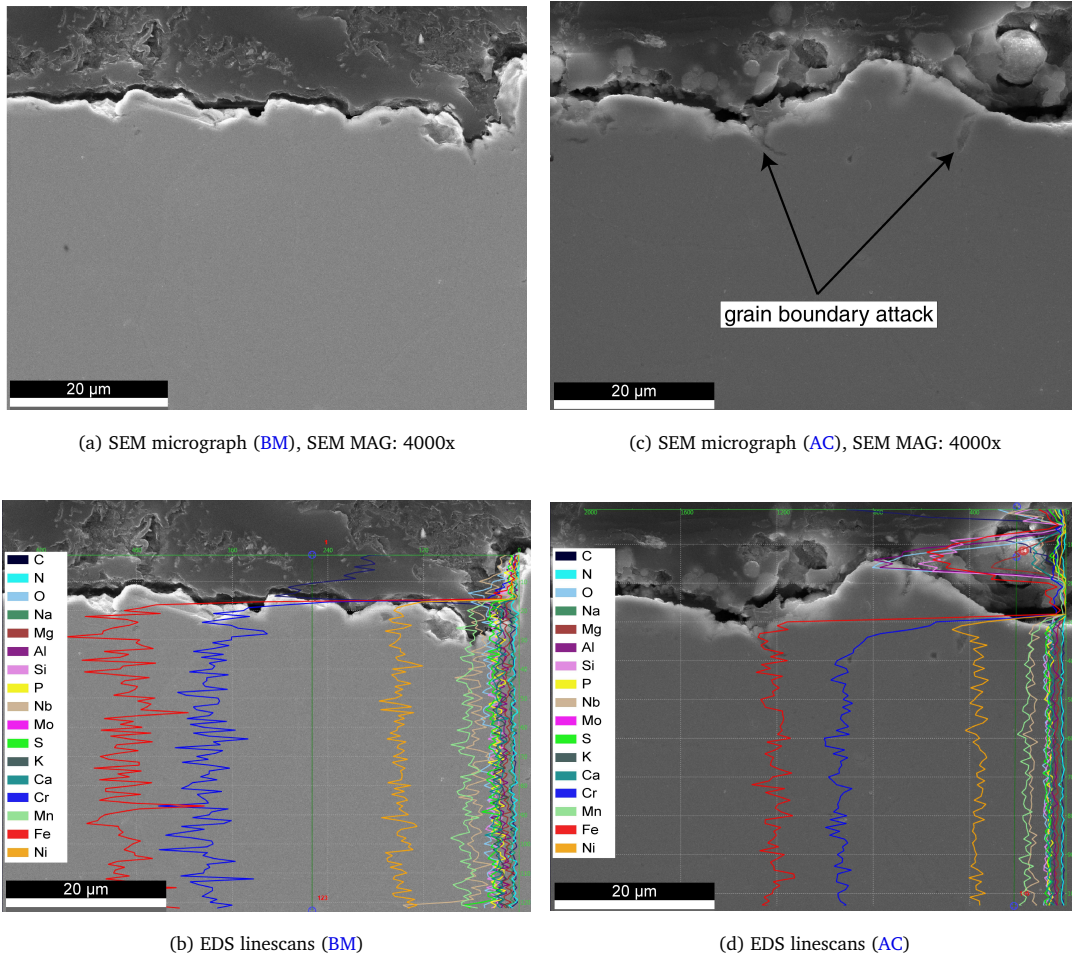


**Figure 5.25.:** SEM micrographs with EDS linescans of DMV310 N after 1000 h at 650 °C, isothermal conditions

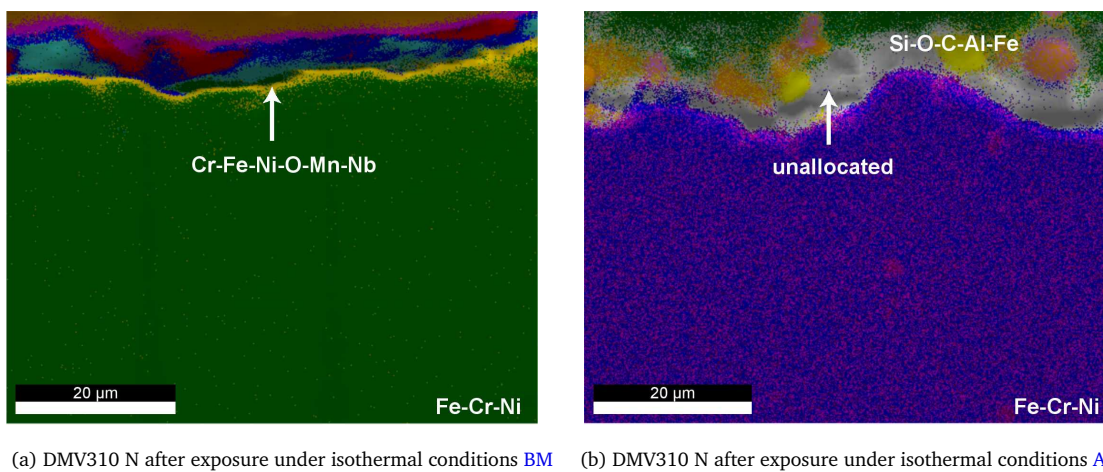
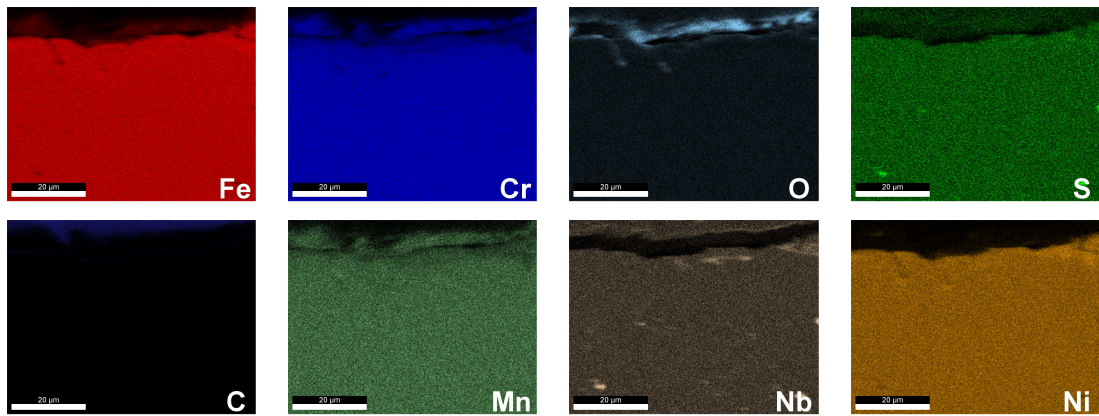
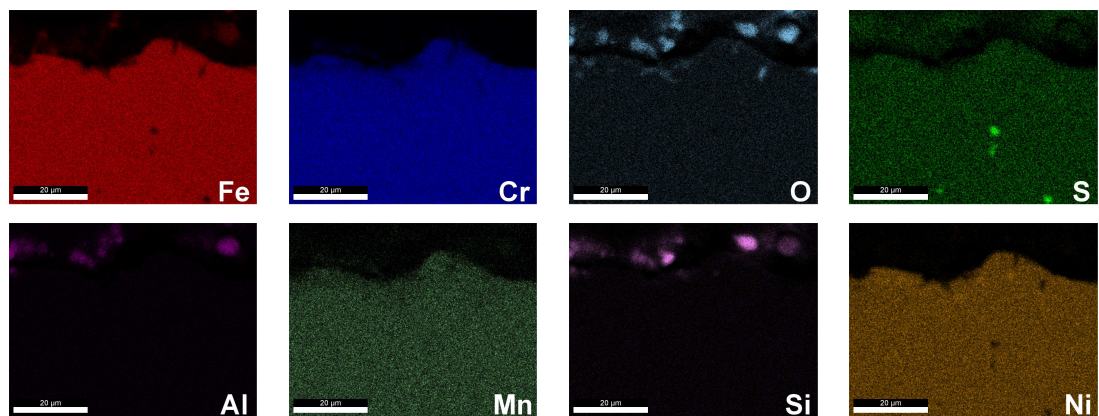


**Figure 5.26.:** Phase mapping of DMV310 N after 1000 h at 650 °C under isothermal conditions





(a) Element mapping of DMV310 N after 1000 h at 650 °C under isothermal conditions, [BM](#)



(b) Element mapping of DMV310 N after 1000 h at 650 °C under isothermal conditions, [AC](#)

**Figure 5.27.:** Element mapping of DMV310 N after 1000 h at 650 °C under isothermal conditions,

## 5.4. Cyclic oxidation after 1000 h

In this section, the results from microstructural analysis ([LOM](#) and [SEM-EDS](#)) of all the commercial alloys after 1000 h of exposure at 650 °C under thermal cycling oxidation conditions are presented. The thermo-cyclic oxidation behavior of the bare metal [BM](#) and the ash covered [AC](#) section are given and a comparison with the isothermal oxidation behavior is presented in [Section 5.3](#).

### 5.4.1. Light optical microscopy

The [LOM](#) images of all candidate alloys after 1000 h of exposure under thermal cycling conditions at 650 °C are presented in [Figures 5.28 to 5.32](#). The low magnification micrographs show that the oxidation of the ferritic-martensitic alloys (TP91 and VM12-SHC)

was uniform i.e. the same rate of attack can be seen throughout the sample, see Figures 5.28 and 5.29. It becomes obvious that the metal wastage or oxidation of the ferritic-martensitic steels significantly increased during thermal cycling compared to isothermal oxidation. Figure 5.28 shows some grain boundary attack in TP91, too, which was not present under isothermal conditions. Like in the case of isothermal oxidation, the ash covered (AC) section was more wasted than the bare metal (BM). The austenitic alloys (TP347-HFG, DMV304-HCu and DMV310 N) did show similar behavior as in isothermal conditions with good resistance against corrosion and minimal oxide scale formation. The austenitic alloy DMV304 HCu showed a form of localized oxidation behavior similar to that in isothermal oxidation – with some areas being more oxidized than others as can be seen in Figure 5.31.

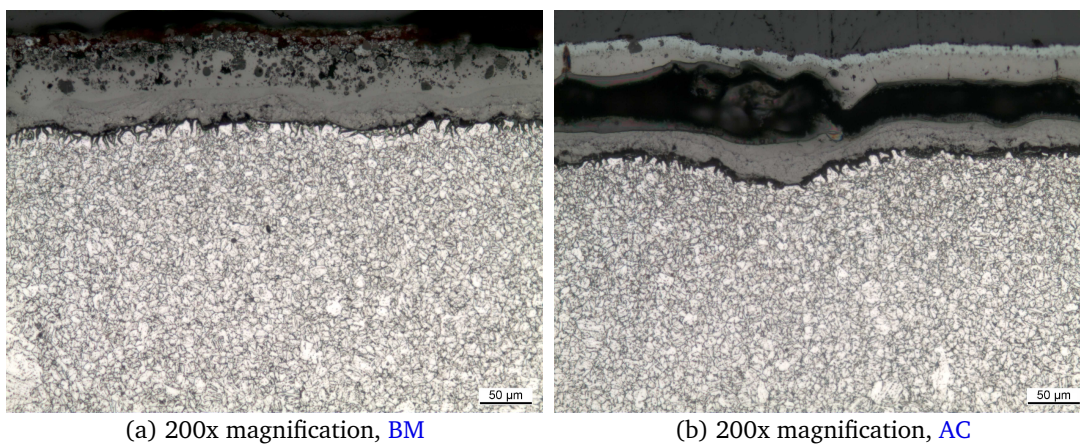


**Figure 5.28.:** Light optical micrographs of TP91 after 1000 *h* exposure, (cyclic conditions)

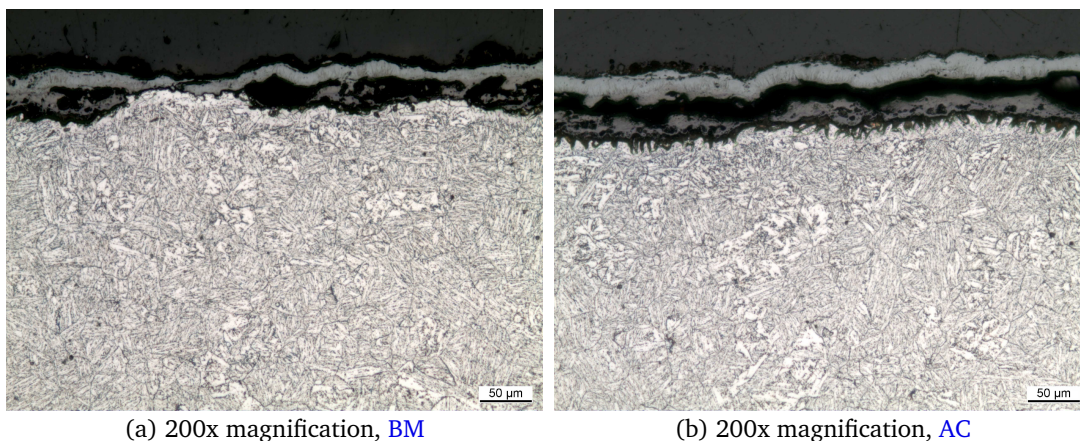


**Figure 5.29.:** Light optical micrographs of VM12-SHC after 1000 *h* exposure (cyclic conditions)

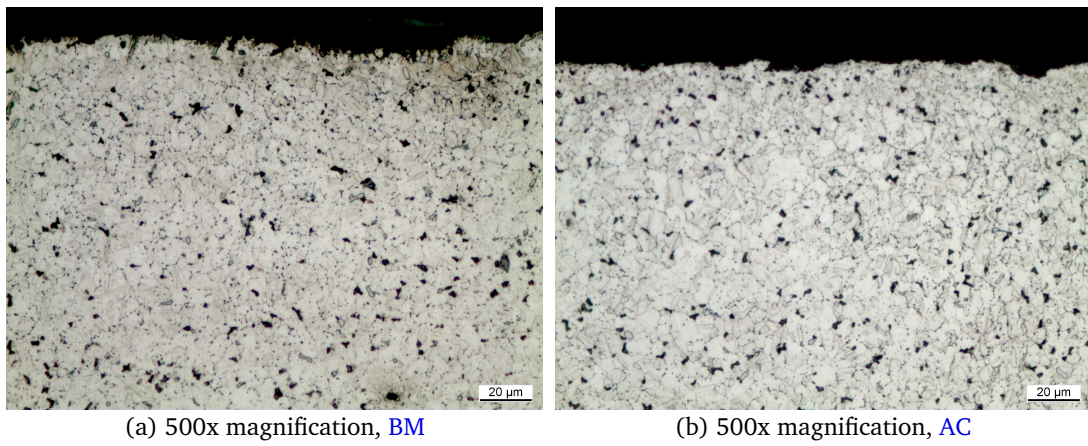


**Figure 5.30.:** Light optical micrographs of TP347-HFG after 1000 *h* exposure (cyclic conditions)

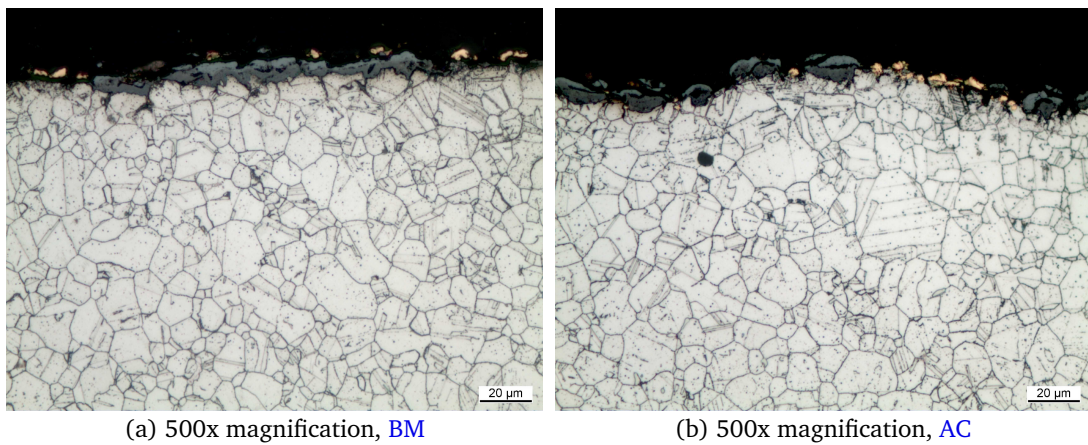


**Figure 5.31.:** Light optical micrographs of DMV304 HCu after 1000 *h* exposure (cyclic conditions)

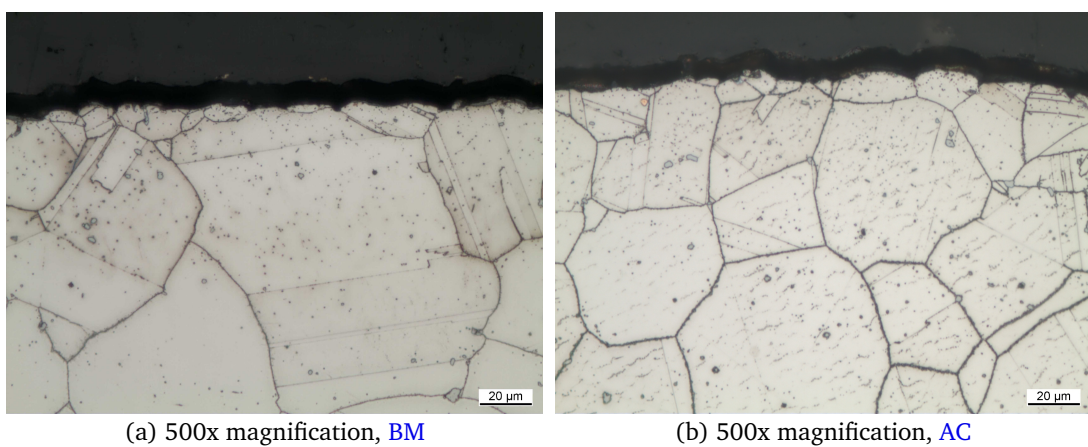


**Figure 5.32.:** Light optical micrographs of DMV310 HCu after 1000 *h* exposure (cyclic conditions)

## 5.4.2. Micro-structural (SEM–EDS) analysis of cyclic oxidation

### 5.4.2.1. Cyclic oxidation of TP91

The SEM cross-sectional micrographs and EDS linescans for ferritic-martensitic TP91 under thermal cycling conditions are presented in Figure 5.33. Average scale thickness measurements from several points on the sample gave an average of  $78\mu\text{m}$  for the bare metal and about  $85\mu\text{m}$  for the ash covered section respectively and are presented in Figure 5.3b. This signifies an increase in scale thickness of about 74% from isothermal conditions which clearly indicates the severe impact of cycling on this metal. The micrographs reveal extreme attack for TP91 accompanied by spallation which is more severe in the ash covered section of the sample. The scales on both test sections (ash and bare alloy) were duplex in nature like under isothermal conditions, too.

The bare alloy section showed two distinct layers as can be seen from the phase mapping diagrams given in Figure 5.34a. The outer epitactic oxide layer on the bare alloy section was about  $57\mu\text{m}$  in thickness and consists mainly of hematite ( $\text{Fe}_2\text{O}_3$ ) – about 45% of all the phases indicated with 40 at% Fe and 60 at% O (according to Table 5.2). Interestingly, this scale contains some magnetite and Fe-Cr spinel with Fe-contents of about 44 at% and O-contents at 56 at%. The inner topotactic layer with about  $\sim 40\mu\text{m}$  thickness consisted presumably of  $\text{FeCr}_2\text{O}_4$  spinel with Fe contents between 30 and 45 at%, Cr content around 11 to 23 at% and O ranging from 43 to 47 at%. Light spalling was also noticed on the bare metal section. A Mn-oxide formation could also be detected from the elemental mappings shown in Figure 5.35a.

On the ash covered section of the test sample, severe spalling occurred. The oxide layer was porous with a fragile ash layer that got damaged during excessive temperature changes – heating and cooling of the sample. EDS phase compositional analysis revealed the outer layer, Figure 5.34b, was possibly a hematite layer with Fe content of  $\sim 41$  at% and O content  $\sim 59$  at%. Among all phases about 33 % belong to this layer and the scale thickness was measured to be  $53\mu\text{m}$ . The inner oxide layer with a scale thickness of  $46\mu\text{m}$  was composed of a mixture of  $\text{Fe}_3\text{O}_4$  and  $\text{FeCr}_2\text{O}_4$  spinel, revealed by the EDS compositional analysis (32 – 42 at% Fe, 10 – 20 at% Cr and 48 at% O). Interestingly, a brittle ash layer (undamaged),  $28\mu\text{m}$  long and  $15\mu\text{m}$  wide was found at the metal/oxide interface on the ash covered section. As already mentioned, such a fragile layer could easily spall and facilitate oxidation leading to excessive metal wastage. The elemental mappings of the ash covered section given in Figure 5.35b also indicate the formation of a Mn-oxide in the inner layer.

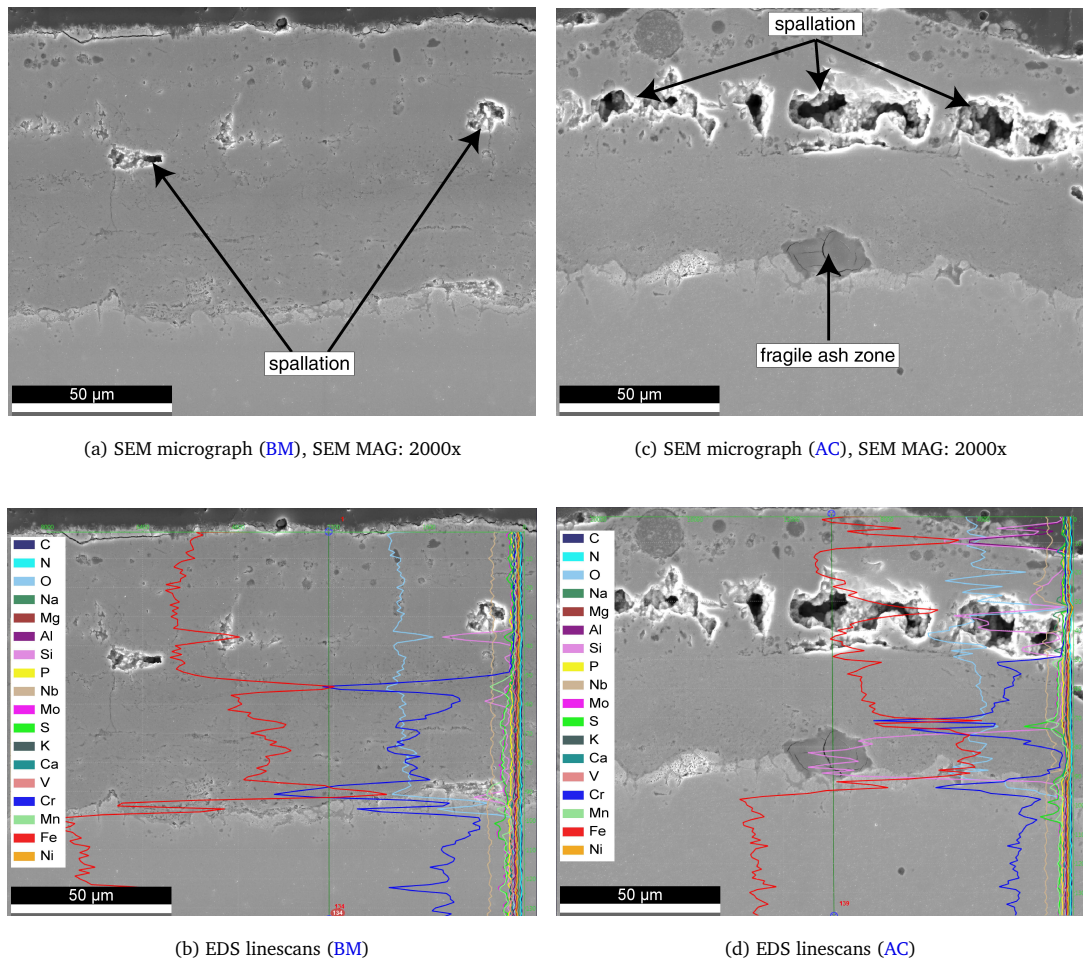


**Figure 5.33.:** SEM micrographs with EDS linescans of TP91 after 1000 h at 650 °C under cyclic conditions

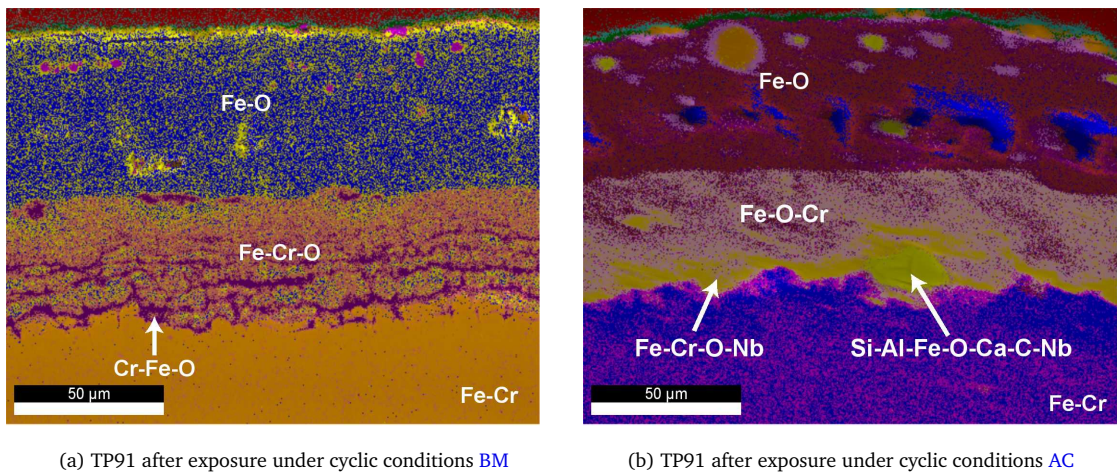
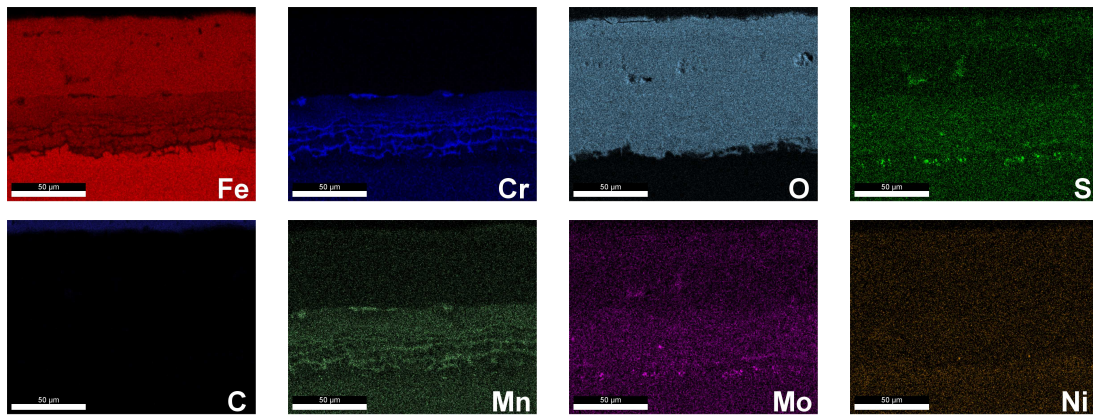
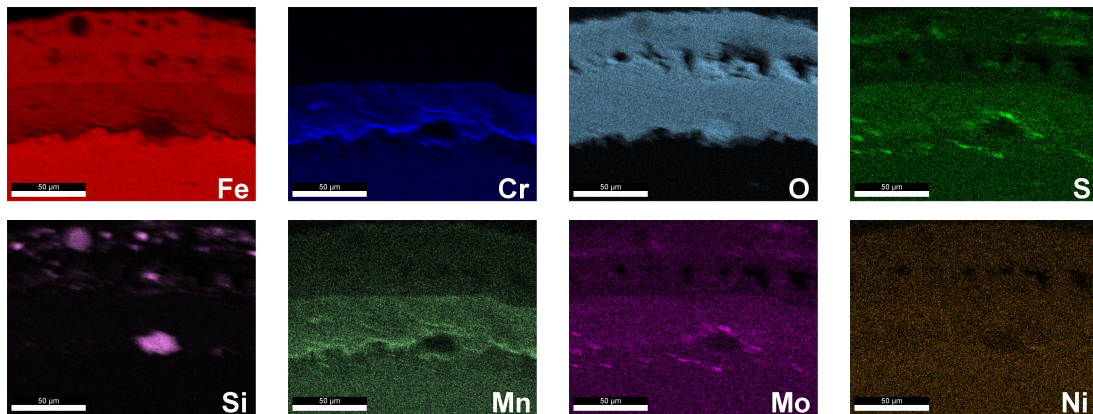


**Figure 5.34.:** Phase mapping of TP91 after 1000 h Exposure under cyclic conditions



(a) Element mapping of TP91 after 1000 h at 650 °C under cyclic conditions (BM)



(b) Element mapping of TP91 after 1000 h at 650 °C under cyclic conditions (AC)

**Figure 5.35.:** Element mapping of TP91 after 1000 h at 650 °C under cyclic conditions

#### 5.4.2.2. Cyclic oxidation of VM12-SHC

Figures 5.36 and 5.37 show SEM cross-sectional micrographs and phase mappings of the ferritic martensitic alloy VM12-SHC after 1000 h of exposure at 650 °C. The elemental mappings of both bare metal and ash covered section are given in Figures 5.38a and 5.38b and the scale thickness measurements are presented in Figure 5.3b. This alloy showed aggravated attack followed by spallation which is quite similar to the cyclic oxidation case of the martensitic steel TP91. The oxide scale on the bare metal section was about 50 µm and slightly thicker on the ash covered section with 55 µm (see Figure 5.3b). The scale formed was duplex in nature with two distinct layers: an outer epitactic layer and an inner topotactic layer.

On the bare metal section, some spalling was noticed but not as severe as on the ash covered area of the test sample. The outer epitactic layer likely consisted of magnetite ( $\text{Fe}_3\text{O}_4$ ) from compositional analysis of the phases. It had an Fe-content of 60 at% and O-content of 40 at%, cf. Table 5.2. The outer scale was about 34 µm thick. The inner scale about

$\sim 31\mu\text{m}$  thick was probably composed of both magnetite and Fe-Cr spinel with increasing Cr-content at the metal-oxide interface. The Fe-content was between 16 – 30 at%, Cr 23 – 38 at% and O around 46 – 48 at%. At the scale metal interface the oxides consisted of Cr-O-Fe-Mn as can be seen on the phase mapping in Figure 5.37a and confirmed by the elemental mappings shown in Figure 5.38a. The lower oxide layer was rich in sulphur as can be seen from the elemental mappings but no internal diffusion of sulphur was found.

The ash covered section showed severe spallation which is possibly the result of fragile ash layers which are easily damaged from rigorous heating and cooling of the material. The scale formed consists of alternating Fe-rich and Cr-rich oxide. The outer epitaxial layer about  $39\mu\text{m}$  thick, showed the formation of hematite ( $\text{Fe}_2\text{O}_3$ ) with 40 at% Fe and 60 at% O. The inner topotactic layer was probably  $\text{Fe}_3\text{O}_4$  and Fe-Cr spinel with increasing Cr-content (14 – 29) at the metal/oxide interface. Fe and O contents were 14 – 29 at% and 56 – 57 at% respectively. The inner layer thickness was about  $26\mu\text{m}$ . The innermost layer was made up of Cr-O-Fe-Nb and elemental mappings (Figure 5.38b) reveal the formation of a Mn-oxide. Similar to the bare metal section, the lower oxide layer was rich in sulphur.

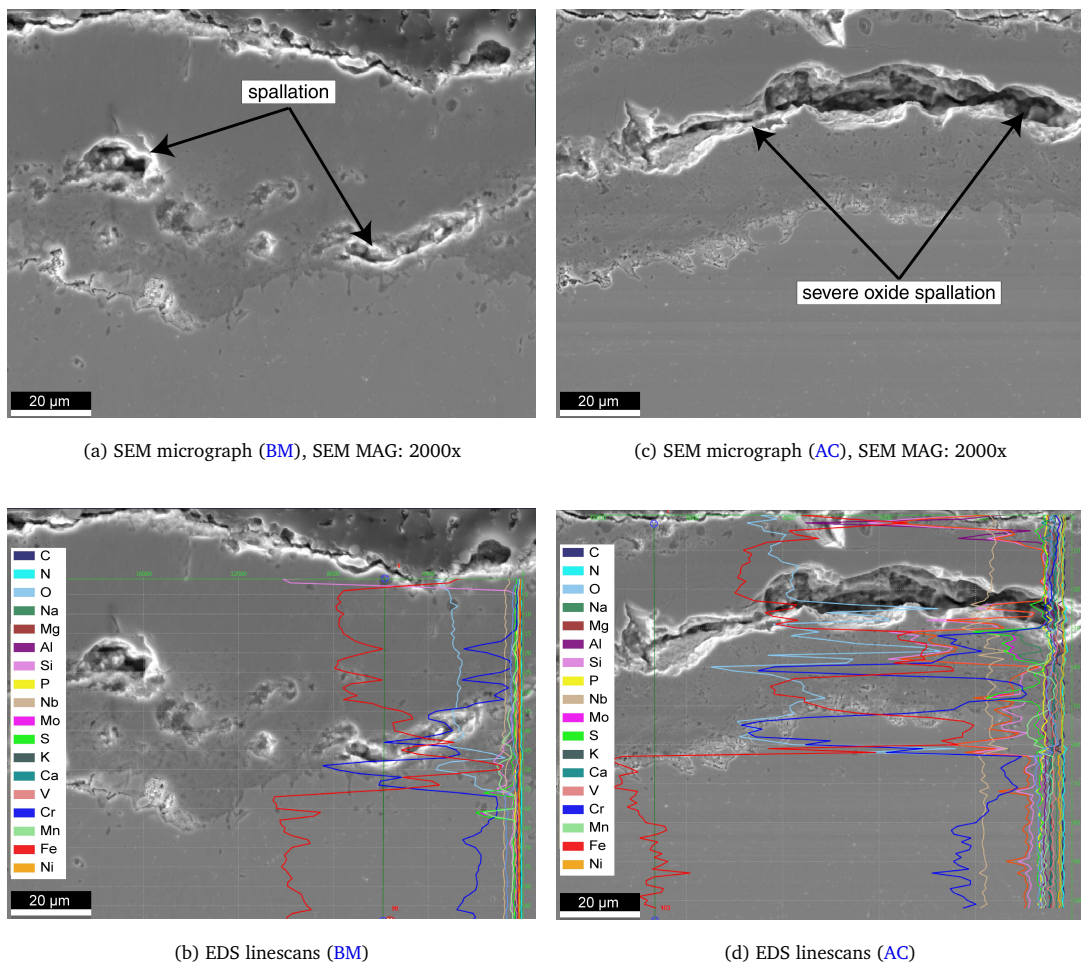
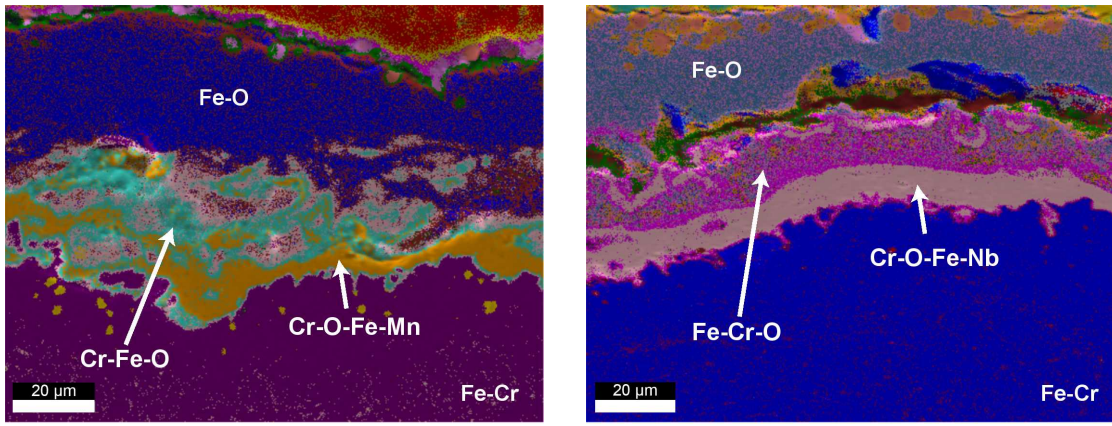


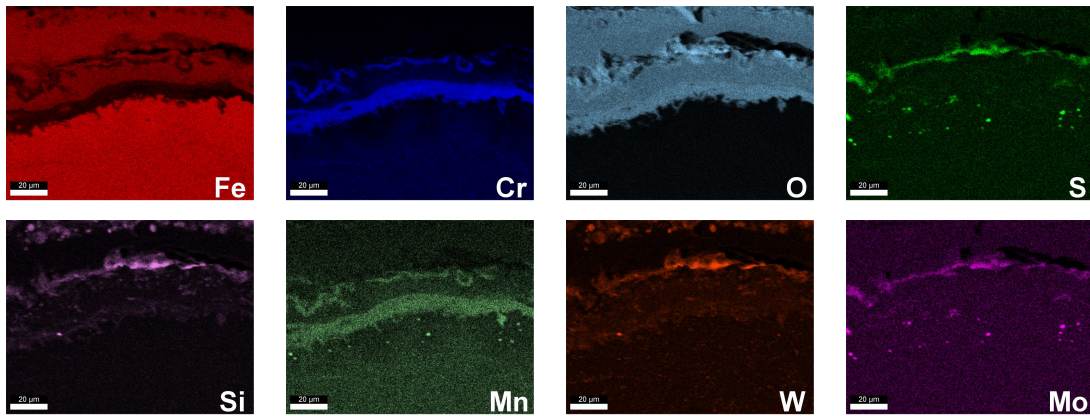
**Figure 5.36.:** SEM micrographs with EDS linescans of VM12-SHC after 1000 h at 650 °C under cyclic conditions



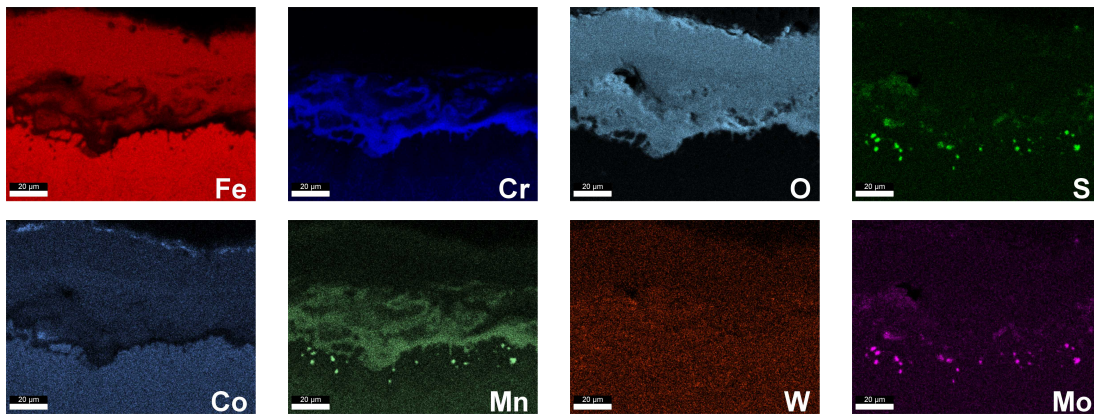
(a) VM12-SHC after exposure under cyclic conditions **BM**

(a) VM12-SHC after exposure under cyclic conditions **AC**

**Figure 5.37.:** Phase mapping of VM12-SHC after 1000 h at 650 °C under cyclic conditions



(a) Element mapping of VM12-SHC after 1000 h at 650 °C under isothermal conditions (**BM**)



(b) Element mapping of VM12-SHC after 1000 h at 650 °C under isothermal conditions (**AC**)

**Figure 5.38.:** Element mapping of VM12-SHC after 1000 h at 650 °C under isothermal conditions



### 5.4.2.3. Cyclic oxidation of TP347-HFG

The austenitic alloy TP347-HFG showed good corrosion resistance in terms of minimal oxide scale growth during thermal cycling as well as under isothermal conditions. However, pitting and internal sulphidation was noticed. The SEM micrographs and EDS linescans are given in Figure 5.39. The phase mappings are shown in Figure 5.40. The scale was partly destroyed during preparation leading to gaps between mount and material. This can give rise to inaccurate scale measurements in general and erroneous phase compositions. Nevertheless, the average scale thickness was approximately  $< 2\mu\text{m}$  (cf. Figure 5.3b) on both the bare metal and the ash covered sections.

In the bare metal section (Figure 5.40a) subsurface oxidation occurred – with an oxide below the metal surface (subsurface oxidation) with a depth of about  $11\mu\text{m}$ . This could result in the formation of pits. The EDS phase mappings revealed the formation of oxides of Cr, Fe, Nb, and Mn in this region. The sample was also partly depleted of Cr. The external oxide layer (about 1% only) was probably a chromia ( $\text{Cr}_2\text{O}_3$ ) layer with 40 at% Cr and 60 at% O, cf. Table 5.2.

The ash covered section (Figure 5.40b) of the test sample revealed minimal scale formation with the possibility of  $\text{Fe}_3\text{O}_4$  and  $\text{FeCr}_2\text{O}_4$  spinel formation with an Fe-content  $\sim 37$  at%, Cr about 15 at% and 48% O. The oxide layer consisted of Fe-Cr-Mn-Si-O-Nb. Additionally, significant internal sulphidation was noticed on this section of the sample, with a total penetration depths ranging between 22 and  $38\mu\text{m}$ . EDS phase mappings revealed the formation of likely Fe, Nb, and Cr sulphides.

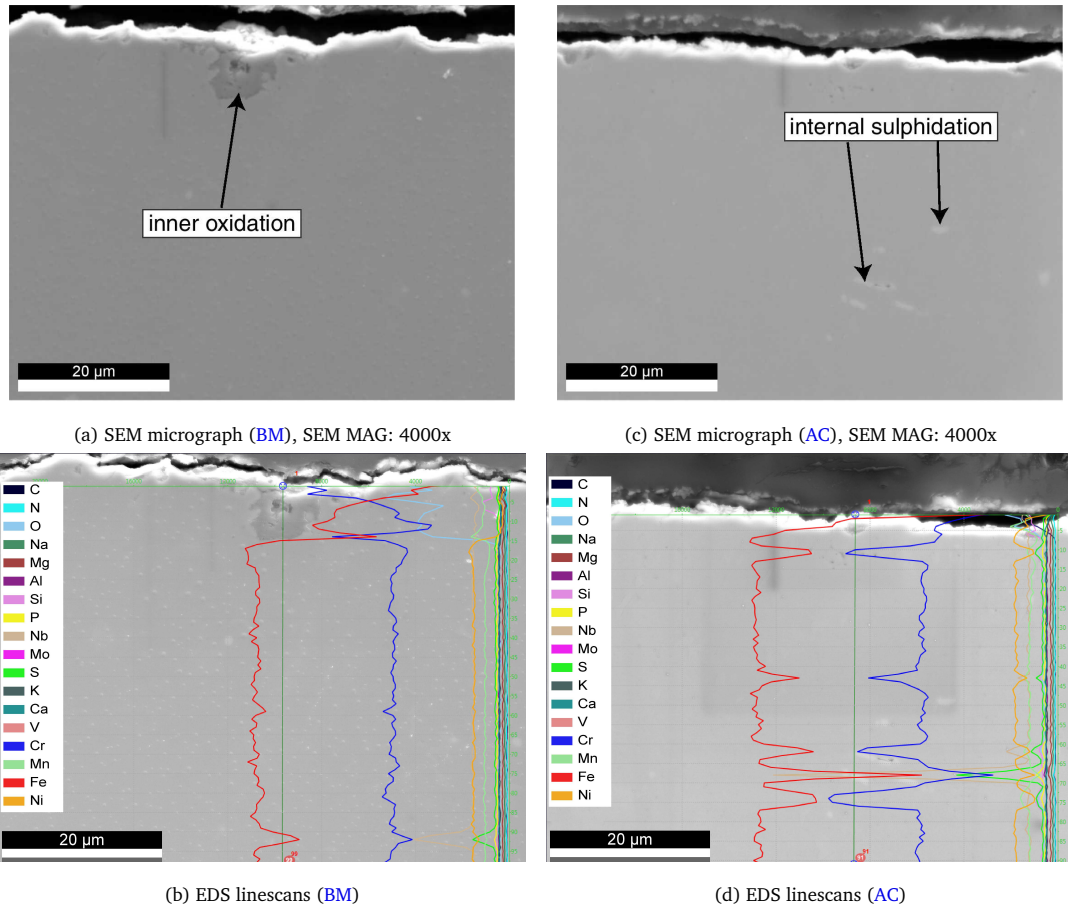


**Figure 5.39.:** SEM micrographs with EDS linescans of TP347-HFG after 1000 h of exposure under cyclic conditions

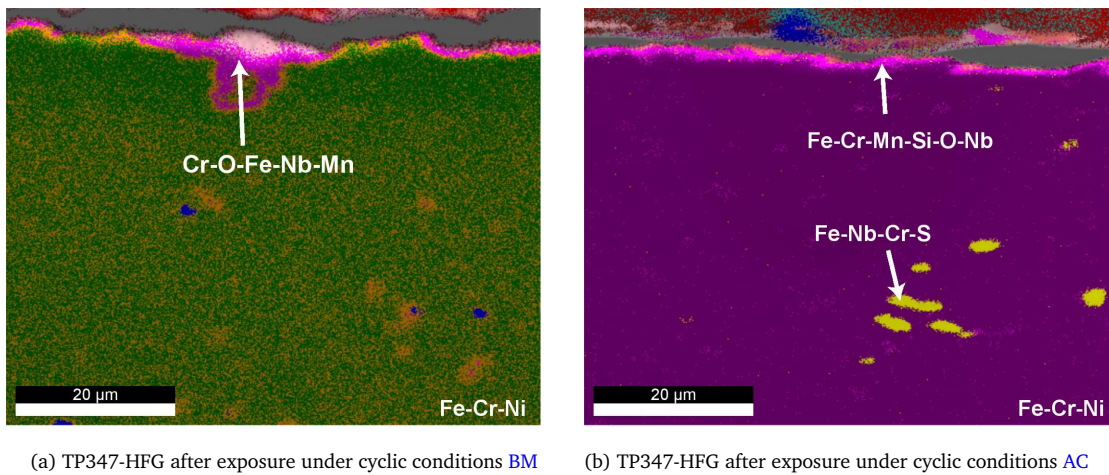
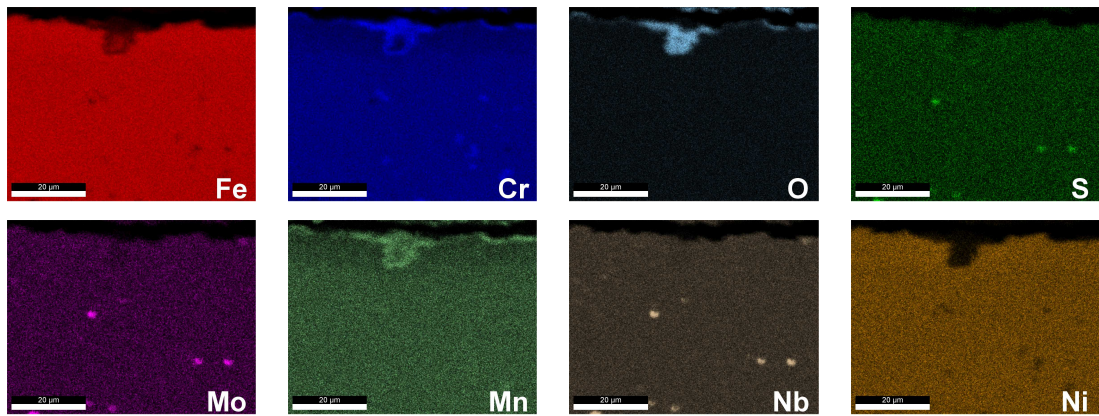
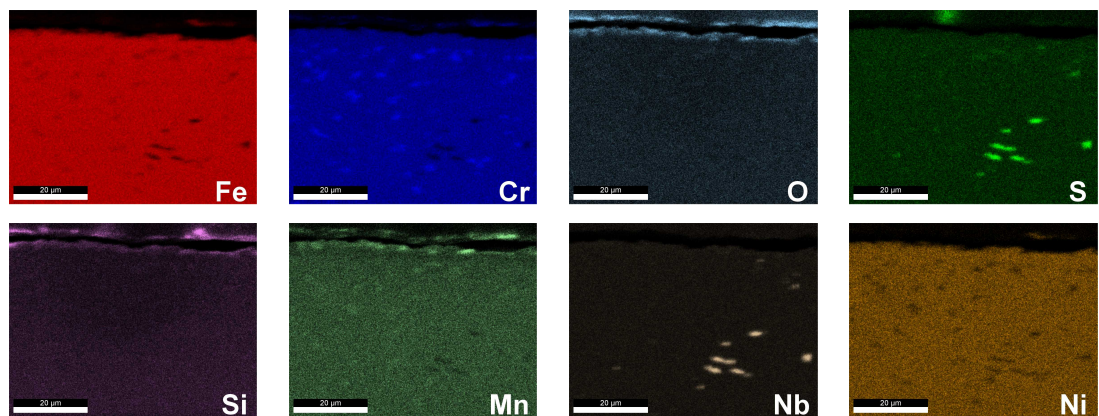


**Figure 5.40.:** Phase mapping of TP347-HFG after 1000 h at 650 °C under cyclic conditions



(a) Element mapping of TP347-HFG after 1000 h at 650 °C under cyclic conditions (BM)



(b) Element mapping of TP347-HFG after 1000 h at 650 °C under cyclic conditions (AC)

**Figure 5.41.:** Element mapping of TP347-HFG after 1000 h at 650 °C under cyclic conditions

#### 5.4.2.4. Cyclic oxidation of DMV304 HCu

The SEM cross sectional micrographs and EDS linescans are shown in Figure 5.42 and the phase mappings are provided in Figure 5.43. From micrographs it is quite clear that cycling had a harmful effect on the austenitic material. Scale thickness measurements showed that the ash covered section was more wasted with a scale thickness of about  $18\mu\text{m}$  than the bare metal with  $8\mu\text{m}$  (Figure 5.3b). The ash section showed a duplex layer like all Fe-based steels in this study. Small traces of internal sulphidation was noticed.

The bare metal section (Figure 5.43a) with minimal scale growth had duplex – outer and inner oxide layers. The outer epitactic layer (Fe-O-Cr-Nb) was about  $4\mu\text{m}$  thick and the inner topotactic oxide layer (Cr-Fe-O-Nb) had a maximum thickness of about  $4\mu\text{m}$ . EDS composition analysis revealed the probability of a hematite ( $\text{Fe}_2\text{O}_3$ ) outer layer with 40 at% Fe and 60 at% O. The inner layer had increasing Cr-content which possibly indicated

the formation of Fe-Cr spinel and magnetite. Elemental analysis (Figure 5.44a) reveals that the alloy was depleted of Cr and the inner layer contained some Nb and Mn oxides.

The ash covered section (Figure 5.43b) showed increased oxidation rates with thicker scales than in the bare metal section. The duplex scale had scale thicknesses of about  $8\mu\text{m}$  for the outer epitaxial layer and about  $12\mu\text{m}$  for the inner topotaxial layer at the maximum locations. The outer layer again was similar to that in the bare metal section, possibly being hematite with typical 40 at% for Fe and 60 at% for O. There may be some magnetite ( $\text{Fe}_3\text{O}_4$ ) with about 43 at% Fe and 57 at% O. The inner layer was the typical magnetite and Fe-Cr spinel combination. Worth noting is that in the ash covered section had some form of grain boundary attack took place. The elemental mappings are given in Figure 5.44b and reveal the presence of Mn-oxide in the lower oxide layer as well as the formation of Ni-oxide.

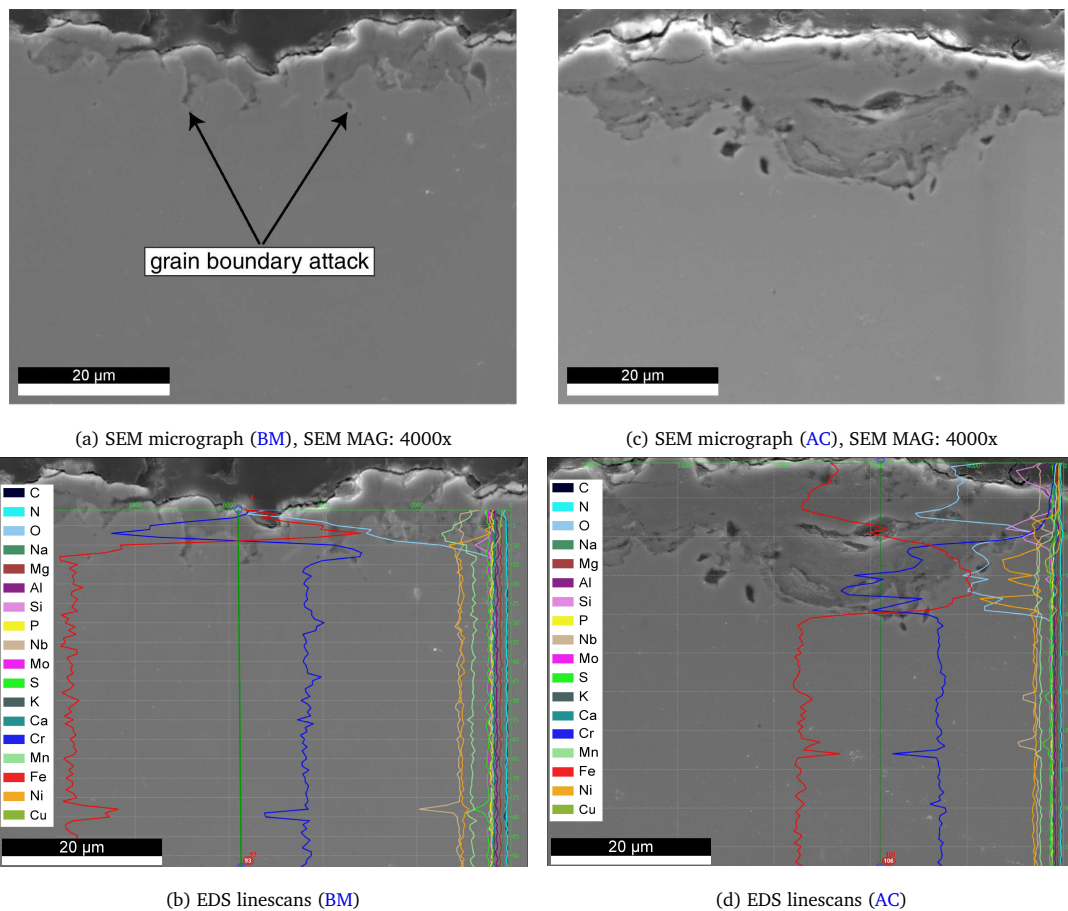


**Figure 5.42.:** SEM micrographs with EDS linescans of DMV304 HCu after 1000 *h* of exposure under cyclic conditions

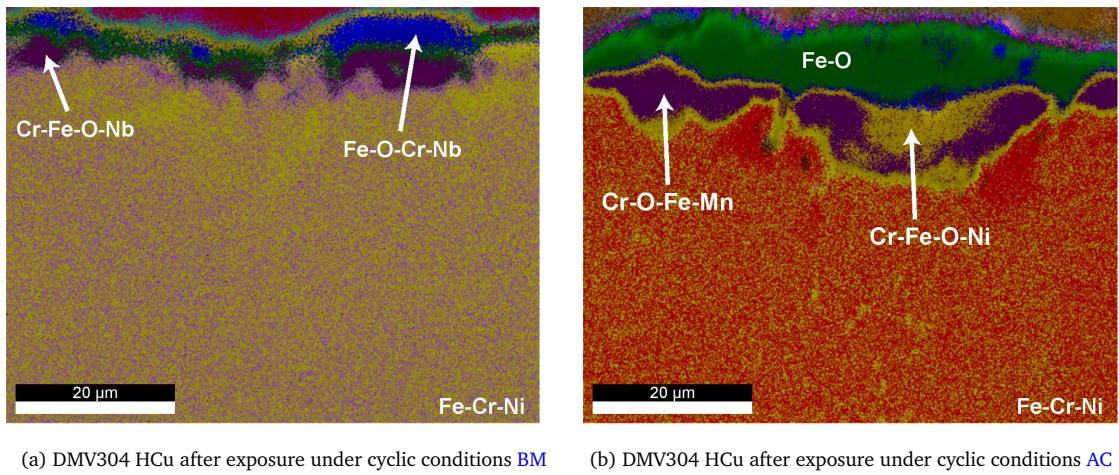
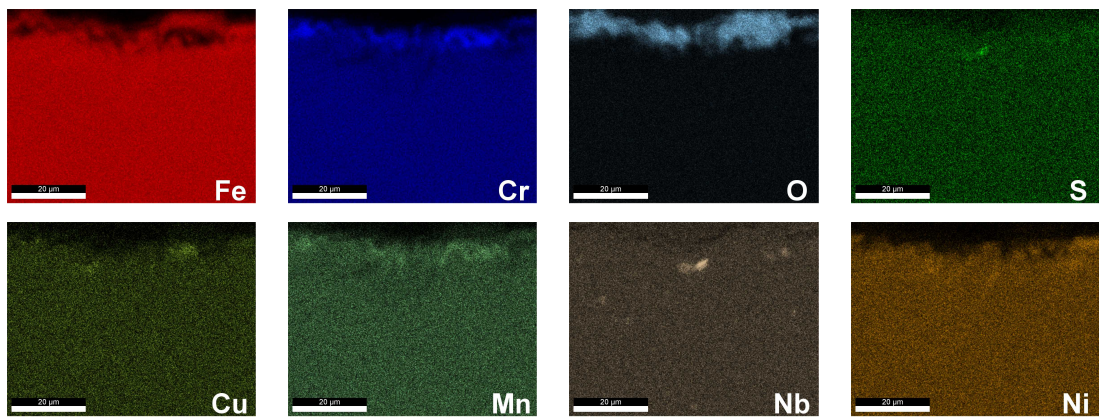
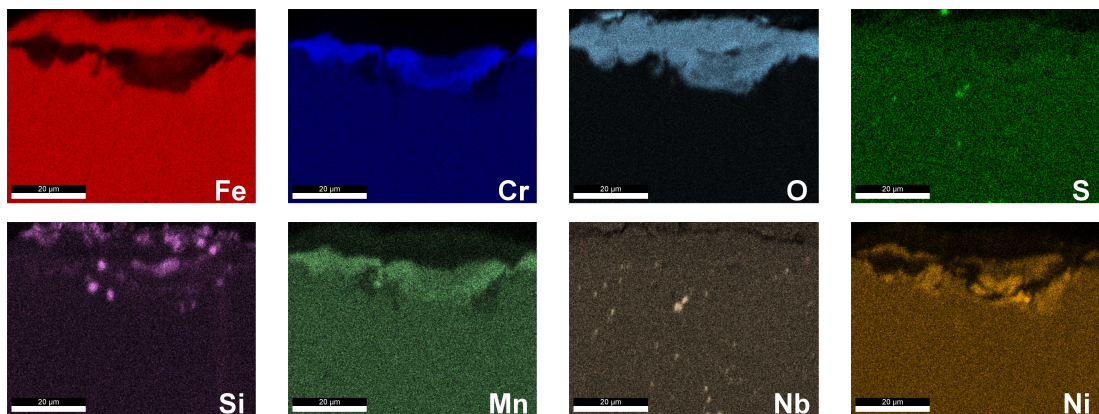


**Figure 5.43.:** Phase mapping of DMV304 HCu after 1000 h of exposure under cyclic conditions



**(a)** Element mapping of DMV304-HCu after 1000 h at 650 ° under cyclic conditions (BM)



**(b)** Element mapping of DMV304-HCu after 1000 h at 650 °C under cyclic conditions (AC)

**Figure 5.44.:** Element mapping of DMV304-HCu after 1000 h at 650 °C under cyclic conditions

#### 5.4.2.5. Cyclic oxidation of DMV310 N

The austenitic alloy DMV310 N showed the best corrosion and oxidation performance with the least oxide scale growth in this study. The scale thickness was approximated to be  $\leq 1\mu\text{m}$  for both the bare metal section and the ash covered section. Due to the damaged oxide scales during metallographic preparation it was difficult to analyze scale thickness and phase compositions accurately. As already seen from the other austenitic alloys, especially TP347-HFG, cavities or pitting corrosion were found which was more noticeable on the ash covered area.

The bare material (Figure 5.46a) showed a thin layer of Cr-Fe-O-Mn-Nb which suggests the possible formation of Cr-Fe spinel and a single iron rich layer made up of Fe-O-Cr-Ni-Nb. As already mentioned cavities were noticed but to a lesser extent in the bare metal section. Elemental mappings revealed internal formation of Nb and Ni sulphides (Figure 5.47a). No indication of manganese oxides was found.

The ash covered section (Figure 5.46b) had deeper pits or cavities more than in the bare metal section. Here a locally damaged layer was found to consist of Cr-Fe-O. A chromium (about 20 at%) and oxygen (above 60 at%) rich layer was formed with only small amounts of 12 at% Fe which could mean that chromia, Fe-Cr spinel and magnetite were formed. Similar to the bare metal section, elemental analysis revealed internal sulphidation of Nb and Ni sulphides (Figure 5.47b). Like in the bare metal section no indication of manganese oxides was found.

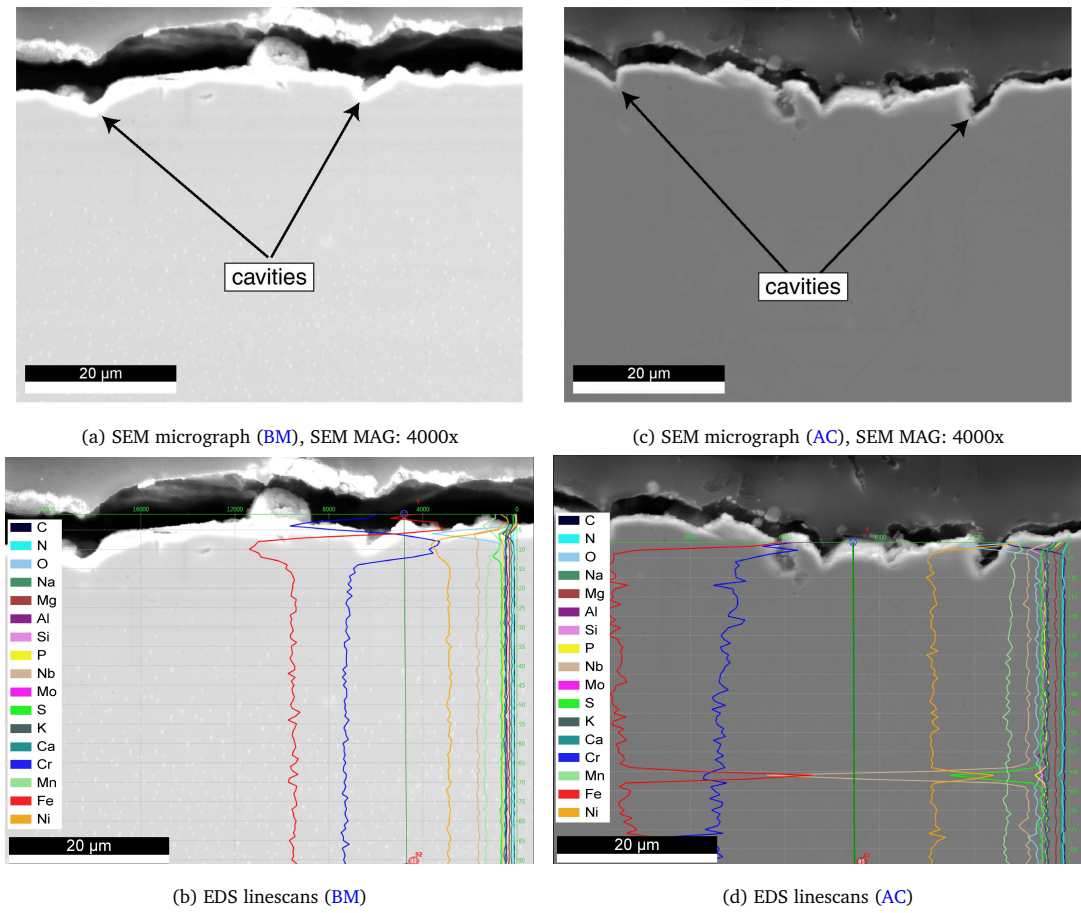


**Figure 5.45.:** SEM micrographs with EDS line scans of DMV310 N after 1000 h of exposure under cyclic conditions

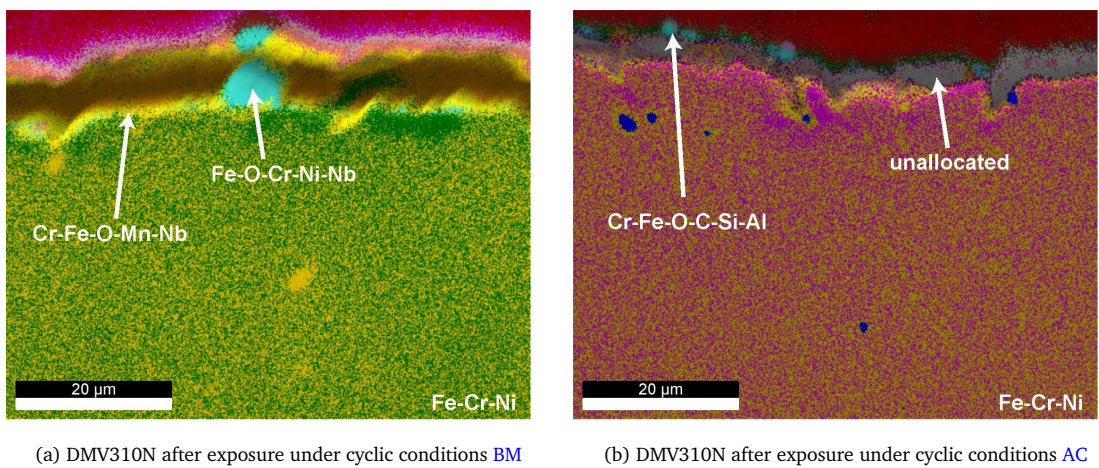
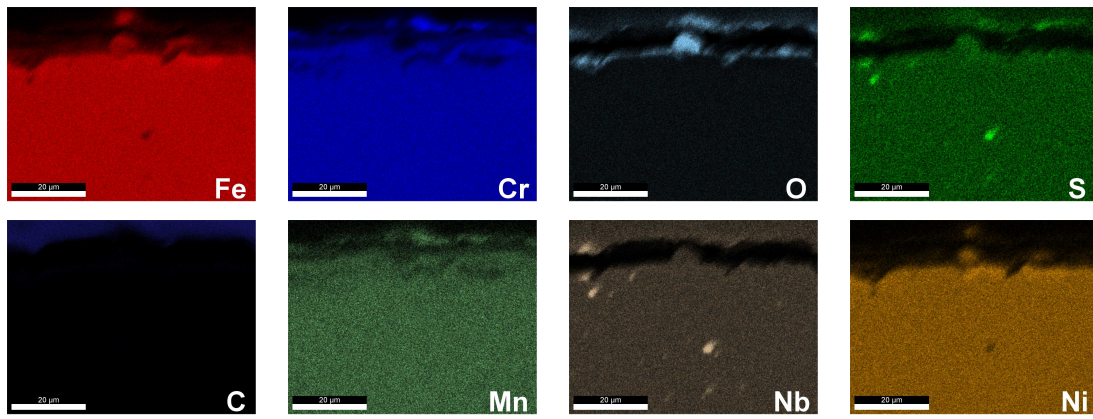
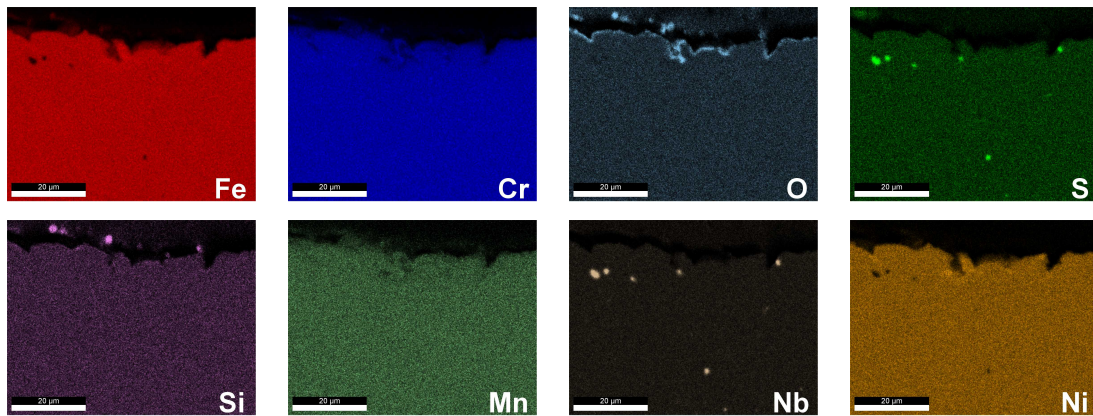


**Figure 5.46.:** Phase mapping of DMV310 N after 1000 h of exposure under cyclic conditions



(a) Element mapping of DMV310 N after 1000 h under cyclic conditions (BM)



(b) Element mapping of DMV310 N after 1000 h under cyclic conditions (AC)

Figure 5.47.: Element Mapping of DMV310 N after 1000 h at 650 °C under cyclic conditions



## 6. Discussion

### 6.1. Isothermal and cycling oxidation

#### 6.1.1. Weight change and parabolic kinetics

High temperature oxidation is a vital process for materials used in high temperature applications such as energy conversion units like coal power plants. In *isothermal* operations, the rate of metal wastage is usually determined by the rate at which solid matter diffuses through the oxide layer. The oxidation rate normally follows parabolic kinetics where the growth rate is inversely proportional to the oxide scale thickness. This is the typical situation for conventional baseload power plants.

However, with the integration of renewables into the energy generation mix, conventional baseload plants are forced to operate in a cyclic mode which involves periodic start-ups and shut-downs of the units. *Cyclic* oxidation therefore becomes important for these units. This mode of operation can lead to increased oxide growth rates and eventually spalling of the oxides during the cooling process and loss of protective oxide scale which exposes the bare material to the corrosive gas for further attack. Therefore the oxidation and corrosion rate of the materials increase.

Cyclic oxidation testing is therefore necessary to evaluate corrosion and oxidation behavior (or the performance) of existing coal boiler materials. This usually involves exposing several materials under well controlled test conditions and then carrying out weight change measurements of exposed materials after a given period of time [119].

In this respect, the isothermal and cyclic oxidation behavior of five commercially used coal-fired superheater and reheater alloys; TP91, VM12-SHC, TP347-HFG, DMV304 HCu and DMV310 N was investigated under simulated coal firing isothermal and flexible (cycling) firing conditions. From the weight change results obtained, it is quite apparent that cycling operation increased the oxidation rate of all the materials (see [Section 5.1](#)) as well as the oxide thickness as presented in [Sections 5.3](#) and [5.4](#). The exposed materials also showed parabolic growth rate as expected in both isothermal and cyclic conditions. These results are in good agreement with the results from previous studies [85, 121–123].

With respect to the weight gained, these five commercial alloys ranked as follows in an increasing order (from least to most weight gained): DMV310 < TP347 HFG < DMV304 HCu < VM12-SHC < TP91. The scale thickness measurements followed the same ranking order as the weight gain measurements for both isothermal and thermal cycling conditions.

### 6.1.2. Effect of Chromium on oxidation rate

Chromium is known to influence the oxidation behavior of iron-based ferritic, martensitic and austenitic steels. High Cr-containing Fe-base alloys have a tendency for good oxidation resistance while low-Cr alloys exhibit poor oxidation behavior. It has been shown that Fe-Cr alloys containing chromium levels less than 18 wt% will first form a protective chromia layer but shortly afterwards accelerated (*or break-away*) oxidation forming alternating layers of Fe-rich and Cr-rich oxides [124]. This was the case for the ferritic-martensitic alloys TP91 and VM12-SHC with about 9%-Cr and 12%-Cr respectively.

The results obtained in this study are in agreement with the literature – the high-Cr alloys had an overall lower scale growth and parabolic rate constants as shown in Figures 6.1a and 6.1b, than the low Cr martensitic steels. From Figures 6.1a and 6.1b, it can be seen that the austenitic alloy DMV310 N (25Cr-21Ni alloy) showed the least oxidation compared to all other tested materials.

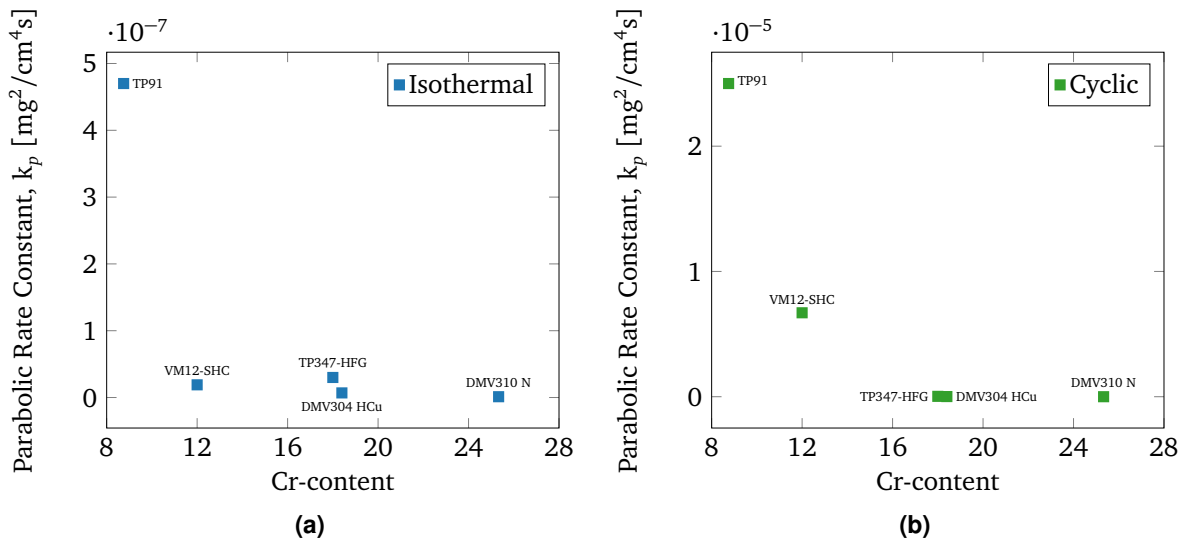


Figure 6.1.: Effect of chromium on oxidation rate

### 6.1.3. Effect of minor alloying elements (Ni, Mn, Mo, and Nb)

#### 6.1.3.1. Nickel

Nickel has beneficial effects with respect to corrosion resistance and can overshadow the effects of other minor elements. The addition of nickel to alloys is mainly to provide toughness, strength and stability. The ferritic martensitic alloys had nickel contents of about 0.4 wt%. Because of its function as austenite stabilizer the austenitic alloys had Ni-contents of about 10, 9.1 and 21.05 wt% for TP347-HFG, DMV304 HCu and DMV310 N respectively. The presence of a Ni-oxide was found in DMV310 N which showed the best oxidation performance especially in the bare metal alloy section for both isothermal and thermal cycling conditions. DMV304 HCu with a substantial Ni-content showed the worst oxidation behavior of all three austenites.

#### 6.1.3.2. Manganese

The addition of manganese takes place during the process of melting the alloy. While decreasing the diffusion velocity it serves two purposes: (1) for deoxidizing and (2) desulphurizing. Mn helps to prevent brittleness by its combination with sulphur. Iron-based alloys generally have a manganese content up to about 1.0 wt%. The investigated commercial alloys had manganese contents as follows: 0.45 wt% for the ferritic-martensitic TP91 and VM12-SHC) while the austenitic steels had Mn-contents of 1.6 wt% for TP347-HFG, 0.79 wt% for DMV304 HCu and 1.2 wt% for DMV310 N.

According to Li [124], manganese could have damaging effects on the oxidation resistance of alloys due to its high diffusion rate through a  $\text{Cr}_2\text{O}_3$  scale and forming a less protective  $\text{MnCr}_2\text{O}_4$  external layer which is vulnerable to spalling. The formation of an alumina scale ( $\text{Al}_2\text{O}_3$ ) can inhibit the outward diffusion of manganese. The ferritic martensitic alloys TP91 and VM12-SHC had oxide layers quite rich in Mn, this may suggest the poor oxidation performance of the materials and spallation under thermal cycling conditions. The austenitic alloys TP347-HFG and DMV304 HCu also had thin layers of a manganese oxide but better performance than the ferritic-martensitic steels. No indication of a Mn-oxide or spinel layer was found in DMV310 N and thus showed the best oxidation resistance. Similar to the results obtained by Li [124], the Fe-Cr-Ni base alloys show varying characteristics which reveal the effect of minor alloying elements such as manganese.

#### 6.1.3.3. Molybdenum

Molybdenum with usually less than 3 wt% also increases strength and hardenability. It increases creep strength by the action of micro-carbides. The oxidation of refractory metals (Mo, Nb, etc.) is unfortunately high [125]. The oxidation of Mo is vital in the evaporation

of oxides at high temperatures and pressures [44]. Sulphidation of Mo, occurs by inward diffusion of sulfur while iron or nickel sulphide formation occurs by outward transport of cation forming on the surface. At high  $p(S_2)$  the inner sulphide layer is usually a combination of  $MoS_2$  and  $FeS$  while at low  $p(S_2)$  it is an  $Fe_xMo_6S_8$  phase (Chevrel). The addition of Mn or a combination of Mn and Al could improve sulphidation resistance of Fe-Mo alloy by forming an intermediate  $Mn(Fe)S$  layer [46]. Internal Mo sulphidation was noticed in the austenitic alloy DMV304 HCu with a Mo-content of 0.26 wt%.

#### 6.1.3.4. Niobium

The oxidation of Nb at high temperature occurs by the inward diffusion of oxygen through the scale. Generally, a protective layer is formed which stresses the oxide formation at the scale–alloy interface as the scale grows. This could lead to cracking of the scale and accelerated oxidation [44]. The addition of niobium has also been found to reduce detrimental carburization [54]. The outer oxide layers of TP91 were found to contain some traces of Nb i.e. an Fe-O-Nb layer.

## 6.2. Ferritic-martensitic and austenitic steels oxidation

### 6.2.1. Oxide morphology

Iron-base (ferritic, martensitic or austenitic) alloys form different oxide layers with complex microstructures on their surfaces when exposed to high temperature conditions. As discussed in Section 2.3.3.4, the oxide with the lowest oxygen content wustite ( $FeO$ ) occupies the innermost layer adjacent to the metal substrate, followed by an intermediate layer of magnetite ( $Fe_3O_4$ ) and an outer oxygen rich layer of hematite ( $Fe_2O_3$ ). However, this sequence can be altered due to the presence of other alloying elements, the corrosive environment or even through heat treatment usually done through precipitation hardening and solid-solution hardening. The thickness of the scale increases with increasing temperatures due to rapid diffusion of iron and oxygen. The diffusion is also affected by cracks which may form during oxide growth, porosity of the oxide and the adhesiveness of the oxide to the base metal [62, 124]. The following sub-sections present the type of oxide structures found in this study for both the ferritic-martensitic as well as the austenitic materials that were exposed to isothermal and cyclic conditions for 1000 hours at 650 °C.

#### 6.2.1.1. Ferritic–martensitic steels (TP91 and VM12-SHC)

The ferritic materials generally showed higher oxidation rates than the austenitic materials. The oxide layers of the ferritic-martensitic steels had the classical outer hematite ( $Fe_2O_3$ ) layer and an inner mixed layer of magnetite and  $FeCr_2O_4$ . TP91 showed an outer

hematite layer and a mixed inner layer consisting of magnetite and Fe-Cr spinel together with manganese oxide and a thin chromia scale on both the bare metal and ash covered section. This is in agreement with the study of Laverde *et al.* [123] who have proposed a similar oxidation mechanism for TP91 alloy. VM12-SHC also showed a similar oxide structure to TP91 with an outer hematite layer and an inner mixed layer composed of magnetite together with manganese oxide and a thin  $\text{Cr}_2\text{O}_3$  scale.

#### 6.2.1.2. Austenitic steels (TP347-HFG, DMV304 HCu and DMV310 N)

The austenitic alloys TP347-HFG and DMV310 N showed thin protective oxide layers mainly consisting of  $\text{Cr}_2\text{O}_3$  on both the bare metal alloy section and the ash covered section. DMV304 showed a moderately higher oxidation rate than the other austenitic materials with the outer layers of hematite ( $\text{Fe}_2\text{O}_3$ ) and an inner layer of magnetite ( $\text{Fe}_3\text{O}_4$ ), Fe-Cr spinel and chromia. As mentioned in Section 4.3.3, the oxide layers in these materials were partially destroyed due to poor adhesion of the mount and it was therefore difficult to get a clear picture of the structure of these layers. Knödler *et al.* [120], exposed the austenitic superheater material 1.4910 (X3CrNiMoN17-13) to steam side conditions at 637 °C for 21,700 h and found also thin protective film which they attributed to the diffusion of chromium and nickel towards the surface forming a Cr-Ni spinel  $\text{Fe}(\text{CrNi})\text{O}_4$ .

#### Grain boundary attack in austenitic steels

Grain boundary chemistry is vital as it can strongly influence the strength of a material thereby causing severe damage in austenitic steels or nickel base alloys. Grain boundary oxidation is known to penetrate the materials more than surface oxidation and can accelerate the formation of fatigue cracks. It is also found to increase fatigue damage due to cyclical stress by the formation and acceleration of cracks. When this happens, the cracks open up, and expose the bare metal to the corrosive environment and further cracks occur by oxidation [126]. All the austenitic materials (TP347-HFG, DMV304 HCu and DMV310 N) investigated in this study showed some form of grain boundary attack or cavitation. Kiamehr *et al.*, [127] also reported similar results for TP347-HFG.

Austenitic steels are generally prone to carbide ( $\text{M}_{23}\text{C}_6$ ) precipitation. A minimum of 12% Cr in solid solution is required for the formation a protective film for good oxidation resistance. At the test temperature of 650 °C austenites are vulnerable to carbide precipitation which results in the depletion of chromium (less than 12%-Cr) and subsequently causing pitting corrosion in the Cr-depleted regions close to the precipitates. Schweitzer suggests using low carbon alloys (< 0.03% C) to prevent carbide precipitation which can lead to intergranular attack in austenitic or nickel based alloys [128].

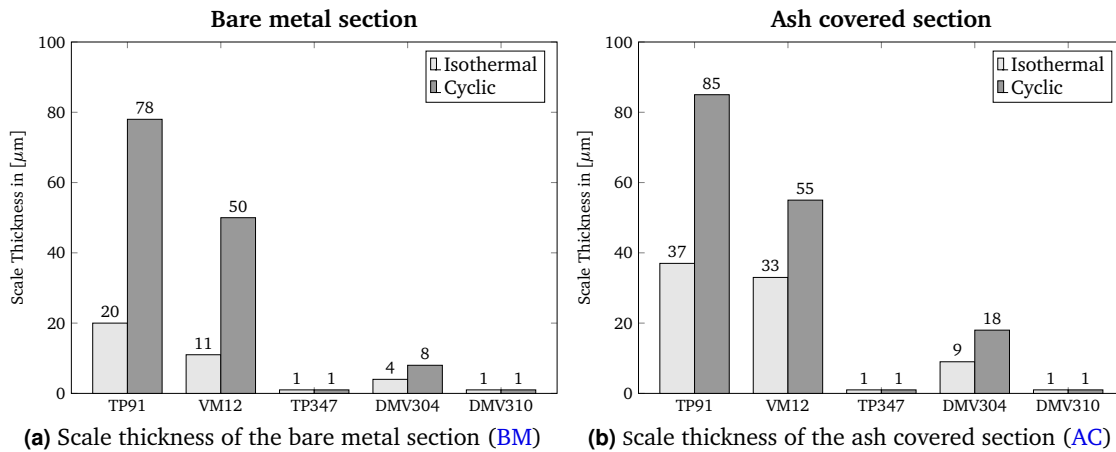


Figure 6.2.: Oxide scale comparison between bare metal and ash covered section

### 6.3. Effect of fly ash deposits

The five commercial alloys investigated were partly covered in ash leaving the uncovered bare alloy section to the corrosive gas mixture only. According to the results of scale thickness measurements the oxidation rate in the ash covered section was generally higher compared to the bare alloy section. This is also in agreement with several studies from the literature on coal ash corrosion [74, 101, 129–132]. As discussed in Section 3.3, fly ash deposits which are by themselves not corrosive can affect the corrosion rate of high temperature materials in two ways: first by acting as barriers between the metal and the corrosive gas and secondly, by reacting with the metal creating porous ash layers or zones and thereby creating a path for oxygen diffusion into the metal which increases the corrosion rate. With increasing thermal stress (e.g. during cycling) such layers will spall and a new oxide layer reforms which leads to metal loss or increased corrosion rate.

#### 6.3.1. Spallation

The reason for increased oxidation rate during cyclic heating and cooling can be explained as mismatch strains which are created between the oxide lattice and the base material because of different thermal expansion coefficients between the oxide and metal as discussed in Section 2.3.4. Metals normally have a higher thermal expansion than their respective oxides, and thus heating and cooling an oxidized metal can lead to a high enough strain in the oxide scale that can rupture or break down the scale. The oxide layers of the ferritic-martensitic steels TP91 and VM12-SHC were relatively spalled compared to the ones of the austenitic alloys. This is attributed to the formation of a fragile ash layers in the oxide which are vulnerable to spalling during thermal cycling.

## 6.4. Comparison of experimental results with thermodynamic modeling

In order to compare experimental and modeling results, it is important to also take into account the irregularities or deviations which might result from real firing conditions. The possible reasons for deviations include [50]:

- *Flue gas velocity*<sup>1</sup>: The flue gas from coal combustion consists of both gas species and aerosols flowing at different velocities in the boiler. This could have an influence on the local corrosion rate depending on the flue gas velocities and geometry of the boiler as a result of gas-side erosion.
- *Composition of mineral deposits*: The composition of fly ash particles is constantly changing and this also could influence the corrosion process. Furthermore, the actual composition of the ash deposits in a boiler is more complex than the one used for simulations.
- *Temperature*: The temperatures of alloys and flue gas fluctuate. This results in thermal stress which together with fly ash erosion and mechanical stress could lead to spallation of protective oxide scales exposing the 'fresh' metal surface to further corrosion attack. Additionally, elevated temperature gradients between the deposits and the material surface can lead to a speculative determination of temperatures for equilibrium calculations.
- *Kinetics*: Processes which are determined by kinetics (e.g. diffusion) can not be exactly described with thermodynamic models.

The correlation and differences between both results are discussed below taking into consideration the above mentioned reasons for deviations.

### Ferritic martensitic alloys

The ferritic–martensitic materials generally showed overall a good correlation with the modeling results. From the non-isothermal one-dimensional phase mappings for TP91 (Figure 3.7), the MeO (metal oxide) phase was the dominant phase and showed the possibility of a FeO, Fe<sub>2</sub>O<sub>3</sub>, and Cr<sub>2</sub>O<sub>3</sub> and MnO forming above 550 °C. This was the case of the oxide layer found in TP91 with a hematite outer layer and MnO inner layer as could be seen from the elemental mappings (Figures 5.15b and 5.35b). A possible spinel magnetite inner layer was calculated. The modeling predicted the formation of small quantities of pure solids such as Nb<sub>2</sub>O<sub>5</sub>. The results from EDS phase mappings indicated that the outer

---

<sup>1</sup>The maximum allowable flue gas velocity in the superheaters section is between 15 – 18 m/s for PF boilers with low or soft ash and around 12 – 14 m/s for PF boilers with abrasive ash due to gas-side erosion [91].

oxide layer was made up of Fe-O-Nb.  $\text{MoS}_2$  was predicted to occur only above 850 °C however at the test temperature of 650 °C, elemental mappings revealed the presence of molybdenum sulphide in the base metal. The spinel phase (made up of magnetite and Fe-Cr spinel) was superimposed above 650°C temperature, therefore small amounts were expected at the test temperature.

For the martensitic alloy VM12-SHC, the modeling results predicted a dominant spinel phase ( $\text{Fe}_3\text{O}_4$ ) followed by the BCC and MeO phase (made up of wustite, hematite, chromia and MnO) for temperatures up to 650 °C (Figure 3.8). EDS phase mappings however showed an overwhelming Fe-oxide (possibly hematite) outer layer followed by magnetite and Fe-Cr spinel (cf. Figures 5.17 and 5.37). MnO was formed as could be seen from the elemental mappings Figures 5.18a, 5.18b, 5.38a and 5.38b.  $\text{Cu}_2\text{S}$  which was suggested from modeling was not found to have formed.

### Austenitic alloys

The austenitic alloys showed varying consistency with modeling calculations. In TP347-HFG the spinel phase (mainly magnetite and Fe-Cr spinel) was dominant for the test temperature at 650 °C followed by the FCC phase, the MeO phase and small amounts of (Mn-Fe)S phase. However, a thin oxide phase was formed on the alloy which due to poor adhesion of the mount led to a partial damage of the layer making it difficult to fully analyze the layer. But EDS phase mappings (Figures 5.20 and 5.40) and elemental mappings Figures 5.41a and 5.41b revealed a Cr-O-Fe scale, which possibly was protective chromia and some magnetite according to the elemental mappings. There was Mn enrichment at the oxide-metal interface which indicated a Mn-oxide formation as predicted by from the calculations. Most important, this alloy suffered immensely from internal sulphidation attack primarily in form of Nb, Mo, Fe and Cr sulphides. This was unexpected from the calculations.

DMV304 HCu showed good correlation with modeling results. The outer oxide layer was hematite and the inner layer magnetite and Fe-Cr spinel as well as chromia together with MnO according to the elemental mappings (Figure 5.44b) and the EDS elemental phase mappings Figure 5.43. DMV310 N showed good correlation with the results from calculations. A corundum phase was predicted which was possibly protective as it was experimentally found. However, there was internal sulphidation in the experiments which was noticed in form of niobium sulphide but was not predicted from calculations. Instead, nickel sulphide was calculated.

### Fly ash chemistry

The results from modeling suggested for the given composition of fly ash, that no molten slag will form at the test temperature of 650 °C which was confirmed experimentally. Furthermore, the reaction of gas with the fly ash deposits was anticipated to reduce oxygen



partial pressures and increase sulphur and sulphur oxides which could alter the oxide chemistry. It was found, in most cases that the ash covered section of the test samples had significant sulphur either in the oxide or in the material.

Finally, thermochemical modeling calculations can be used to predict to a good approximation what types of solution, condensed phases or pure solids might form from the reaction of high temperature alloys with corrosive environments which could serve as a first step in studying these systems. However, experimental work is necessary to confirm or contrast the results as has been done in the study.



## 7. Conclusion

Coal-fired power plants especially baseload power plants are increasingly required to operate in a highly flexible or cyclic operating mode in order to accommodate the integration of RES into the generation mix. This trend is however set to increase even further in the near future and power plants must have to adjust to these new pattern. Although cycling is in its entirety not new to conventional units since demand has always also been variable (*demand-driven* cycling), this new mode of operation so-called *generation-driven* cycling is completely new to conventional coal-firing units especially baseload power plants. The technical demand for high operational flexibility includes frequent start-ups and shut-downs, load following operations, temperature ramping, two-shifting, just to name a few. Baseload plants are not used to this mode of operation unlike the medium and peak load counterparts which are designed specially for high flexibility. In order to stay in business baseload units will have to compete by eventually increasing flexible operation. This can have detrimental effects on vital plant components because this kind of operation will exceed originally intended design limits and subsequently lead to severe repercussions for the plants from material failure, forced outages, economic penalties among others. It is therefore important – in order to avoid unexpected material failures, reduce maintenance and operating cost, to analyze the corrosion/oxidation risks related to increased flexible or cyclic operation.

It was the goal of this study to analyze these risks and help provide answers to some of the questions such as how fast (oxidation rate) and what kind of corrosion mechanisms might occur under flexible operating conditions. The task was split into two: first thermochemical modeling of corrosion of high temperature corrosion of selected commercial coal boiler superheater and reheater materials, to get first insights of the problem, then carrying out experimental tests to obtain a clearer picture. The tests were subdivided into two parts: i.e. isothermal firing conditions and cyclic or flexible firing modes so as to be able to directly determine the impact of cycling on the plant materials. The five commercial alloys chosen for this study included two ferritic–martensitic materials; TP91 and VM12-SHCC and three austenitic materials TP347-HFG, DMV304 HCu and DMV310 N which are high temperature materials used in superheater and reheater components. The materials were exposed under isothermal and thermal cycling conditions for 1000 h each at 650 °C

metal surface temperature. The results from this study are summarized below and some suggestions and recommendations for future work are given.

### Experimental studies

- The oxidation rate of the materials increased significantly during thermal cycling conditions compared to isothermal conditions. This was especially the case for the ferritic-martensitic materials TP91 and VM12-SHC. Scale thickness measurements showed  $28\mu\text{m}$  for TP91 under isothermal conditions increasing to  $82\mu\text{m}$  under cyclic firing conditions. VM12 had  $22\mu\text{m}$  under isothermal conditions and  $52\mu\text{m}$  under cyclic conditions. The austenitic alloy DMV304 HCu showed moderate increase in oxidation rate with scale thickness measuring about  $7\mu\text{m}$  in isothermal conditions and  $13\mu\text{m}$  under thermal cycling conditions. TP347-HFG and DMV310 N showed quite good oxidation resistance with approximately  $1 - 2\mu\text{m}$  scale thickness under both isothermal and thermal cycling conditions. Overall, the austenitic materials performed better than the ferritic-martensitic materials. This result was confirmed by kinetic modeling studies. Increasing protection is related to the Cr-content of the materials as materials with less than 18 wt% Cr generally show less oxidation resistance. This is because a minimum of 12%-Cr is required in solid solution to form a protective film.
- Coal ash deposits change the stoichiometry of the oxide scale and consequently lead to a variation in the oxidation/corrosion rate of the materials. Sections covered with fly ash were found to have an increased oxide growth with layer thickness larger than the one of the bare alloy. This was mostly the case for the ferritic martensitic materials TP91 and VM12-SHC with significantly increased scale thickness under cycling modes.
- The formation of brittle ash layers or zones within oxide layers and on the oxide-metal interface that break and spall led to porous oxide layers open to more corrosion attack from the corrosive gas media. This effect is more pronounced in thermal cycling than under isothermal conditions especially for the ferritic martensitic alloys.
- Austenitic materials are vulnerable to grain boundary attack or cavitation/pitting. Although all the austenites showed good oxidation resistance some form of grain boundary attack was found to occur. DMV310 N which especially showed the best performance under both test conditions had a profound increase in cavitation attack under thermal cycling conditions.
- Internal sulphidation attack was found in all the austenitic materials in various forms as Mo, Nb, Cr, or Fe sulphides. However, this could not be attributed to either cycling

or ash deposits as this phenomenon was found to occur both under thermal cycling and isothermal conditions as well as in the bare metal and the ash covered layer.

- MnO was found in almost all the material sections with larger oxide scale thickness. In the ferritic–martensitic steels it was a substantial part of the inner scale close to the metal substrate (oxide-metal interface) while in the austenitic steels it was either in substantial amounts in the oxide scale or found as traces. This Mn was completely depleted of iron but rich in Cr in some cases suggesting a Mn-Cr spinel. This is also qualitatively confirmed by thermodynamic modeling. MnO formation can therefore play a negative role in the oxidation of the materials due to the reduction of Cr in solid solution. DMV310 N showed no traces of Mn-oxide and had the best performance of all the materials.

### Thermodynamic modeling studies

- The alloy composition is critical in the corrosion behavior of a material. Fe-Cr-Ni alloys will generally form a chromia ( $\text{Cr}_2\text{O}_3$ ) scale which if compact will provide protection for the material against corrosion attack. However, this leads to the depletion of Cr from the material which could cause the formation metal carbide phases such as  $\text{M}_{23}\text{C}_6$  and can lead to inter-crystalline corrosion and intergranular attacks. Some grain boundary attack was found especially in the austenitic alloys.
- The role of the partial pressures of the corrosive gas species and the temperature of the system cannot be overstressed. Non-isothermal one–dimensional alloy phase mappings clearly show the influence of temperature on the alloy system. Increasing or decreasing partial pressures of one or more gas components or reversed together with changing temperatures can lead to completely different stable products being formed.
- The reaction of the ash deposit with the gas mixture and metal oxide is complex. This leads to decreasing oxygen partial pressures, however depending on the flue gas concentration which can increase sulphur and sulphur oxides partial pressures. This increase in sulphur will alter the chemistry of an otherwise protective oxide layer and cause more attack.

### Recommendations for future studies

The present study has been vital to evaluate the oxidation and corrosion risks on commercial boiler superheater and reheater materials associated with increased thermal cycling or flexible operation. The oxidation kinetics have been analyzed as well as the corrosion mechanisms prone to occur on commercial boiler superheater and reheater materials. The

study has opened up the way for future studies in this particular field of research. Some recommendations and suggestions for future works are given below.

For high temperature corrosion testing, it would be of particular interest to investigate under different flue gas atmospheres with varying concentrations of the individual gas species to analyze sulphidation ( $H_2S$ ), carburization (CO) etc., using different fly ash deposits or even synthetic ash deposits (with different levels of sulphates, chlorides). The impact of flexible operation impact on coatings and welds, longer exposure duration to analyze the precipitation of Cr-carbides especially in austenitic steels with relatively good oxidation resistance, tests at different temperatures especially for high Cr alloys such as DMV310 N have to be carried out. Finally, using different thermal cycling modes will also be beneficial towards a better understanding of the problem.

# A. Thermochemical Results Table

## Structure

**Table A.1.:** TP91 reaction with corrosive flue gas at 650 °C (showing only stable phases)

T = 650.00 C				
P = 1.0000E+00 atm				
V = 3.3823E+00 litre				
STREAM	CONSTITUENTS	AMOUNT [g]		
	CO2	2.81E-01		
	O2	2.39E-02		
	N2	4.11E-01		
	SO2	1.43E-03		
	H2O	1.34E-01		
	Fe	8.86E+01		
	Cr	8.75E+00		
	Ni	4.00E-01		
	Mo	9.50E-01		
	Mn	4.50E-01		
	Al	2.00E-02		
	Si	3.50E-01		
	C	1.05E-01		
	S	1.00E-02		
	P	2.00E-02		
	Nb	8.00E-02		
	N	5.00E-02		
	V	2.15E-01		
		EQUIL AMOUNT	VOL%	FUGACITY
PHASE: GAS		[bar]		
	N2_FactPS	1.31E+02	5.23E+01	5.23E-01
	H2_FactPS	4.82E+01	1.93E+01	1.93E-01
	CO_FactPS	3.35E+01	1.34E+01	1.34E-01
	CO2_FactPS	2.13E+01	8.50E+00	8.50E-02
	H2O_FactPS	1.48E+01	5.91E+00	5.91E-02
	CH4_FactPS	1.51E+00	6.06E-01	6.06E-03

continued on next page

Table A.1 (continued)

H2S_FactPS	3.50E-02	1.40E-02	1.40E-04
NH3_FactPS	1.57E-02	6.27E-03	6.27E-05
(P2O3)2_FactPS	8.04E-03	3.21E-03	3.21E-05
COS_FactPS	7.76E-04	3.10E-04	3.10E-06
HCN_FactPS	7.31E-05	2.92E-05	2.92E-07
H2CO_FactPS	1.02E-05	4.10E-06	4.10E-08
...	...	...	...
PHASE: BCC_A2#1	gram	WEIGHT %	ACTIVITY
Al1C3_FSstel	3.59E-21	1.30E-20	8.38E-34
Cr1C3_FSstel	1.05E-11	3.79E-11	2.25E-32
Fe1C3_FSstel	2.29E-03	8.30E-03	2.12E-23
Mn1C3_FSstel	6.14E-12	2.23E-11	1.62E-11
Mo1C3_FSstel	3.70E-06	1.34E-05	1.16E-17
Nb1C3_FSstel	3.77E-16	1.37E-15	5.64E-36
...	...	...	...
TOTAL :	2.76E+01	1.00E+00	1.00E+00
PHASE: M23C6	gram	WEIGHT %	ACTIVITY
Cr20Cr3C6_FSstel	4.39E-14	1.06E-12	5.96E-155
Fe20Cr3C6_FSstel	3.96E-08	9.60E-07	1.16E-24
Mn20Cr3C6_FSstel	2.47E-19	6.00E-18	4.00E-172
Ni20Cr3C6_FSstel	1.25E-12	3.04E-11	2.36E-59
V20Cr3C6_FSstel	1.01E-21	2.45E-20	9.61E-206
Cr20Fe3C6_FSstel	1.45E-07	3.51E-06	2.08E-135
Fe20Fe3C6_FSstel	1.31E-01	3.17E+00	4.05E-05
...	...	...	...
TOTAL :	4.13E+00	1.00E+00	1.00E+00
PHASE: M2O3 (Coru)#1	gram	WEIGHT %	ACTIVITY
Al2O3_FToxid	1.43E-02	7.73E-01	1.01E-02
Cr2O3_FToxid	1.75E+00	9.41E+01	8.90E-01
Fe2O3_FToxid	9.46E-02	5.10E+00	8.96E-03
Mn2O3_FToxid	1.91E-06	1.03E-04	1.12E-12
TOTAL :	1.86E+00	1.00E+00	1.00E+00
PHASE: Olivine	gram	WEIGHT %	ACTIVITY
Fe1Fe1Si104_FToxid	2.26E+00	8.89E+01	8.89E-01
Mn1Mn1Si104_FToxid	5.35E-03	2.11E-01	2.13E-03
Fe1Mn1Si104_FToxid	5.49E-02	2.16E+00	2.17E-02
Mn1Fe1Si104_FToxid	2.20E-01	8.68E+00	8.71E-02
Fe1Ni1Si104_FToxid	1.42E-04	5.58E-03	6.06E-05
Ni1Fe1Si104_FToxid	4.83E-06	1.90E-04	2.30E-06
Mn1Ni1Si104_FToxid	1.38E-05	5.44E-04	1.99E-06
Ni1Mn1Si104_FToxid	1.17E-07	4.63E-06	1.06E-11
Ni1Ni1Si104_FToxid	3.03E-10	1.19E-08	1.57E-10
TOTAL :	2.54E+00	1.00E+00	1.00E+00
Pure solids	g		ACTIVITY

continued on next page



Table A.1 (continued)

---

FeV2O4(s)_FactPS	4.68E-01	1.00E+00
MoS2(s)_FSstel	1.99E-01	1.00E+00
Nb2O5(s)_FSstel	1.14E-01	1.00E+00

---

end



## B. Supplementary Figures

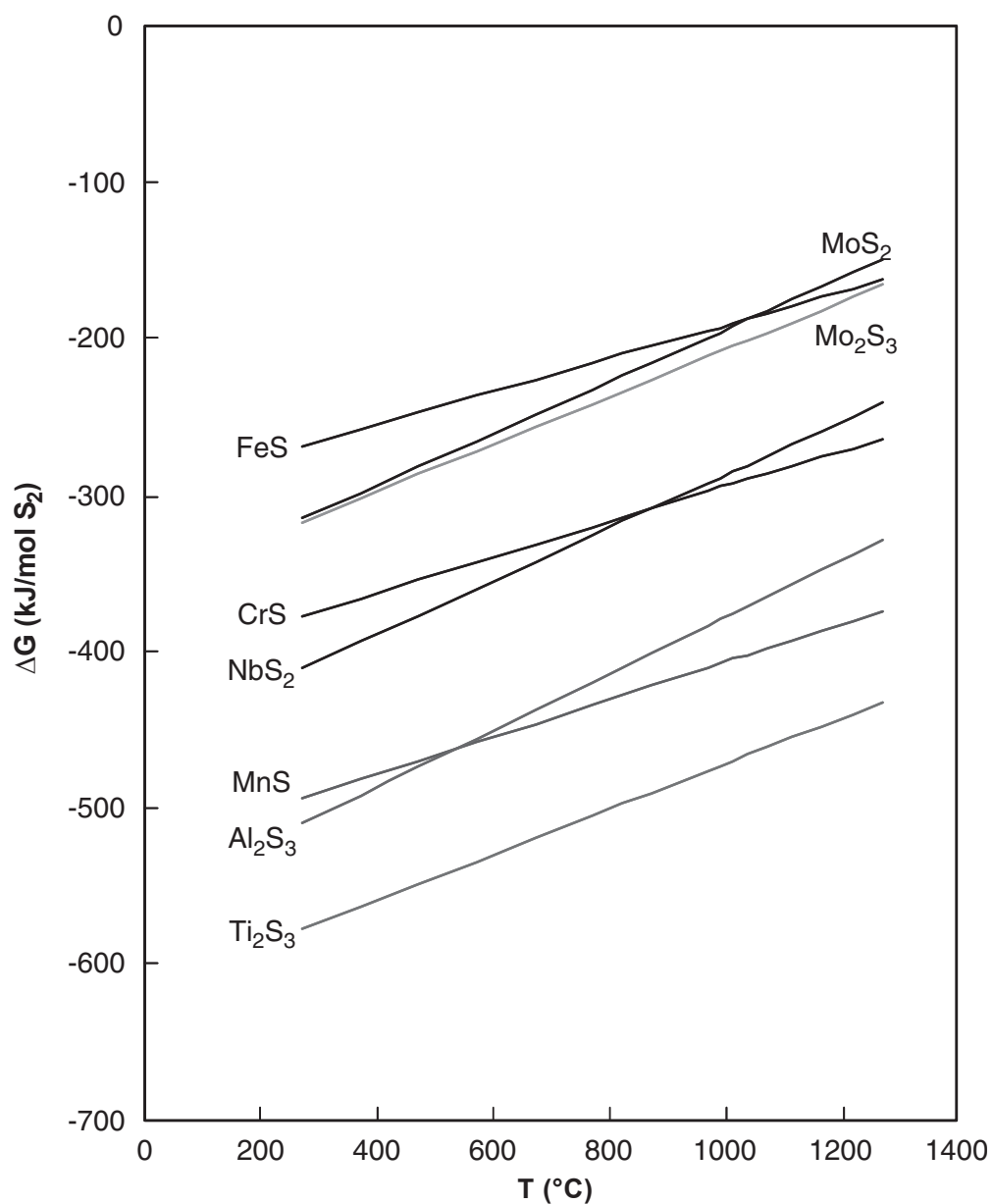


Figure B.1.: Ellingham diagram for selected sulphides [46]

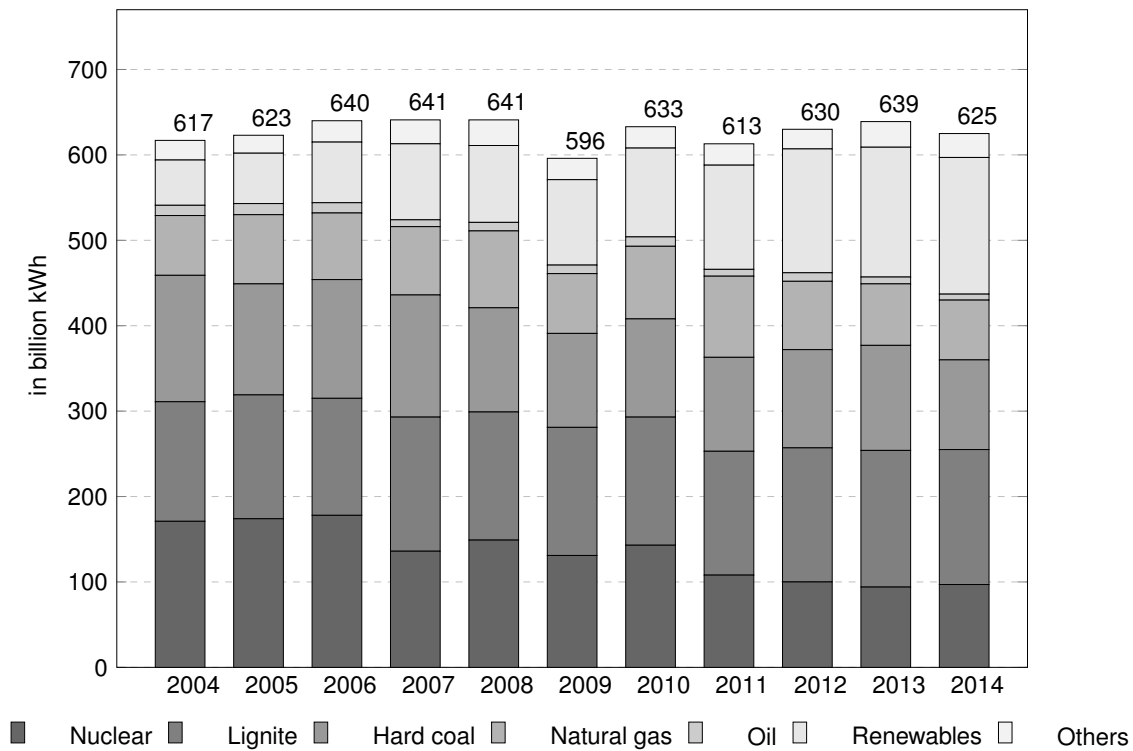


Figure B.2.: Gross Electricity Generation in Germany 2004 – 2014

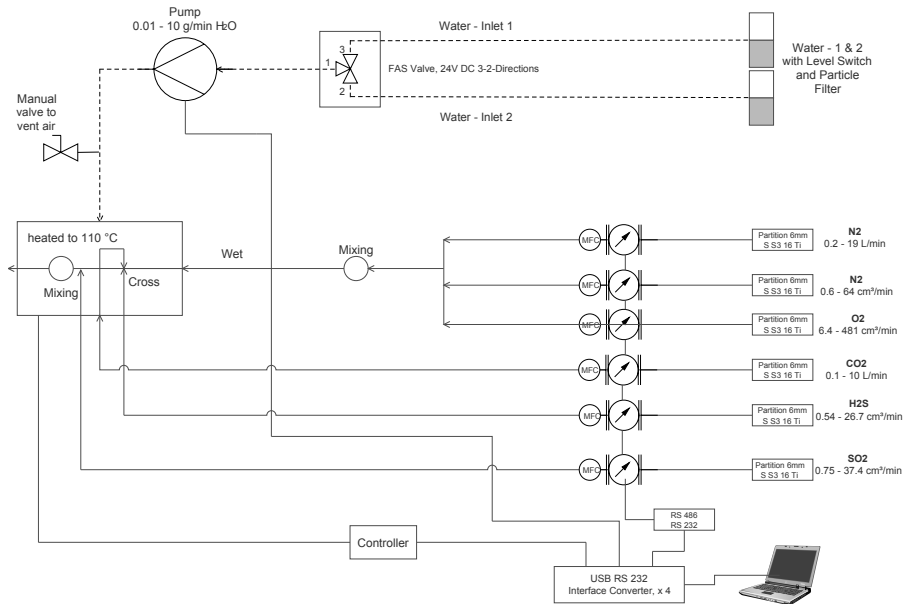


Figure B.3.: Process and Instrumentation Diagram of Gas Mixing Station

## C. Glossary

A B C D E F G H I J K L M N O P Q R S T U V W X Y Z

### A

**Annealing:** Annealing is a heating and cooling process but with relatively slow cooling [128]. This usually involves heating to and holding at a favorable temperature and then cooling at a suitable rate, mainly to soften metallic materials [133]. The operating temperature and cooling rate all depend on the material undergoing treatment as well as the goal of the treatment process. There are several other reasons for such a heat treatment and these include: stress removal; to cause softness; to change physical properties such as the toughness, ductility, magnetic or electric properties etc.; to change the crystalline structure; remove gases or obtain a fixed microstructure [128]. (see also *process annealing* and *normalizing*).

**Austenitic steels:** Austenitic steels or alloys are the most widely used type of stainless alloys. They have a wide range of application from less corrosive to aggressive and very corrosive atmospheres. They are non-magnetic highly favorable for industrial process applications. They have a face-centered cubic (FCC) austenitic structure from less

than zero up about melting temperatures due to the addition of alloying components such as nickel and manganese. They cannot be hardened through heat treatment but through cold work they can be strain hardened.

To obtain the austenitic structure about 18%-Cr and 8%-Ni are usually added to induce the transition from ferritic to austenitic. They are relatively very rough, weldable, formable compared to ferritic steels. The nickel serves to improve the corrosion resistance in less corrosive environment (such as foods, organic and soft inorganic chemicals as well as a broad range of most natural atmospheres).

Austenitic alloys are also stabilized, e.g. alloy 321 is stabilized with titanium while alloy 347 is stabilized with niobium. Also, to prevent carbide precipitation which is the main cause of intergranular corrosion in these materials, the carbon content is usually lowered to a minimum ( $< 0.03\% \text{ C}$ ) [128]. [Back to Menu](#)

**E**

**Equivalent forced outage rate (EFOR)** is a measure of a plant's unreliability. The EFOR for baseload power plants is about 6.4%. There are also other measures used to assess a plant's reliability and these include: the unit capability factor, the equivalent availability factor, and unplanned capability loss factor [30]. [Back to Menu](#)

**F**

**Forced Outage** : A force outage is an unplanned component failure or any other situation where the unit has to be removed from service instantly within six hours or before the end of the next weekend [30]. [Back to Menu](#)

**H**

**Hardening**. This is the process of heating and quenching (cooling) certain iron-based alloys from a temperature either within or above the critical range to obtain a hardness higher to that produced when the alloy is not cooled or quenched. This process is only usually use in the formation marten-site. [Back to Menu](#)

**L**

**Load-following**: Load following is the mode of operation where the plant is on for more than 48 hours at a time but has to change its output accordingly to follow the daily demand trend for electricity. This is the demand driven cycling which baseload

plants are used to as the demand daily electricity demand pattern is highly predictable. This kind of cycling has little impacts on the metal and steam temperatures as can be seen from [Figure 2.3 \[92\]](#). [Back to Menu](#)

**M**

**Martensitic alloys**: Martensitic alloys which have very high hardness and strength are obtained by heating above critical temperature (above 870 °C) and then quenched (rapid cooling) to form martensite microstructure. To increase corrosion resistance and ductility, the alloys are usually tempered or stress relieved between 150 – 370 °C. They are also hardenable because of the transformation from body-centered cubic (BCC) to body-centered tetragonal (BCT). [Back to Menu](#)

**N**

**Nominal power**: Nominal power, output or capacity, is the maximum potential full load power of a plant which is not necessarily the same as the actual full load output of the plant. The ratio of the actual output to maximum output over a given period of time is known as the *capacity factor*. Dispatchable (regulated) plants like coal and nuclear have a high capacity ratio (which depends on the technical capabilities of the plant) than v-RES power from solar and wind that depend on the weather condition.

**Normalizing** (heat treatment). This involves heating iron-based alloys to about 500 °C above the critical temperature range, then cooled in still air below that range at ordinary temperature. [Back to Menu](#)

## O

**On-load cycling:** On-load cycling is the mode of operation in which, e.g. the plant operates at base load during the day and then ramps down to minimum stable generation overnight [92]. [Back to Menu](#)

## P

**Process annealing:** Process annealing is the process of heating iron-based alloys to a temperature less than or near the lower critical temperature limit, normally between 540 to 725C. [Back to Menu](#)

## Q

**Quenching.** This is rapid or fast cooling by immersion in liquids or gases or by contact with metal. [Back to Menu](#)

## R

**Ramping:** During ramping the output of the plant is varied between minimum and full levels in order to follow changes in power demand [30].

**Residual load:** the difference between actual power demand and the feed-in from intermittent non-dispatchable generators [17]. It can be summarized in [Equation \(C.1\)](#) as follows:

$$\text{Residual Load} = \text{Demand} - \text{RES} \quad (\text{C.1})$$

*Example:* on a windy night when wind power is high, no further fossil power generation will be needed. In this case, the residual load will be negative because demand is low at night and feed in from wind power is high (i.e. there is an overcapacity). On the other hand, on a day with low wind and sun feed in and there is also high demand for power, will be positive and in this case, conventional baseload plants are expected to compensate for this [22]. [Back to Menu](#)

## S

**Sporadic operation:** This involves irregular or occasional operation for periods of less than two weeks and then the plant is shutdown for more than several days [92].

**Start ups:** This entails starting of a unit that is offline; there are three types of starts, these include: *hot*, *warm*, or *cold*, depending on the temperatures of the metal in the boiler or turbine [30]. *Hot* starts are generally defined to have very high boiler or turbine temperatures between 370 °C to 485 °C, and less than 8 to 12 hours off-line. *Warm* starts have boiler or turbine temperatures between 120 °C to 370 °C and have been off-line for 12 to 48 hours. *Cold* starts are ambient temperature starts, the temperature of the boiler and turbine temperatures below fracture appearance transition temperatures (*FATT*) i.e. 120 °C or less, and have been offline for 48 to 120 hours. These definitions may vary depending on the unit size, manufacturer and dispatcher/Independent System Operator (*ISO*) definitions. [Back to Menu](#)

## T

**Tempering.** This is the process of reheating hardened steel to a temperature below the lower critical temperature, followed by cooling at a desired rate. This process is also known as drawing.

**Two-shifting:** Two shifting is the mode of operation where the plant is started up and shut down once a day i.e. running during the day and stopping during the night; “*Spinning reserve*”, or the maximum technical load is kept on-line (at very low load) especially when there is low demand [5, 92]. *Double two-shifting* is the operating mode in which the plant is started up and shut down twice a day. In this case it is called 4-shifting [30]. [Back to Menu](#)

## W

**Wear and Tear:** *Wear* is used to refer to the case where a component reaches the end of its natural life through ordinary causes such as thermal fatigue, corrosion. *Wear* can however be accelerated. *Tear* is used to refer to an unusual event that accelerates the life, for instance during poor control of operating conditions. *Tear* can occur during base-load operations, but it is generally more pronounced during cycling operations [30].

**Weekend shutdowns:** As the name implies the plant shuts down at weekends. This mode is usually combined with two-shifting and load-following operations. Boiler shutdown is less complicated than start-up but emphasis is laid on safety and protection of unit materials. There are basically two ways in which a plant is shut down: a controlled shutdown where the combustion rate is slowly reduce, or an emergency emergency. [Back to Menu](#)



# Bibliography

- [1] Dimitri Pescia, Patrick Graichen, Mara Marthe Kleiner, and David Jacobs. Understanding the *Energiewende*. Technical Report 080/06-H-2015/EN, Agora Energiewende, October 2015.
- [2] Ray King and Laurent Demortier. Flexible generation for a smart grid world. *Electric Light & Power and POWERGRID International (online publications)*, August 2010.
- [3] Craig Morris and Martin Pehnt. *Energy Transition, The German Energiewende*. An initiative of the Heinrich Böll Foundation, Schumannstr. 8, 10117 Berlin, Germany, July 2015.
- [4] Stephen Stec and Besnik Baraj. *Energy and Environmental Challenges to Security*. Springer Science & Business Media, 2009.
- [5] Giuseppe Lorubio. Flexible generation: Backing up renewables. Technical Report D/2011/12.105/47, eurelectric – ELECTRICITY FOR EUROPE, October 2011.
- [6] Verband kommunaler Unternehmen e. V. (VKU). *Energiezukunft gestalten: Perspektiven kommunaler Energieerzeugung*. Königsdruck, Berlin, 2012.
- [7] Steve Hesler. Mitigating the effects of flexible operation on coal-fired power plants. *Power*, 155(8):p50, August 2011.
- [8] Eventful Power. Power plant flexibility, 13 - 15 march 2013, Vienna, europe 2013, 2013.
- [9] Steven A Lefton and Phil Besuner. The cost of cycling coal fired power plants. *Coal Power Magazine*, 2006:16 –20, Winter 2006.
- [10] Steven A. Lefton and Douglas Hilleman. Make your plant ready for cycling operations. *Power*, 155(8):p58, August 2011.
- [11] Sebastian Strunz. The german energy transition as a regime shift. *Ecological Economics*, 100:150 – 158, 2014.
- [12] Dagmar Dehmer. The German *Energiewende*: The First Year. *The Electricity Journal*, 26(Issue 1):71 – 78, January/February 2013.

- [13] Staffan Jacobsson and Volkmar Lauber. The politics and policy of energy system transformation – Explaining the german diffusion of renewable energy technology. *Energy Policy*, 34, 2006.
- [14] International Renewable Energy Agency ([IRENA](#)). Remap 2030, a renewable energy roadmap. Renewable Energy Prospects: Germany. Technical report, [IRENA](#), November 2015.
- [15] Wolf-Peter Schill. Residual load, renewable surplus generation and storage requirements in germany. Deutsches Institut für Wirtschaftsforschung (DIW Berlin), 2013.
- [16] Johannes Lambertz, Hans-Wilhelm Schiffer, Ivan Serdarusic, and Hendrik Voß. Flexibilität von kohle- und gaskraftwerken zum ausgleich von nachfrage- und einspeiseschwankungen. *Energiewirtschaftliche Tagesfragen (et) ; Zeitschrift für Energiewirtschaft, Recht, Technik und Umwelt*, 67(7):16 – 20, 2012. *Energiewirtschaftliche Tagesfragen* 62. Jg. (2012) Heft 7.
- [17] Wolf-Peter Schill. Residual load, renewable surplus generation and storage requirements in germany. *Energy Policy*, 73:65 – 79, 2014.
- [18] Hartmut Spliethoff, Arnim Wauschkuhn, and Christian Schuhbauer. Anforderungen an zukünftige kraftwerke. *Chemie Ingenieur Technik*, 83(11):1792 – 1804, 2011.
- [19] Deutsche Energie Agentur (German Energy Agency) ([dena](#)). Flexibilität von Bestandskraftwerken - Entwicklungsoptionen für den Kraftwerkspark durch Retrofit. Workshop Ergebnispapier, February 2013.
- [20] Jan Keil. The german energy transition – issues and perspectives. AICGS, December 2012.
- [21] Arbeitsgruppe Erneuerbare Energien-Statistik (Working Group on Renewable Energy-Statistics) ([AGEE-Stat](#)). Development of renewable energy sources in germany 2014, 2015.
- [22] Andreas Pickard and Gero Meinecke. The future role of fossil power generation. *energize*, 6:19 – 22, August 2013.
- [23] F. Gutiérrez-Martín, R.A. Da Silva-Álvarez, and P. Montoro-Pintado. Effects of wind intermittency on reduction of co<sub>2</sub> emissions: The case of the spanish power system. *Energy*, 61(2013):108 – 117, November 2013.
- [24] Deutsche Energie Agentur (German Energy Agency) ([dena](#)). Integration der erneuerbaren Energien in den deutsch-europäischen Strommarkt. Workshop Ergebnispapier, August 2012.

- [25] Ahmed Shibli. *Coal Power Plant Materials and Life Assessment: Developments and Applications*. Elsevier, 2014. Google Books.
- [26] Eleanor Denny and Mark O'Malley. The impact of carbon prices on generation-cycling costs. *Energy Policy*, 37(4):11204 – 1212, April 2009.
- [27] Benjamin Häusinger, Julian Dieler, and Jana Lippelt. Kurz zum Klima: Kohlekraft im Schatten der Snergiewende. *ifo Schnelldienst*, (22), 2012.
- [28] Kenneth van den Bergh and Erik Delarue. Facilitating variable generation of renewables by conventional power plant cycling. Working paper: Energy and environment, University of Leuven (KU Leuven), Belgium, March 2014.
- [29] John Gostling. Two shifting of power plant: Damage to power plant due to cycling - a brief overview. *OMMI – Power Plant: Operation Maintenance and Materials Issues*, 1(1), April 2002.
- [30] Jaquelin Cochran, Debra Lew, and Nikhil Kumar. Flexible coal – evolution from baseload to peaking plant. Technical report, National Renewable Energy Laboratory and Intertek, December 2013.
- [31] Matti Rautkivi and Melle Kruisdijk. Flexible energy allows efficient and cost effective integration of renewables into power systems. *Wärtsilä Technical Journal*, 2013.
- [32] Kenneth van den Bergh, Erik Delarue, and William D'haeseleer. The impact of renewable injections on cycling of conventional power plants. In *Proceedings of the 10th Int. Conference on the European Energy Market*, number 10. University of Leuven (KU Leuven), Belgium, May 2013.
- [33] Sean Connolly, Keith Parks, and Charles Janecek. Wind induced coal plant cycling costs and the implications of wind curtailment for public service company of colorado. Technical report, Xcel Energy, 2011.
- [34] P. Keatley, A. Shibli, and N.J. Hewitt. Estimating power plant start costs in cyclic operation. *Applied Energy*, 111(2013):550 – 557, November 2013.
- [35] Darryl Taylor and Akber Pasha. Economic operation of fast-starting HRSGs. *Power Magazine*, 2010.
- [36] A. Mirandola, A. Stoppato, and E. Lo Casto. Evaluation of the effects of the operation strategy of a steam power plant on the residual life of its devices. *Energy*, 35(2):1024 – 1032, 2010.

- [37] G. Brauner. Erneuerbare energie braucht flexible kraftwerke - szenarien bis 2020. studie der energietechnischen gesellschaft im vde (etg). Technical report, VDE-(ETG), 2012.
- [38] J. Kahlert, V. Schüle, and H. Altmann. Möglichkeiten und grenzen zur optimierung betrieblicher flexibilität in existierenden kraftwerken. *VGB PowerTech – International Journal for Electricity and Heat Generation*, 93(Heft 1/2):59–63, 2013.
- [39] Hans Christian Schröder and Achim Foos. From maintenance expert to operations analyst. *European Energy Review*, November 2014.
- [40] Kenneth Engblom. Flexible power generation enabling wide integration of res. In *The European Power Generation Strategy Summit & Power Project Financing and New Technologies Forum*. Prague | Czech Republic, December 2012.
- [41] Ralf Bürgel, Hans Jürgen Maier, and Thomas Niendorf. *HandbuchHochtemperatur-Werkstofftechnik. Grundlagen, Werkstoffbeanspruchungen, Hochtemperaturlegierungen und -beschichtungen*. Vieweg+Teubner Verlag. Springer Fachmedien Wiesbaden GmbH 2011, March 2011.
- [42] Pierre R. Roberge. *Handbook of Corrosion Engineering*. McGraw-Hill, 2000. ISBN 0-07-076516-2.
- [43] Pierre R. Roberge. *Corrosion Engineering: Principles and Practice*. McGraw-Hill, 2008.
- [44] N. Birks, G. H. Meier, and Frederick S. Pettit. *Introduction to the High-Temperature Oxidation of Metals*. Cambridge University Press, 2<sup>nd</sup> edition, 2006.
- [45] R. Winston Revie and Herbert H. Uhlig. *Corrosion and Corrosion Control: An Introduction to Corrosion Science and Engineering*. John Wiley & Sons, Inc., 4<sup>th</sup> edition, 2008.
- [46] David John Young. *High Temperature Oxidation and Corrosion of Metals*, volume 1 of *Elsevier Corrosion Series*. Elsevier Ltd, 2008. ISBN: 978-0-08-044587-8 ISSN: 1875-9491.
- [47] P. R. Roberge. *Corrosion Engineering: Principles and Practice*. McGraw-Hill, 2008.
- [48] Lawrence J. Korb and David L. Olson. *ASM Handbook Vol. 13, Corrosion*, volume 13. ASM International, 1992. ISBN 0-87170-007-7 (v.1).
- [49] John D. Ramshaw. Fugacity and activity in a nutshell. *Journal of Chemical Education*, 72(7):601 – 603, July 1995.

- [50] B. Meyer and H. Gutte. Thermochemische modellierung der rauchgasseitigen korrosion von hochtemperatur-stählen beim einsatz in steinkohle- und braunkohle-gefeuerten dampferzeugern, *Institut für Energieverfahrenstechnik und Chemieingenieurwesen*, IEC; Abschlussbericht, April 2002.
- [51] Arabinda Sarangi and Bidyapati Sarangi. *Alternatives Routes to Iron Making*. PHI Learning Private Limited, 2nd edition, January 2016.
- [52] Stephen D. Cramer and Bernard S. Covino-Jr. *ASM Handbook Vol. 13A, Corrosion: Fundamentals, Testing, and Protection*, volume 13 A. ASM International, 2003.
- [53] A. S. Khanna. *Introduction to High Temperature Oxidation and Corrosion*. ASM International, March 2002. ISBN-10: 0871707624; ISBN-13: 978-0871707628.
- [54] Russell D. Kane. High-temperature gaseous corrosion. In *Corrosion: Fundamentals, Testing, and Protection*, volume 13a of *ASM Handbook*, pages 572 – 590. ASM International, 2003.
- [55] George Y. Lai. *High-temperature Corrosion and Materials Applications*. ASM International, December 2007. ISBN-10: 0871708531; ISBN-13: 978-0871708533.
- [56] Robert H. Perry, Don W. Green, and James O. Maloney. *Perry's Chemical Engineers' Handbook*. The McGraw-Hill Companies, Inc., 7th ed. edition, 1997.
- [57] ASM International. *ASM Handbook, Volume 3: Alloy Phase Diagrams*, volume 3. ASM International, 1992.
- [58] A. Kanni Raj. *CREEP: Cases with 310S Alloy*. 1st edition, April 2015.
- [59] David Baxter and Liisa Heikinheimo. Opticorr guide book: Optimisation of in-service performance of boiler steels by modelling high temperature corrosion. Technical Report Research Notes 2309, Vtt Tiedotteita, 2005.
- [60] Herbert Uhlig. *Uhlig's Corrosion Handbook*. John Wiley & Sons, Inc., 3rd edition, 2011.
- [61] Wei Gao and Zhengwei Li. *Developments in high-temperature corrosion and protection of materials*. Woodhead Publishing Limited, Cambridge England and CRC Press LLC, 2008.
- [62] S. Biroasca, G. D. West, and R. L. Higginson. Microstructural investigation of the oxide scale on low carbon steel. *Metal*, 2005.
- [63] David Talbot and James Talbot. *Corrosion Science and Technology*. CRC Press, 1998.

- [64] V. B. Trindade, U. Krupp, PH. E-G. Wagenhuber, S. Yang, and H-J. Christ. The different role of alloy grain boundaries on the oxidation mechanisms of cr-containing steels and ni-base alloys at high temperatures. In M. Schütze and W. J. Quadackers, editors, *Novel Approaches to Improving High Temperature Corrosion Resistance*, number 47. Woodhead Publishing Limited and CRC Press LLC, 2008.
- [65] L L Shreir. *Corrosion: Metal/Environment Reactions*, volume 1. Newnes-Butterworths, 2nd edition, 1976.
- [66] R. Viswanathan, J. Sarver, and J.M. Tanzosh. Boiler materials for ultra supercritical coal power plants-steamside oxidation. *Materials Engineering and Performance*, 15(3):255–274, 2006.
- [67] B. Meyer and H. Gutte. Thermodynamic modelling of steel corrosion in flue gas atmospheres. *VGB PowerTech*, 2:82 – 85, 2002.
- [68] Nestor Perez. *Electrochemistry And Corrosion Science*. Kluwer Academic Publishers, 2004.
- [69] John Stringer and Ian G. Wright. Current limitations of high temperature alloys in practical applications. *Oxidation of Metals*, 44(1/2):265–308, 1995.
- [70] S. Mrowec and K. Przybylski. Transport properties of sulfide scales and sulfidation of metals and alloys. *Oxidation of Metals*, 23(3/4), 1985.
- [71] K.N. Strafford and J.R. Bird. The kinetics of sulphidation of niobium. *Journal of the Less Common Metals*, 68(2):223 – 228, December 1979.
- [72] J. H. Devan, H. S. Hsu, and M. Howell. Sulfidation/oxidation properties of iron-based alloys containing niobium and aluminum. Technical Report ORNL/TM-11176, Oak Ridge National Laboratory, May 1989.
- [73] Stephen D. Cramer and Jr Bernard S. Covino, editors. *ASM Handbook. Volume 13C Corrosion: Environments and Industries*. ASM International, 2006.
- [74] K. Natesan, A. Purohit, and D. L Rink. Fireside corrosion of alloys for combustion power plants. Technical report, Argonne National Laboratory, 2002. Power Plant Chemistry.
- [75] K. Natesan. High-temperature corrosion in power-generating systems. Technical report, Argonne National Laboratory, 9700 S Cass Avenue, Argonne, IL 60439, 2002.
- [76] Michael S. Gagliano, Horst Hack, and Greg Stanko. Fireside corrosion resistance of proposed usc superheater and reheater materials: Laboratory and field test results.

- In *The 2008 Clearwater Coal Conference*, volume 33th International Technical Conference on Coal Utilization & Fuel Systems. Foster Wheeler North America Corp., 2008.
- [77] S. Van Weele and J. L. Blough. Literature search update: Fireside corrosion testing of candidate superheater tube alloys, coatings, and claddings. Technical Report Project N.: 9-61-5329, Foster Wheeler Development Corporation, 1990.
- [78] J. L. Blough. Fireside corrosion testing of candidate superheater tube alloys, coatings, and claddings – phase ii field testing. Technical report, Foster Wheeler Development Corporation, 12 Peach Tree Hill Road Livingston, New Jersey 07039, 1996.
- [79] Philip A. Schweitzer. *Encyclopedia of Corrosion Technology*. Marcel Dekker, Inc., 2<sup>nd</sup> edition, 2004. Revised and Expanded, New York, Basel.
- [80] J. P. Abellan, T. Olszewski, G. H. Meier, and L. Singheiser. Scale formation mechanisms of martensitic steels in high CO<sub>2</sub>/H<sub>2</sub>O-containing gases simulating oxyfuel environment. *Microscopy of oxidation 7*, University of Chester, UK, September 2008.
- [81] Juan Carlos Nava and Jeff Henry. Material degradation mechanisms in coal-fired boilers. *Materials at high temperatures*, 20(No. 1):pp. 55–60, 2003.
- [82] D. Lopez-Lopez, A. Wong-Moreno, and L. Martinez. Carburization process involved in boiler-tube failures. *Corrosion Science*, 35(5–8):1151–1158, 1993.
- [83] Steven C. Kung, R.J. Seely, Phillip Daniel, and Babcock & Wilcox. Effect of chlorine on furnace wall corrosion in utility boilers. In *CORROSION 96*, March 24 - 29 1996. NACE International.
- [84] A.J. Minchener and J.T. McMullan. Clean coal technology r, d&d: Significant achievements of european coal and steel community r&d programmes in the development of clean coal power generation technology, February 2007.
- [85] M. Schütze, M. Malessa, S. Y. Coleman, L. Niewolak, and W. J. Quadackers. Influence of cycling parameter variation on thermal cyclic oxidation testing of high temperature materials (cotest). In M. Schütze and W. J. Quadackers, editors, *Novel Approaches to Improving High Temperature Corrosion Resistance*, number 47. Woodhead Publishing Limited and CRC Press LLC, 2008.
- [86] M. Schütze and M. Malessa. Reliable assessment of high temperature oxidation resistance by the development of a comprehensive code of practice for thermocycling oxidation testing (cotest). In M. Schütze and W. J. Quadackers, editors, *Novel Approaches to Improving High Temperature Corrosion Resistance*, number 47. Woodhead Publishing Limited and CRC Press LLC, 2008.

- [87] R.W. Cahn and P Haasen. *Physical Metallurgy, Volume 1*. Elsevier, 4th edition, 1996.
- [88] James L. Smialek and Judith V. Auping. COSP for Windows – strategies for rapid analyses of cyclic-oxidation behavior. *Oxidation of Metals*, 57(5/6):559 – 581, June 2002.
- [89] Nikhil Kumar, Philip M. Besuner, Steven A. Lefton, Dwight D. Agan, and Douglas D. Hilleman. Power plant cycling costs. Technical Report AES 12047831-2-1, Intertek APTECH, April 2012.
- [90] Steven Lefton, Nikhil Kumar, Doug Hilleman, and Dwight Agan. The increased cost of cycling operations at combined cycle power plants. Technical Report TP203, Intertek APTECH – Sunnyvale, CA USA, November 2012.
- [91] Kumar Rayaprolu. *Boilers: A Practical Reference*. CRC Press, 2013.
- [92] Market Monitoring Unit ([MMU](#)). Single market electricity, power plant cycling. Technical Report SEM-10-002, Market Monitoring Unit, MMU, 2010.
- [93] Babcock & Wilcox Company (B&W). *Steam - Its generation and use*. The Babcock & Wilcox Company, 41 edition, 2005.
- [94] A. Stoppato, A. Mirandola, G. Meneghetti, and E. Lo Casto. On the operation strategy of steam power plants working at variable load: Technical and economic issues. *Energy*, 37(1):228 – 236, 2012.
- [95] S. A. Lefton, P. M. Besuner, and G. P. Grimsrud. The real cost of cycling power plants: What you don't know will hurt you. *Power*, 2002:29 – 34, November/December 2002.
- [96] K Hack and T Jantzen. Development of toolboxes for the modelling of hot corrosion of heat exchanger components (opticorr). In M Schütze and W Quadackers, editors, *Novel Approaches to Improving High Temperature Corrosion Resistance*. Elsevier, 2008.
- [97] Winny Wulandari, Geoffrey A. Brooks, M. Akbar Rhamdhani, and Brian J. Monaghan. Thermodynamic modelling of high temperature systems. In *Chemeca 2009 – Engineering our Future: Are We Up to the Challenge?*, 2009.
- [98] C.W. Bale, P Chartrand, S.A. Deckerov, G. Eriksson, K. Hack, R. Ben Mahfoud, J. Melançon, A.D. Pelton, and S. Petersen. Factsage thermochemical software and databases. *CALPHAD - Computer Coupling of Phase Diagrams and Thermochemistry*, 26:189 – 228, 2002.



- [99] C.W. Bale, E. Bélisle, P. Chartrand, S.A. Deckerov, G. Eriksson, K. Hack, I.-H. Jung, Y.-B. Kang, J. Melançon, A.D. Pelton, C. Robelin, and S. Petersen. Factsage thermochemical software and databases – recent developments. *CALPHAD - Computer Coupling of Phase Diagrams and Thermochemistry*, 33:295 – 311, 2009.
- [100] Marwa Said, Laurent Cassayre, Jean-Louis Dirion, Ange Nzihou, and Xavier Joulia. Behavior of heavy metals during gasification of phytoextraction plants: thermochemical modeling. In Khrist V. Gernaey, Jokb K. Huusom, and Rafiqul Gani, editors, *12th International Symposium on Process Systems Engineering (PSE) and 25th European Symposium on Computer Aided Process Engineering (ESCAPE), PART A*. Elsevier, 2015.
- [101] David N. French. Fuel ash corrosion. Technical report, David N. French, 1996.
- [102] Rudy Michel, Mohamed Ramzi Ammar, Jacques Poiriern, and Patrick Simon. Phase transformation characterization of olivine subjected to high temperature in air. *Ceramics International*, 39:5287 – 5294, 2013.
- [103] Dietmar Lobe. Schaeffler-diagramm, December 2015.
- [104] Mohammed Saber. *Experimental and Finite Element Studies of Creep and Creep Crack Growth in P91 and P92 Weldments*. Phd thesis, The University of Nottingham, Faculty of Engineering. Department of Mechanical, Materials and Manufacturing Engineering, September 2011.
- [105] A. H. Yaghi, T. H. Hyde, A. A. Becker, and W. Sun. Finite element simulation of residual stresses induced by the dissimilar welding of a p92 steel pipe with weld metal in625. *International Journal of Pressure Vessels and Piping*, 111-112:173 – 186, 2013.
- [106] Kent K. Coleman and W. F. Newell Jr. P91 and beyond - - welding the new-generation cr-mo alloys for high-temperature service. *Welding Journal*, pages 29 – 33, August 2007.
- [107] ThyssenKrupp Materials International. Alloy steel tubes for high temperature service – material datasheet, p91, t91 (x10crmovnb9-1), October 2011.
- [108] Vallourec. Vm12-shc technical-datasheet, v b01b0015b-15gb, November 2014.
- [109] Patrick Bullinger. Enhanced water/steam cycle for advanced combined cycle technology. In *Power Gen Asia*, October 2012.
- [110] Andreas Thomas and Peter Seliger. Creep properties and damage behaviour of component-like tubes of vm12 materials. *Materials at High Temperatures*, 28(2):114 – 119, June 2011.

- [111] Chengyu Chi, Hongyao Yu, and Xishan Xie. Advanced austenitic heat-resistant steels for ultra-super-critical (usc) fossil power plants. *IntechOpen Journal*, December 2011.
- [112] Salzgitter Mannesmann Stainless Tubes GmbH. *Boiler Grade DMV 347 HFG*. Salzgitter Mannesmann Stainless Tubes GmbH, 2008.
- [113] Salzgitter Mannesmann Stainless Tubes GmbH. *DMV 347 HFG - Datasheet*. Salzgitter Mannesmann Stainless Tubes GmbH, 2008.
- [114] Salzgitter Mannesmann Stainless Tubes GmbH. Boiler grade dmv 304 hcu, smst-tubes dmv 304hcu 04/2008, April 2008.
- [115] Salzgitter Mannesmann Stainless Tubes GmbH. Datasheet dmv 310 n, November 2008.
- [116] Salzgitter Mannesmann Stainless Tubes GmbH. Boiler grade dmv 310 n, smst-tubes dmv 310 n 04/2008, April 2008.
- [117] V. G. Behal and Albert S. Melilli, editors. *Stainless Steel Castings*, volume ASTM Special Technical Publication 756, 1916 Race Street, Philadelphia, 1980.
- [118] W. Wessling and G. Schubert. Schmiedewerkstoffe für korrosionsbeanspruchung (aus schmiedestücke im maschinen- und anlagenbau). *Schmiede Journal*, 1984.
- [119] James L. Smialek. A deterministic interfacial cyclic oxidation spalling model. *Acta Materialia*, 51:469 – 483, 2003.
- [120] Reinhard Knödler, Stefan Straub, and Brendon Scarlin. Oxidation of steels and coatings during exposure in a bypass of a steam power plant at 605 – 637 °c. correction and investigations of the morphology of the layers. *VGB*, 9, 2008.
- [121] M. G. Hebsur and R. V. Miner. High temperature isothermal and cyclic oxidation behavior of a single crystal ni base superalloy. *J. Materials For Energy Systems, ASM International*, 8(4):363 – 370, 1987.
- [122] D.K. Das, Vakil Singh, and S.V. Joshi. The cyclic oxidation performance of aluminide and pt-aluminide coatings on cast ni-based superalloy cm-247. *Journal of Metals: JOM-e*, 52(1), 2000.
- [123] Dionisio Laverde, Tomas Gomez-Acebo, and Francisco Castro. Continuous and cyclic oxidation of t91 ferritic steel under steam. *Corrosion Science*, 46:613 – 631, 2004.
- [124] Bingtao Li. *Long-term cyclic oxidation behavior of wroughtcommercial alloys at high temperatures*. PhD thesis, Iowa State University, 2003.

- [125] Z Grzesik, K. Takahiro, S. Yamaguchi, and K. Hashimoto. An RBS study of the sulphidation behaviour of niobium and nb–al alloys. *Corrosion Science*, 37:801 – 810, 1995.
- [126] Petar Agatonovic. Damaging process in creep-fatigue-oxidation environment and its consideration in life prediction, (undated).
- [127] S. Kiamehr, K. V. Dahl, M. Montgomery, and M. A. J. Somers. KCl-induced high temperature corrosion of selected commercial alloys. *Materials and Corrosion*, 2015.
- [128] Philip A. Schweitzer. *Metallic Materials: Physical, Mechanical, and Corrosion Properties*. Marcel Dekker Inc., 2<sup>2</sup> edition, 2003.
- [129] K. Natesan, A. Purohit, and D. L. Rink. Coal-ash corrosion of alloys for combustion power plants. Technical report, Argonne National Laboratory, 9700 South Cass Avenue, Argonne, IL 60439, 2003.
- [130] Bettina Bordenet. *High Temperature Corrosion in Gas Turbines: Thermodynamic Modelling and Experimental Results*. Doktorarbeit, Rheinisch-Westfaelischen Technischen Hochschule Aachen, Feb 2004.
- [131] Bettina Bordenet and Frank Kluger. Thermodynamic modelling of the corrosive deposits in oxy-fuel fired boilers. *Materials Science Forum*, 595–98(1):261–269, 2008.
- [132] Bernard S. Covino Jr., James H. Russell, Stephen D. Cramer, Gordon R. Holcomb, Sophie J. Bullard, Margaret Ziomek-Moroz, and Steven A. Matthes. The role of ash deposits in the high temperature corrosion of boiler tubes. Technical report, U. S. Department of Energy, Albany Research Center, 2003.
- [133] Stephen M. Copley, William P. Koster, Klaus M. Zwilsky, Edward L. Langer, and Robert D. Halverstadt. *ASM Handbook: Volume 4 - Heat Treating*, volume 4. ASM International, 1991.



# Index

Page numbers written in **bold** refer to the page where the corresponding entry is described, an *italic* page number indicates the secondary reference, and an n or f after a page number denotes that the item appears in a footnote or a figure respectively.

## A

### Alloying elements

Chromium .....	132
Manganese .....	133
Molybdenum .....	133
Nickel .....	133
Niobium .....	134

### Alloys

CMSX-4 .....	50
DMV304 HCu .....	81
DMV310 N .....	82
ferritic alloys .....	40
HCM12 .....	40
heat resistant .....	40
low-Cr .....	40
T122 .....	41
T347-HFG .....	81
T91 .....	79
TP304 .....	81
TP316H .....	81
TP321H .....	81
TP347 H .....	81
TP92 .....	41
VM12-SHC .....	81
X20CrMoV11-1 .....	81
X20CrMoV12-1 .....	81

### Analytical methods

Light (optical) microscopy .....	89
----------------------------------	----

SEM-EDS .....	89
---------------	----

sputtering .....	89
------------------	----

Austenitic steels .....	135, 135, 138
-------------------------	---------------

## B

baseload .....	1, 2, 2, 5, 6
----------------	---------------

### Boiler

coal-fired .....	38, 45
<i>corrosion</i> .....	47f
<i>heat transfer surfaces</i> .....	46
pulverized fuel .....	46
superheater and reheater tubes ..	38
<i>tubes</i> .....	40
water wall tubes .....	38

## C

Capacity factor .....	152n
-----------------------	------

Carburization .....	45
---------------------	----

CCGT .....	12
------------	----

Chlorination, Cl-corrosion .....	46
----------------------------------	----

COSP .....	95
------------	----

Modeling development .....	95
----------------------------	----

Cyclic oxidation testing .....	48
--------------------------------	----

Cyclic oxidation tests .....	86
------------------------------	----

Cycling .....	2, 10
---------------	-------

cold start .....	1, 14
------------------	-------

hot start .....	1, 14
-----------------	-------

warm start .....	1, 14
------------------	-------

**D**

- DMV304 HCu  
 cyclic oxidation ..... 125  
 description ..... 81  
 isothermal oxidation ..... 111
- DMV310 N  
 cyclic oxidation ..... 128  
 description ..... 82  
 isothermal oxidation ..... 113

**E**

- Ellingham diagram ..... 19  
 oxides ..... 21f  
 sulphides ..... 20n, 149f
- Energiewende ..... 1, 2  
 technical challenges ..... 4
- External oxidation ..... 42
- external stress ..... 37

**F**

- FactSage ..... 58  
 compound database ..... 58  
 solution database ..... 58
- Ferritic-martensitic steels ..... 134, 137
- fireside corrosion ..... 39
- flexibility ..... 1
- Flue gas velocity ..... 137
- Fly ash  
 composition ..... 61  
 thermodynamic modeling ..... 61
- free Cr-content ..... 82
- Fukushima ..... 2

**G**

- Galvanized corrosion ..... 16
- Gibbs energy ..... 57, 58  
 minimization ..... 57, 58
- Gibbs free energy ..... 18, 18, 19  
 minimization ..... 20
- Grain boundary attack ..... 135

**H**

- Heat treatment  
*annealing* ..... 151  
 normalizing ..... 151  
 process annealing ..... 151
- Heat treatment ..... 81  
 normalized ..... 81  
 quenching ..... 81  
 solution treatment ..... 81  
 tempered ..... 81
- High temperature corrosion  
 Carburization ..... 15  
 dry corrosion ..... 15  
 Oxidation ..... 15  
 scaling ..... 15  
 Sulphidation ..... 15
- hot corrosion ..... 39

**I**

- Internal oxidation ..... 42
- Isothermal oxidation tests ..... 82  
 continuous ..... 48  
 discontinuous ..... 48
- Isothermal stability diagrams ..... 24
- ITDS ..... 58

**L**

- Localized corrosion  
 crevice ..... 16  
 pitting ..... 16

**M**

- Material degradation mechanisms  
*creep* ..... 52  
*elephant skin (cracking)* ..... 54  
*fatigue* ..... 52  
*fireside corrosion* ..... 43, 54  
*fouling* ..... 46  
*furnace wall corrosion* ..... 54  
*hot corrosion* ..... 44  
*slagging* ..... 46

- stress cracking corrosion* ..... 53  
 mechanical stress ..... 37  
 micro-environments ..... 25  
 Model flue gas mixture composition .. 85
- N**
- Nominal power, output, capacity ... 11n,  
     152n  
 nuclear power ..... 2
- O**
- Oxidation ..... 39, 42  
     rate ..... 40  
 Oxidation kinetics ..... 91  
 oxide morphology ..... 134  
 Oxide stress relief mechanisms ..... 49n
- P**
- Parabolic rate kinetics ..... 92  
 Pilling Bedworth ratio ..... 30  
 predominance area diagrams ..... 24
- Q**
- quenching ..... 81
- R**
- Reheater ..... 2, 43
- S**
- Sample preparation  
     etching ..... 88  
     grounding ..... 88  
     mounting ..... 88  
     polishing ..... 88  
     sectioning ..... 88  
 solution treatment ..... 81  
 Spallation ..... 23, 136
- specific weight change ..... 91  
 steam-side oxidation ..... 39  
 Sulphidation ..... 42, 46  
 Superheater ..... 2, 43
- T**
- T91  
     cyclic oxidation ..... 118  
     description ..... 79  
     isothermal oxidation ..... 102  
 thermal stress ..... 37  
 Thermodynamic activity ..... 18  
 Thermodynamic modeling ..... 57  
     fly ash ..... 61  
     Gas metal equilibria ..... 62  
     Gas phase equilibria ..... 58  
     two phase flow model ..... 71  
 Thermogravimetric testing ..... 48  
 tie lines ..... 22  
 TP347-HFG  
     cyclic oxidation ..... 123  
     description ..... 81  
     isothermal oxidation ..... 108  
 Two-shifting ..... 1n
- U**
- Uniform corrosion ..... 16
- V**
- Vapour species diagrams ..... 22  
 variable RES ..... 1  
 VM12-SHC  
     cyclic oxidation ..... 120  
     description ..... 81  
     isothermal oxidation ..... 105





